Impact of tropical and boreal biomass burning on atmospheric composition

By

Margaret Bruckner

A dissertation submitted in partial fulfillment of
the requirements for the degree of

Doctor of Philosophy
(Atmospheric and Oceanic Sciences)

at the
UNIVERSITY OF WISCONSIN-MADISON
2024

Date of final oral examination: 8/12/2024

The dissertation is approved by the following members of the Final Oral Committee:
R. Bradley Pierce, Professor, Atmospheric and Oceanic Sciences (AOS)
Tracey Holloway, Professor, AOS and Nelson Institute for Environmental Studies
Matthew H. Hitchman, Professor, AOS
Jack Fishman, Professor, Saint Louis University, Department of Earth and Atmospheric Sciences
Daniel J. Vimont, Professor, AOS

Dissertation Declaration and Approval

I, Margaret Bruckner, declare that this Dissertation titled ‘Impact of tropical and boreal biomass burning on atmospheric composition’ and the work presented in it are my own.

Margaret Bruckner		
Author	Signature	Date

I hereby approve and recommend for acceptance this work in partial fulfillment of the requirements for the degree of Doctor of Philosophy:

R. Bradley Pierce		
Committee Chair	Signature	Date
Tracey Holloway		
Faculty Member	Signature	Date
Matthew H. Hitchman		
Faculty Member	Signature	Date
Jack Fishman		
Outside Member	Signature	Date
Daniel J. Vimont		
Faculty Member	Signature	Date

Abstract

Impact of tropical and boreal biomass burning on atmospheric composition

by Margaret Bruckner

Atmospheric trace gases and aerosols emitted from biomass burning significantly influence atmospheric composition globally and locally on short-term and climatological time scales. Global chemical transport models (CTMs) can be used to predict the transport and evolution of biomass burning emissions but have high uncertainties for reasons including computational constraints on model complexity and uncertainties in biomass burning emissions inventories. Chemical data assimilation systems can be used to reduce the impacts of emissions uncertainty and model deficiencies in representing sub-grid scale processes by constraining CTM analyses with satellite atmospheric composition observations. Chemical re-analyses produce best-estimates of the real atmospheric composition through the application of chemical data assimilation. In this dissertation I evaluate how tropical biomass burning emissions impact variability in tropical tropospheric ozone concentrations and improve the representation of tropical and boreal biomass burning emissions in global CTMs. I ask how variability in tropical tropospheric ozone is related to biomass burning emissions, how well global models capture emissions from biomass burning globally, and what the contribution of biomass burning emissions is to global background air quality. First, I use a global chemical reanalysis from the Real-time Air Quality Modeling System (RAQMS) to show that variability in tropical convection and

Indonesian biomass burning emissions contribute to observed El Niño Southern Oscillation (ENSO) variability in tropical tropospheric ozone. Next, I show through comparisons with satellite, ground based, and airborne measurements that the biomass burning emissions inventory used in the Unified Forecast System/Real-time Air Quality Modeling System (UFS-RAQMS) global model significantly underestimates CO emissions from Siberian and Indonesian biomass burning in July-September 2019. I demonstrate that assimilation of satellite carbon monoxide (CO) retrievals significantly reduces this bias. I then present results from an iterative finite difference mass balance approach designed to adjust the CO biomass burning emissions. Finally, I show that the adjusted CO biomass burning emissions inventory improves agreement between UFS-RAQMS CO and observations and increases background tropospheric ozone concentrations. Due to projected increases in biomass burning in a changing climate, improved predictions of biomass burning emissions are necessary for providing accurate air quality forecasts.

Acknowledgements

There are so many people without whom this dissertation would not be possible and to who I am immensely grateful. First, my advisor Brad Pierce without whose mentorship and patience I could not have made it through graduate school. I feel lucky that I got to be your student. Thank you for your guidance on how to shape my research into a cohesive story and for putting up with the rambling mess of plots I threw in slide sets while getting to that story. Thank you for sending me on field campaigns. Field deployments were a lot of work and I didn't make much progress on this dissertation during them, but the professional connections I made during those deployments are invaluable. Thank you for supporting me through the personal setbacks, and for providing space for me to be a person when my stress levels got high.

I'd like to acknowledge Allen Lenzen for his assistance with UFS-RAQMS. Without his knowledge I would not have been able to compile the model or run the experiments. I also must acknowledge the research teams whose data I use in this work. The effort that goes into collecting, processing, and distributing the satellite, ground-based, and airborne datasets used here is immense.

During my PhD I was fortunate to be part of the forecast team for the FIREX-AQ, SABRE, and AGES+ field campaigns. These campaigns were very different from one another but all taught me a lot about the strengths and limitations of chemical forecast models. Thank you to the FIREX-AQ forecast crew- Dave, Pablo, Ed, Pete, Laura, Philippe, Francis, Christel, Melinda, Charley, and Anxhelo- for being a great group to both put together a forecast brief with and to hang out with during our down time. A great thank you to Amy, Eleanor, Rei, Troy, Sophie, and others with the SABRE campaign for your support and encouragement. I was very nervous about the responsibility of being the chemical forecaster, and y'all made me feel confident in my ability to communicate the forecast and its limitations. To Harold and Siyuan, my fellow AGES+ forecasters, it was a blast getting to know you and to work together.

I'd also like to acknowledge the other members of the MELODIES MONET development team for their support and contributions to my development as a coder. Thank you Ravan for encouraging me to try the tool during my Lapenta Internship so that I wouldn't spend too much time duplicating code for comparing HRRR-Smoke to Aeronet observations. Thank you Becky and Barry for encouraging my interest in expanding the satellite validation side of MELODIES MONET and to join the satellite team. David, Rebecca, Louisa, and Meng, thank you for all the discussions about how to generalize code and how to divide the data processing steps in order to limit memory requirements. I'm a much better coder today because of it.

Next, I'd like to express my sincere gratitude to my committee members- Matt Hitchman, Tracey Holloway, Dan Vimont, and Jack Fishman. Thank you for believing in me and trusting that I would be able complete this work. Your comments and feedback have helped me focus my dissertation as well as guided which ideas needed more developing. I always came away from our meetings feeling like I had a clearer sense of what my next step needed to be. Additional thanks to Dan for stepping in as a replacement committee member for Michael Morgan.

I'm thankful to have been part of such a vibrant, welcoming AOS community during my time in Madison. To my incoming grad cohort (Zoe, Kelton, Julia, Juliet, Miguel, Vijit, Ashtin, and Austin)- I'm thankful that due to your support I didn't struggle through this alone. To my first batch of officemates (Kelton, Austin, David, Coda, and Chuck)- thank you for helping me feel like I was part of a SSEC/CIMSS graduate student research group and providing some of the cross-group mentorship I might have gotten as part of a more formal research group. To Jerrold, Shane, Doreen, and Jongjin, my current officemates- thank you for your support and community these last few years. Jerrold and Shane, the other members of the Pierce group, you've made this experience even better by allowing me to talk in depth about air quality modeling with others and just being all around cool people. I cannot thank my writing buddy Rosa enough. Writing with you helped me push past a resistance to writing and kept me on track. Thank you to all the graduate students, faculty, and staff of AOS for intentionally building a supportive community here.

On a personal note, I'd like to acknowledge all the friends I've made during my time in Madison. To the Friday beer call gang, your congeniality and friendliness has made going to beer call a highlight of my week. I don't think I would have stayed sane during the pandemic without the social outlet. A massive thank you to my frisbee community. Zoe, I'm so glad that you invited me to join the same summer league team as you. Frisbee became an essential outlet for me. Thank you to all my Heist and Freshwater teammates- your support means the world. I'm especially thankful for your willingness to make space for me to still be involved when I tore my ACL. Thank you to everyone who drove me somewhere and checked in to see how I was doing mentally- without your support the loss of my physical outlet from work would have been a lot worse.

Finally, I'd like to thank my family for all their love and support over the years. I know you don't quite understand what I do but that you have my back in everything I do. I love you.

This dissertation was funded by the National Oceanic and Atmospheric Administration under grant no. NA20NES4320003.

Contents

List of Figures

List of Tables

Abbreviations

3Dvar	**3-D**imensional **v**ariational **D**ata **A**ssimilation
AIRS	**A**tmospheric **I**nfra**r**ed **S**ounder
AOD	**A**erosol **O**ptical **D**epth
ATom	**A**tmospheric **Tom**ography mission
BEC	**B**ackground **E**rror **C**ovariance
CAMP^{2}Ex	**C**loud, **A**erosol and **M**onsoon **P**rocesses **P**hilippines **Ex**periment
CAMS	**C**opernicus **A**tmospheric **M**onitoring **S**ervice
CB-Z	**C**arbon **B**ond mechanism - **Z**averi and Peters (1999)
CCM3	NCAR **C**ommunity **C**limate **M**odel
CEDS	**C**ommunity **E**missions **D**ata **S**ystem
CO	**C**arbon m**o**noxide
CTM	**C**hemical **T**ransport **M**odel
DA	**D**ata **A**ssimilation
DACOM	**D**ifferential **A**bsorption **C**arbon Monoxide **M**easurement
DJF	**D**ecember-**J**anuary-**F**ebruary
ENSO	**E**l **N**iño **S**outhern **O**scillation
EOF	**E**mpirical **O**rthogonal **F**unction
ESMF	**E**arth **S**ystem **M**odeling **F**ramework
LETKF	**l**ocal **e**nsemble **t**ransform **K**alman **f**ilter
FDMB	**F**inite-**D**ifference **M**ass-**B**alance
FINN	Fire Inventory from NCAR

FIREX-AQ	**F**ire **I**nfluence on **R**egional to Global **E**nvironments and **A**ir **Q**uality
FRP	**F**ire **R**adiative **P**ower
FTIR	Fourier-transform infrared spectrometer
FV3	**F**inite **V**olume Cubed Sphere
GBBEPx	Blended **G**lobal **B**iomass **B**urning **E**missions **P**roduct
GDAS	**G**lobal **D**ata **A**ssimilation **S**ystem
GEFS	**G**lobal **E**nsemble **F**orecasting **S**ystem
GFED	**G**lobal **F**ire **E**missions **D**atabase
GFS	**G**lobal **F**orecast **S**ystem
GOCART	**G**oddard **C**hemistry **A**erosol **R**adiation and **T**ransport model
GSI	**G**rid point **S**tatistical **I**nterpolation
HTAP	**H**emispheric **T**ransport of **A**ir **P**ollution
ICPP	**I**ntergovernmental **P**anel on **C**limate **C**hange
IMPACT	NASA Langley Research Center **I**nteractive **M**odeling **P**roject for **A**tmospheric **C**hemistry and **T**ransport model
ITCZ	**I**nter**t**ropical **C**onvergence **Z**one
JAS	**J**uly-**A**ugust-**S**eptember
JJA	**J**une-**J**uly-**A**ugust
MAM	**M**arch-**A**pril-**M**ay
MLS	**M**icrowave **L**imb **S**ounder
MODIS	**Mod**erate Resolution **I**maging **S**pectrometer
MOPITT	**M**easurements **o**f **P**ollution **i**n **t**he **T**roposphere
MPAN	methacryloyl peroxynitrate
NCEP	**N**ational **C**enter for **E**nvironmental **P**rediction
NDACC	**N**etwork for the **D**etection of **A**tmospheric **C**omposition **C**hange
NGFS	NOAA **N**ext **G**eneration **F**orecast **S**ystem
NMHC	**N**on-**M**ethane **H**ydro**c**arbon
NOx	**N**itrogen **Ox**ides

NUOPC	**N**ational **U**nified **O**perational **P**rediction **C**apability
OMI	**O**zone **M**onitoring **I**nstrument
PAN	**P**eroxy**a**cetyl **N**itrate
PC	**P**rincipal **C**omponent
PEM-Tropics	**P**acific **E**xploratory **M**issions in the Tropics
Pg	**P**eta**g**rams
PM	**P**articulate **M**atter
QBO	**Q**uasi-**B**iennial **O**scillation
QFED	**Q**uick **F**ire **E**missions **D**ataset
RAQMS	**R**eal-time **A**ir **Q**uality **M**odeling **S**ystem
RMSE	**R**oot **M**ean **S**quare **E**rror
SDF	**s**tatistical **d**igital **f**ilter
SHADOZ	**S**outhern **H**emisphere **Ad**ditional **Oz**onesondes
SON	**S**eptember-**O**ctober-**N**ovember
TCR-2	**T**ropospheric **C**hemistry **R**eanalysis version 2
TMPA	TRMM Multi-satellite precipitation Analysis
TOAR	**T**ropospheric **O**zone **A**ssessment **R**eport
TOR	**T**ropospheric **O**zone **R**esidual
TRMM	**T**ropical **R**ainfall **M**easuring **M**ission
TROPOMI	Tropospheric Monitoring Instrument
TTOC	**T**ropical **T**ropospheric **O**zone **C**olumn
UFS	**U**nified **F**orecasting **S**ystem
VIIRS	**V**isible **I**nfrared **I**maging **R**adiometer **S**uite
VOC	**V**olatile **O**rganic **C**arbon
WE-CAN	Western wildfire **E**xperiment for **C**loud chemistry, **A**erosol absorption and **N**itrogen

Chapter 1

Introduction

1.1 Global Impact of Wildfire on Air Quality

Wildfires, agricultural fires, and managed burns are collectively referred to as biomass burning (Wiedinmyer et al., 2011). Biomass burning is a major source of trace gases and aerosols to the atmosphere, releasing large quantities of particulate matter (PM), volatile organic carbons (VOCs), and nitrogen oxides (NOx) (Akagi et al., 2011, Andreae, 2019, Andreae and Merlet, 2001, Crutzen et al., 1979). Hereafter the mixture of trace gases and aerosols emitted from biomass burning will be referred to as wildfire smoke or biomass burning emissions. The contribution of wildfire smoke to tropospheric ozone concentrations has been estimated to be nearly equal that of urban anthropogenic emissions in the tropics and Northern Hemisphere and be 2-10 times the contribution of urban emissions in the Southern Hemisphere (Bourgeois et al., 2021). Global biomass burning emissions peak in August-September due to the combined influence of temperate and boreal burning seasons in the Northern Hemisphere and the burning seasons for Southern Hemisphere Africa and South America (van der Werf et al., 2017, Wiedinmyer et al., 2023). Biomass burning in tropical regions accounts for a significant percentage of both the global burned area and biomass burning emissions (Liu and Ding, 2024, van der Werf et al., 2017). Boreal biomass burning accounts for less than 5% of the global burned area at present but contributes ∼9% of the global biomass burning emissions (Liu and Ding, 2024, van der Werf et al., 2017).

Biomass burning emissions influence air quality on local, regional, and global scales. Elevated tropospheric ozone over the South Atlantic was first linked to African biomass burning emissions through use of in-situ and satellite measurements (Fishman et al., 1991, Watson et al., 1990). Aircraft observations from campaigns such as the Pacific Exploratory Missions in the Tropics (PEM-Tropics) further elucidated that biomass burning emissions from fires in South Africa and South America are lofted into the troposphere and then transported throughout the Southern Hemisphere (Singh et al., 2000). The NASA Atmospheric Tomography Missions (ATom) campaign, consisting of 4 flight campaigns between 2016 and 2018, found global chemical transport models underpredict the contribution of wildfire smoke to background tropospheric ozone (Bourgeois et al., 2021). The 2019 NASA/NOAA Fire Influence on Regional to Global Environments and Air Quality (FIREX-AQ) (Warneke et al., 2023) and the 2018 Western wildfire Experiment for Cloud chemistry, Aerosol absorption and Nitrogen (WE-CAN 2018) (Lindaas et al., 2021, Permar et al., 2021) campaigns produced improved emission factors for vegetation types in the US (Gkatzelis et al., 2024). Emissions from boreal biomass burning can be injected into the upper troposphere, or even the lower stratosphere, as a result of convection and pyro convection (e.g. Lewis et al., 2013, Parrington et al., 2013, Peterson et al., 2015, Yu et al., 2019). Emissions from Siberian biomass burning have been found to influence surface ozone and particulate matter concentrations in North America (e.g. Cottle et al., 2014, Jaffe et al., 2004).

Atmospheric dynamics significantly influence the distribution of ozone and ozone precursors. Large-scale dynamical transport patterns leave signatures in O_3. El Niño-Southern Oscillation (ENSO) is a major driver of interannual variability in both tropical and mid-latitudes (e.g. McPhaden et al., 2006, Trenberth, 1997), and has been found to be a dominant driver of interannual variability in the distribution of tropospheric ozone in the tropical Pacific (e.g. Doherty et al., 2006, Oman et al., 2013, Peters et al., 2001, Sekiya and Sudo, 2012, Ziemke et al., 2010). ENSO variability in tropical tropospheric ozone columns has been reproduced in chemical transport models and climate models (e.g. Chandra et al., 2002, Doherty et al., 2006, Peters et al., 2001, Sekiya and Sudo, 2014, Sudo and Takahashi, 2001). Biomass burning in the maritime continent is strongly related to ENSO, with increased occurrence in El Niño due to enhanced drying of the peatlands (van der Werf et al., 2008, 2017). van der Werf et al. (2008) found that biomass burning emissions from Borneo were more than 30 times larger in El Niño years due to the combined effect of drought on peatlands and deforestation. ENSO variability in equatorial Pacific tropospheric ozone was initially thought to be equally due to shifts in biomass burning emissions and meteorological conditions (Chandra et al., 2002, Sudo and

Takahashi, 2001). More recent studies postulate that enhancement in biomass burning during El Niño results in regional enhancement of ozone with little contribution to global tropospheric ozone variability and that the response of tropospheric ozone to ENSO is primarily due to dynamical processes (e.g. Doherty et al., 2006, Inness et al., 2015a). In Chapter 3 I revisit the contributions of biomass burning and dynamics to ENSO variability in tropical tropospheric ozone by using a global chemical reanalysis to evaluate the roles of dynamics and biomass burning in tropical tropospheric ozone variability.

In recent years, summertime surface air quality in the continental United States has been significantly degraded due to the influx of wildfire smoke. In 2020 extreme wildfire activity in the Western US degraded air quality both near the fires in California, Oregon, and Washington as well as far downwind along the east coast of the US (Eck et al., 2023, Li et al., 2021, Makkaroon et al., 2023). In 2023, Canadian wildfires burned a record 18.4 million hectares, above the 10-year average of 2.7 million hectares and more than doubling the previous record of 7.6 million hectares in 1989 (`https://cwfis.cfs.nrcan.gc.ca/report`). Transported smoke from the 2023 Canadian wildfires resulted in hazardously degraded surface air quality in US cities at various points from May through September. US wildfire emissions, and associated surface air pollution, are projected to increase under climate change (Abatzoglou and Williams, 2016, Liu et al., 2021, Tian et al., 2023, Xie et al., 2022, Yue et al., 2015).

Climate change projections show significant alterations to global biomass burning activity and emissions (e.g. Chen et al., 2023, Senande-Rivera et al., 2022, Zheng et al., 2021).

Spatiotemporal variability in biomass burning is strongly determined by climate factors including precipitation, temperature, relative humidity, and wind (e.g. Abatzoglou and Williams, 2016, Archibald et al., 2013, Jolly et al., 2015). Land management practices also impact fire activity (e.g. Andela et al., 2017, Archibald et al., 2013, Deeter et al., 2018, Miettinen et al., 2017). Global burned area has declined by 24% since 2000, though this is primarily due to decreases in tropical biomass burning regions (Chen et al., 2023, Jones et al., 2022). Burned area trends in temperate and boreal regions are slightly increasing, though the trend is not significant. Metrics based on fire season length, precipitation, temperature anomaly, and fire frequency have been used to explain the observed changes in global burned area (e.g. Abatzoglou and Williams, 2016, Jolly et al., 2015) and project future changes (e.g. Senande-Rivera et al., 2022). The number fire-prone years per decade used by Senande-Rivera et al. (2022) aggregates climatic influences on fire activity. A year is classified as fire-prone when at least one month per year has a high likelihood of fire occurrence. The number of fire-prone years per decade is projected to increase by >4 between 1996–2016 and 2070-2099 in boreal North America and Siberia (Figure 1.1)(Senande-Rivera et al., 2022).

Associated with the climatic change in biomass burning activity, biomass burning emissions are also changing. Global carbon monoxide column concentrations have declined since the 2000s (Buchholz et al., 2021, Jiang et al., 2017, Zheng et al., 2019). While globally carbon monoxide and burned area are decreasing, trends in global biomass burning emissions are not significant (van der Werf et al., 2017, Wiedinmyer et al., 2023, Zheng et al., 2021). Regional trend analyses show that increased emissions from biomass burning

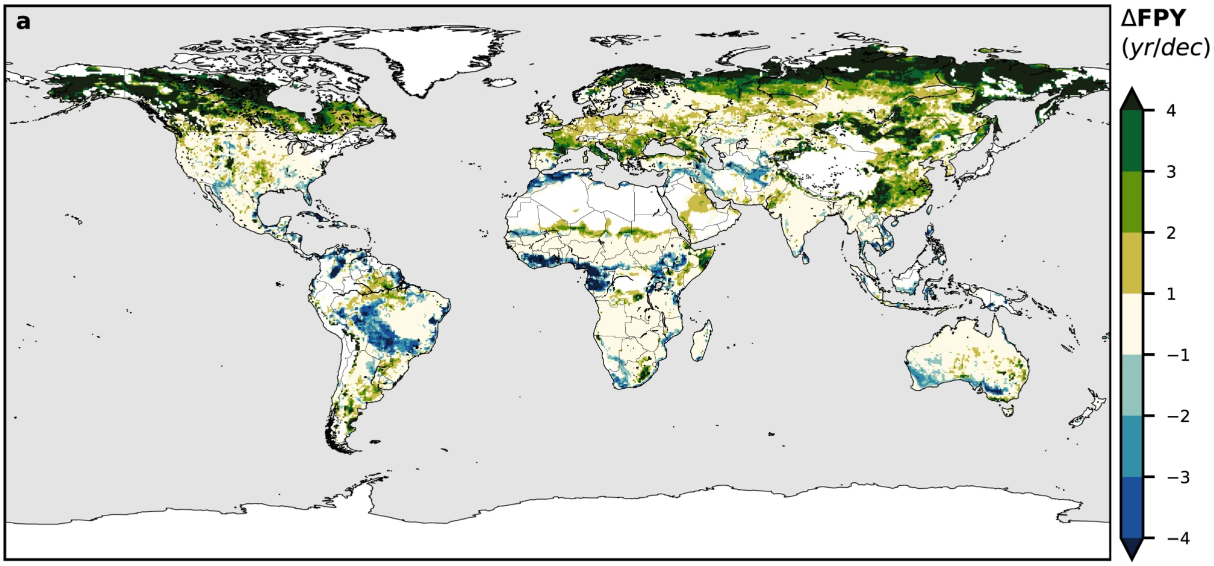

Figure 1.1: Projected increase in number of fire-prone years per decade by 2070-2099. From Senande-Rivera et al. (2022) Figure 4.

in forests and boreal areas compensate for decreased emissions from tropical regions (Liu and Ding, 2024, Zheng et al., 2021). Biomass burning emissions inventories have high uncertainties, as discussed in section 1.2.1, and present a significant challenge to modeling tropospheric air quality (Archibald et al., 2020, and references therein). Inverse methods have been used to infer biomass burning emissions based on observed atmospheric composition (e.g. Gaubert et al., 2023, Jiang et al., 2017).

1.2 Ozone production from biomass burning

The VOCs and NOx emitted from biomass burning produce tropospheric ozone as a secondary pollutant during photochemical reactions. A schematic including the generalized framework for VOC-NOx-O_3 chemistry is shown in Figure 1.2. In brief, tropospheric ozone is produced in-situ through a complex series of cyclical reactions involving VOCs

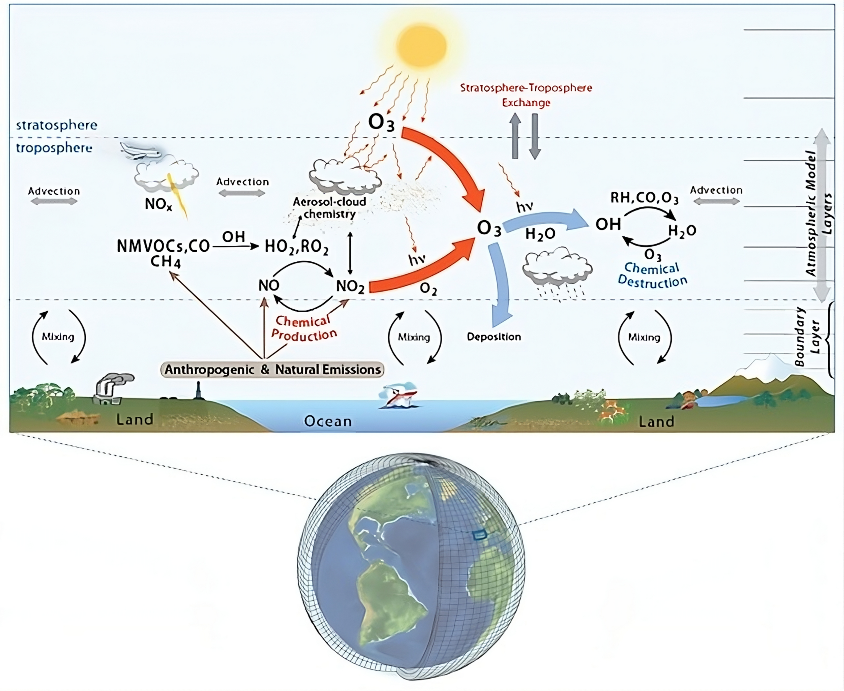

FIGURE 1.2: Schematic of chemical and physical processes controlling tropospheric ozone concentrations. From Young et al. (2018).

and NOx. VOC oxidation products initiate chemical cycling of NOx, which produces O_3. In non-urban environments, the main sources of NOx are lightning and peroxyacetyl nitrate (PAN) (Archibald et al., 2020). PAN is a temporary reservoir species for NOx and produces ozone away from the source region when it thermally decomposes.

NOx emitted from biomass burning can be temporarily sequestered as PAN (Jaffe and Wigder, 2012). For biomass burning emissions plumes containing large emissions of VOCs, and smaller NOx/CO ratios, rapid sequestration of NOx as PAN occurs (Jaffe and Wigder, 2012).

While not directly involved in the VOC-NOx-O3 chemistry, aerosol emissions from biomass burning increase aerosol optical depth, thereby reducing transmission of solar radiation and limiting production of the OH radical (Jaffe and Wigder, 2012). Natarajan et al. (2012) shows biomass burning aerosol emissions increase AOD and significantly impact regional radiative forcing. Martin et al. (2003b) finds that aerosols decrease photolysis frequencies.

1.2.1 Uncertainties in biomass burning emissions inventories

Estimates of biomass burning emissions provided through emissions inventories vary significantly from one another (Pan et al., 2020, Stockwell et al., 2022, Wiedinmyer et al., 2023). Following the pioneering work of Seiler and Crutzen (1980), biomass burning emissions inventories are an accounting of chemical mass emitted from a species as function of the dry matter burned and an emission factor. Improvements in biomass burning emissions inventories have been achieved through increasing incorporation of satellite observations (Chuvieco et al., 2019, Wooster et al., 2021). The use of satellite observations has gradually increased the temporal resolution of biomass burning emissions inventories from annual (e.g. Lobert et al., 1999) to monthly (e.g. Duncan et al., 2003) to daily (e.g. Al-Saadi et al., 2008, Wiedinmyer et al., 2006, Zhang et al., 2019) or greater (e.g. van der Werf et al., 2017, Wiggins et al., 2020). Modern emissions inventories utilize satellite observations to calculate emissions using either a burned area-based approach (e.g. van der Werf et al., 2017, Wiedinmyer et al., 2011, 2023) or a fire radiative power approach (e.g. Darmenov and da Silva, 2015, Kaiser et al., 2012, Zhang et al., 2019).

Burned area-based approaches for calculating biomass burning emissions rely on estimates of burned area, biomass density, and fuel consumption. These quantities are difficult to measure on a global scale. Top down, fire radiative power (FRP)-based approaches like the Blended Global Biomass Burning Emissions Product (GBBEPx) (Zhang et al., 2019), the Quick Fire Emissions Dataset (QFED) (Darmenov and da Silva, 2015), and the Global Fire Assimilation System (GFAS) (Kaiser et al., 2012) avoid this by calculating emissions using FRP and combustion rate following from the linear relationship between the energy and mass emitted by biomass burning (Wooster et al., 2003).

The incomplete knowledge of the spatiotemporal distribution of emissions sources and limitations in capturing variation in fuel and fire behavior characteristics contribute to differences between inventories (e.g. Hyer and Reid, 2009, Pan et al., 2020). Predictions from chemical transport models (CTMs) will vary significantly depending on which biomass burning emission inventory is used (e.g. Bian et al., 2007, Pan et al., 2020, Stockwell et al., 2022).

1.3 Real-time Air Quality Modeling System (RAQMS)

In this dissertation I use two versions of the Real-time Air Quality Modeling System (RAQMS) (Pierce et al., 2007). RAQMS is a global chemical transport model with full stratospheric and tropospheric chemistry. Here I will briefly discuss the evolution of RAQMS and key implementations. Additional detail regarding the versions of RAQMS I use is presented in Chapter 2.

Development of RAQMS began in the early 2000s as a collaboration between scientists at the NASA Langley Research Center and the University of Wisconsin. RAQMS was originally titled the Regional Air Quality Modeling System and was envisioned as a multi-scale modeling system (Pierce et al., 2003). The global component of RAQMS combined the chemistry module from the NASA Langley Research Center Interactive Modeling Project for Atmospheric Chemistry and Transport (IMPACT) model (Eckman et al., 1995, Pierce et al., 2000) with the UW hybrid model dynamical core (Schaack et al., 2004). Biomass burning CO emissions were originally specified with a seasonally varying climatology (Duncan et al., 2003).

Non-methane hydrocarbon (NMHC) chemistry and chemical data assimilation was later added to RAQMS (Pierce et al., 2009, 2007), and the resulting configuration has been run during various field campaigns since the late 2000s and continuously since the early 2010s. Pierce et al. (2007) incorporated the lumped-structure Carbon Bond Mechanism Z (CBM-Z) (Zaveri and Peters, 1999) that was modified with an expanded isoprene oxidation mechanism. Biomass burning emissions in RAQMS were updated from a climatology to daily ecosystem and fire intensity based emissions estimates calculated using Moderate Resolution Imaging Spectroradiometer (MODIS) fire detections (Soja et al., 2004). RAQMS real-time chemical analyses assimilate satellite ozone and AOD observations with the statistical digital filter (SDF) (Stobie, 2000) to constrain the model first-guess.

A RAQMS chemical reanalysis for the 2006-2016 period was conducted in the late 2010s and constrains RAQMS chemical analyses with trace gas and aerosol retrievals from the Terra, Aqua, and Aura satellites using 3d variational data assimilation (Bruckner et al., 2024). During this same period, the RAQMS chemistry module has been incorporated into NOAA's next generation forecast system (NGFS), replacing the UW-Hybrid dynamical core with the NOAA Unified Forecasting System (UFS) and replacing the RAQMS biomass burning emissions inventory with the Blended Global Biomass Burning Emissions Product (GBBEPx) (Zhang et al., 2019).

1.3.1 Biomass burning emissions in RAQMS

Biomass burning emissions in RAQMS-Aura use Terra and Aqua MODIS fire detections and are calculated using a bottom-up approach developed by Soja et al. (2004) and compared to other approaches in Al-Saadi et al. (2008). The methodology used is an expansion of the burned-area based approach of Seiler and Crutzen (1980). The approach estimates total carbon emissions at MODIS fire detections and uses the US Forest Service Haines Index (Haines, 1989) to determine fire severity and gridded, ecosystem-dependent estimates of carbon consumption for low, medium, and high fire severity fires. Emission ratios are then used to estimate emissions of CO, NOx, and hydrocarbons from the calculated total carbon emissions. Al-Saadi et al. (2008) compared the RAQMS CO emissions to three other inventories, finding similarity in the distribution of CO emissions but large uncertainty in the area burned. Globally in 2006, RAQMS real-time predictions underestimated CO columns relative to MOPITT in the northern hemisphere.

GBBEPx CO emissions are used in UFS-RAQMS in place of the burned area-based approach used by RAQMS real-time and the RAQMS-Aura chemical reanalysis. GBBEPx calculates daily biomass burning emissions using FRP estimates from MODIS and the

Visible Infrared Imaging Radiometer Suite (VIIRS). GBBEPx blends VIIRS-based emissions with MODIS-based emissions provided by QFED.

1.4 Dissertation overview

Modeling uncertainties pertaining to biomass burning emissions include: 1) transport errors, 2) injection height errors, and 3) errors and omissions in biomass burning emissions. My dissertation addresses some of these uncertainties as I seek to further improve our ability to model ozone production from biomass burning. The overarching questions of my Ph.D. work are:

1) How is variability in tropical tropospheric ozone related to biomass burning emissions?

2) How well do global models capture emissions from biomass burning?

3) What is the contribution of biomass burning emissions to global background air quality?

Chapter 2 provides details about the CTMs, analysis techniques, and observational datasets used in this dissertation. Chapter 3 addresses question 1 using the RAQMS Aura Re-analysis, ENSO compositing, and Empirical Orthogonal Function analysis and other statistical techniques to understand how variability in biomass burning and dynamics relate to tropical tropospheric ozone variability. Chapter 4 address question 2 by evaluating biomass burning emissions in UFS-RAQMS. Answering question 3 requires accurate CO biomass burning emissions in UFS-RAQMS since VOC and NOx emissions are obtained through applying emission factors to the CO emissions. Chapter 5 focuses on obtaining accurate CO biomass burning emissions, which are then used in Chapter 6 to evaluate the contribution of biomass burning to global background concentrations of CO, O_3, and other atmospheric constituents.

Chapter 2

Data and Methodology

Within this dissertation I evaluate analyses from RAQMS-Aura and UFS-RAQMS with in-situ and remote sensing atmospheric composition observations. This chapter describes the RAQMS models used in this study, and the observational datasets used.

2.1 RAQMS

RAQMS is a global chemical transport model with full stratospheric and tropospheric chemistry (Pierce et al., 2009, 2007). RAQMS utilizes a family approach to reduce the number of species considered in the chemical mechanism, requiring solving of continuity equations for 55 chemical families and constituents and determination of equilibrium concentrations for 86 separate species (Pierce et al., 2007). Non-methane hydrocarbon chemistry in RAQMS follows the lumped-structure Carbon Bond Mechanism Z (CB-Z)

(Zaveri and Peters, 1999), which was modified in Pierce et al. (2007) to include an explicit isoprene oxidation scheme. Standard hydrogen oxide (HOx), chlorine oxide (ClOx), bromine oxide (BrOx), and NOx ozone photochemistry (Eckman et al., 1995) is also included.

Here I describe two versions of RAQMS used in this study. The first is a RAQMS chemical reanalysis for the period 2006 through 2016. The second is a new generation of RAQMS where the RAQMS chemistry modules have been incorporated into NOAA's Unified Forecasting System (UFS).

2.1.1 RAQMS-Aura Reanalysis

The RAQMS-Aura Reanalysis is a chemical re-analysis that constrains RAQMS chemical predictions with satellite trace gas and aerosol retrievals from the NASA satellites (Terra, Aqua, and Aura) covering 2006 through 2016. RAQMS-Aura provides 1°x1° global chemical analyses, on 35 hybrid model levels from the surface to approximately 60 km above ground level, at 3-hour time steps. The operational grid point statistical interpolation (GSI) 3-dimensional variational analysis system (Wu et al., 2002) is used to assimilate retrievals from the following Aura instruments: Aura Ozone Monitoring Instrument (OMI) cloud cleared total column ozone (McPeters et al., 2008), Microwave Limb Sounder (MLS) (Froidevaux et al., 2008) stratospheric ozone profiles, and OMI tropospheric column NO_2 (Boersma et al., 2007, Bucsela et al., 2013). NASA Terra and Aqua Moderate Resolution Imaging Spectrometer (MODIS) aerosol optical depth (AOD) (Remer et al., 2005) and Atmospheric Infrared Sounder (AIRS) carbon monoxide profile (Maddy and Barnet, 2008, McMillan et al., 2005, Yurganov et al., 2008) are also assimilated at three-hour intervals. Analysis increments from the OMI tropospheric column NO2 retrievals are used for off-line adjustment of apriori 2010 Hemispheric Transport of Air Pollution (HTAP, 2010) anthropogenic emission inventories following an offline mass balance approach similar to East et al. (2022). RAQMS-Aura biomass burning emissions of CO, NOx, and hydrocarbons are obtained through applying emissions ratios to total carbon emissions calculated from Terra and Aqua MODIS fire detections and fire severity (Al-Saadi et al., 2008, Soja et al., 2004).

The dynamical core of RAQMS is the UW hybrid model (Schaack et al., 2004). The UW hybrid model utilizes physical parameterizations from the NCAR Community Climate Model (CCM3) (Kiehl et al., 1998), including the moist convection scheme. The CCM3 moist convection scheme combines the Zhang and McFarlane (1995) deep convection scheme with shallow and midlevel convection following Hack (1994). The deep convection scheme treats convection as an ensemble of updrafts and downdrafts, and the shallow convection scheme treats convection as separate plumes within 3 successive layers whereby mass is detrained from one layer into the next (Kiehl et al., 1998, Zhang et al., 1998). RAQMS-Aura initializes its meteorological fields with archived analyses from the National Center for Environmental Prediction (NCEP) Global Data Assimilation System (GDAS) (Kleist et al., 2009, Wang et al., 2013). These fields are impacted by updates to physics, resolution, and data assimilation used in the GDAS system (`https://www.emc.ncep.noaa.gov/gmb/STATS/html/model_changes.html`, last access: 4 August 2024).

2.1.2 UFS-RAQMS

UFS-RAQMS is an updated version of RAQMS where the RAQMS stratosphere/troposphere chemistry modules are coupled to NOAA's Unified Forecast System (UFS) version 9.1 Finite Volume Cubed Sphere (FV3) dynamical core (Harris and Lin, 2013, Putman and Lin, 2007). The UFS-RAQMS configuration utilized in Chapters 4-6 of this dissertation is an extension of the operational NOAA Global Ensemble Forecasting System with Aerosols (GEFS-Aerosols) (Bhattacharjee et al., 2023, Zhang et al., 2022). GEFS-Aerosols includes bulk aerosol modules from the Goddard Chemistry Aerosol Radiation and Transport model (GOCART) (Chin et al., 2002).

The extension is accomplished by coupling RAQMS chemistry, photolysis, and wet and dry deposition modules with the UFS dynamical core through the National Unified Operational Prediction Capability (NUOPC, `https://earthsystemmodeling.org/nuopc/`) layer. The NUOPC layer defines conventions and generic components for building coupled models using the Earth System Modeling Framework (ESMF, `https://earthsystemmodeling.org`). This NUOPC based coupling allows the GOCART aerosol predictions to impact the RAQMS Fast-J2 (Bian and Prather, 2002) photolysis scheme and also allows the RAQMS OH and H_2O_2 predictions to impact the GOCART sulfate aerosol formation.

In this study I conduct UFS-RAQMS retrospective simulations during July 15, 2019 through September 30, 2019 at a Cubed Sphere resolution of 192 (C192, 192x192 gridpoints within each 6 cubes or approximately 0.5° x 0.5° horizontal resolution) with 64 hybrid vertical levels from the surface to upper stratosphere (approximately 0.2hPa). The UFS-RAQMS atmospheric composition experiments are conducted in “replay” mode, with UFS-RAQMS meteorological fields initialized with GFS analyses at 6-hour intervals followed by 6-hour UFS-RAQMS forecasts. UFS-RAQMS was initialized on July 15^{th}, 2019 at 12Z with 1x1 degree analyses from the real-time RAQMS system, which includes assimilation of NASA MODIS AOD on the Terra and Aqua satellites and the NASA OMI cloud cleared total column ozone and MLS stratospheric ozone profiles. Global anthropogenic emissions in UFS-RAQMS are obtained from the Community Emissions Data System (CEDS) (McDuffie et al., 2020). Daily global biomass burning CO emissions are specified from GBBEPx (Zhang et al., 2019) and expanded using species-specific emissions factors from the RAQMS biomass burning scheme (Soja et al., 2004). FRP is used to calculate GBBEPx plume rise. GBBEPx calculates daily biomass burning emissions using observations of FRP from MODIS (Aqua and Terra satellites) and VIIRS (Suomi NPP and NOAA-20 satellites). Additional details on GBBEPx will be discussed in Chapter 4 and Chapter 5.

UFS-RAQMS forecasts with the standard GBBEPx emissions and without data assimilation are used as the control experiment. UFS-RAQMS DA experiments in Chapter 4 and Chapter 5 use GSI 3Dvar DA to assimilate CO column observations from the Tropospheric Monitoring Instrument (TROPOMI).

2.2 Analysis Tools

Anomaly composites are used in Chapter 3 to evaluate how well RAQMS-Aura reproduces observed ENSO variability. El Niño and La Niña periods are determined by use of the Niño 3.4 index. ENSO events are defined as occurring when the index is at least 0.4°C greater (El Niño) or less (La Niña) than average for 5 consecutive months (e.g Trenberth, 1997, Ziemke et al., 2015). Anomalies are defined as the deviation from the average annual cycle during the RAQMS-Aura analysis period (2006-2016). Anomaly composites for El Niño and La Niña periods are generated for precipitation, convective mass flux, diabatic heating, ozone concentration, carbon monoxide, and net ozone production from monthly mean RAQMS-Aura analyses. Anomaly composites are also generated for satellite observations of tropospheric ozone column, total column carbon monoxide, and total precipitation. To investigate the vertical structure of ENSO variability in RAQMS-Aura, anomaly cross section composites are calculated between 7.5°S to 2.5°N for convective mass flux, diabatic heating, ozone, carbon monoxide, and net ozone production.

Empirical Orthogonal Function (EOF) analysis is a statistical technique that has been used for identifying dominant modes of temporal and spatial variability in atmospheric data. EOF analysis may also be referred to as principal component (PC) analysis. Application of EOF analysis identifies the dominant patterns of spatial variability within a dataset (the EOF) and a timeseries of how the associated pattern varies in time (the PC). Within Chapter 3 of this dissertation, I apply EOF analysis to detrended, deseasonalized monthly means of tropical tropospheric column ozone (TTOC), carbon monoxide total columns, and total precipitation from RAQMS-Aura to study interannual variation of tropical ozone. Following Doherty et al. (2006) the resulting EOF patterns for each RAQMS-Aura variable are multiplied by the standard deviation of the associated principal component (PC) to produce the physical magnitude of change associated with the mode. The PCs are correlated against the Niño 3.4 index to assess whether the mode captured by the EOF accounts for ENSO variability. A multiple linear regression is constructed using the precipitation and CO PCs to investigate how variability in convection and biomass burning emissions drive the ozone ENSO signal.

2.3 Observational Datasets

Tropospheric ozone residual (TOR) methods derive tropospheric column ozone through removal of stratospheric column ozone calculated from profiler measurements from total column ozone (Fishman and Larsen, 1987, Fishman et al., 1990). The OMI-MLS TOR is a satellite residual product where total ozone columns from the OMI instrument and stratospheric columns from MLS instrument (both on-board the Aura satellite) are combined to infer the tropospheric ozone column (Ziemke et al., 2006). The OMI-MLS TOR dataset is used in Chapter 3 to validate RAQMS-Aura TTOC analyses.

The Tropical Rainfall Measuring Mission (TRMM) Multi-satellite precipitation Analysis (TMPA) 3B43 product merges satellite IR and microwave precipitation estimates with rain gauge data to produce a best estimate of monthly mean precipitation rate from 50°S to 50°N at 0.25x0.25 degree resolution (Huffman et al., 2007). I average TRMM 3B43 precipitation estimates onto the RAQMS 1x1 degree grid. TRMM 3B43 precipitation estimates are used in Chapter 3 to evaluate RAQMS-Aura convective precipitation.

Measurements of Pollution in the Troposphere (MOPITT) CO (Emmons et al. 2004) Level 3 gridded products are used throughout this study to evaluate model CO columns. MOPITT is in orbit on-board the NASA Terra satellite and provides near-global coverage every 3 days at approximately 22x22 km^2 resolution. Level 3 gridded average CO has a 1x1 degree resolution, and is produced on daily and monthly averaging periods. Monthly level 3 MOPITT is used in Chapter 3 to evaluate RAQMS-Aura The daily level 3 product is used in Chapters 4 and 6 to evaluate UFS-RAQMS experiments.

The Tropospheric Monitoring Instrument (TROPOMI) (Veefkind et al., 2012) is a higher resolution follow-on to NASA OMI currently in orbit on-board ESA's polar-orbiting Sentinel-5 precursor satellite that observes in the UV-near IR and shortwave IR. I use the v2.4.0 CO total column retrieval with the striping correction applied (Borsdorff et al., 2019). Following recommended quality assurance guidelines (`https://sentinel.esa.int/documents/247904/3541451/Sentinel-5P-Carbon-Monoxide-Level-2-Product-Readme-File.pdf`, last access: 18 July 2024), the DA applications in Chapters 4 and 5 use observations with a quality assurance value 1 (best) over land and 0.7 (OK, but mid-level clouds present) over ocean. This leads to assimilation of only cloudy data over ocean, as the clear sky ocean retrieval signal intensity is too weak (Inness et al., 2022b). Spatial resolution was upgraded to 5.5 x 3.5 km in August 2019 from its initial resolution of 7 x 3.5km. TROPOMI CO observations are used for three purposes: 1) to evaluate

UFS-RAQMS control forecasts; 2) to constrain UFS-RAQMS CO analyses; and 3) to adjust GBBEPx CO emissions.

Ozonesondes from the Southern Hemisphere Additional Ozonesondes (SHADOZ) network (Sterling et al., 2018, Thompson et al., 2017, Witte et al., 2017, 2018) are used in Chapter 3 to evaluate RAQMS-Aura tropical O_3 vertical profiles. I use the reprocessed v06 ozone profiles (Thompson et al., 2021).

Chapters 4 and 6 evaluate UFS-RAQMS analyses with in-situ observations from two field campaigns that occurred in the summer of 2019. The NASA Cloud, Aerosol and Monsoon Processes Philippines Experiment (CAMP^{2}Ex) field campaign sampled airmasses over the Philippines 25 August–5 October 2019 with the NASA P-3 aircraft to investigate the role of aerosols in the Southeast Asian southeast monsoon (Reid et al., 2023). In-situ CO measurements were made by a commercial cavity ringdown spectrometer (G2401-m, PICARRO, Inc.) modified with a custom gas sampling system (DiGangi et al., 2021). UFS-RAQMS analyses are sampled along the P-3 flight track. The NOAA/NASA Fire Influence on Regional to Global Environments and Air Quality (FIREXAQ) campaign coordinated sampling of fires in the US with the NASA DC-8, NASA ER-2, NOAA Met and Chem Twin Otter aircraft, as well as several ground sites, during two operational phases (Warneke et al., 2023). During the first phase the DC-8 was based out of Boise, ID and focused on western wildfires from July 24th through August 16th. The second phase took place from August 19th through September 3rd and focused on small, primarily agricultural fires in the Southeast. I use CO observations from the Differential Absorption

Carbon Monoxide Measurement (DACOM) instrument (Sachse et al., 1991) which was on the DC-8.

The Network for the Detection of Atmospheric Composition Change (NDACC) is a global network consisting of 80 currently active stations providing high quality observations of atmospheric trace gases and aerosols with ground-based techniques including ozonsondes, Fourier-transform infrared (FTIR) spectrometers, lidar, and UV/visible spectroscopy (De Mazière et al., 2018). I use FTIR CO profile observations in Chapter 4 and Chapter 6 to evaluate UFS-RAQMS experiments. NDACC FTIRs retrieve volume mixing ratio profiles from solar absorption spectra with optimal estimation using the SFIT4 or PROFITT algorithms. Thule, Eureka, Jungfraujoch, and Rikubetsu have been considered as remote as local anthropogenic pollution is small at these locations, while St. Petersburg and Toronto are urban sites (Lutsch et al., 2020).

Chapter 3

Examining ENSO related variability in tropical tropospheric ozone in the RAQMS-Aura chemical reanalysis

This chapter is a lightly modified version of Bruckner, M., Pierce, R. B., and Lenzen, A.: Examining ENSO related variability in tropical tropospheric ozone in the RAQMS-Aura chemical reanalysis, EGUsphere [preprint], https://doi.org/10.5194/egusphere-2024-1178, 2024.

3.1 Introduction

The development of methods to calculate tropospheric ozone residuals (TOR) from satellite total column observations (e.g. Fishman and Balok, 1999, Fishman and Larsen, 1987, Fishman et al., 1990) provided the first global view of tropospheric ozone and showed a systematic zonal wave one structure in the tropics. This zonal wave one structure is consistent with the climatological average state of tropical atmosphere, which is dominated by the Pacific Walker circulation, defined by ascending motion over warm SSTs near the maritime continent and descending over cooler SSTs in the eastern Pacific, with easterlies at surface and westerlies aloft. Climatologically, tropospheric ozone columns are lowest over the Pacific and highest downwind of western Africa (Fishman et al., 1996, 1990, 2003). The enhancement downwind of western Africa is strongest during September-October-November (SON) and is associated with photochemical production of ozone from biomass burning emissions (Fishman et al., 2005, 1996, 2003). Tropospheric ozone concentrations over Africa and South America are lowest in March-April-May (MAM) (Fishman et al., 1990, 2003). The Fishman, Wozniak, and Creilson 2003 TOR seasonal climatology also shows a variance of 5-10 DU over the maritime continent from December-January-February (DJF) to June-July-August (JJA). The El Niño-Southern Oscillation (ENSO) is a major driver of interannual variability in both tropical and mid-latitudes (e.g. McPhaden et al., 2006, Trenberth, 1997), and has been found to have a strong impact on the distribution of tropospheric ozone in the tropical Pacific (Doherty et al., 2006, Peters et al., 2001, Sekiya and Sudo, 2012, Ziemke et al., 2010).

ENSO phases of El Niño and La Niña are tracked using a variety of indexes including the Niño 3.4 index (Bamston et al., 1997, Trenberth, 1997) and the Ozone ENSO Index (Ziemke et al., 2010). El Niño events occur when a warm SST anomaly develops in the eastern Pacific and reduces the east-west temperature gradient across the equatorial Pacific. In response to the SST anomaly, the trade winds weaken. Convection is enhanced over the eastern Pacific, leading to increased precipitation in the region and an eastward shift of the Walker Circulation. Correspondingly convection is suppressed over the maritime continent and leads to drier than usual conditions During El Niño events, tropospheric ozone is lower over the Pacific as the enhanced convection lofts low ozone air masses from near the ocean surface higher into the column, and higher over the maritime continent as high upper tropospheric ozone descends (e.g. Doherty et al., 2006, Hou et al., 2016, Sudo and Takahashi, 2001). Variability in the location of the maximum SST anomaly during the El Niño phase has led to a distinction between canonical (eastern Pacific) El Niño events and El Niño Modoki (central Pacific) events (e.g. Kim and Yu, 2012, Larkin and Harrison, 2005, Santoso et al., 2017). In the canonical El Niño, the maximum SST anomaly extends into the eastern tropical Pacific cold pool while during El Niño Modoki the maximum SST anomaly is in the central Pacific. The ascending branches of the Walker circulation are over the central Pacific during El Niño Modoki (Ashok et al., 2007). Following from the differences in the Walker circulation, the pattern of the ENSO response in tropical tropospheric ozone depends on the type of El Niño (Hou et al., 2016).

La Niña events occur when the eastern Pacific is cooler than average, and the atmosphere responds in a generally opposite, though not symmetric, manner to El Niño as enhanced vertical motion and convection occurs over the maritime continent, suppression of convection occurs over the east Pacific, and enhanced downwelling over the east Pacific. Tropical tropospheric ozone columns reflect the impacts of higher concentration upper tropospheric ozone descending over the Pacific and comparatively lower concentration lower tropospheric ozone ascending near the maritime continent during La Niña (e.g. Doherty et al., 2006, Ziemke and Chandra, 2003).

As discussed in Chapter 1, the influence of ENSO on tropospheric ozone has previously been investigated in observational datasets, chemical transport models, and chemistry-climate models. In this chapter I investigate the interannual variability of tropical tropospheric ozone in the RAQMS-Aura chemical re-analysis extending from 2006 through 2016. A chemical re-analysis produces a long-term data record by cycling a model forecast and data assimilation system to combine forecasts and observations in a statistically consistent manner that accounts for forecast and observation error (Miyazaki et al., 2020, Yumimoto et al., 2017). The data record obtained is a best-estimate of the true composition of the atmosphere, as analyses are constrained by observations of a limited number of species and the evolution of those species by model physics (Miyazaki et al., 2020). A comparison of several recent chemical reanalyses including the Copernicus Atmospheric Monitoring Service (CAMS) reanalysis (Inness et al., 2019), and the Tropospheric Chemistry Reanalysis version 2 (TCR-2) (Miyazaki et al., 2020) found that these analyses are suitable for generating ozone climatologies and looking at trends, though individual reanalyses will differ due to model configuration (Huijnen et al., 2020). While reanalysis has been used to look at the ENSO signal in CO, O_3, NOx, and smoke aerosols (Inness et al., 2015a), my analysis makes use of the chemical production and loss terms, convective mass flux, and diabatic heating from the reanalysis to examine variability in tropospheric ozone. The analysis also focuses on the 2006-2016 period, which includes significant biomass burning events in the maritime continent during the 2015/2016 El Niño event.

3.2 Validation of RAQMS-Aura Precipitation

Prior to investigating variability of the RAQMS-Aura chemical fields, I evaluate RAQMS-Aura convection and precipitation processes through comparisons with satellite precipitation observations. In RAQMS-Aura, sub-grid-scale mass flux between model layers occurs through shallow and deep convective schemes. Diabatic heating is generated by the sub-grid-scale convective parameterizations and influences the grid-scale thermodynamics. Convective mass flux and diabatic heating will be used in the composite analysis to look at the impact of ENSO on vertical transport and tropical tropospheric ozone concentrations.

Monthly mean total and convective precipitation from RAQMS-Aura is compared to estimates of precipitation from the TRMM Multi-satellite precipitation Analysis (TMPA) 3B43 product (Huffman et al., 2007). My analysis focuses on meridional structure and seasonal maps to look at average regional biases, and time-series of the maritime continent and Pacific Intertropical convergence zone (ITCZ) regions to look at longer-term trends.

3.2.1 Meridional Structure

Figure 3.1 displays the meridional averaged convective, large-scale, and total precipitation for RAQMS-Aura and total precipitation from TRMM 3B43 for each season. The seasonal average meridional precipitation maxima in RAQMS-Aura are broader than observed in TRMM 3B43. During DJF and MAM, observed tropical precipitation peaks in both the northern hemisphere (NH) and southern hemisphere (SH). During JJA and SON, observed tropical precipitation peaks only in the NH.

In DJF the observed hemispheric peaks are of similar magnitude with the NH peaking at 0.247 mm/hour and the SH peaking at 0.233 mm/hour. TRMM 3B43 MAM indicates that the NH branch is more active during this season than the SH branch, as the NH peak is 0.293 mm/hour, and the SH peak is 0.229 mm/hour. RAQMS-Aura reproduces the observed double peaks for DJF and MAM, though the magnitude is overestimated in RAQMS-Aura by 0.08-0.12 mm/hour, and the DJF SH peak is larger than the NH peak and 5 degrees to the south of the observed peak. In JJA and SON, the reanalysis reproduces the observed single maxima, though it is broader by more than 15 degrees latitude, and the absolute maximum is displaced approximately 2.5 degrees to the north.

Between 40°N and 40°S the total precipitation in RAQMS-Aura is predominately convective precipitation, with ratios of convective precipitation to total precipitation exceeding

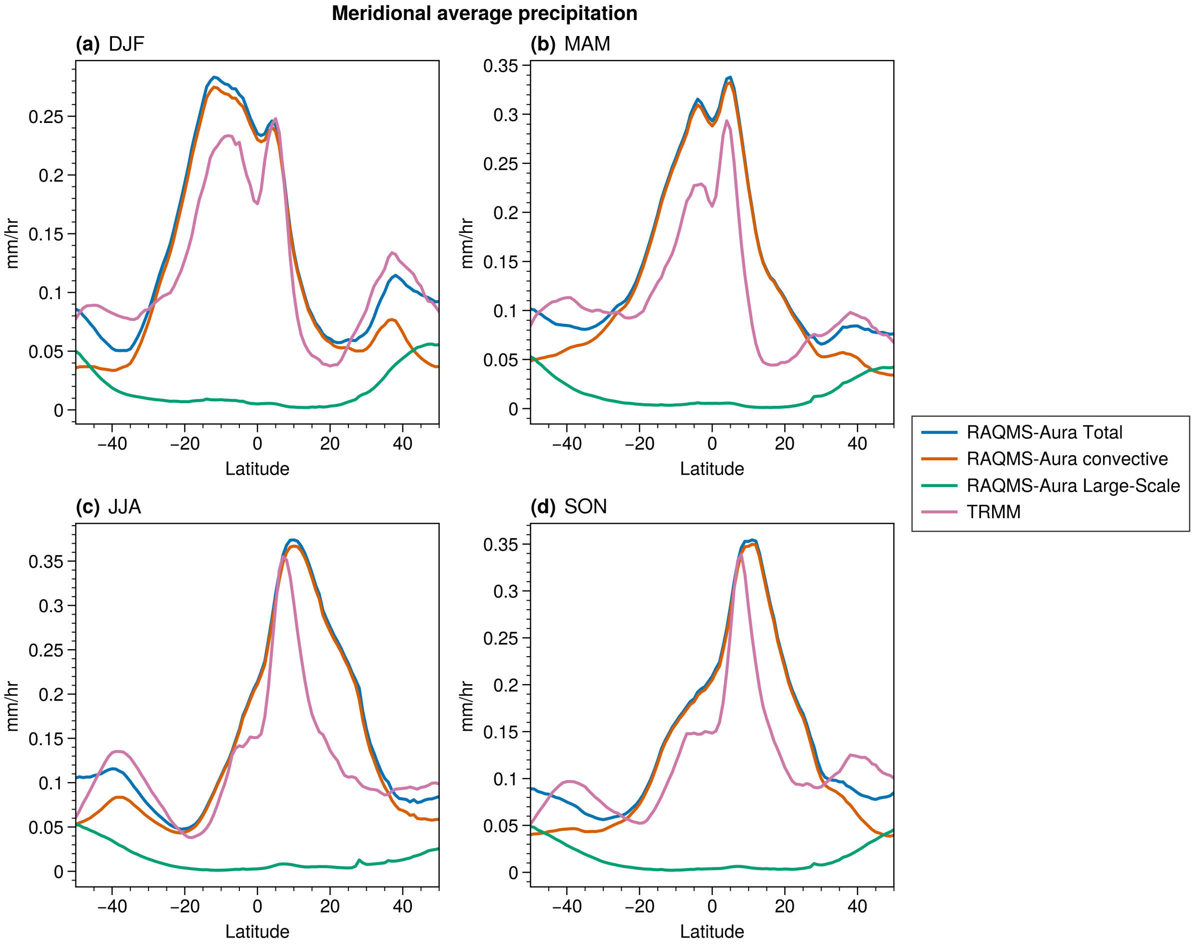

FIGURE 3.1: Zonally and seasonally averaged precipitation from RAQMS-Aura and TRMM 3B43 for a) DJF, b) MAM, c) JJA, and d) SON.

0.6 on average. It is common for tropical precipitation to be predominately convective precipitation in global models, leading to a “drizzling bias”. This ”drizzling bias” is the result of convective parameterizations producing convective precipitation that is too frequent and long-lasting but not as intense as observed while the total precipitation amount is realistic (Chen and Dai, 2019, Chen et al., 2021).

3.2.2 Horizontal Structure

While RAQMS-Aura reasonably reproduces the seasonality of the observed meridional structure, the distributions are broader than in observations. Seasonal maps of precipitation allow me to examine the reasons for this in more detail. Figure 3.2 shows seasonal maps of precipitation from the TRMM 3B43 observations and RAQMS-Aura. TRMM 3B43 and RAQMS-Aura are well correlated for all seasons, with DJF displaying a spatial correlation of 0.86, MAM a spatial correlation of 0.75, JJA a spatial correlation of 0.71, and SON a spatial correlation of 0.77. These correlations show that the RAQMS-Aura reanalysis broadly captures the seasonal changes in the spatial pattern of tropical precipitation.

Precipitation over land in South America and Africa is consistently overestimated relative to TRMM 3B43 by 0.2-0.3 mm/hour. This overestimation over land is a long-standing bias of the dynamical component of RAQMS (Schaack et al., 2004). RAQMS-Aura overestimates precipitation in the Gulf of Mexico and Caribbean by >0.3 mm/hour during JJA and SON. During DJF and MAM, the average bias over the Gulf of Mexico is less than ± 0.1 mm/hour. RAQMS-Aura overestimates precipitation over the Caribbean by ∼0.14 mm/hour during DJF and by ∼0.16 during MAM. RAQMS-Aura overestimates precipitation near India by >0.3 mm/hour during MAM and JJA. In the northwest Pacific, RAQMS-Aura shows larger overestimates of precipitation in JJA and SON relative to DJF and JJA, with overestimates relative to TRMM of 0.05 mm/hour in DJF, >0.3 mm/hour in JJA, 0.15 mm/hour in MAM, and >0.3 mm/hour in SON.

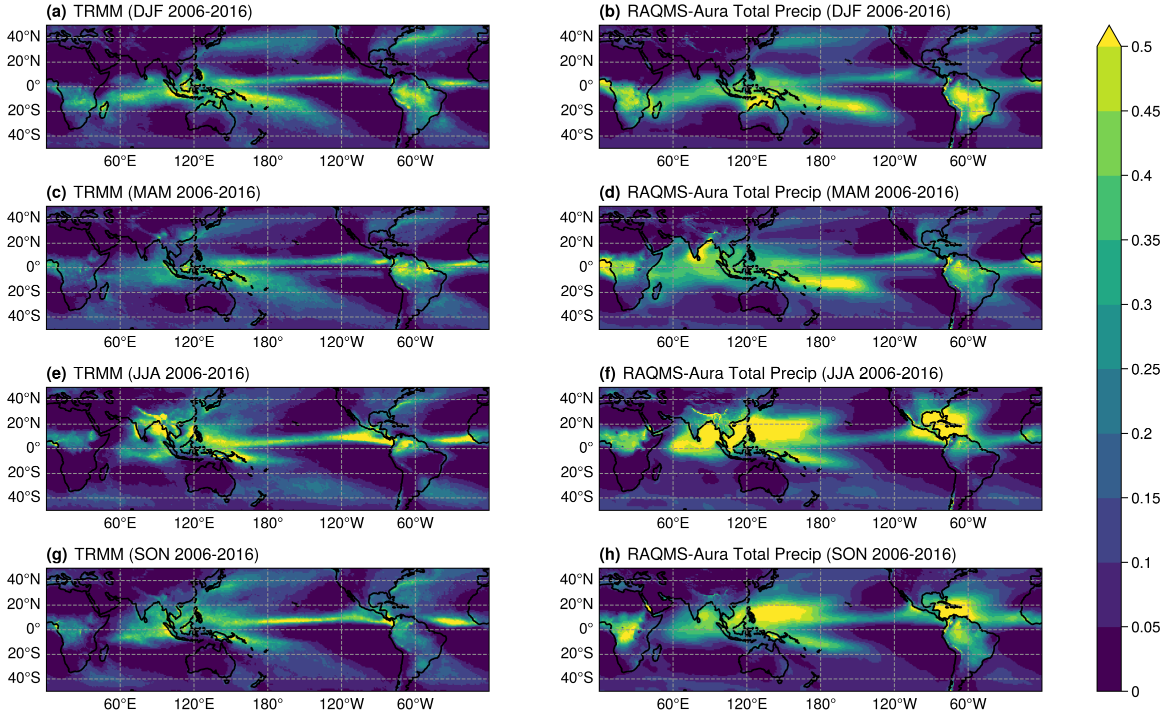

FIGURE 3.2: Seasonal mean precipitation for TRMM 3B43 (a, c, e, g) and RAQMS-Aura (b, d, f, h).

RAQMS-Aura does capture precipitation features like the ITCZ and western North Atlantic storm track well, though there is bias in the precipitation amount. RAQMS-Aura underestimates precipitation in the western North Atlantic off the east coast of the US along the storm track region by 0.17 mm/hour in DJF, ~0.15 mm/hour in JJA, ~0.15 mm/hour in MAM, and ~0.17 mm/hour in SON. During DJF, precipitation is overestimated by 0.2-0.3 mm/hour in RAQMS-Aura in the Southern Hemisphere maximum over the Pacific and off the northern coast of Australia. The strength of the SH maximum is consistently overestimated by RAQMS-Aura, as it is higher than TRMM 3B43 by ~0.1 mm/hour in JJA, 0.25-0.3 mm/hour in MAM, and ~0.1 mm/hour in SON. RAQMS-Aura tends to underestimate the strength of the ITCZ in all seasons, with a small underestimate of ~0.05mm/hour in MAM and ~0.15 mm/hour in DJF. RAQMS-Aura underestimates

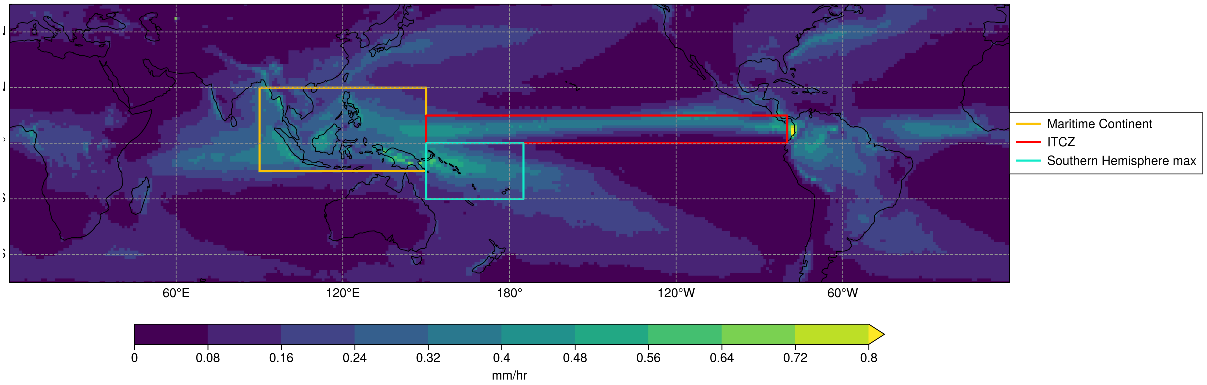

Figure 3.3: Regions for timeseries overlaid on mean 2006-2016 TRMM precipitation.

the ITCZ over the east and central Pacific by a max of ∼0.25 mm/hour in SON and JJA.

3.2.3 Time series

The comparison of TRMM 3B43 precipitation and RAQMS-Aura shows that RAQMS-Aura captures the expected seasonality in the ITCZ and over landmasses though tends to overestimate convective precipitation. Following this characterization of regional biases in RAQMS-Aura, I look closer at how the RAQMS-Aura represents precipitation within the tropics by evaluating the time series for 3 key regions, which are defined in Figure 3.3. The region over the maritime continent is defined by broadscale ascent in the average Walker Circulation. Time series for the maritime continent, NH ITCZ, and SH maximum regions are displayed in Figure 3.4.

Over the maritime continent, RAQMS-Aura has a temporal correlation of 0.619 with TRMM and a mean bias of 0.064 mm/hour (22.27%). The bias between TRMM and RAQMS-Aura is initially higher, ∼0.2 mm/hour at a max, then decreases after 2010 within this region. There is also an increased bias in 2015 and late 2016 over the maritime continent. Across the ITCZ in the northern hemisphere RAQMS-Aura has a temporal correlation of 0.715 and bias of -0.0115 mm/hour (-4.90%) with TRMM. Prior to 2010 RAQMS-Aura displays a small bias relative to TRMM 3B43. Post 2010 RAQMS-Aura underestimates peak precipitation, though the temporal correlation of the measurements with TRMM 3B43 slightly increases to 0.774 within this region. Within a section of the SH precipitation maximum, RAQMS-Aura has a temporal correlation of 0.599 and bias of 0.038 mm/hour (13.53%) with TRMM. The good correlation and bias of less than 25% for each region indicate that RAQMS-Aura has skill in reproducing the observed precipitation in the regions of interest for this study. Shifts in bias observed between 2009 and 2011 appear to be associated with upgrades to the GDAS system. Changes to GDAS implemented in 2009 included use of variational quality control in the assimilation system and flow dependent reweighting of background error variance (`https://www.emc.ncep.noaa.gov/gmb/STATS/html/model_changes.html`, last access: 4 August 2024).

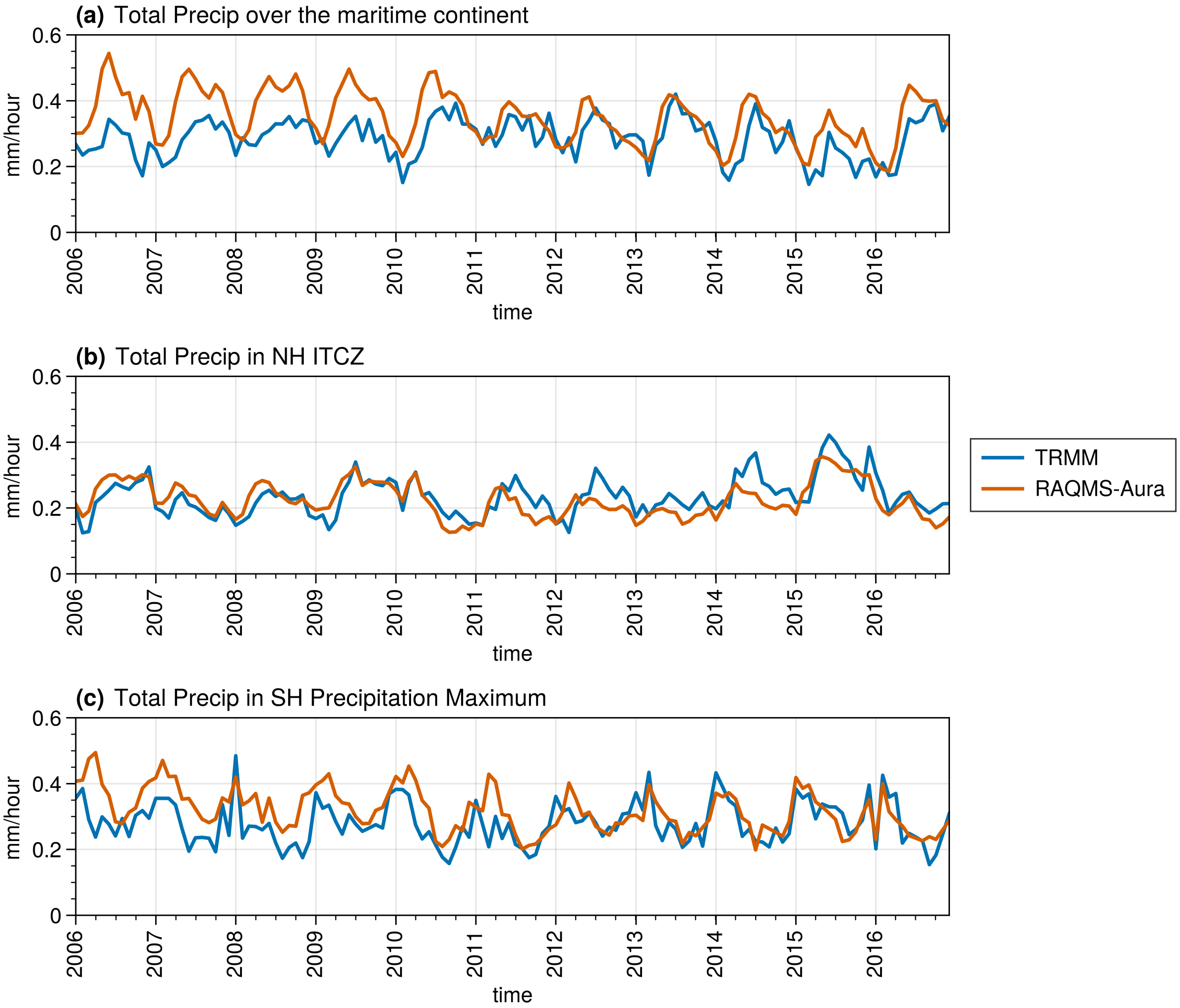

Figure 3.4: Mean precipitation for TRMM 3B43 and RAQMS-Aura Precipitation over the maritime continent (a), in the NH ITCZ region (b), and in the SH maximum precipitation region (c). Over the maritime continent, RAQMS-Aura precipitation is on average biased 0.064 mm/hour (22.27%) higher than TRMM 3B43. In the NH ITCZ region RAQMS-Aura precipitation is on average biased 0.012 mm/hour (4.90%) lower than TRMM 3B43. In the SH maximum precipitation region RAQMS-Aura precipitation is on average biased 0.038 mm/hour (13.53%) higher than TRMM 3B43.

3.3 Validations of RAQMS-Aura O_3 and CO

To establish fidelity of the RAQMS-Aura chemical fields, I evaluate ozone profiles, tropospheric ozone column, and CO column. The RAQMS-Aura monthly mean tropospheric ozone column is compared to the OMI-MLS TOR (Ziemke et al., 2006). Monthly mean CO column from RAQMS-Aura is compared to CO column retrievals from Measurements of Pollution in the Troposphere (MOPITT) (Emmons et al., 2004). Both the OMI-MLS TOR and the MOPITT CO data used are monthly mean Level 3 products. I evaluate the RAQMS-Aura tropical O_3 vertical profiles with observations from 12 sites in the Southern Hemisphere Additional Ozonesondes (SHADOZ) network (Sterling et al., 2018, Thompson et al., 2017, Witte et al., 2017, 2018).

3.3.1 Horizontal structure in CO and tropospheric O_3 columns

Seasonal maps of CO column and tropospheric ozone column are evaluated for RAQMS-Aura and satellite datasets. Figure 3.5 shows seasonal maps of CO columns from MOPITT and RAQMS-Aura. MOPITT and RAQMS-Aura are well correlated for all seasons, as DJF has a spatial correlation of 0.945, MAM a spatial correlation of 0.955, JJA a spatial correlation of 0.911, and SON a spatial correlation of 0.919. South American CO columns are overestimated in RAQMS-Aura by 0.4-0.8 x 10^{18} mol/cm^2 in SON and 0.4-0.5 x 10^{18} mol/cm^2 in JJA, and $<$ 0.3 x 10^{18} mol/cm^2 during DJF and MAM. Over the maritime continent, bias is $< \pm$ 0.2 x 10^{18} mol/cm^2 during DJF, MAM, and JJA and

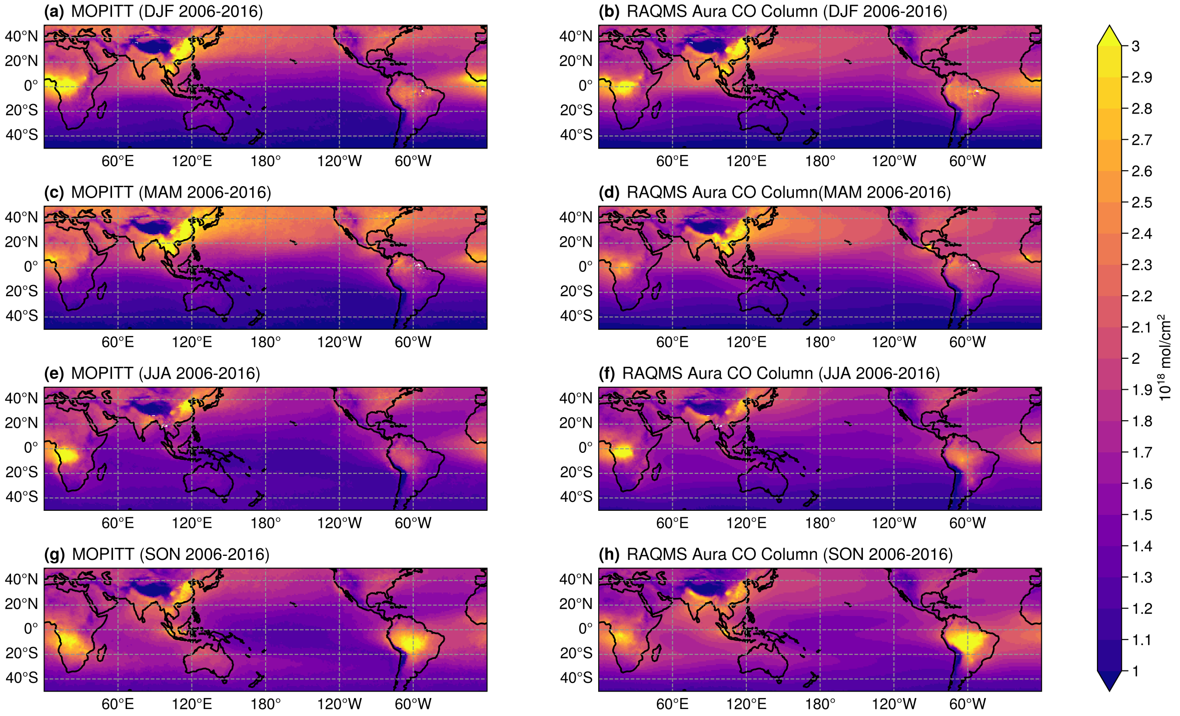

Figure 3.5: Seasonal mean CO column for MOPITT (a, c, e, g) and RAQMS-Aura (b, d, f, h).

biased low during SON by ~0.3 x 10^{18} mol/cm^2. Over the Pacific, RAQMS-Aura has a high bias of 0.15-0.3 x 10^{18} mol/cm^2 (<25% difference).

Figure 3.6 shows seasonal maps of Tropospheric O_3 columns from OMI-MLS and RAQMS-Aura. OMI-MLS and RAQMS-Aura are well correlated for all seasons, as DJF has a spatial correlation of 0.822, MAM a correlation of 0.995, JJA a correlation of 0.934, and SON a correlation of 0.941. While the correlation is strong, RAQMS-Aura tropospheric O_3 is consistently biased high by >2DU in the tropics relative to OMI-MLS.

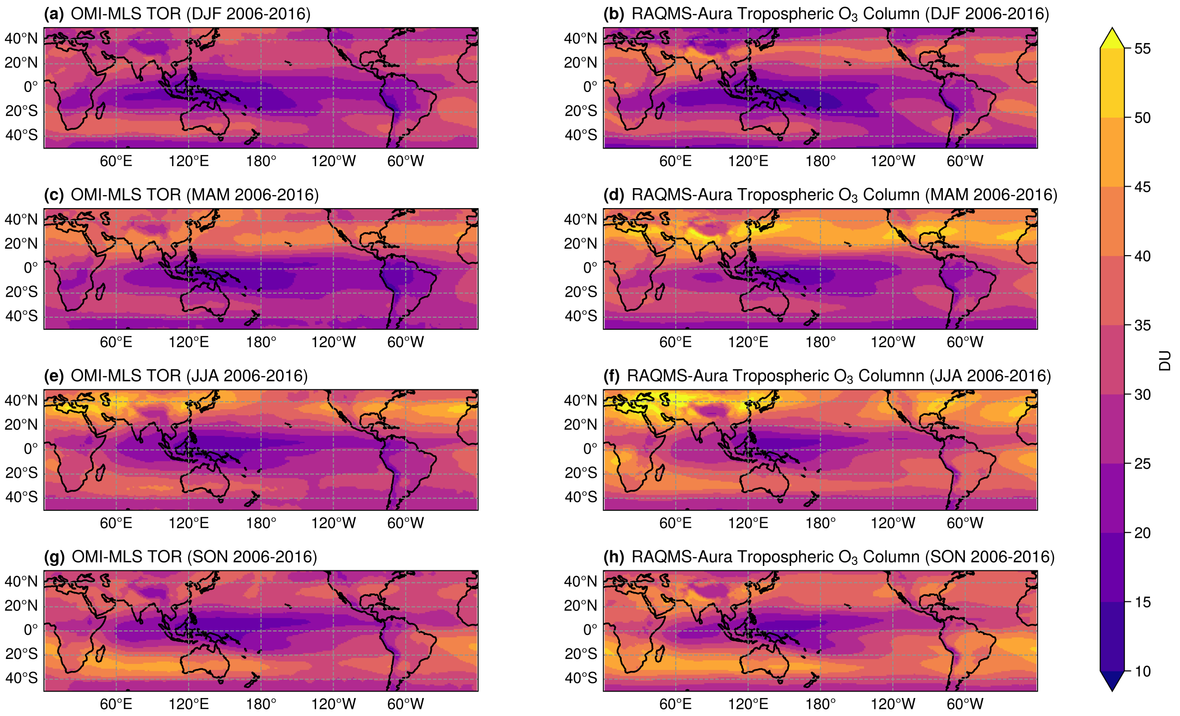

FIGURE 3.6: Seasonal mean tropospheric O_3 column for OMI-MLS (a, c, e, g) and RAQMS-Aura (b, d, f, h).

3.3.2 Time series of CO and tropospheric O_3 columns over the Maritime Continent

Following the characterization of seasonal mean regional biases in RAQMS-Aura CO column and tropospheric O_3 column, I look at how well RAQMS-Aura represents variability over the maritime continent (as defined in Figure 3.3). Timeseries of CO column and tropospheric O_3 over the maritime continent are displayed in Figure 3.7. Unlike in the precipitation fields, the RAQMS-Aura CO columns and tropospheric O_3 columns do not exhibit a large shift in the bias over time.

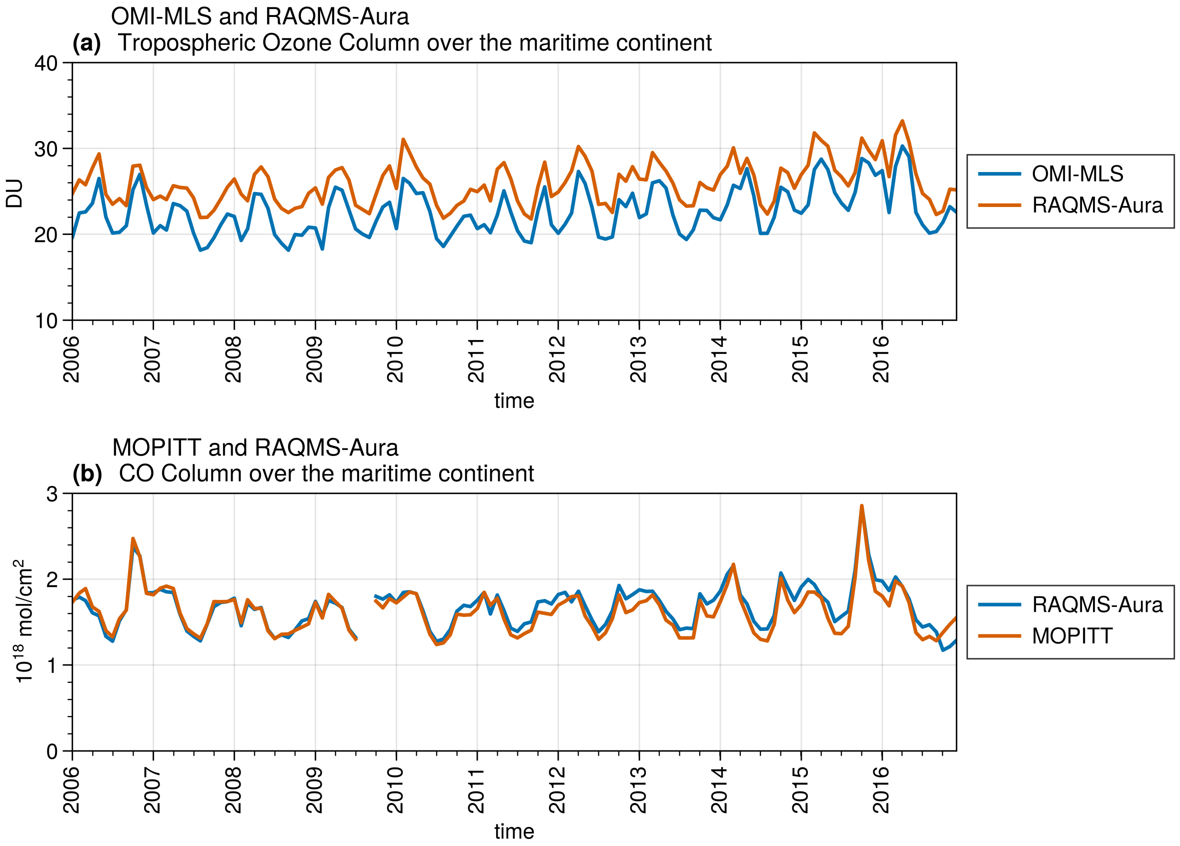

FIGURE 3.7: Time series of mean tropospheric O_3 column (a) and CO column (b) over the maritime continent for RAQMS-Aura, MOPITT CO, and OMI-MLS TOR.

RAQMS-Aura mean maritime continent tropospheric O_3 column has a temporal correlation of 0.937 with the OMI-MLS TOR and a mean high bias of 3.273 DU (14.435%). RAQMS-Aura mean maritime continent CO column has a temporal correlation of 0.943 with MOPITT and a mean high bias of 0.0477 x 10^{18} mol/cm^2 (2.93%). The very good temporal correlation and bias of less than 25% for both CO column and tropospheric O_3 column indicate that RAQMS-Aura has skill in reproducing the observed CO column and tropospheric O_3 column in a key region of interest for this study.

3.3.3 Vertical structure of O_3

RAQMS-Aura ozone profiles are compared to the reprocessed v06 SHADOZ ozone profiles for the SHADOZ sites shown in Figure 3.8. Figure 3.8 also shows the 2006-2016 mean tropospheric ozone column from RAQMS-Aura. RAQMS-Aura and SHADOZ ozone profiles are compared in 100m altitude bins from 0km to 30km. The vertical distribution of mean bias in RAQMS-Aura O_3 profiles for all SHADOZ sites is presented in Figure 3.9. RAQMS-Aura O_3 exhibits a high bias of >20% near the surface. Above 3km, the average bias in RAQMS-Aura O_3 is <10%.

Bias, correlation, and RMSE for each site are given in Table 3.1. These statistics are evaluated for all observations within 4 altitude ranges: surface- 5km, 5-10 km, 10-15 km, and 15-20km. The mean percent bias for the surface – 5km altitude range for all sites is 9.17%. The surface – 5km bias is larger than the mean at the Hilo, American Samoa, Costa Rica, San Cristobal, Nairobi, and Natal sites. This enhanced lower troposphere bias is associated with very low (< 20 ppbv) surface O_3 concentrations at American Samoa, San Cristobal, and Hilo. RAQMS-Aura is moderately correlated (0.5-0.75) in time and space with SHADOZ between the surface and 5km for most sites. At the Kuala Lumpur site, RAQMS-Aura displays a small bias (6.909%) but a correlation of 0.458 with SHADOZ ozone profiles. RAQMS-Aura strongly overestimates the surface O_3 concentration by >40% at Kuala Lumpur, though above the surface the average bias in this region is < 10% and the RAQMS-Aura O_3 analysis is moderately (0.5-0.8) correlated with SHADOZ. Between 5-10km, the mean percent bias is < ± 10% for all sites except

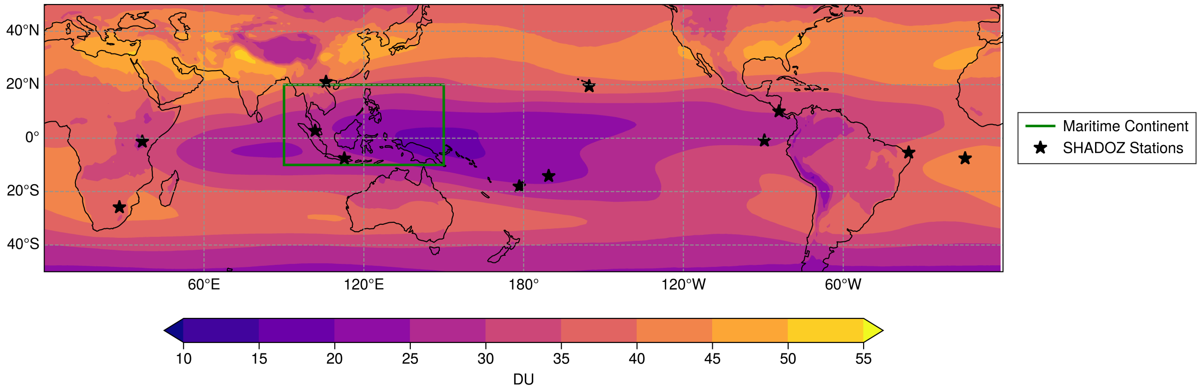

FIGURE 3.8: SHADOZ ozonesonde sites (stars) and mean RAQMS-Aura tropospheric ozone column (contours).

Java where it is 20.22%. However, RAQMS-Aura has a correlation of 0.6585 with Java between 5 and 10km.

Overall, RAQMS-Aura does capture a substantial portion of the observed variability in tropical ozone profiles as indicated by the moderate to strong correlations with SHADOZ ozone profiles, though it does significantly overestimate near-surface ozone concentrations.

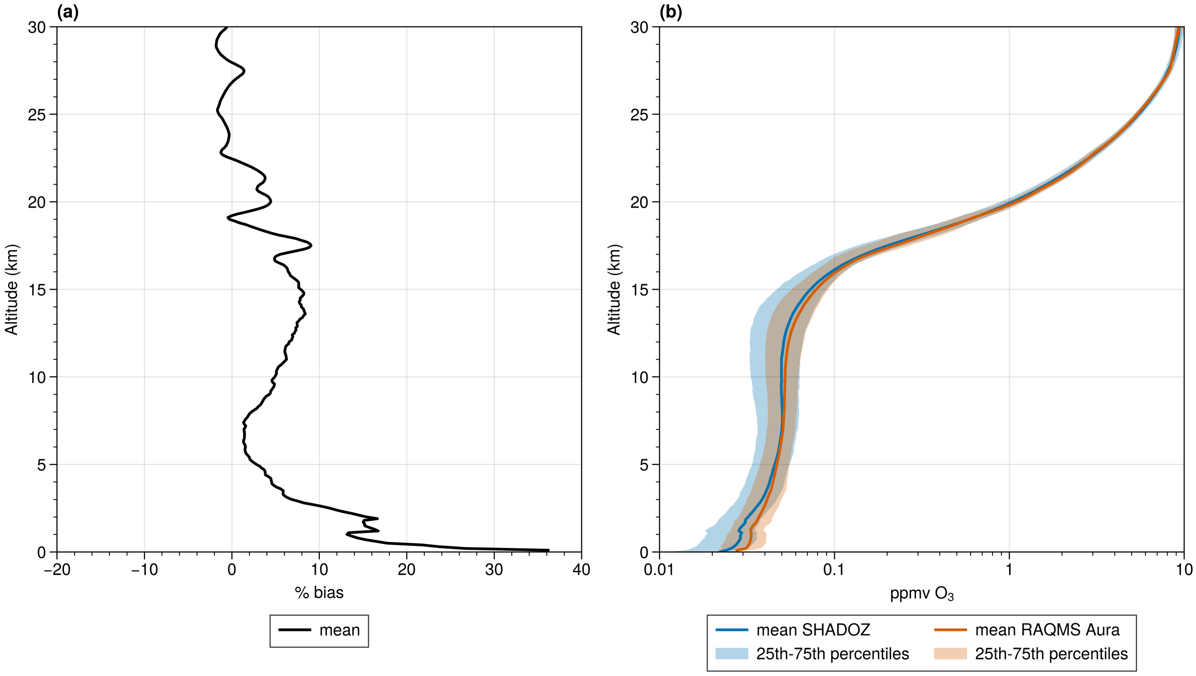

FIGURE 3.9: Comparison of RAQMS-Aura O_3 mixing ratio to tropical SHADOZ ozonesondes. Panel a shows the percent bias in RAQMS-Aura relative to the ozonesondes. Panel b is percentiles for SHADOZ (blue) and RAQMS-Aura (orange).

Table 3.1: Correlation, bias, and RMSE between SHADOZ ozonesondes and coincident RAQMS-Aura Ozone mixing ratio.

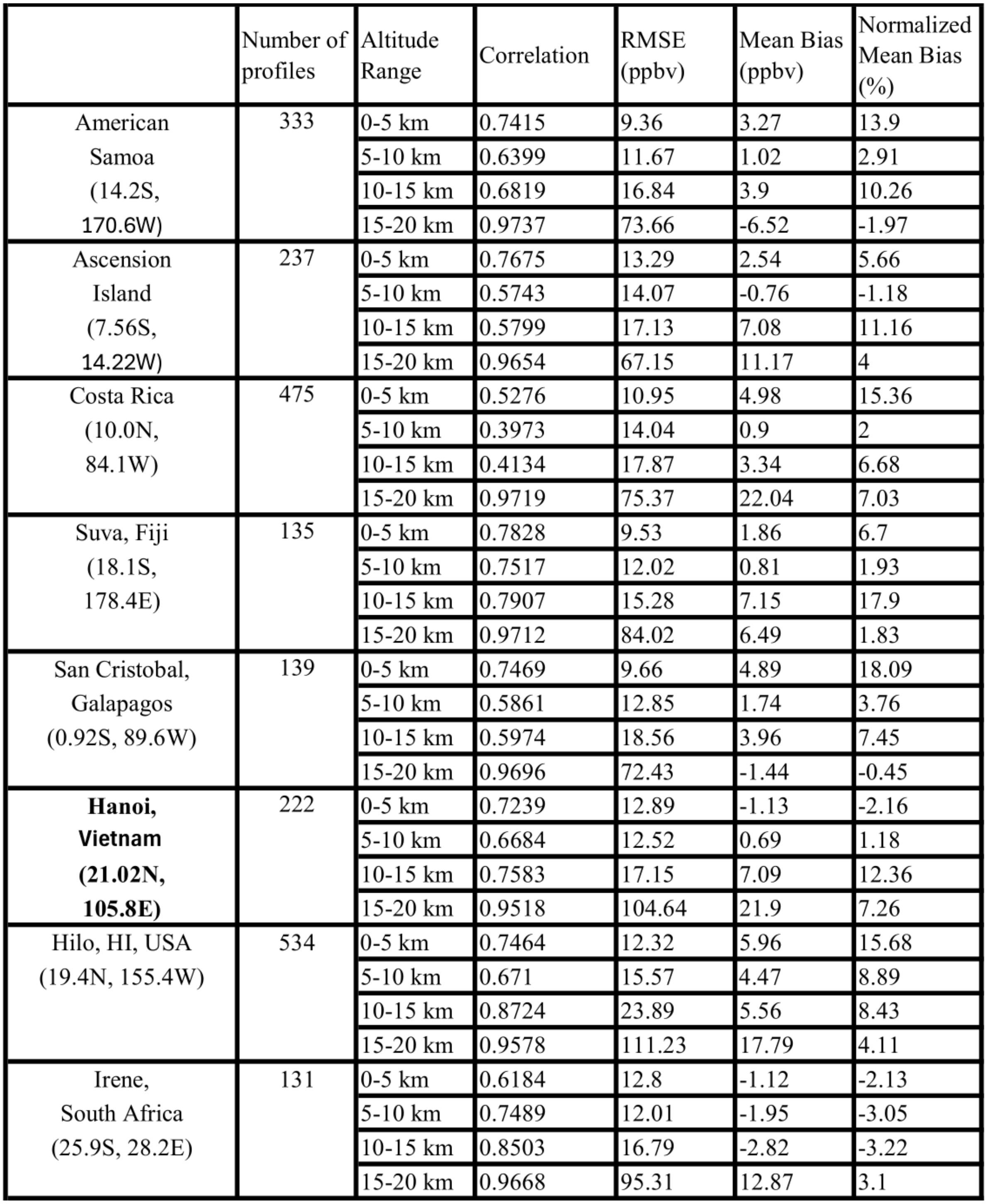

	Number of profiles	Altitude Range	Correlation	RMSE (ppbv)	Mean Bias (ppbv)	Normalized Mean Bias (%)
American Samoa (14.2S, 170.6W)	333	0-5 km	0.7415	9.36	3.27	13.9
		5-10 km	0.6399	11.67	1.02	2.91
		10-15 km	0.6819	16.84	3.9	10.26
		15-20 km	0.9737	73.66	-6.52	-1.97
Ascension Island (7.56S, 14.22W)	237	0-5 km	0.7675	13.29	2.54	5.66
		5-10 km	0.5743	14.07	-0.76	-1.18
		10-15 km	0.5799	17.13	7.08	11.16
		15-20 km	0.9654	67.15	11.17	4
Costa Rica (10.0N, 84.1W)	475	0-5 km	0.5276	10.95	4.98	15.36
		5-10 km	0.3973	14.04	0.9	2
		10-15 km	0.4134	17.87	3.34	6.68
		15-20 km	0.9719	75.37	22.04	7.03
Suva, Fiji (18.1S, 178.4E)	135	0-5 km	0.7828	9.53	1.86	6.7
		5-10 km	0.7517	12.02	0.81	1.93
		10-15 km	0.7907	15.28	7.15	17.9
		15-20 km	0.9712	84.02	6.49	1.83
San Cristobal, Galapagos (0.92S, 89.6W)	139	0-5 km	0.7469	9.66	4.89	18.09
		5-10 km	0.5861	12.85	1.74	3.76
		10-15 km	0.5974	18.56	3.96	7.45
		15-20 km	0.9696	72.43	-1.44	-0.45
Hanoi, Vietnam (21.02N, 105.8E)	222	0-5 km	0.7239	12.89	-1.13	-2.16
		5-10 km	0.6684	12.52	0.69	1.18
		10-15 km	0.7583	17.15	7.09	12.36
		15-20 km	0.9518	104.64	21.9	7.26
Hilo, HI, USA (19.4N, 155.4W)	534	0-5 km	0.7464	12.32	5.96	15.68
		5-10 km	0.671	15.57	4.47	8.89
		10-15 km	0.8724	23.89	5.56	8.43
		15-20 km	0.9578	111.23	17.79	4.11
Irene, South Africa (25.9S, 28.2E)	131	0-5 km	0.6184	12.8	-1.12	-2.13
		5-10 km	0.7489	12.01	-1.95	-3.05
		10-15 km	0.8503	16.79	-2.82	-3.22
		15-20 km	0.9668	95.31	12.87	3.1

Table 3.1 – continued from previous page

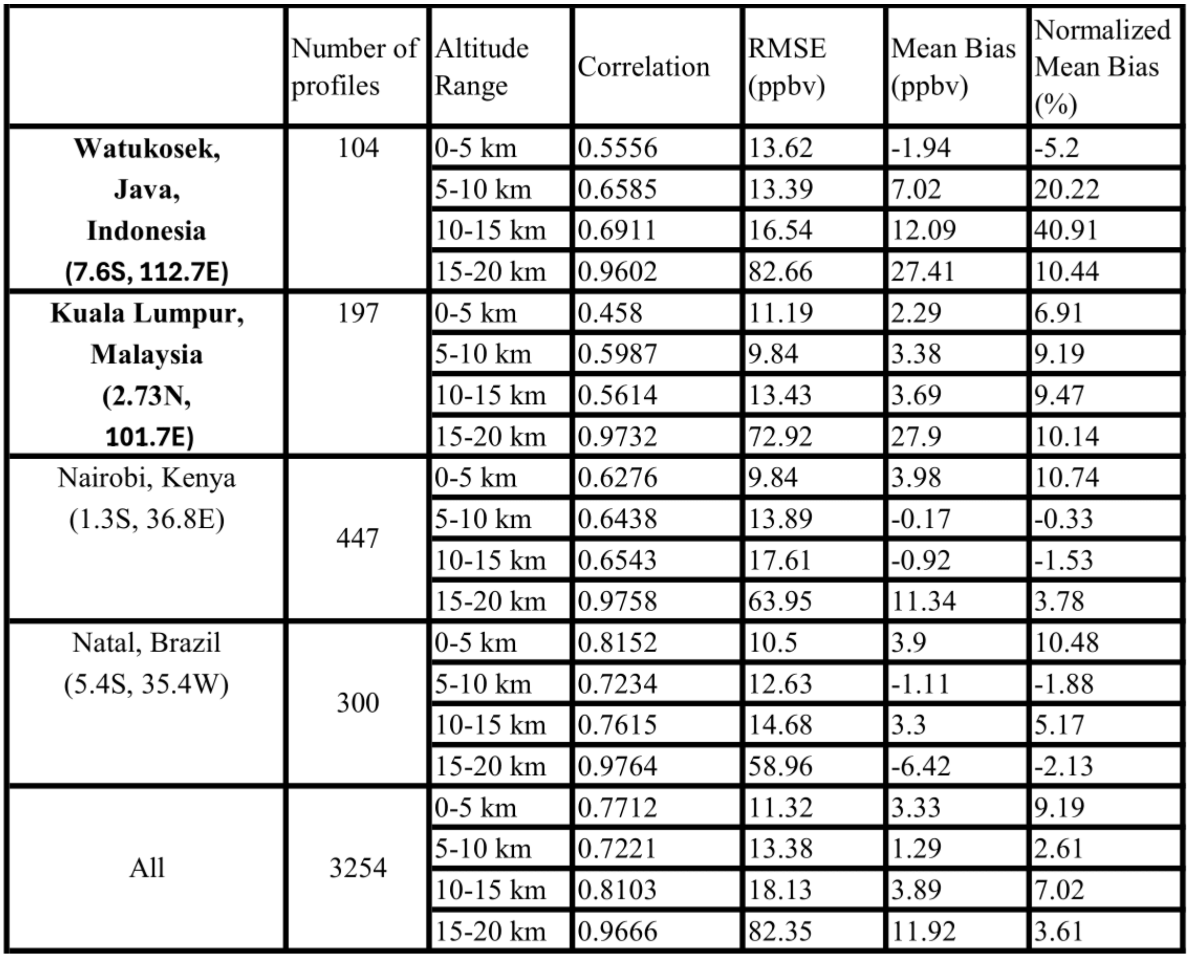

	Number of profiles	Altitude Range	Correlation	RMSE (ppbv)	Mean Bias (ppbv)	Normalized Mean Bias (%)
Watukosek, Java, Indonesia (7.6S, 112.7E)	104	0-5 km	0.5556	13.62	-1.94	-5.2
		5-10 km	0.6585	13.39	7.02	20.22
		10-15 km	0.6911	16.54	12.09	40.91
		15-20 km	0.9602	82.66	27.41	10.44
Kuala Lumpur, Malaysia (2.73N, 101.7E)	197	0-5 km	0.458	11.19	2.29	6.91
		5-10 km	0.5987	9.84	3.38	9.19
		10-15 km	0.5614	13.43	3.69	9.47
		15-20 km	0.9732	72.92	27.9	10.14
Nairobi, Kenya (1.3S, 36.8E)	447	0-5 km	0.6276	9.84	3.98	10.74
		5-10 km	0.6438	13.89	-0.17	-0.33
		10-15 km	0.6543	17.61	-0.92	-1.53
		15-20 km	0.9758	63.95	11.34	3.78
Natal, Brazil (5.4S, 35.4W)	300	0-5 km	0.8152	10.5	3.9	10.48
		5-10 km	0.7234	12.63	-1.11	-1.88
		10-15 km	0.7615	14.68	3.3	5.17
		15-20 km	0.9764	58.96	-6.42	-2.13
All	3254	0-5 km	0.7712	11.32	3.33	9.19
		5-10 km	0.7221	13.38	1.29	2.61
		10-15 km	0.8103	18.13	3.89	7.02
		15-20 km	0.9666	82.35	11.92	3.61

3.4 ENSO Composites

Based on comparison of RAQMS-Aura total precipitation with TRMM 3B43 I conclude that RAQMS-Aura reasonably reproduces convection over the Pacific Ocean, particularly within the ITCZ. RAQMS-Aura captures the observed variability in tropospheric ozone but has a ∼2DU high bias relative to the OMI-MLS TOR. RAQMS-Aura captures the observed CO columns in the tropics very well. Based on comparison of RAQMS-Aura ozone profiles with SHADOZ profiles, I conclude that RAQMS-Aura reasonably captures observed variability in tropical ozone profiles but overestimates the near-surface concentrations. To characterize the anomaly associated with ENSO, composites for El Niño and La Niña periods are generated for precipitation, convective mass flux, diabatic heating, ozone concentration, carbon monoxide, and net ozone production from monthly mean RAQMS-Aura analyses.

3.4.1 Precipitation

Composites of the de-seasonalized anomaly in precipitation for TRMM and RAQMS-Aura for positive ENSO and negative ENSO are presented in Figure 3.10. The TRMM and RAQMS-Aura composites are well correlated, with a spatial correlation of 0.77 for El Niño composites and 0.739 for the La Niña composites. The dominant feature of the El Niño phase in the TRMM data and RAQMS-Aura reanalysis is an enhancement of precipitation in the tropics east from 150°E to the western coast of Central America and suppressed precipitation over the maritime continent. RAQMS-Aura however diverges from observations by displaying suppression of precipitation in regions around 7.5°S-39°S, 150°W-120°W and 7.5°N-20°N, 150°E-180°E where precipitation is enhanced in TRMM. During the La Niña phase, precipitation is suppressed over the central Pacific and enhanced over the maritime continent. For both TRMM and RAQMS-Aura the El Niño and La Niña composites are near mirrors of one another, with the location of the maximum change shifted west during the negative phase from the positive phase.

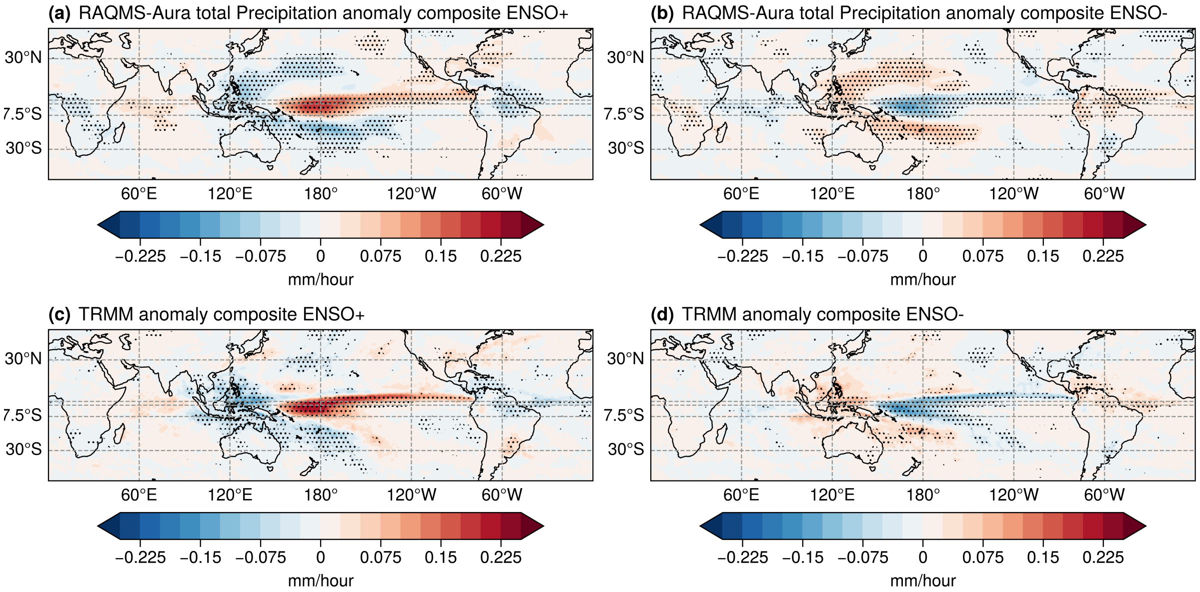

Figure 3.10: Composited precipitation anomalies for El Niño in RAQMS-Aura (a) and TRMM 3B43 (b) and La Niña in RAQMS-Aura (c) and TRMM 3B43 (d). Shaded regions indicate where the composite is significant at the 95% confidence level from a t test.

3.4.2 Response of Tropospheric Total Column Ozone and Carbon Monoxide column to ENSO

ENSO composites for OMI-MLS TOR (Ziemke et al., 2006) and Measurements of Pollution in the Troposphere (MOPITT) CO (Emmons et al., 2004) are used to confirm the representativeness of RAQMS-Aura ENSO chemical signals.

Tropical tropospheric ozone column (TTOC) anomalies in RAQMS-Aura and the OMI-MLS TOR for the positive and negative phases of ENSO are shown in Figure 3.11. TTOC anomalies are 1-2 DU larger during the positive phase of ENSO than in the negative phase. Within both the RAQMS-Aura TTOC and OMI-MLS TOR, El Niño is associated with an increase over the maritime continent and a decrease over the central and eastern Pacific

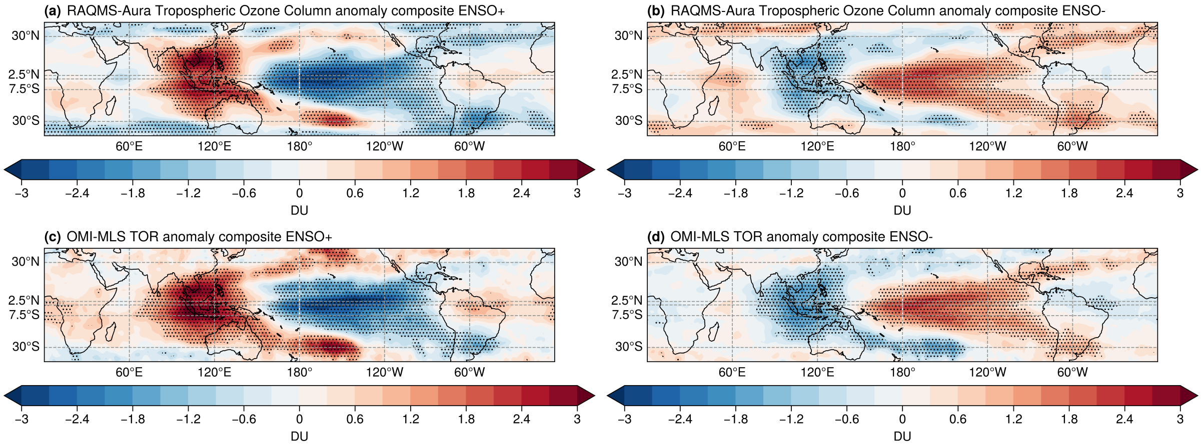

Figure 3.11: Composited TTOC anomalies associated with El Niño in RAQMS-Aura (a) and OMI-MLS TOR (c) and La Niña in RAQMS-Aura(b) and OMI-MLS TOR(d). Shaded regions indicate where the composite is significant at the 95% confidence level from a t test.

Ocean. The decrease over the Pacific Ocean is flanked by increased concentrations to the north and south. Outside of the Pacific region, the tropospheric column anomaly associated with the ENSO phase is less than 1 DU. During La Niña, a small decrease in tropospheric ozone occurs over the maritime continent while an increase occurs over the central-eastern Pacific. The location of the peak decrease in TTOC in the eastern Pacific depicted in the El Niño composite is comparable to that found by Olsen et al. (2016), Oman et al. (2011). Earlier studies of Doherty et al. (2006), Peters et al. (2001), Ziemke and Chandra (2003) show this peak decrease in TTOC is more towards the southeast. As my analysis is consistent with observations, the differences from earlier analyses are likely due to variability in ENSO and the influence of the large 2015 El Niño event during the 2006-2016 period under consideration in this study.

CO column anomalies for RAQMS-Aura and MOPITT are presented in Figure 3.12. MOPITT CO anomalies appear nosier due to the sparse spatial sampling of the MOPITT

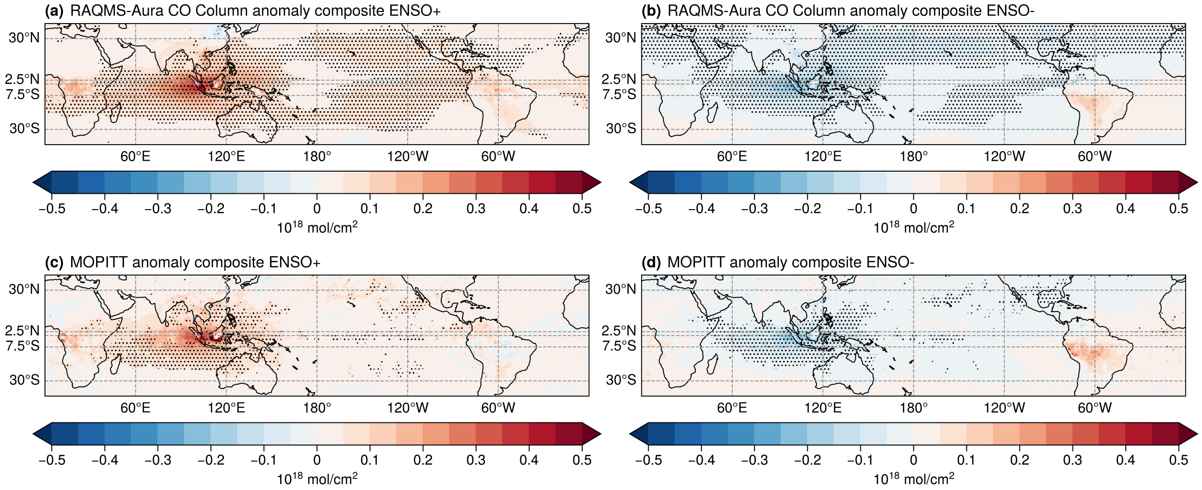

FIGURE 3.12: Composited CO column anomalies associated with El Niño in RAQMS-Aura (a) and MOPITT (c) and La Niña in RAQMS-Aura(b) and MOPITT(d). Shaded regions indicate where the composite is significant at the 95% confidence level from a t test.

instrument. RAQMS-Aura reproduces ENSO-related variability in CO as observed by MOPITT with both El Niño and La Niña composites having a spatial correlation of 0.850. RAQMS-Aura CO column is on average increased across the tropics during El Niño, with stronger enhancements of 0.4 x 10^{18} mol/cm^2 observed over the maritime continent. Enhanced CO over the maritime continent is tied to enhanced biomass burning during El Niño as precipitation is suppressed, increasing fuel aridity, and thereby increasing susceptibility to fire (Reid et al., 2013, van der Werf et al., 2017, Yin et al., 2016). RAQMS-Aura CO column decreases over the maritime continent during La Niña and is enhanced over South America. During La Niña, rainfall is enhanced over the maritime continent, resulting in CO decreases as fires are suppressed.

3.4.3 Vertical structure of tropospheric response to ENSO

As this study utilizes reanalysis data, I provide further context to the patterns in TTOC and CO columns. In particular, I explore how the vertical structure of convective mass flux, large-scale diabatic heating, and ozone production/loss terms respond to ENSO. Meridionally averaged vertical profile cross sections are calculated between 7.5°S and 2.5°N. This latitude band was selected as it cuts across the maximum and minimum precipitation anomalies associated with ENSO (Figure 3.10) and for consistency with the cross-sections analyzed by Doherty et al. (2006).

Convective mass flux anomalies between 7.5°S and 2.5°N for the positive and negative phases of ENSO are presented in Figure 3.13. The strongest convective mass flux anomaly is over the Pacific Ocean during both the positive and negative phase of ENSO. This strong convective mass flux anomaly is also where the absolute maximum precipitation anomaly occurs, which is expected given the dominance in convective precipitation in this region. Diabatic heating anomalies presented in Figure 3.14 are qualitatively similar to the convective mass flux ENSO anomalies. This is because the majority of the diabatic heating in this region is associated with the large-scale response to sub-grid-scale convective precipitation. The convective mass flux and diabatic heating anomalies during El Niño indicate decreased upward vertical transport over the maritime continent where precipitation is suppressed and increased upward vertical transport over the central Pacific where precipitation is enhanced. Conversely, the convective mass flux and diabatic heating anomalies during La Niña both indicate enhanced vertical transport over the maritime

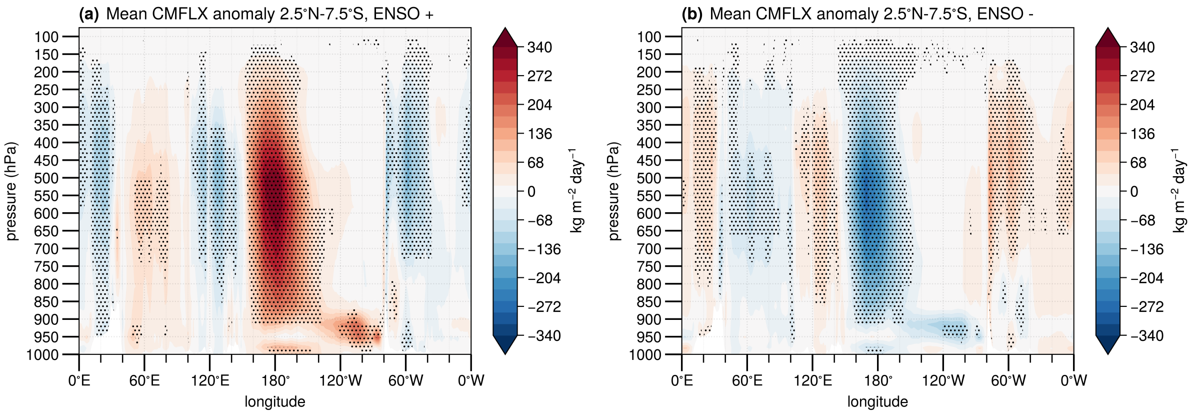

FIGURE 3.13: RAQMS-Aura convective mass flux (CMFLX) anomalies for a) positive and b) negative ENSO phases. Shaded regions indicate where the composite is significant at the 95% confidence level from a t test.

continent and increased downward vertical transport over the central Pacific. In Doherty et al. (2006), Sudo and Takahashi (2001) the positive and negative mass flux anomalies are of similar magnitudes while here the negative flux anomaly over Micronesia is $\frac{1}{2} - \frac{1}{3}$ the strength of the anomaly over the central-eastern Pacific. This may be a consequence of the high bias in precipitation over Micronesia in the RAQMS-Aura reanalysis, as the precipitation anomaly El Niño composite indicates that precipitation is not suppressed as much as in observations over the region. However, these differences in the strength of the vertical motion anomalies are consistent with the ENSO precipitation anomaly over the central Pacific being larger than that of the anomaly over the maritime continent in TRMM observations and RAQMS-Aura analyses. The precipitation and mass flux anomaly patterns display suppressed (enhanced) vertical motion over the Pacific and enhanced (suppressed) vertical motion over the maritime continent during the negative (positive) phase.

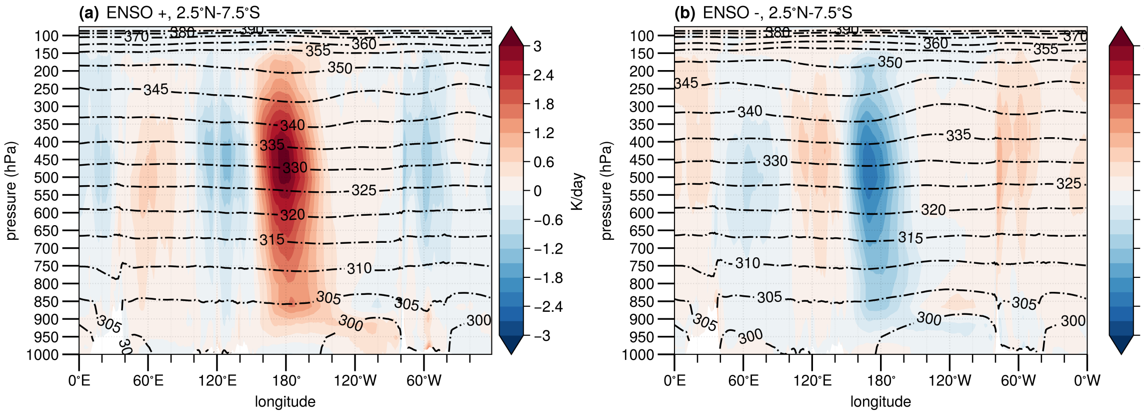

FIGURE 3.14: RAQMS-Aura diabatic heating anomalies (colors) and theta (contours) for a) positive and b) negative ENSO phases.

Ozone anomaly cross-sections associated with ENSO are presented in Figure 3.15. During El Niño the tropospheric ozone anomaly extends across the depth of the troposphere over the maritime continent, with two distinct stronger (>3 ppbv) enhancements above 550 hPa and below 700 hPa. Over the central Pacific (from 160°E to 140°W) where the convective mass flux is enhanced in the El Niño composite through the depth of the troposphere, a decrease in the ozone concentration of 3-5 ppbv occurs. The lower troposphere enhancement over the maritime continent is accompanied by a positive anomaly in net O_3 production (Figure 3.17a), indicating that some of the enhancement in TTOC over the maritime continent during El Niño is due to enhancement in chemical production and not solely due to shifts in the circulation pattern. The El Niño ozone anomaly cross-section is <1 ppbv throughout the majority of the troposphere off the South American Coast, indicating that the TTOC decrease is due to the decreased (>9 ppbv) concentrations near the tropopause, above 200 hPa. The La Niña ozone anomaly cross-section section shows enhancement in ozone over the central Pacific and decrease over the maritime continent. Over the maritime continent a distinct stronger (>2 ppbv) decrease is seen below

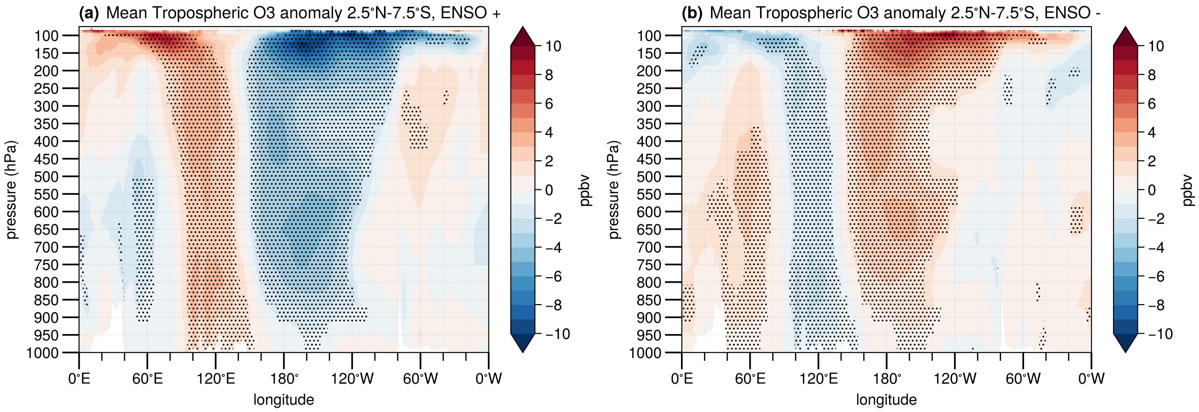

Figure 3.15: Anomalies in RAQMS-Aura ozone profiles below the tropopause associated with a) El Niño and b) La Niña. Shaded regions indicate where the composite is significant at the 95% confidence level from a t test.

700 hPa and above 350 hPa. Tropical upper troposphere ozone is also impacted by the quasi-biennial oscillation (QBO) (Oman et al., 2013), so I evaluated the QBO signatures for both zonal mean zonal wind and ozone. I find RAQMS-Aura does a reasonable job of capturing the stratospheric QBO signal. However, I find the influence of the QBO on RAQMS-Aura ozone in the tropical upper troposphere is smaller than the of ENSO influence during the 2006-2016 period considered in this study (Appendix A).

CO anomaly cross-sections for each ENSO phase are presented in Figure 3.16. Tropical CO is anomalously high during El Niño and anomalously low during La Niña. Tropical CO is enhanced over the maritime continent during El Niño throughout the tropical troposphere, with the strongest enhancement near the surface indicative of a strong increase in biomass burning emissions. The near-surface enhancements in CO over South America and Africa during El Niño are also likely tied to CO emissions from biomass burning, though these enhancements are not spread through the depth of the troposphere as occurs over the maritime continent. The negative CO anomalies associated with La Niña

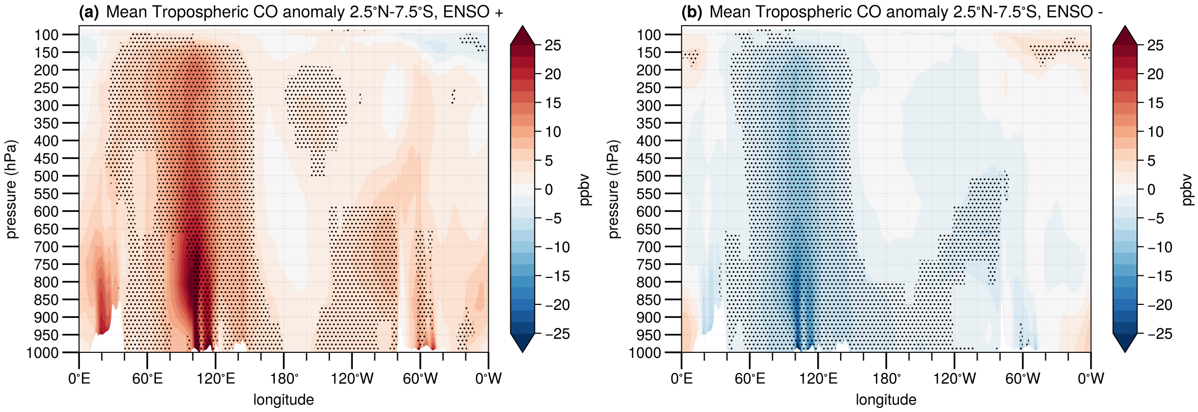

FIGURE 3.16: Anomalies in RAQMS-Aura CO profiles below the tropopause associated with a) El Niño and b) La Niña. Shaded regions indicate where the composite is significant at the 95% confidence level from a t test.

are largest over the maritime continent and are present through the depth of the troposphere. The enhancement in CO Column over South America associated with La Niña is not present in the La Niña vertical cross-section as it is to the south of the latitudes used to generate the cross-section composite.

Net ozone production (production - loss terms) anomalies are presented in Figure 3.17. RAQMS has standard hydrogen oxide (HO_x), chlorine oxide (ClO_x), bromine oxide (BrO_x), and NO_x ozone photochemistry (Eckman et al., 1995) with Carbon Bond-Z (CB-Z) (Zaveri and Peters, 1999) treatment of non-methane hydrocarbon chemistry. Chemical production and loss are calculated explicitly for the Ox family, which in RAQMS includes $O(^1D)$, $O(^3P)$, O_3, NO_2, HNO_3, NO_3, N_2O_5, HNO_4, peroxynitrates (PAN), and methacryloyl peroxynitrate (MPAN). Since the shifts in precipitation within the tropics are largely associated with shifts in convective clouds (Figure 3.1) and the photolysis rates in RAQMS respond only to changes in atmospheric transmittance due to large-scale resolved clouds, changes in net ozone production associated with changes in convective cloud distributions are not accounted for in this study. The largest net ozone production anomalies are closest to the surface and below 700 hPa. The change in net ozone production is smaller in La Niña than El Niño. Enhanced production of 2-3 ppbv/day is found over central Africa, Indonesia, and the Amazon rainforest in Brazil. These regions show reductions of ~ 1.3 ppbv/day in ozone production in the La Niña composite. El Niño is known to increase fire emissions in Indonesia as a consequence of the decreased rainfall over the region (Field et al., 2016, Park et al., 2021), and so the increased production of ozone during El Niño captured by RAQMS-Aura is likely to be partially due to enhanced chemical production of ozone in biomass burning plumes. Enhanced production during El Niño occurs over all 3 biomass burning regions but only the maritime continent shows a significant (>4 ppbv) enhancement in O_3 below 700 hPa. In contrast, the enhanced production over South America and Africa is associated with weak (<2 ppbv) ozone enhancement. The average winds below 800hPa during El Niño over South America (not shown) are northeasterly, resulting in transport of the ozone associated with biomass burning to the south and out of the latitudes included in the cross-section (7.5°S to 2.5°N). Over the maritime continent, the average winds below 750 hPa are southerly and decline in strength through the cross-section. Based on these wind patterns, ozone associated with biomass burning over the maritime continent experiences less meridional transport and has stronger influences on the ozone profile within this meridional cross-section.

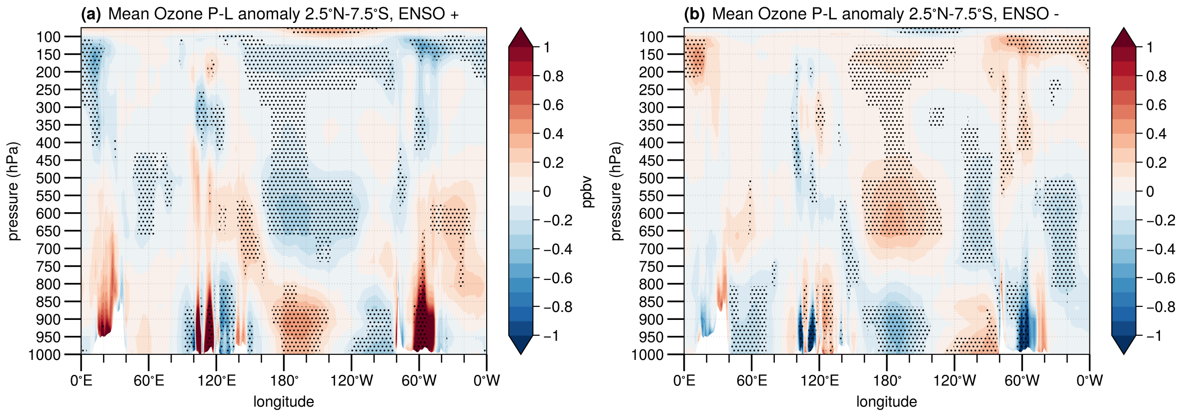

FIGURE 3.17: Anomalies in RAQMS-Aura net O_3 production associated with a) El Niño and b) La Niña. Shaded regions indicate where the composite is significant at the 95% confidence level from a t test.

3.5 EOF and Multiple Linear Regression Analysis

In addition to composite analysis, I apply Empirical Orthogonal Function (EOF) analysis to investigate the role played by ENSO in TTOC variability. The first EOF of TTOC has been previously found to be associated with ENSO, while TTOC EOFs 2 and 3 are uncorrelated with ENSO (Doherty et al., 2006, Sekiya and Sudo, 2012). ENSO positive and negative phases are near opposites of each other, and so it is reasonable to expect that much of the variability associated with ENSO can be captured with a single EOF. The EOF spatial patterns are displayed for TTOC, precipitation, and CO column in Figures 3.18-3.20. PC time series are presented in Figure 3.21, alongside the Niño 3.4 index for reference.

3.5.1 EOFs of RAQMS-Aura total precipitation, tropical tropospheric ozone column, and Carbon monoxide column

EOF patterns for TTOC are displayed in Figure 3.18. The TTOC PC_1 has a correlation of 0.747 with the Niño 3.4. The associated EOF indicates a 2-2.5 DU enhancement over the maritime continent and a 1.6-2 DU decrease over the Pacific (Figure 3.18a). EOF_1 captures similar features to those in the El Niño TTOC composite, though the enhancement in TTOC near Vietnam is weaker relative to the enhancement near Indonesia in the EOF compared to the composite. TTOC PC_2 and PC_3 are weakly correlated with the Niño 3.4 index, with correlations of -0.144 and -0.209 respectively. TTOC EOF_2 explains around half as much variance as TTOC EOF_1 and shows a wave 1 like pattern with a peak in the northeast Pacific. TTOC EOF_3 accounts for changes of less than 1 DU on average, and a maximum near 3 DU. At the most, this is 10% of the mean TTOC and less than 1% on average. TTOC EOF_3 captures an increase across the equatorial Pacific and decreases elsewhere.

EOF patterns for total precipitation are displayed in Figure 3.19. The precipitation PC_1 is strongly correlated with the Niño 3.4 index, with a temporal correlation of 0.870, as well as a strong temporal correlation with the TTOC PC_1 (0.818). The associated EOF pattern is similar to the El Niño precipitation composite in Figure 3.10a, though the magnitude of the decreased precipitation in the western Pacific relative to the enhancement in the central Pacific is smaller than in the composite. Precipitation EOFs 2 and 3 combined capture a similar amount of variability in precipitation as EOF_1 alone. Their PCs are not

(a) Tropospheric Ozone Column EOF 1

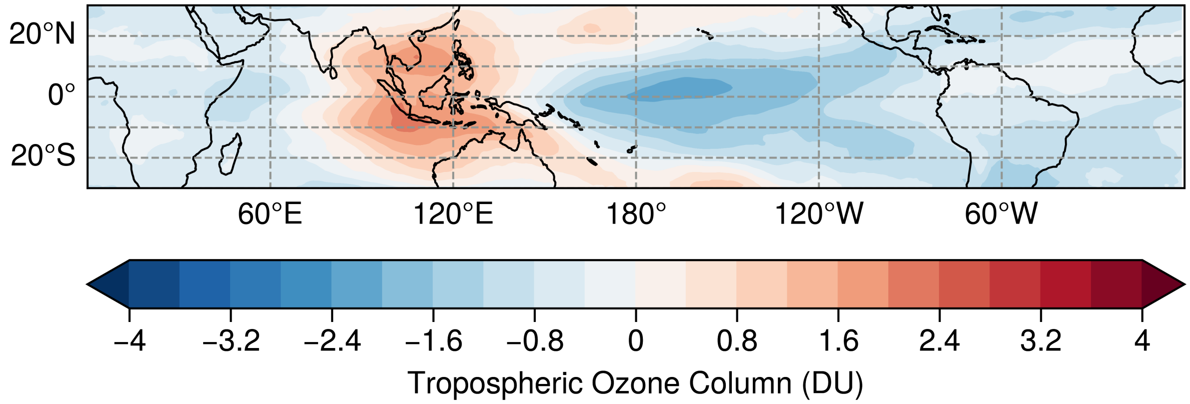

(b) Tropospheric Ozone Column EOF 2

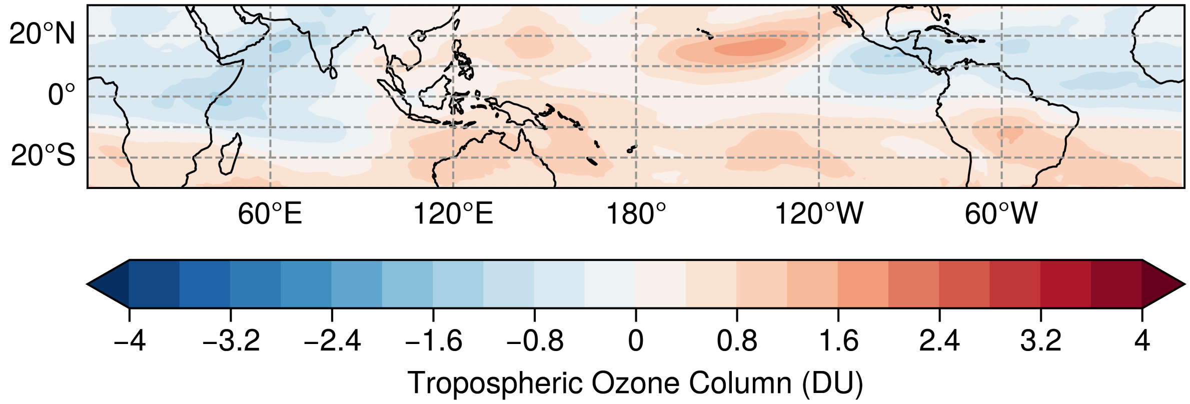

(c) Tropospheric Ozone Column EOF 3

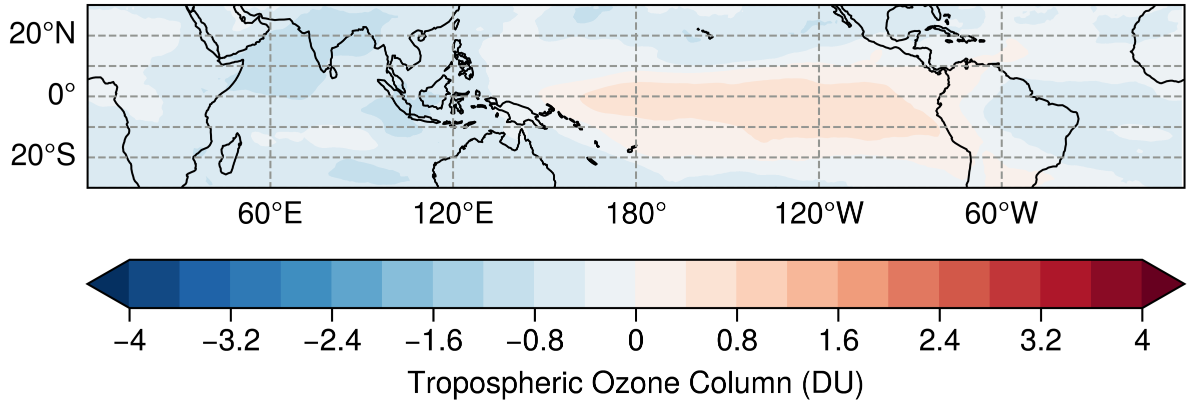

FIGURE 3.18: Patterns for RAQMS-Aura TTOC EOFs 1-3, scaled by 1 standard deviation of the associated PC. EOF_1 explains 17.20% of the non-seasonal variance in TTOC, EOF_2 explains 8.70% and EOF_3 explains 6.00%.

correlated with the Niño 3.4 index, with a PC_2 temporal correlation of -0.02, and a PC_3 temporal correlation of -0.093. The EOF_2 pattern depicts a small, localized enhancement in the central southern Pacific Ocean, slightly stronger enhancements of ~0.06 mm/hour in the Caribbean and NW equatorial Pacific, and decreased precipitation in the remainder of the northern hemisphere Pacific. The EOF_3 pattern accounts for changes of <0.03 mm/hour on average. The largest of these small changes are a decrease in precipitation in the central Pacific to the east of where the maximum precipitation anomaly associated with ENSO is located. Precipitation PC_3 has a temporal correlation of 0.695 with TTOC PC_2, indicating there is some co-variability between the two that I will not examine in depth in this work as it is not related to ENSO.

EOF patterns for CO column are displayed in Figure 3.20. Interannual variability in tropical CO has been shown to be predominately influenced by biomass burning emissions (Rowlinson et al., 2019). All 3 CO column EOF patterns appear to be heavily influenced by extreme biomass burning events, as the strongest changes are over the maritime continent and South America and the peaks in the PCs correspond with years with enhanced biomass burning in the regions highlighted by the largest values in the EOF (van der Werf et al., 2017, eg). CO PC amplitude peaks are larger than 2 for PC_1 in late 2015; PC_2 in 2006, 2007, 2010, and 2015; and PC_3 in 2006, 2015, and 2016 (Figure 3.21). EOF_1 explains 46.96% of the non-seasonal variance in CO, while EOF_2 explains 9.46% and EOF_3 explains 6.48%.

Most variability in CO columns from 2006-2016 is explained by EOF_1. The physical

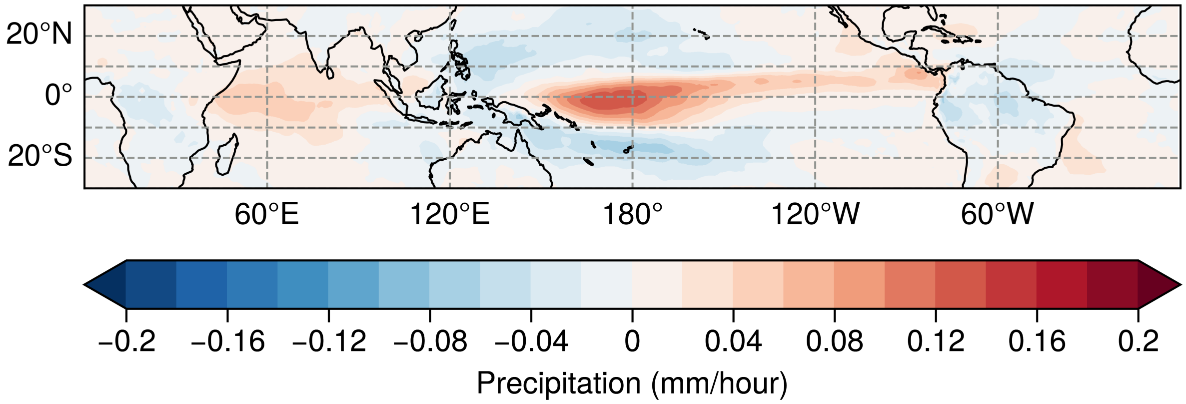

(a) Total Precipitation EOF 1

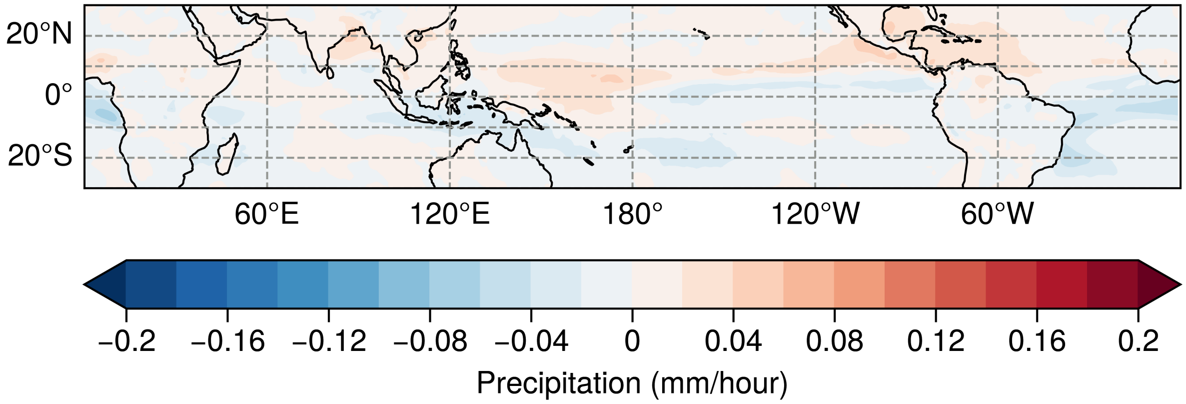

(b) Total Precipitation EOF 2

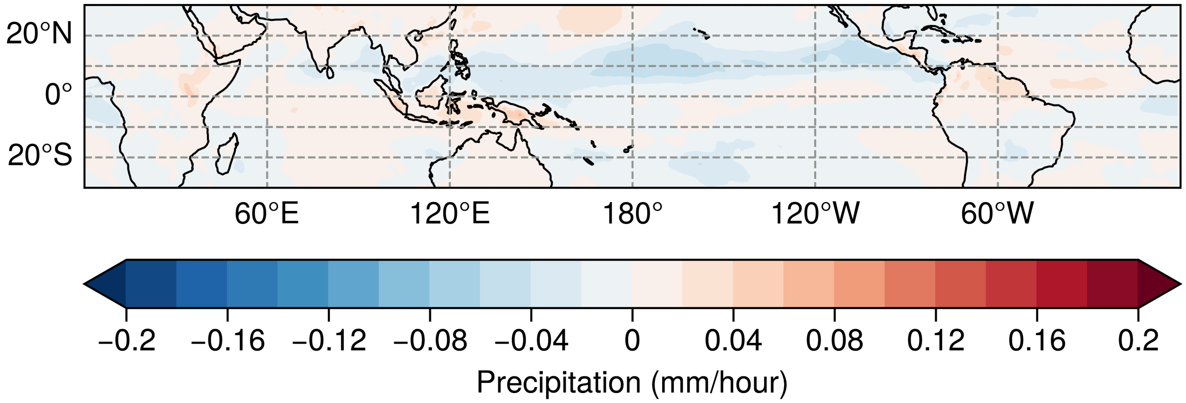

(c) Total Precipitation EOF 3

FIGURE 3.19: Patterns for RAQMS-Aura total precipitation EOFs 1-3, scaled by 1 standard deviation of the associated PC. EOF_1 explains 8.33% of the non-seasonal variance in total precipitation, EOF_2 explains 4.73% and EOF_3 explains 4.46%.

(a) CO Column EOF 1

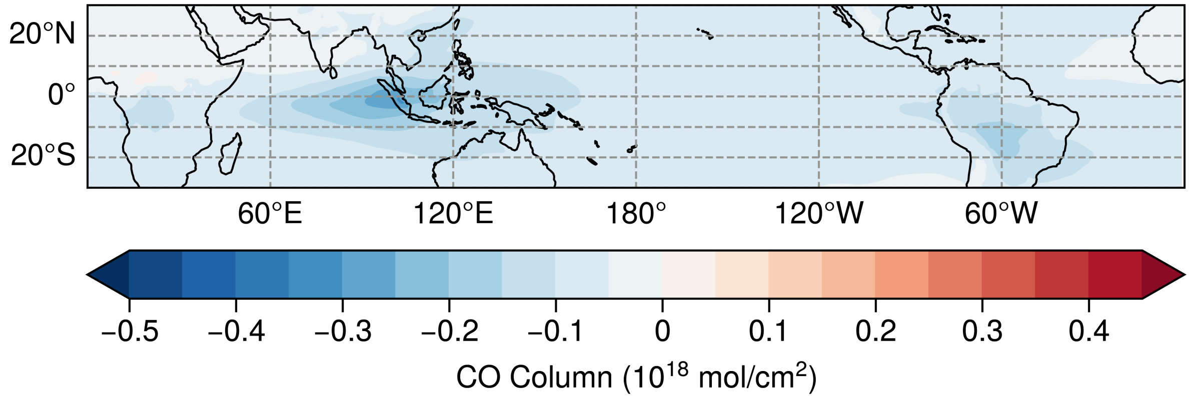

(b) CO Column EOF 2

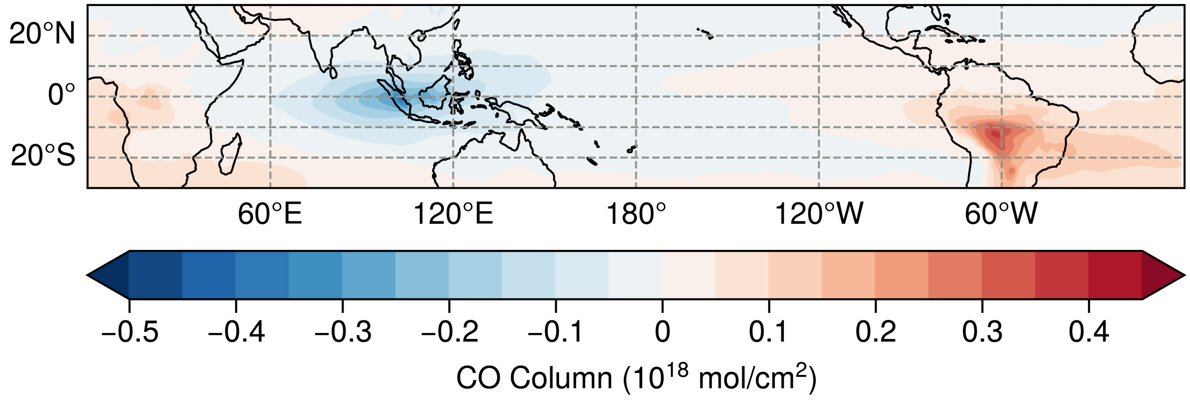

(c) CO Column EOF 3

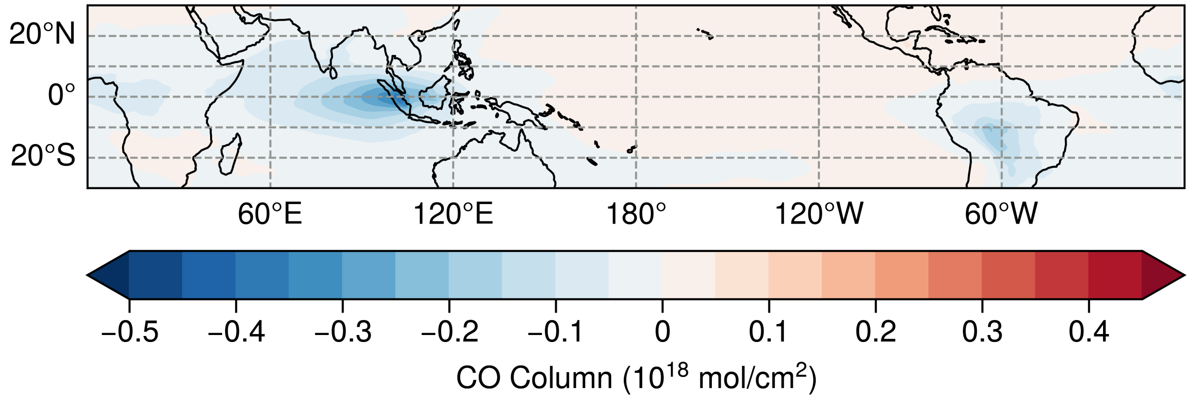

FIGURE 3.20: Patterns for RAQMS-Aura total precipitation EOFs 1-3, scaled by 1 standard deviation of the associated PC. EOF_1 explains 8.33% of the non-seasonal variance in total precipitation, EOF_2 explains 4.73% and EOF_3 explains 4.46%.

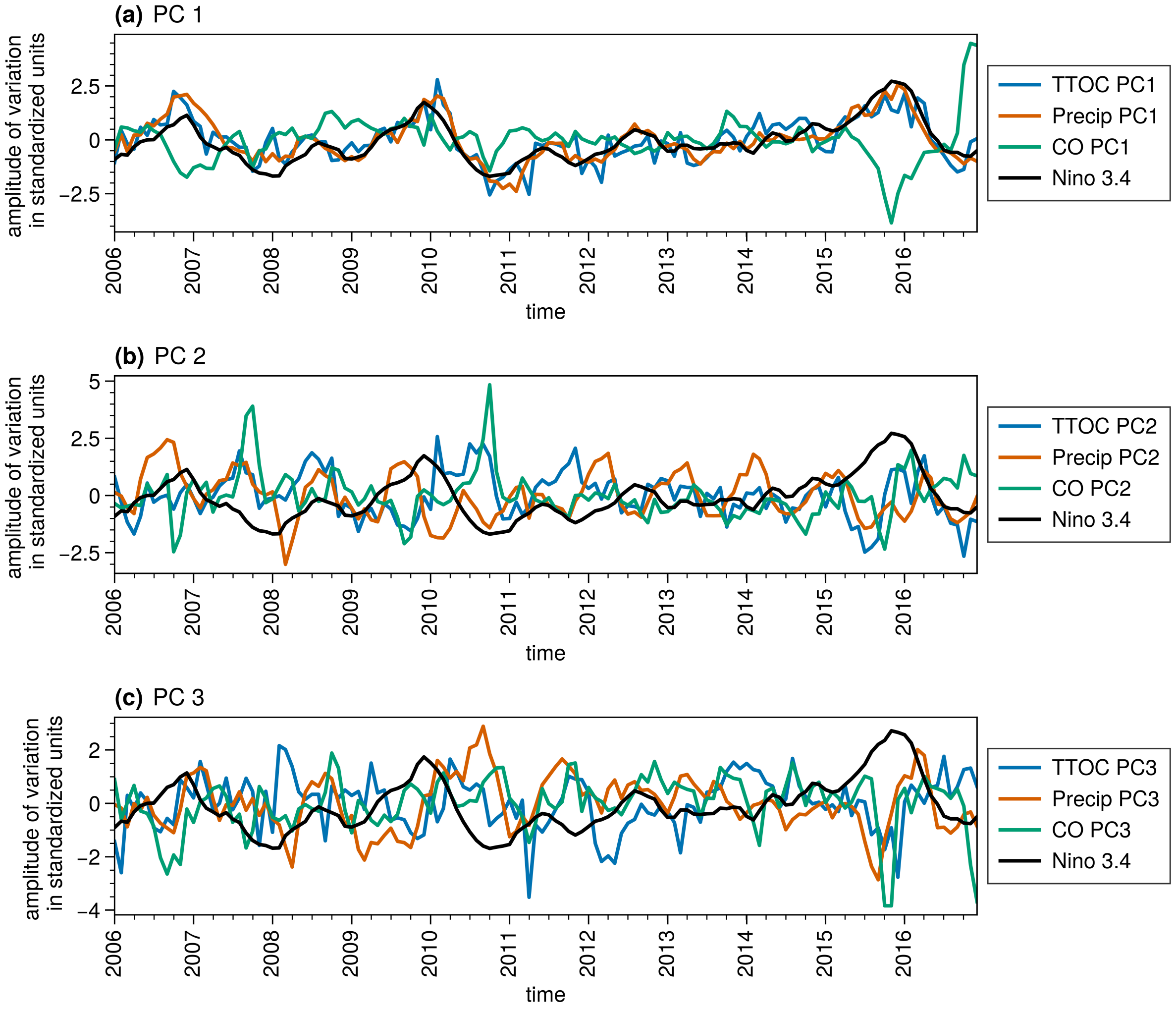

FIGURE 3.21: Timeseries of PC_1 (a), PC_2 (b), and PC_3 (c) for TTOC, total precipitation, and CO Column. Niño 3.4 Index time series included for reference.

pattern is indicative of a tropics-wide decrease (increase) in CO, with the peak change of ~0.3 x 10^{18} mol/cm^2 centered over the maritime continent. CO PC_1 has a temporal correlation of -0.399 with the Niño 3.4 index, which indicates an ENSO influence on CO variability. Additionally, CO PC_1 is temporally correlated with precipitation PC1 (-0.435), suggesting that ENSO related changes in precipitation contribute to the ENSO driven CO variability. This is consistent with precipitation influences on biomass burning. The CO EOF_2 pattern shows CO column enhancements over Brazil and decreases over the maritime continent. CO PC_2 has a temporal correlation of -0.297 with the Niño 3.4 index, and a temporal correlation of -0.435 with TTOC PC_1, suggesting that ENSO related changes in CO contribute to ENSO driven TTOC variability. EOF_3 pattern again highlights the maritime continent and Brazil varying together, with an opposing change in CO across the Pacific. CO PC_3 displays a correlation of -0.145 with the Niño 3.4 index.

3.5.2 Multiple linear regression reconstruction of TTOC PC_1

In the composite analyses I show that ENSO related shifts in precipitation correspond with changes in vertical motion, CO concentration, net ozone production, and tropospheric ozone concentrations. The composite analysis also indicates that some of the enhancement in TTOC over the maritime continent during El Niño is due to enhanced production of ozone from biomass burning emissions. The EOF analysis further links variation in biomass burning to the TTOC variation as CO PCs 1 and 2 are mildly temporally anti-correlated with TTOC PC_1 and precipitation PC_1. This negative correlation is due to the suppression of biomass burning during precipitation. To quantify the relative importance of dynamical and biomass burning variability on ENSO related variability in TTOC, I construct a multiple linear regression analysis using the principal components. The regression equation is shown in equation 3.1.

$$PC1_{TTOC} = w_1 PC1_{CO} + w_2 PC2_{CO} + w_3 PC3_{CO} + w_4 PC1_{precip} + e \tag{3.1}$$

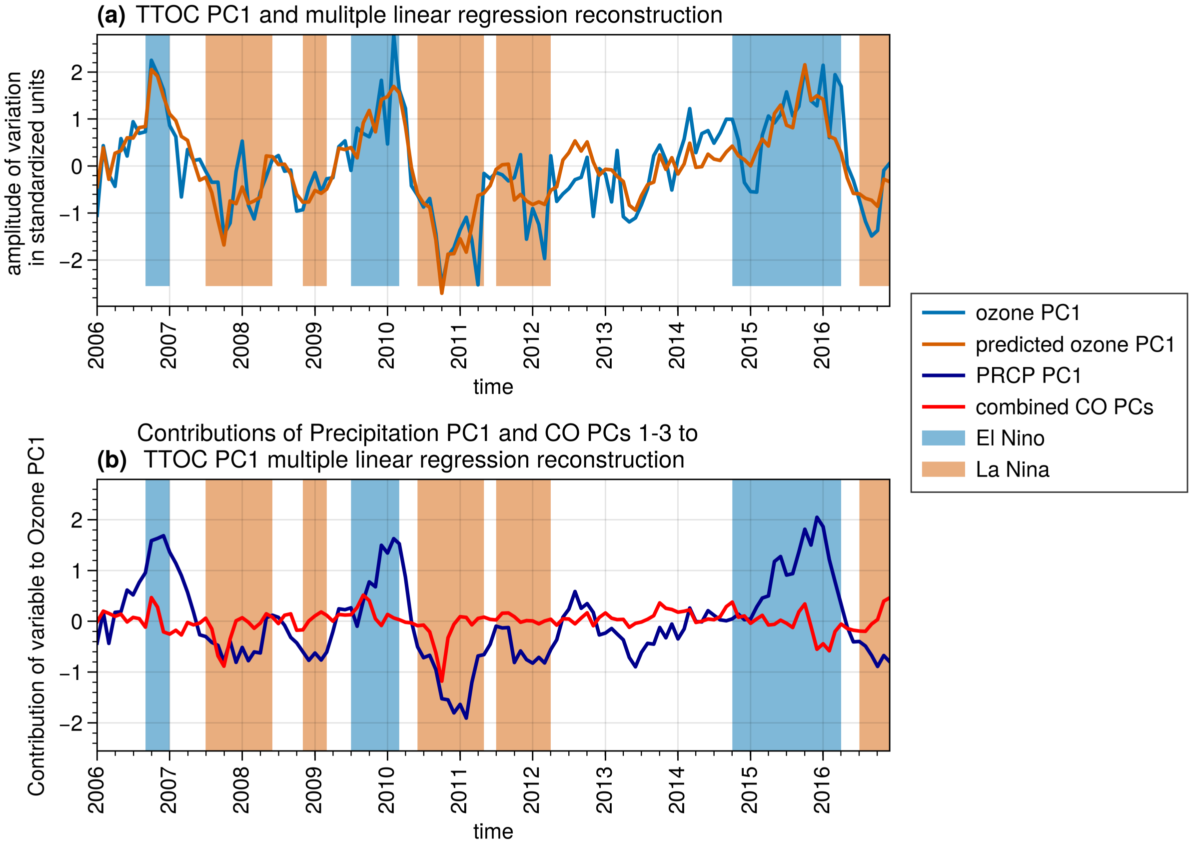

FIGURE 3.22: a) TTOC PC_1 from EOF analysis and reconstructed from multiple linear regression. b) Contribution to regression of Precipitation PC_1 and combined contribution of CO PCs 1-3.

The principal components are from the EOF analysis; w_1, w_2, w_3, w_4, and e are regression coefficients as determined using a least squares fit. The resulting regression model is shown in equation 3.2.

$$PC1_{TTOC} = 0.11*PC1_{CO}-0.2*PC2_{CO}+0.004*PC3_{CO}+0.8*PC1_{precip}-3.3x10^{-10} \quad (3.2)$$

This multiple PC regression reproduces the TTOC PC_1 very well, with the regression-based estimate correlating with the original TTOC PC_1 at 0.85 (Figure 3.22a).

The strongest weighted PC in the regression is the precipitation PC_1, which is expected given its strong correlation with TTOC PC_1. This supports the result from Doherty et al. (2006) and Inness et al. (2015a) that ENSO variability in TTOC is primarily driven by convective transport. The weights for CO PC_1 and PC_2 are also significant, indicating that CO, as a proxy for biomass burning, also contributes to TTOC variability.

A timeseries showing the contributions of precipitation PC_1 and the combined CO PCs to the TTOC PC_1 predicted by the regression is shown in Figure 3.22b. The precipitation PC_1 regression contribution is positive during El Niño periods and negative during La Niña periods. The combined regression contribution of the CO PCs shows that variability in CO contributes to ENSO variability in TTOC episodically. As the CO column anomaly is linked to anomalous biomass burning emissions and net ozone production near the surface, it can be concluded that a portion of the ENSO variability in TTOC is due to biomass burning though it is a smaller portion than that linked to the dynamical effects of ENSO.

Additionally, each component of the regression can be removed independently in order to evaluate the impact of co-variability between the CO PCs and precipitation PC_1 on the overall fit. RMSE and R^2 for the standard fit and the alternate fits are given in Table 3.2. R^2 is maximized and RMSE minimized for the case where all CO PCs are considered. The poorest fit is obtained when precipitation PC_1 is removed. The linear regression that relates ENSO TTOC variability to only ENSO precipitation variability performs similarly to the regression with CO PC_2 removed, highlighting that the redistribution of O_3 and

Table 3.2: RMSE and R2 for TTOC PC1 multiple linear regression models.

Regression equation	R^2	RMSE
$PC1_{TTOC} = 0.11 * PC1_{CO} - 0.2 * PC2_{CO} + 0.004 * PC3_{CO} + 0.8 * PC1_{precip} - 3.3x10^{-10}$	0.724	0.5258
$PC1_{TTOC} = -0.2177 * PC2_{CO} - 0.0526 * PC3_{CO} + 0.7440 * PC1_{precip} - 2.072x10^{-10}$	0.714	0.5347
$PC1_{TTOC} = 0.1433 * PC1_{CO} - 0.0262 * PC3_{CO} + 0.8752 * PC1_{precip} - 4.507x10^{-10}$	0.687	0.5591
$PC1_{TTOC} = 0.1151 * PC1_{CO} - 0.1984 * PC2_{CO} + 0.8102 * PC_{precip} - 5.293x10^{-10}$	0.722	0.5273
$PC1_{TTOC} = -0.2373 * PC1_{CO} - 0.4351 * PC2_{CO} - 0.2023 * PC3_{CO} + 9.887x10^{-10}$	0.287	0.8446
$PC1_{TTOC} = 0.812 * PC1_{precip} - 4.777x10^{-10}$	0.669	0.5750

O_3 precursors by convection is the most significant contributor to ENSO variability in TTOC. The best regression fits (R^2 >0.7) include CO PC_2 and precipitation PC_1. This confirms that while variability in CO is not independent of variability in precipitation, it does meaningfully contribute to ENSO variability in TTOC.

As inferred from the regression, El Niño increases in TTOC over the maritime continent are associated with CO PC_1 enhancements in CO over the maritime continent while CO PC_2 is associated with enhancements in CO over South America and Africa and decreases over Indonesia. Timeseries of the CO column and TTOC anomalies (not shown) have a correlation of 0.668 over the maritime continent and 0.566 over South America. The TTOC and CO anomalies over the maritime continent are positive during El Niño events and negative during La Niña events. Over South America, the sign of the TTOC and CO anomalies are less consistent with ENSO phase.

3.6 2015/2016 extreme El Niño

Through the satellite era, extreme El Niño events in 1982/1983, 1997/1998, and 2015/2016 have been observed alongside weak and moderate events. These extreme events have a larger impact on the distribution of TTOC and have a larger contribution from biomass burning emissions than weaker El Niño events (Doherty et al., 2006, Inness et al., 2015a). The 2015/2016 extreme El Niño was the strongest El Niño since the 1997/1998 event (Santoso et al., 2017). 2015 and 1997 are also among the most extreme maritime continent biomass burning events, with 1997 ranking first followed by 2015 in an analysis of surface visibility at airports in Sumatra and Kalimantan from 1990-2015 (Field et al., 2016). Here I investigate how the inclusion of the 2015 extreme El Niño influences our interpretation of the importance of biomass burning on TTOC ENSO variability. As in prior analyses (Chandra et al., 2009, 1998, Sudo and Takahashi, 2001), I focus on October as biomass burning in the maritime continent peaks around October and would have its greatest impact on TTOC around the same time (Field et al., 2016). In RAQMS-Aura, the CO PC amplitudes have the largest variability in October and the largest contributions of the CO PCs to the TTOC PC_1 regression occur in October.

The RAQMS-Aura 2015 October TTOC anomaly is shown in Figure 3.23a. This pattern is similar to the October 1997 anomaly in TTOC modeled by Sudo and Takahashi (2001) with an increase over the maritime continent that is 2-3 times stronger than the decrease over the eastern Pacific. However, the peak decrease over the eastern Pacific is more towards the central Pacific during 2015 than in 1997. The maximum increase over the maritime continent is 10-15 DU in October 2015, less than the maximum 20-24 DU increase in October 1997. RAQMS-Aura TTOC increases over South America in October 2015 by 1-4 DU, while the Sudo and Takahashi simulated October 1997 changes by less than 2 DU over South America. These differences over Africa and South America in 2015 versus 1997 are consistent with the differences in patterns of convective mass flux. In 2015 mass flux is decreased aloft over Brazil and Africa (Figure 3.23b), while in 1997 changes in mass flux over Brazil and Africa are weaker and are slightly positive (Sudo and Takahashi, 2001). The core of the upward mass flux anomaly over the Pacific is ∼30-40 degrees closer to the dateline in 2015.

Over the maritime continent, the ozone concentration anomaly below 650 hPa is stronger than in the 2006-2016 El Niño average. The 2006-2016 October El Niño average anomalies are shown in Figure A.4 (Appendix A). This is linked to stronger ozone production in October 2015. This enhancement in O_3 production in 2015 is likely due to increased fire activity, as CO column is increased throughout the tropics in 2015 (Figure 3.23e) and the CO anomaly over the maritime continent is more widespread and stronger by $\sim 0.2\text{x}10^{18}$ mol/cm^2 than the 2006-2016 El Niño average. There is also an enhancement in CO, ozone, and net ozone production over South America in October 2015 relative to the 2006-2016 El Niño composite. This shows that the biomass burning activity in 2015 was anomalous compared to the other El Niño years included in the RAQMS-Aura reanalysis, with significant burning occurring over both South America and the maritime continent.

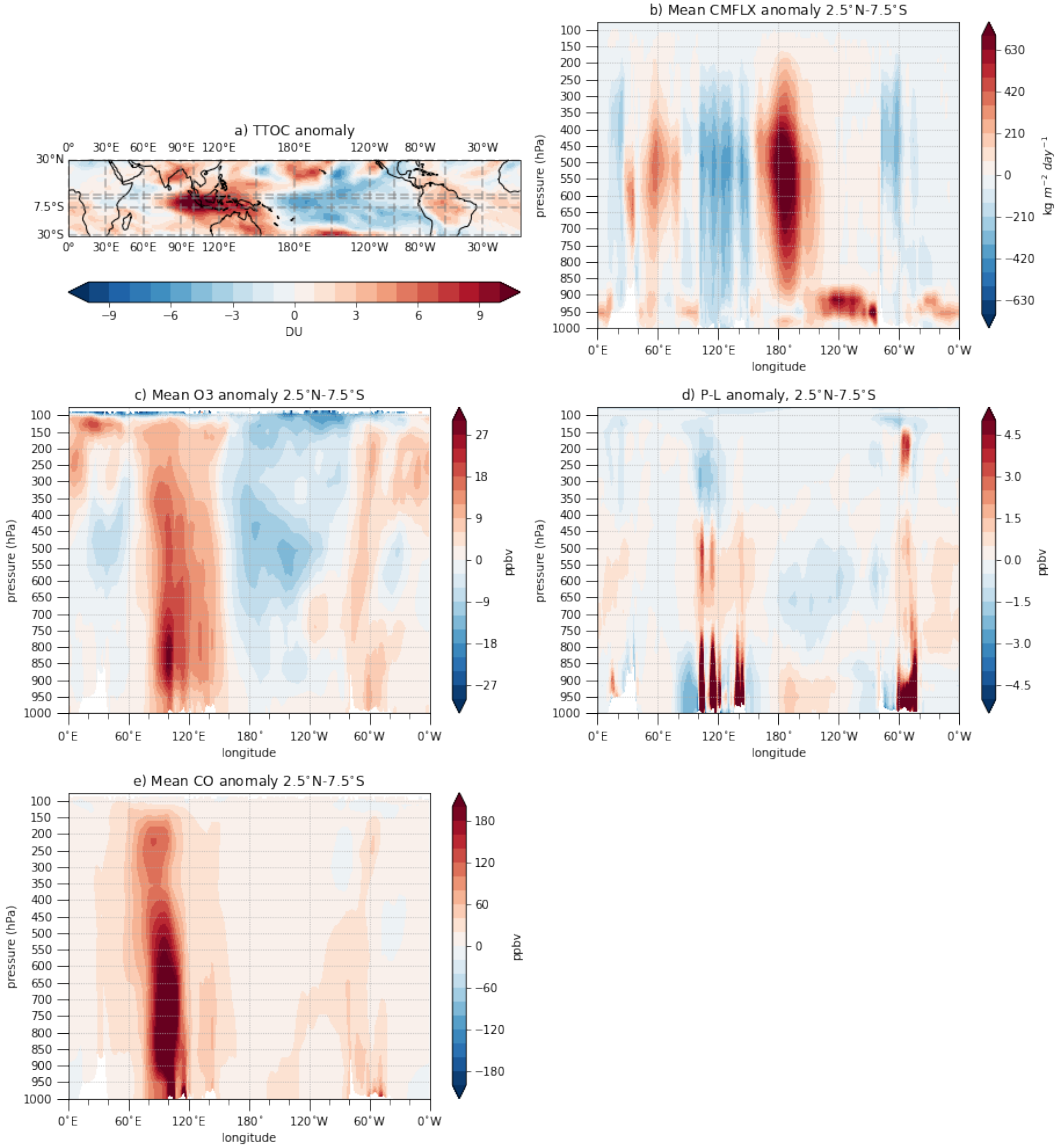

a) TTOC anomaly

b) Mean CMFLX anomaly 2.5°N-7.5°S

c) Mean O3 anomaly 2.5°N-7.5°S

d) P-L anomaly, 2.5°N-7.5°S

e) Mean CO anomaly 2.5°N-7.5°S

FIGURE 3.23: RAQMS-Aura October 2015 a) TTOC anomaly, b) convective mass flux anomaly, and c) tropospheric ozone profile anomaly, d) P-L, e) CO.

3.7 Conclusions

The RAQMS-Aura reanalysis captures observed ENSO variability in TTOC, CO, and precipitation. ENSO composites of tropospheric ozone, carbon monoxide, convective mass flux, diabatic heating, and ozone net chemical production show that the observed ENSO signatures in TTOC result from a combination of convective redistribution and variability in production of ozone from biomass burning emissions, which are modulated by ENSO variability in precipitation. The location of the peak decrease in TTOC resulting from increased vertical motion in the eastern Pacific depicted in the El Niño composite found by this study is comparable to other studies of TTOC variability in the 2000s and 2010s (Olsen et al., 2016, Oman et al., 2011). The location of the peak decrease in TTOC contrasts with that found by analyses of 1970s-2000 where it is more towards the southeast and near the South American coast (Doherty et al., 2006, Peters et al., 2001, Ziemke and Chandra, 2003). The RAQMS-Aura El Niño TTOC composite is in agreement with the El Niño composite OMI-MLS TOR observations, and the analysis of convective flux indicates that the ozone decreases over the central Pacific are due to enhanced vertical motion. Therefore, I believe the difference in position of the peak decrease in TTOC is due to characteristics of El Niño during the 2006-2016 analysis period. El Niño events from 2006-2016 were predominately El Niño Modoki events, while El Niño events between 1979 and 2002 display greater variability in type of El Niño and includes more canonical ENSO events (Hou et al., 2016, Lee and McPhaden, 2010, Santoso et al., 2017). The ascending branches of Walker circulation cell is over the central Pacific during El Niño

Modoki (Ashok et al., 2007), while during canonical El Niño the ascending branch is over the eastern Pacific. Since TTOC is decreased where vertical motion is enhanced during ENSO and increased where vertical motion is suppressed, it is expected that under El Niño Modoki conditions the largest decrease in TTOC will be in the central Pacific with TTOC increases in the western and eastern Pacific. This response of TTOC to El Niño Modoki is shown by Hou et al. 2016 and is in-line with the El Niño RAQMS-Aura TTOC anomaly composite calculated by this study (Figure 3.11).

The strongest ENSO variability in tropospheric ozone is shown to occur near the tropopause. Enhancement in ozone below 700 hPa during El Niño over the maritime continent is coincident with enhanced net ozone production and dependent on the strength of the biomass burning emissions. The EOF analyses and multiple linear regression further indicate that ENSO variability in TTOC is driven by shifts in the location of the ascending and descending branches of the Walker circulation. The EOF and multiple linear regression analyses also indicate that variability in biomass burning, as inferred from CO anomalies, contributes to ENSO variability in TTOC. During the 2015/2016 strong El Niño event TTOC, CO, and convective mass flux anomalies were stronger than in the weaker ENSO events captured by the RAQMS-Aura reanalysis. The 2015 CO concentrations align with the mode captured by CO EOF_1 while the other El Niño years included in my analysis align with the mode in CO EOF_2. Biomass burning enhanced TTOC and CO anomalies occurred over both South America and the maritime continent in October 2015 in contrast to the other El Niño years between 2006 and 2016 where biomass burning enhanced TTOC and CO was only found over the maritime continent.

Chapter 4

Evaluating Biomass Burning CO Emissions in UFS-RAQMS Through Application of TROPOMI CO Column Data Assimilation

4.1 Introduction

In Chapter 3 I showed that variability in CO emissions from biomass burning in the maritime continent contributes to climatic variability in the tropical tropospheric ozone distribution. Extreme biomass burning emissions from the maritime continent in 2015 amplified production of tropospheric ozone over the maritime continent more than during the average El Niño years. In the remainder of this dissertation I further evaluate the impact of biomass burning emissions from tropical biomass burning, and contrast it with the impact of boreal biomass burning emissions, utilizing UFS-RAQMS experiments of July-August-September (JAS) 2019.

Global biomass burning emissions typically peak around August-September (van der Werf et al., 2017). Siberian wildfire emissions peaked during July and August 2019, and by September global biomass burning emissions were predominantly due to burning in the tropics (Figure 4.1). In September 2019 smoke from drought-enhanced biomass burning in the maritime continent contributed to the 3rd highest AOD in the MODIS record, behind significant enhancements in 2006 and 2015 (Reid et al., 2023). South America and central Africa burned throughout JAS 2019. Smoke from the Siberian wildfires was transported over North America, where it impacted tropospheric composition and surface air quality (Johnson et al., 2021). During JAS the 2019 NASA/NOAA Fire Influence on Regional to Global Environments and Air Quality (FIREX-AQ) field campaign (Warneke et al., 2023) sampled smoke plumes over North America. The NASA Cloud, Aerosol and Monsoon Processes Philippines Experiment (CAMP^{2}Ex) field campaign (Reid et al., 2023) occurred 25 August - 5 October 2019 and sampled airmasses over the maritime continent. Fire activity in the continental US in 2019 was significantly below average, thought to be the result of higher fuel moisture content (Warneke et al., 2023).

CO is an important atmospheric trace gas due to both its influence on OH and O_3 chemistry and its use as a pollution transport tracer. The major loss pathway for CO is its

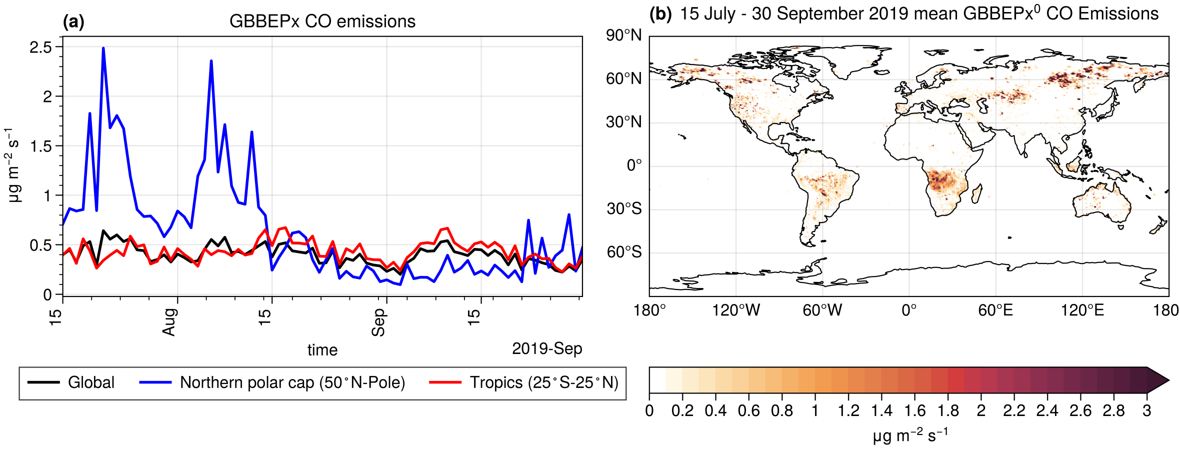

Figure 4.1: Standard GBBEPx CO emissions during 15 July - 30 September 2019. Panel (a) displays time series of over selected regions. Panel (b) mean spatial distribution of GBBEPx emissions.

reaction with OH (Logan et al., 1981), and this reaction significantly impacts the oxidizing capacity of the atmosphere. CO sources include production during VOC oxidation and direct emission from biomass burning and fossil fuel combustion. CTMs frequently underestimate CO (e.g. Holloway et al., 2000, Naik et al., 2013, Shindell et al., 2006, Strode et al., 2015). Potential reasons for this include underestimation of anthropogenic and/or biomass burning emissions, overestimation of OH, and underestimation of secondary CO production from VOCs.

Biomass burning emissions inventories have a high uncertainty due to factors including the incomplete knowledge of the spatiotemporal distribution of sources and limitations in capturing variation in fuel and fire behavior characteristics (e.g. Hyer and Reid, 2009, Pan et al., 2020). CTM forecasts vary significantly depending on which biomass burning emission inventory is used (e.g. Bian et al., 2007, Pan et al., 2020, Stockwell et al., 2022). Additionally, biomass burning emissions schemes use emission ratios relative to CO for determining the release of VOCs and other non-CO emissions further compounding the effect of poor biomass burning emissions on CTM forecast skill for VOC-NOx-O_3 chemistry.

A strong relationship between black carbon aerosols and CO has been observed in air-masses dominated by biomass burning emissions (e.g. Arellano Jr. et al., 2010, Spackman et al., 2008) due to their co-emission during combustion. Similarly, satellite AOD and CO column observations are strongly correlated over regions where biomass burning is the dominant contributor to fine mode AOD (e.g. Bian et al., 2010, Edwards et al., 2006, 2004). The correlation in space and time between AOD and CO is stronger in the southern hemisphere, while in the NH peak AOD and CO loadings are offset due to the higher anthropogenic pollutant loading (Bian et al., 2010, Buchholz et al., 2021, Edwards et al., 2004). Due to the shorter lifetime of biomass burning aerosols, enhancements in AOD are a strong indicator of biomass burning emissions sources while CO is a good tracer of down-wind impacts of those emissions due to its longer lifetime (e.g. Bian et al., 2010, Buchholz et al., 2021, Edwards et al., 2006). Edwards et al. (2006) also finds that the correlation between CO and AOD is strongest during the first few days of a biomass burning event and declines as the local CO concentration becomes less representative of daily emissions.

Chemical data assimilation (DA) systems can be used to reduce the impacts of emissions uncertainty and model deficiencies in representing sub-grid scale processes by using atmospheric composition measurements to constrain CTM fields. Chemical DA capabilities have been developed by modifying meteorological DA systems to use chemical concentration measurements. DA methods implemented for chemical DA include optimal interpolation-based methods (e.g. Lamarque and Gille, 2003, Lamarque et al., 1999, Pierce et al., 2009), 3D variational methods (Pagowski et al., 2010), and 4D variational methods (Inness et al., 2022a, 2015b). Chemical DA improves the CTM analysis through minimizing the difference between observations and model analyses. Observation datasets with a higher spatial coverage during the assimilation window provide more information about the true atmospheric composition. DA systems have been used to assimilate remote sensing observations of CO from Measurement of Air Pollution from Space (MAPS), Interferometric Monitor for Greenhouse Gases (IMG), MOPITT, Infrared Atmospheric Sounding Interferometer (IASI), and TROPOMI (e.g. Barré et al., 2015, Clerbaux et al., 2001, Inness et al., 2022a, 2015b, Lamarque et al., 1999). In this chapter I evaluate the GBBEPx CO emissions during JAS 2019 through applying TROPOMI CO DA to UFS-RAQMS.

4.2 GBBEPx CO Emissions

The GBBEPx CO emissions were briefly described in Chapter 1, Section 1.3.1. Here I further describe the approach as laid out in the algorithm theoretical basis document (Zhang et al., 2019). The GBBEPx product blends emissions estimated from Visible Infrared Imaging Radiometer Suite (VIIRS) observations with QFED emissions estimates.

QFED calculates emissions from MODIS observations, with the scaling factors for relating FRP to emissions tuned based on MODIS AOD and AOD analyses from the NASA Goddard Earth Observing System Model (GEOS-5). The scaling factor for VIIRS emissions were derived under the assumption that VIIRS fire emissions will be the same as the QFED emissions using data from April 2016 - March 2017.

4.3 TROPOMI CO DA

I use the GSI 3DVAR DA system (Kleist et al., 2009, Wu et al., 2002) to assimilate TROPOMI CO columns. Within this implementation, the UFS-RAQMS 3D CO volume mixing ratio is used as the analysis variable in the minimization procedure. The background error covariance (BEC) statistics for CO are obtained using the NMC method (Descombes et al., 2015, Parrish and Derber, 1992). The NMC method typically uses differences between 24-hour forecasts and 48-hour forecasts to estimate BEC statistics. Here, in addition to the standard BEC implementation, I apply the NMC method to a pair of forecasts that have different biomass burning emissions to account for uncertainties in CO emissions. The biomass burning emission BEC statistics are computed from the differences between 100% GBBEPx CO emissions and 85% GBBEPx CO emissions UFS-RAQMS CO forecasts. The biomass burning and forecast BEC statistics are then combined together in a piecewise-linear fashion to create "blended" BEC statistics. I set the blended BEC statistics equal to the standard, forecast-sensitive BEC statistics above model level 25 (approximately 480hPa). Below model level 15 (approximately 780hPa), the blended BEC statistics are equal to the biomass burning BEC statistics with an inflation factor of 5 applied to the standard deviation. Between model levels 15 and 25, the two BEC estimates are linearly blended.

The level 2 TROPOMI CO column product has a spatial resolution of 5.5 x 3.5 km (7 x 3.5km prior to August 6, 2019), which is higher than UFS-RAQMS resolution. Owing to this difference in resolution, multiple TROPOMI observations may fall within a model grid box during the assimilation window. Unlike other studies that utilize satellite CO “super-observations” (e.g. Gaubert et al., 2020, Inness et al., 2022a, Sekiya et al., 2021), I assimilate observations individually since using super-observations smooths the spatial variability in analysis increments (Sekiya et al., 2021). Super-observation smoothing could lead to underestimates in localized CO column enhancements associated with biomass burning.

Figure 4.2a shows the mean TROPOMI CO columns over the continental US during the FIREX-AQ field campaign and the NASA DC-8 flight tracks. CO columns over the central and eastern US are ∼2x higher than over the western US largely due to higher topography in the western US and thus thinner atmospheric columns. Figure 4.2b shows the mean TROPOMI CO columns over SE Asia during the CAMP2Ex field campaign and the NASA P-3 flight tracks. During CAMP^{2}Ex high CO columns (>4x10^{18} mol/cm^2) over the islands of Borneo and Sumatra are due to the sustained burning of peatlands (Reid et al., 2023).

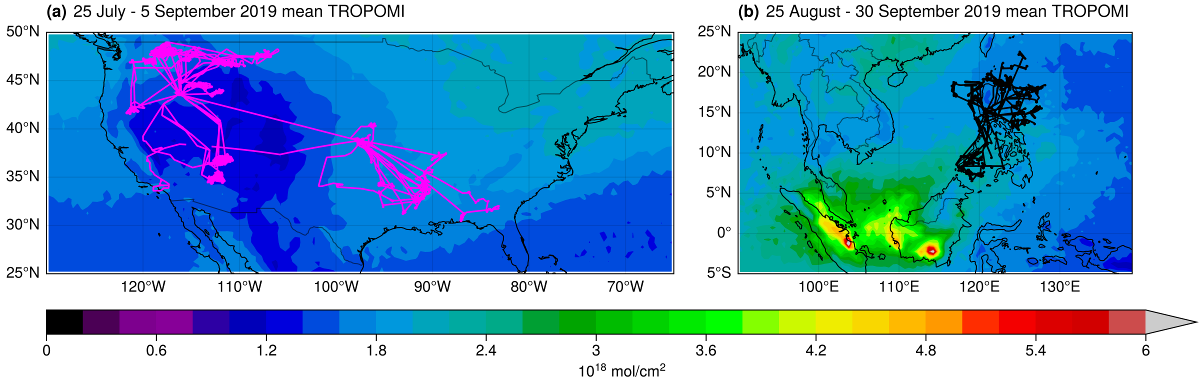

FIGURE 4.2: Mean TROPOMI CO columns over the US (a) and SE Asia (b). FIREX-AQ DC-8 flight tracks (pink) and CAMP^{2}Ex P-3 (black) flight tracks are shown over the respective campaign domains.

4.4 Impact of TROPOMI CO Assimilation on UFS-RAQMS CO

The UFS-RAQMS control CO columns are lower than the TROPOMI CO column observations in the NH and higher in the SH (Figure 4.3). Figure 4.3 also shows the FIREX-AQ and CAMP^{2}Ex field campaign domains and the locations of NDACC FTIR spectrometers used to validate UFS-RAQMS CO profiles. The NDACC FTIR CO, in-situ CO observations from FIREX-AQ and CAMP^{2}Ex, and MOPITT CO column retrievals are used to validate the UFS-RAQMS TROPOMI CO DA experiment.

The UFS-RAQMS control experiment significantly underpredicts CO columns over central Africa, the maritime continent, and Siberian Russia. Figure 4.1 shows that each of these regions are associated with significant biomass burning during this period.

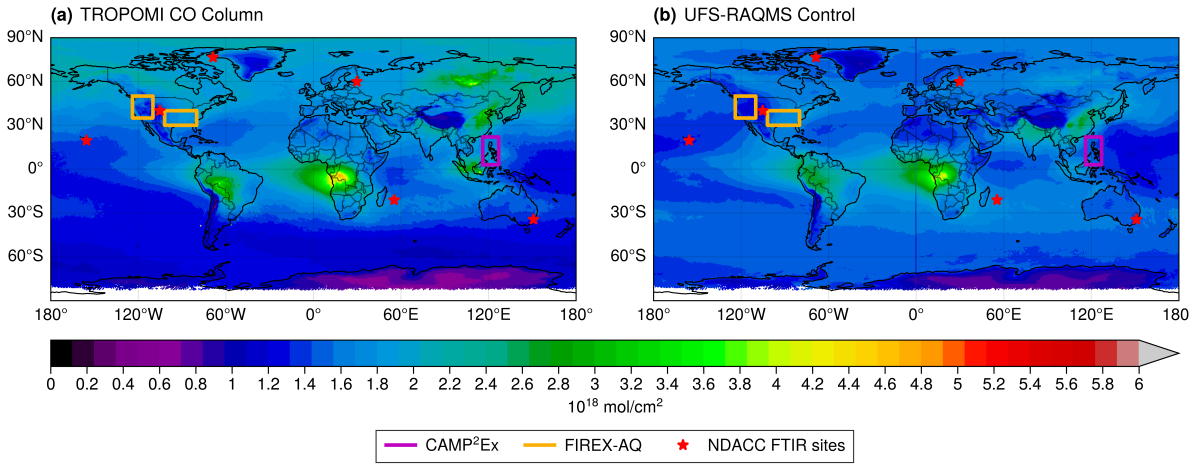

FIGURE 4.3: 15 July- 30 September 2019 average CO column concentrations for (a) TROPOMI and (b) UFS-RAQMS control. Boxes indicate domains for CAMP^{2}Ex (purple) and FIREX-AQ (yellow) campaigns. NDACC FTIR locations utilized in this study are denoted by red stars.

4.4.1 Differences in CO between control and DA experiments

To quantify the impact of assimilating TROPOMI CO columns on UFS-RAQMS analyses, I calculate the average percent change in zonal mean CO and CO total column between the control and DA experiments. Figure 4.4a shows that the assimilation increases tropospheric zonal mean CO north of 20°S and decreases zonal mean CO above the tropopause. Above the tropopause the largest impact of the TROPOMI CO DA on zonal mean CO is a decrease of 32-52% in the southern hemisphere (SH) between 40°S and 60°S and 11-13 km. The stratospheric regions with the largest decreases are in the midlatitudes and characterized by a strong vertical gradient in CO that sharpens as a result of the TROPOMI CO DA. These stratospheric percentage changes are associated with low CO concentrations. These large stratospheric differences are not a direct consequence of the TROPOMI CO column assimilation, as zonal mean cross sections of the analysis increments (not shown) illustrate that the TROPOMI CO DA primarily adjusts CO in the troposphere. Stratospheric CO analysis increments are concentrated near the tropopause and largest in the polar NH. Consequently, these large SH stratospheric CO percentage changes most likely arise from reductions in CO in the tropical upper troposphere through TROPOMI CO DA and then cross tropopause transport of reduced tropospheric CO into the stratosphere.

The largest increases in zonal mean CO are between 45° N and 80°N below 5km and in excess of 60%. Figure 4.4b shows that the assimilation tends to increase CO total column north of 30°S and decrease CO total column south of 30°S. The largest increases in CO total column are in excess of 60% and in Siberia and the maritime continent, which during this time period experienced significant biomass burning activity.

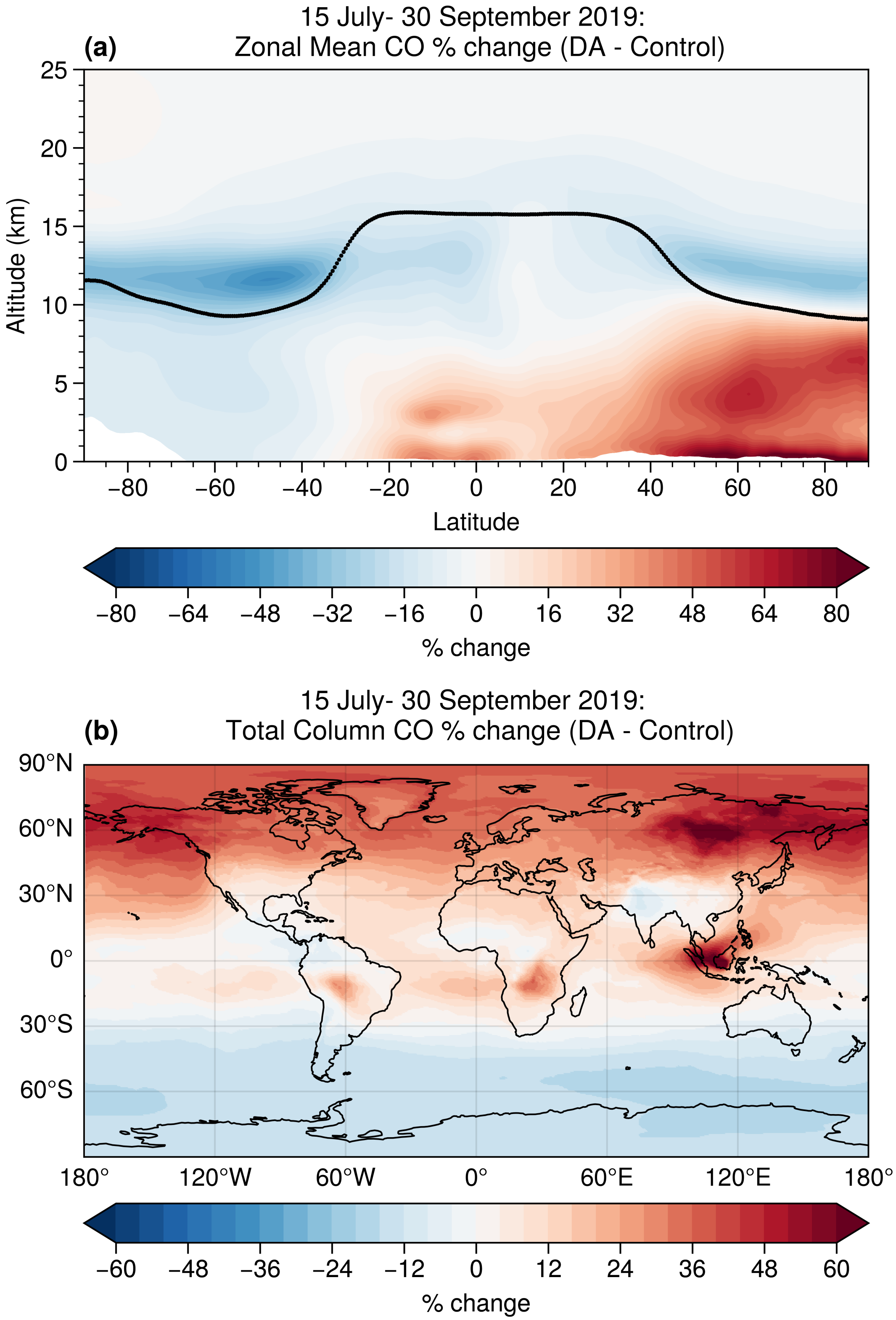
(a) 15 July- 30 September 2019: Zonal Mean CO % change (DA - Control)

(b) 15 July- 30 September 2019: Total Column CO % change (DA - Control)

FIGURE 4.4: Percent difference in zonal mean CO profile (a) and total column CO (b) between UFS-RAQMS TROPOMI CO DA and control experiments.

4.4.2 Validation of UFS-RAQMS CO with independent datasets

UFS-RAQMS CO analyses for both the control and TROPOMI CO DA are evaluated with MOPITT, NDACC FTIR, and in-situ aircraft observations to determine how well the true CO distribution is captured by the model. The control and TROPOMI CO DA experiments are spatially and temporally interpolated to the observation, creating coincident model and observation pairs. For the MOPITT and NDACC comparisons, I apply the observation averaging kernels to the UFS-RAQMS coincident profiles.

4.4.2.1 MOPITT

I compare daily mean UFS-RAQMS total column CO analyses with the MOPITT version 9 Level 3 daily mean CO column product (Deeter et al., 2022). Due to an event upset affecting instrument operation MOPITT data is unavailable for a large portion of the study period (26 July - 24 August 2019) (`https://www2.acom.ucar.edu/mopitt/status`). The MOPITT level 3 data is 1x1 degree, a coarser resolution than UFS-RAQMS, and so daily average UFS-RAQMS CO is binned onto the MOPITT level 3 grid. Next, the binned daily average UFS-RAQMS CO profiles are linearly interpolated to the MOPITT vertical levels. The MOPITT averaging kernels (a), apriori profile ($x_{apriori}$), and apriori column ($C_{apriori}$) are then used to calculate the model column following equation 4.1, where the CO profiles $x_{ufs-raqms}$ and $x_{apriori}$ are expressed as $\log_{10}$(VMR) (`https://www2.acom.ucar.edu/sites/default/files/documents/v9_users_guide_20220203.pdf`, last access: 22 July 2024).

$$C_{ufs-raqms} = C_{apriori} + a(x_{ufs-raqms} - x_{apriori}) \tag{4.1}$$

The average daily MOPITT CO column for 15 July - 30 September 2019 is shown in Figure 4.5a. A root mean square error (RMSE) skill score (equation 4.2) is used to quantify the improvement in the DA experiment. The RMSE for UFS-RAQMS control and UFS-RAQMS TROPOMI CO DA experiments are calculated relative to the MOPITT observations. Negative skill scores indicate that the assimilation degraded the forecast while positive skill indicates the assimilation increased the accuracy of the forecast. A skill score of 1 indicates that the TROPOMI CO DA experiment captures the CO columns as depicted by MOPITT. A skill score of 0 indicates that the assimilation did not improve the agreement between MOPITT and UFS-RAQMS or that the model has no skill in capturing CO in that region.

$$SS_{RMSE,(i,j)} = 1 - \frac{RMSE_{DA(i,j)}}{RMSE_{ctrl(i,j)}} \tag{4.2}$$

For most grid cells the UFS-RAQMS TROPOMI CO DA experiment exhibits improved skill (Figure 4.5c). The largest improvements in skill are over Russia, Europe, Alaska, and Canada. Due to the MOPITT data outage, the large Siberian biomass burning events are not captured within the MOPITT observations except for in the first 10 days of the experiment. Therefore, while I am unable to directly verify the increased UFS-RAQMS CO columns within the Siberian smoke plume during August 2019, I do show that assimilating TROPOMI CO column throughout the period significantly improved background

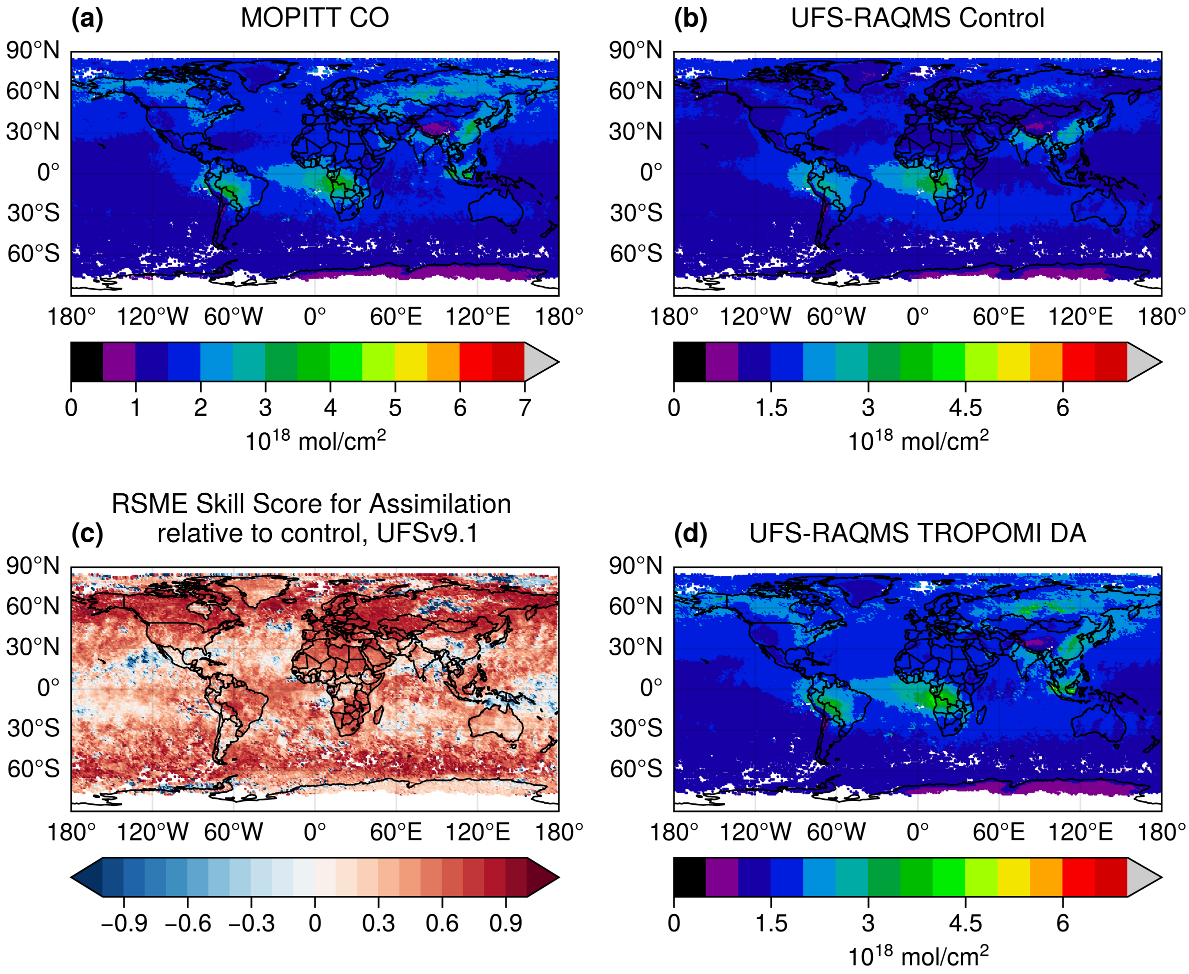

Figure 4.5: Comparison of MOPITT CO column with UFS-RAQMS control and TROPOMI CO DA CO columns. 15 July- 30 September 2016 mean CO column for MOPITT (a), UFS-RAQMS control (b), and UFS-RAQMS TROPOMI CO DA (d), with 26 July - 24 August 2019 excluded due to MOPITT data outage. RMSE Skill Score (c) shows improved agreement with MOPITT in UFS-RAQMS TROPOMI CO DA over UFS-RAQMS control.

CO columns in the NH middle and high latitudes. UFS-RAQMS TROPOMI CO DA CO columns are moderately improved relative to the control over Borneo, Sumatra, and portions of Africa where there was widespread biomass burning during the analysis period. TROPOMI CO DA results in weak improvements over the Pacific Ocean and negative skill in the eastern Tropical Pacific near the coast of Mexico.

In addition to the RMSE skill score, I compare the daily mean UFS-RAQMS CO column analyses with MOPITT CO columns over the FIREX-AQ and CAMP^{2}Ex field campaign domains in Figure 4.6. Correlation and bias are calculated between all observations made 15 July-30 September 2019 over 30°N - 49.5°N 82°W - 123°W (Figure 4.6 a,b) and 6°N - 23°N 116°E - 129°W (Figure 4.6 c,d). Over the FIREX-AQ spatial domain, TROPOMI CO DA increases correlation of UFS-RAQMS with MOPITT from 0.661 to 0.8317 and decreases the bias from -0.2507 x10^{18} mol/cm^2 to -0.0354 x10^{18} mol/cm^2. Over the CAMP^{2}Ex spatial domain, TROPOMI CO DA increases correlation of UFS-RAQMS with MOPITT from 0.495 to 0.9446 and decreases the bias from -0.3114 x 10^{1}8 mol/cm^2 to 0.1437 x 10^{18} mol/cm^2.

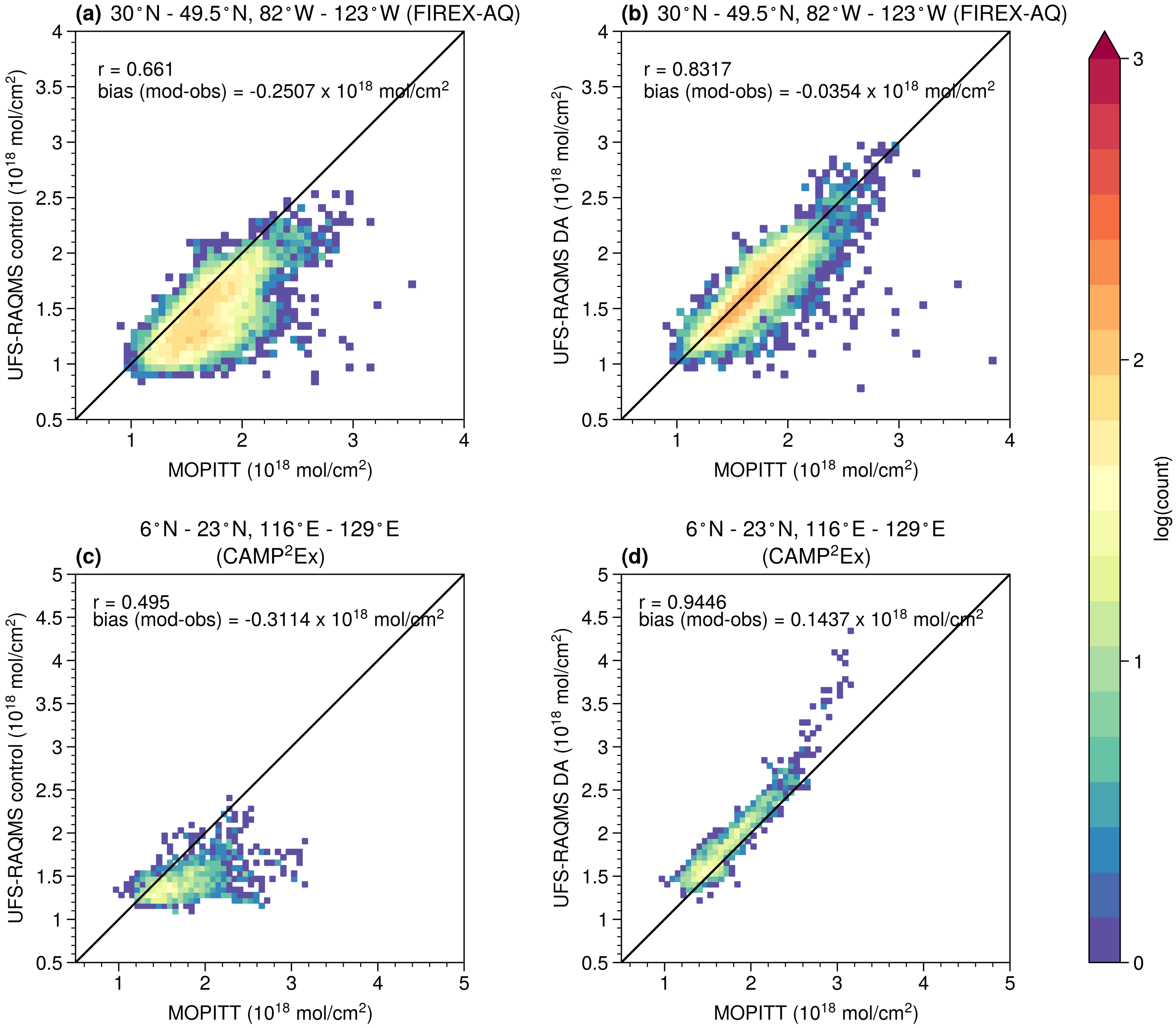

FIGURE 4.6: Comparisons of MOPITT and UFS-RAQMS CO columns over FIREX-AQ (a,b) and CAMP^{2}Ex (c,d) domains. TROPOMI CO DA increases correlation and decreases bias between UFS-RAQMS and MOPITT.

4.4.3 FIREX-AQ In-situ CO Measurements

The Differential Absorption Carbon Monoxide Measurement (DACOM) instrument (Sachse et al., 1991) made measurements over the continental US from July-September 2019 on-board the NASA DC-8 aircraft as part of the FIREX-AQ field campaign (see Figure 4.2).

FIREX-AQ sampling of smoke plumes with the DC-8 consisted of multiple perpendicular transects through the plume, with each perpendicular leg sampling smoke emitted around the same time, and the legs starting in the freshest smoke (Warneke et al., 2023). The resulting FIREX-AQ highly detailed measurements capture fine-scale changes in composition in both the cross-plume direction and as the emissions age. In-plume measurements are excluded from the analysis as the horizontal resolution of the UFS-RAQMS simulations is not fine enough to capture the observed in-plume enhancements that were measured by the DC-8 close to the western US wildfires and SE US agricultural fires targeted during FIREX-AQ.

Figure 4.7 shows the comparison between UFS-RAQMS and the DC8 DACOM CO observations for non-smoke plume observations during all flights during FIREX-AQ. UFS-RAQMS CO is strongly correlated with the observed CO for both the control (0.7956) and the DA experiment (0.8129). TROPOMI CO DA improves the average bias from -9.6635 ppbv to 6.2821 ppbv.

Figure 4.8 shows a comparison of the vertical profiles for the FIREX-AQ DACOM CO non-smoke observations and coincident UFS-RAQMS analyses. Following the interpolation of the UFS-RAQMS analyses along the DC8 flight track and filtering out smoke observations, the modeled and measured values were binned into 200m altitude bins. The median (vertical profile), 25th and 75th (shaded) percentiles of the modeled and observed distributions within each 200m altitude bin are shown. Below 2 km the control and TROPOMI CO DA experiment profiles are both within the spread for the observed

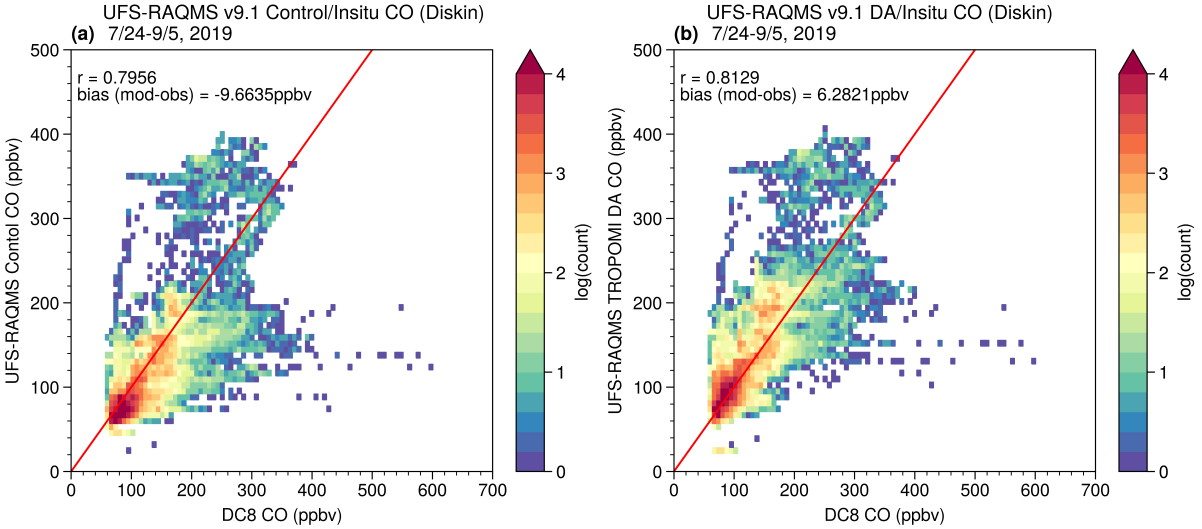

FIGURE 4.7: Comparison of DC8 DACOM CO and (a) UFS-RAQMS Control experiment and (b) UFS-RAQMS TROPOMI CO DA experiment.

profile. Above 2.5 km the control experiment profile is consistently biased low relative to the observed profile. The TROPOMI CO DA experiment profile is higher than in the control experiment and shows improved agreement with the DC-8 observations.

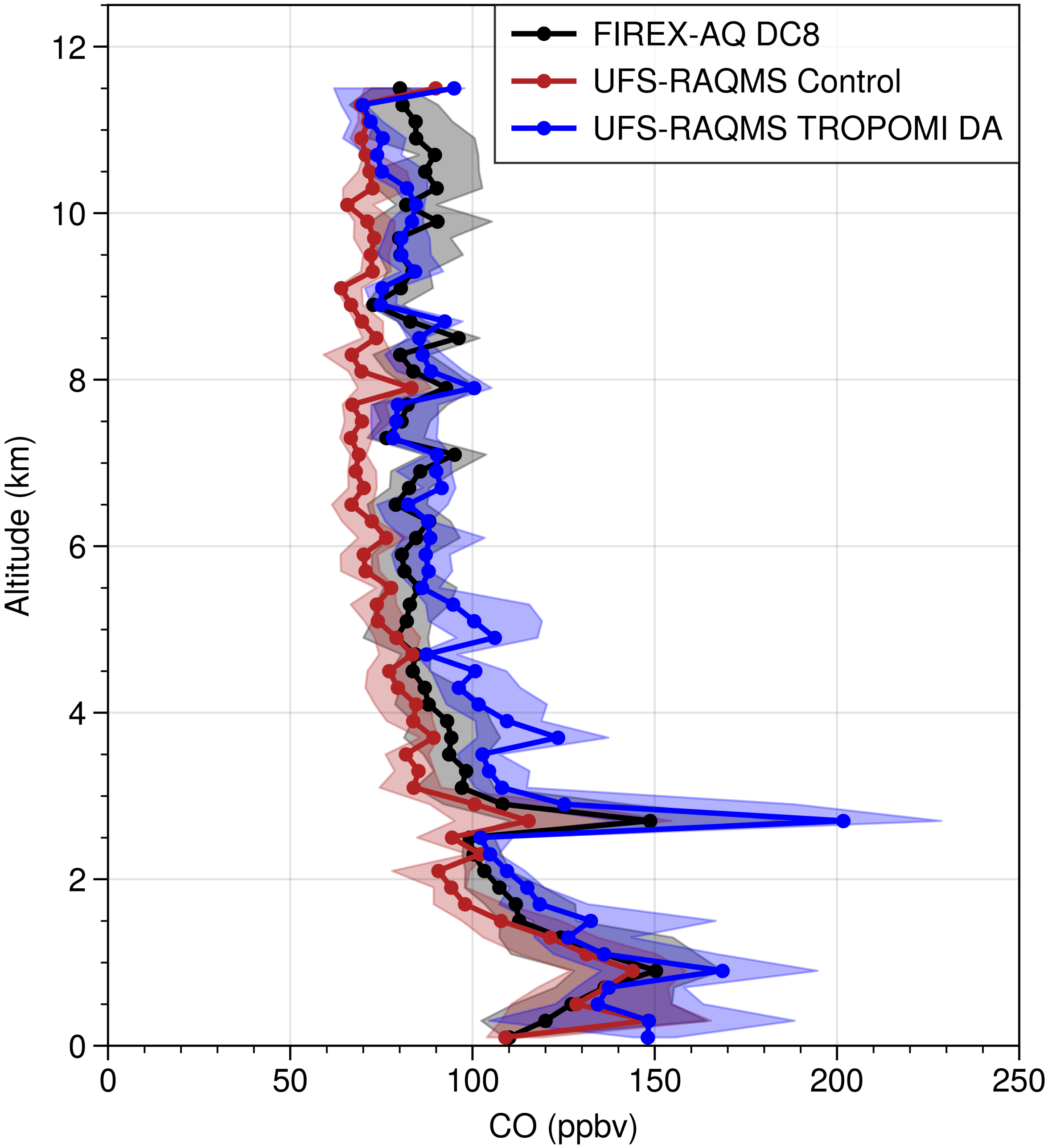

Figure 4.8: Vertical profiles of non-smoke CO during FIREX-AQ for DC8 DACOM CO (black), UFS-RAQMS Control experiment (red), and UFS-RAQMS TROPOMI CO DA experiment (blue).

4.4.4 CAMP^{2}Ex In-situ CO measurements

The NASA CAMP^{2}Ex field campaign sampled airmasses over the Philippines 25 August - 5 October 2019 with the NASA P-3 aircraft to investigate the role of aerosols in the Southeast Asian southeast monsoon (Reid et al., 2023). During the campaign, the region was impacted by biomass burning emissions from Borneo and Sumatra. In-situ CO measurements were made by a commercial cavity ringdown spectrometer (G2401-m, PICARRO, Inc.) modified with a custom gas sampling system (DiGangi et al., 2021). UFS-RAQMS analyses are sampled along the P-3 flight track. Figure 4.9 shows the comparison between UFS-RAQMS and the CAMP^{2}Ex P-3 CO measurements. The UFS-RAQMS Control experiment has a low bias of -34.553 ppbv relative to the observations but is well correlated (0.7332). Assimilating TROPOMI CO decreases the bias in the analysis significantly to -1.8373 ppbv and improves the correlation (0.8202).

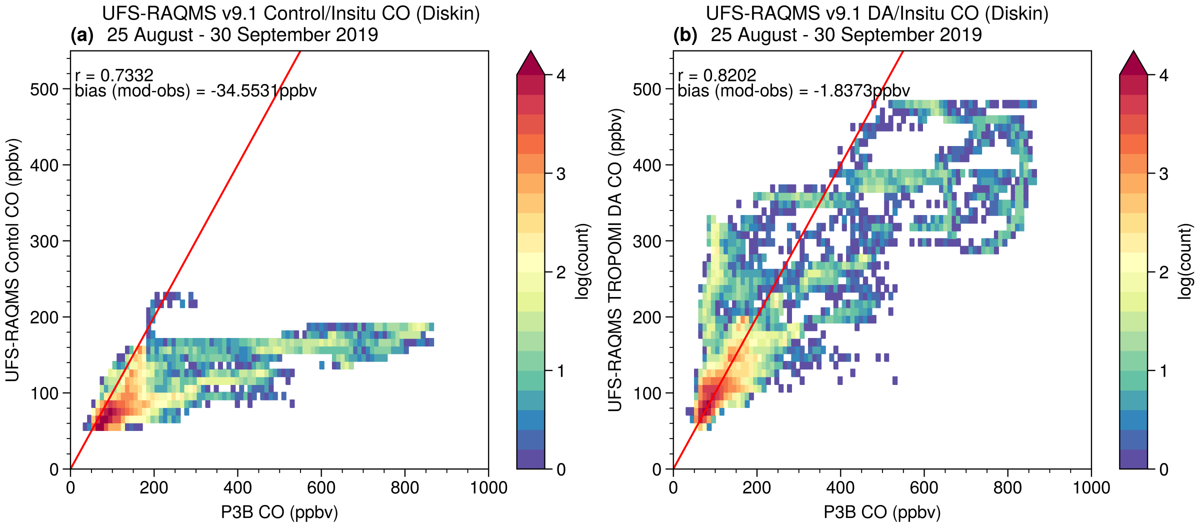

Figure 4.9: Comparison of CAMP^{2}Ex P3-B CO and (a) UFS-RAQMS Control experiment and (b) UFS-RAQMS TROPOMI CO DA experiment.

Figure 4.10 shows a comparison of the vertical profiles for the CAMP^{2}Ex CO observations and coincident UFS-RAQMS analyses. Following the interpolation of the UFS-RAQMS analyses along the P-3 flight track, the modeled and measured values were binned into 200 m altitude bins. The median (vertical profile), 25th and 75th (shaded) percentiles of the modeled and observed distributions within each 200m altitude bin are shown. Below 7km, the UFS-RAQMS control experiment profile is biased low by $\geq$ 20 ppbv ($\geq$ 20%) relative to the observed profile. This low bias is largest in the lowest 1.5km where it exceeds -40%. The UFS-RAQMS TROPOMI CO DA experiment profile is generally within the 25th-75th percentiles of the CAMP^{2}Ex observations, though between $\sim$3.5km and 5km the UFS-RAQMS TROPOMI CO DA CO profile is biased high and may indicate a slight overcorrection. The lowest 1km of the profile is still biased low, though it is now only 10-20%.

The comparisons of UFS-RAQMS to the in-situ FIREX-AQ and CAMP^{2}Ex observations show that TROPOMI CO DA improves the correlation and bias statistics for UFS-RAQMS CO mixing ratios, consistent with the MOPITT statistics over the campaign domains. However, the improvement in the statistics is better for UFS-RAQMS CO columns than for the UFS-RAQMS CO profile. This is a result of using a total column satellite measurement to constrain a profile. UFS-RAQMS control CO is well correlated with the in-situ observations, indicating along with the profiles that the vertical structure and temporal variation in CO concentration is reasonably captured in UFS-RAQMS for these regions. The DA system distributes the analysis increment vertically based on

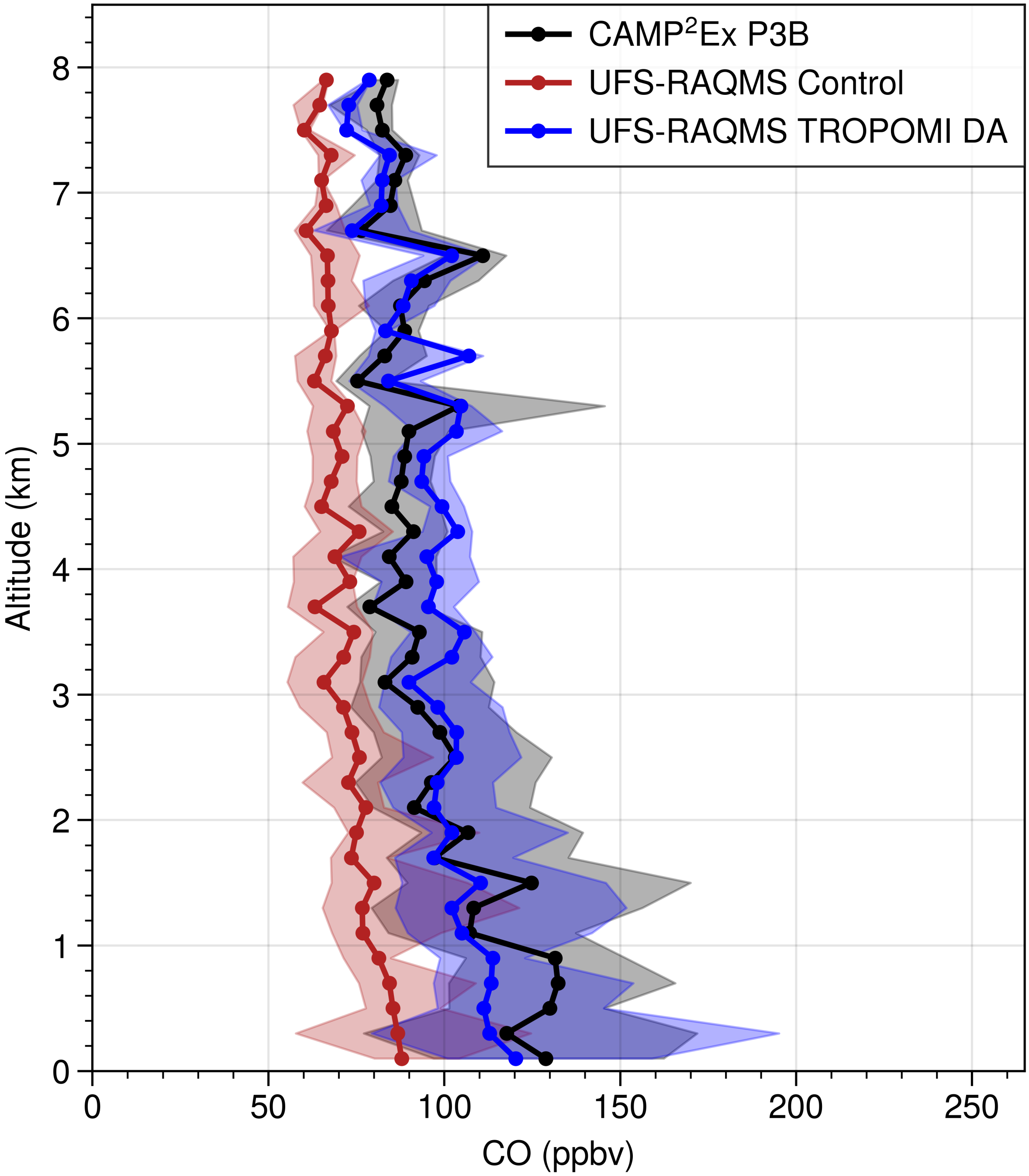

FIGURE 4.10: Vertical profiles of CO during CAMP^{2}Ex for P-3 CO observations (black), UFS-RAQMS Control experiment (red), and UFS-RAQMS TROPOMI CO DA experiment (blue).

model blended BEC statistics and knowledge of observation errors and vertical sensitivities. Over the CAMP^{2}Ex domain this leads to an overestimation of CO at 3-6km. Over the FIREX-AQ domain this leads to an overestimate of CO below 6km and underestimates above 10km. In the UFS-RAQMS TROPOMI CO DA experiment CO column, the effects of the vertical distribution compensate for each other.

4.4.5 NDACC FTIR CO profiles

UFS-RAQMS CO profiles are also evaluated with FTIR CO profile observations from 6 NDACC sites (Table 4.1). The selected NDACC FTIR spectrometers retrieve volume mixing ratio profiles from solar absorption spectra with optimal estimation using the SFIT4 algorithms (`https://wiki.ucar.edu/display/sfit4/`, last access: 19 July 2024).

Figure 4.11 shows a comparison of NDACC FTIR CO profiles with UFS-RAQMS. The influence of TROPOMI CO DA on the CO profile is small above 15km, with both the control and the TROPOMI CO DA experiment generally overestimating CO concentrations in this region. The most significant differences between the control and TROPOMI CO

TABLE 4.1: Location of NDACC FTIR sites used in this study. Number of profiles taken 15 July- 30 September 2019 included.

NDACC Site Name	Number of Profiles	Location (Latitude/Longitude)
Boulder, CO, USA	288	39.99^{o}N, 105.26^{o}W
La Reunion, Maido, France	531	21.1^{o}S, 55.4^{o}E
Mauna Loa, HI, USA	54	19.54^{o}N, 155.58^{o}W
St. Petersburg, Russian Federation	76	59.9^{o}N, 29.8^{o}E
Thule, Greenland	655	76.53^{o}N, 68.74^{o}W
Wollongong, Australia	263	34.41^{o}S, 150.88^{o}E

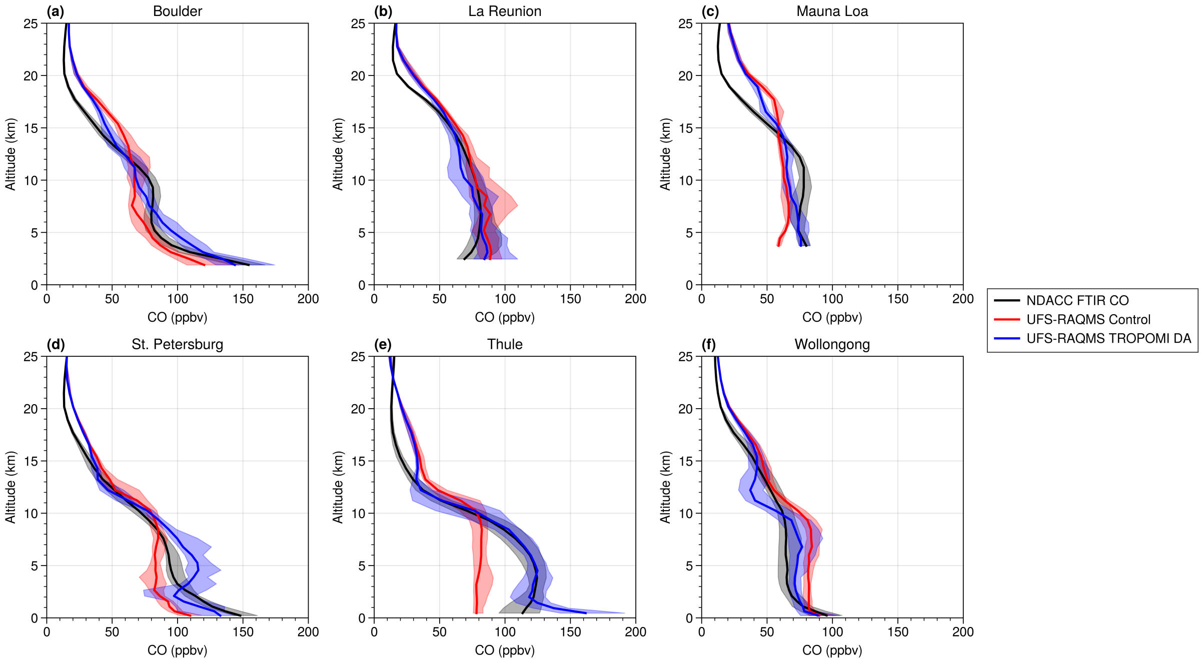

FIGURE 4.11: Comparison of CO profiles from NDACC FTIR (black), UFS-RAQMS control (red), and UFS-RAQMS TROPOMI CO DA (blue). Solid lines indicate the median, shading 25th-75th percentile.

DA experiment occur below 10km except for at Wollongong where the most significant difference is at 11-12km (Figure 4.11f). The Wollongong site is at 34.41ºS, 150.88ºE, where the mean impact of the DA is a 20-30% decrease in CO (Figure 4.4). At Wollongong, the TROPOMI CO DA reduces the average high bias by 5-15 ppbv from 1-5km and ∼10 ppbv from 5-10km but creates a low bias of ∼15-20 ppbv from 10-12km.

Consistent with the percent change in CO between the control and TROPOMI CO DA experiments at high latitudes in Figure 4.4, the Thule profile shows a significant increase in the profile due to TROPOMI CO DA and results in very good agreement with the observed NDACC profile from 2-13km. At Thule the near-surface CO concentration is biased high in the TROPOMI CO DA experiment while it is biased low in the control.

This behavior is not apparent at the other sites and may be a consequence of the use of static BEC at these latitudes. Recall, the BEC statistics obtained by this study are a function of latitude and altitude, and in the lower troposphere reflect the sensitivity of UFS-RAQMS to biomass burning emissions. Profiles of the analysis increments at NDACC locations on the days that measurements were made (not shown) indicate that the near-surface analysis increment is comparatively large (>∼15ppbv) at Boulder, St. Petersburg, and Thule. For Boulder and St. Petersburg, it appears the TROPOMI CO DA is able to correct CO for biases in anthropogenic emissions since these sites were not significantly impacted by wildfires.

At the tropical NDACC sites of Mauna Loa and La Reunion TROPOMI CO DA results in small changes relative to the control in the UFS-RAQMS CO profile. TROPOMI CO DA slightly decreases UFS-RAQMS CO at La Reunion and increases it below 15km at Mauna Loa.

4.5 Consistency in biomass burning aerosol and CO signatures

As previously noted, a strong correlation is expected between AOD and CO column recently emitted from wildfires. It has been suggested that this relationship can be exploited to evaluate biomass burning emissions inventories (Edwards et al., 2006). Here, I evaluate the relationship between AOD and CO column over two biomass burning events. VIIRS AOD and TROPOMI CO columns are used to evaluate how realistic the

UFS-RAQMS AOD/CO relationship is. I selected scenes over Siberia and over Indonesia during their respective peaks in biomass burning during the July-September 2019 analysis period.

UFS-RAQMS CO column and AOD analyses are interpolated in latitude, longitude, and time to TROPOMI and VIIRS L2 observations respectively. TROPOMI averaging kernels are applied to UFS-RAQMS CO profiles. UFS-RAQMS speciated aerosol extinction profiles at 532nm are integrated to obtain AOD. The coincident model and observation data is then binned onto a 0.1x0.1 degree grid over each domain. The anticipated linear relationship between AOD and CO is evaluated for the observations, UFS-RAQMS control, and UFS-RAQMS DA.

4.5.1 Case Study: 22 July 2019 Siberian Smoke

During July and August 2019 significant wildfire activity occurred in Siberian Russia, with a major cluster in Eastern Siberia and a major cluster in Central Siberia (Johnson et al., 2021). Wildfire activity peaked in both regions of Siberia between 18 July and 26 July. I evaluate binned AOD and CO column on 22 July 2019 for the region 90°E -150°E, 50°N - 70°N.

The spatial distributions of AOD and CO over Siberia on 22 July 2019 are shown in Figure 4.12 for VIIRS, TROPOMI, the UFS-RAQMS control, and the UFS-RAQMS TROPOMI CO DA experiment. The UFS-RAQMS AOD field is unchanged between the control and DA experiments and thus is only shown once. UFS-RAQMS does a

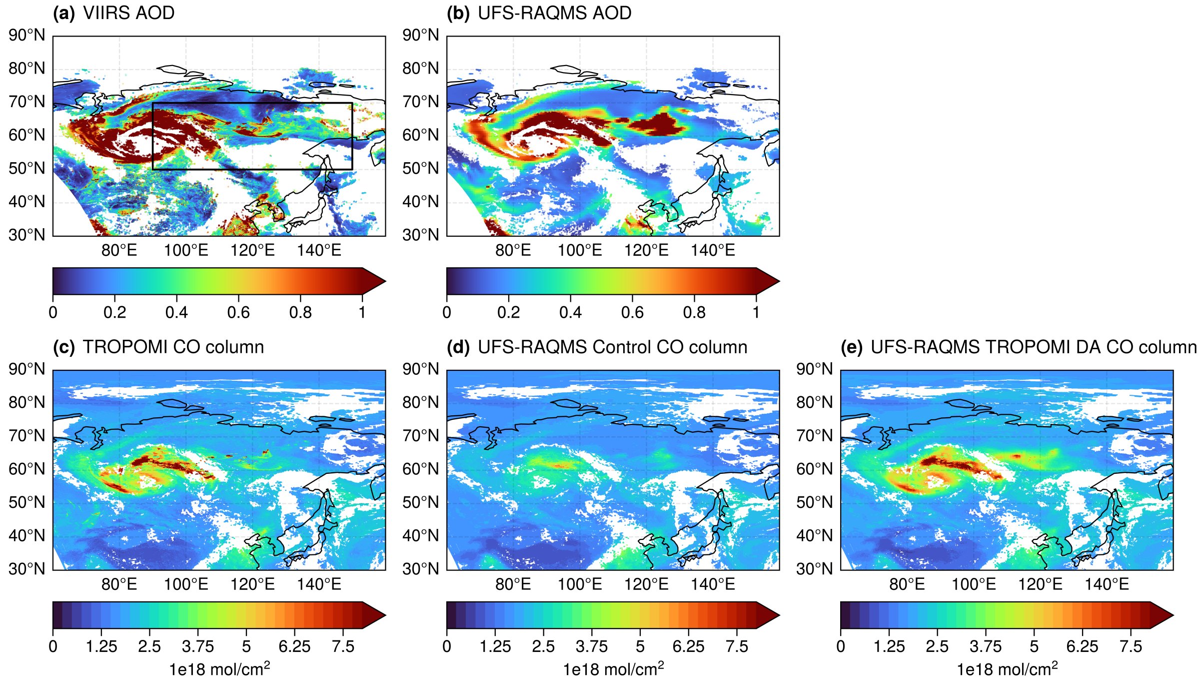

Figure 4.12: 22 July 2019 AOD and CO columns over Siberia. VIIRS AOD (a), UFS-RAQMS AOD (b), TROPOMI CO column (c), and UFS-RAQMS control (d) and TROPOMI CO DA (e) CO column. Black box in panel a defines region (90°E -150°E, 50°N - 70°N) for AOD/CO column relationship analysis.

very good job of capturing the observed synoptic scale features but does not capture fine-scale structure seen in the AOD or CO observations. UFS-RAQMS AOD is slightly overestimated outside of the plume (AOD ≥ 1) and in the plume feature around 60°N - 70°N, 120°E - 130°E. CO column is significantly underestimated in UFS-RAQMS control. Agreement with the TROPOMI observations is significantly improved in UFS-RAQMS DA.

Scatterplots illustrating the relationship between AOD and CO column in Siberian wildfire smoke are shown in Figure 4.13 for the observations (grey), UFS-RAQMS control (red), and UFS-RAQMS TROPOMI CO DA (blue). The linear regressions are summarized in Table 4.2. VIIRS AOD and TROPOMI CO column exhibit a compact linear

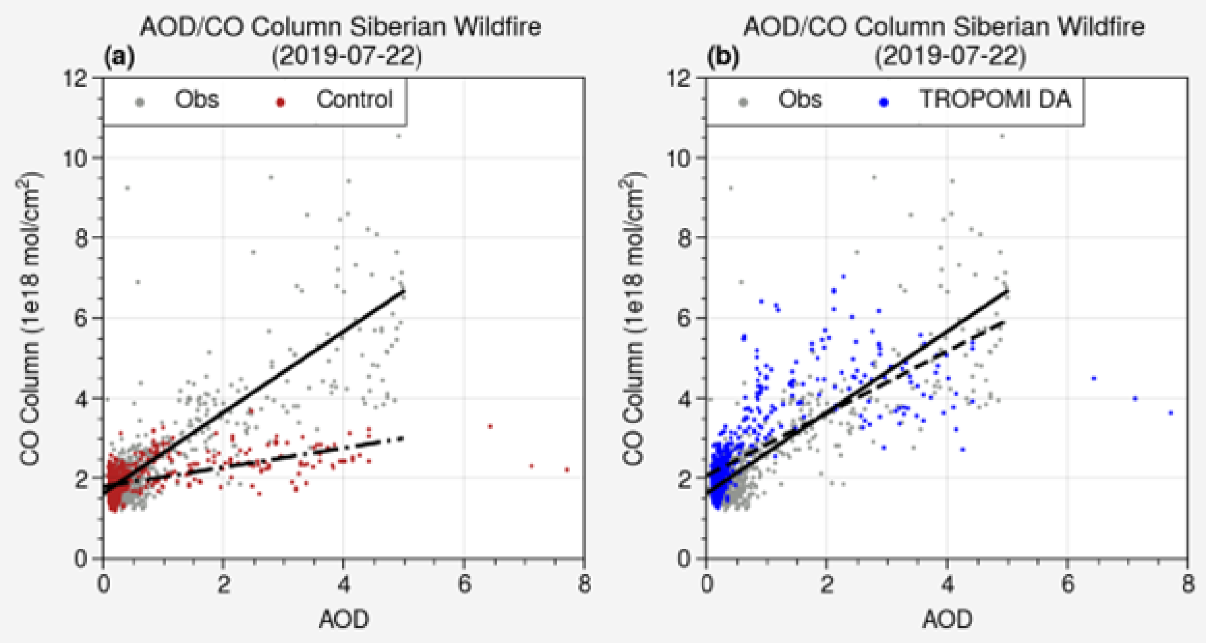

Figure 4.13: Linear relationship between AOD and CO column in Siberian wildfire smoke (90°E -150°E, 50°N - 70°N) on 22 July 2019. UFS-RAQMS control (a, red) and UFS-RAQMS TROPOMI CO DA (b, blue) AOD/CO relationships are compared to observed VIIRS AOD/TROPOMI CO (grey).

relationship with a slope near 1 and correlation of 0.8043. UFS-RAQMS control CO column and AOD are moderately correlated (0.5648), and the slope of the linear relationship is 0.2407 as UFS-RAQMS control underestimates of CO column for high AOD. TROPOMI CO DA improves the correlation between AOD and CO column as well as increases the slope of the linear relationship. The UFS-RAQMS TROPOMI CO DA AOD/CO column slope is 0.7749 and the correlation is 0.7106. This improved representation of the observed linear relationship and correlation in the UFS-RAQMS TROPOMI CO DA experiment is due to the increased CO column within the Siberian wildfire plume.

Table 4.2: Linear relationship between AOD and CO column in Siberian wildfire smoke (90°E -150°E, 50°N - 70°N) on 22 July 2019.

	slope	intercept	r
VIIRS AOD/TROPOMI CO column	1.0092	1.629	0.8043
UFS-RAQMS Control AOD/CO column	0.2407	1.7948	0.5648
UFS-RAQMS TROPOMI CO DA AOD/CO column	0.7749	2.0724	0.7106

4.5.2 Case Study: 16 September 2019 Indonesian Smoke

During September 2019 wildfire activity over Indonesia contributed to an extreme AOD enhancement in the region. I evaluate binned AOD and CO column on 16 September 2019 for the region 100°E -130°E, 15°S - 15°N.

The spatial distributions of AOD and CO column over Indonesia on 16 September 2019 are shown in Figure 4.14 for VIIRS, TROPOMI, the UFS-RAQMS control, and the UFS-RAQMS TROPOMI CO DA experiment. UFS-RAQMS significantly underestimates AOD enhancements in this region, as evident in the Borneo smoke plume and over China. As a result, I also show the UFS-RAQMS AOD scaled by a factor of 3. The CO column is significantly underestimated over the maritime continent in UFS-RAQMS control. Agreement with the TROPOMI observations is significantly improved in the UFS-RAQMS TROPOMI CO DA experiment.

Scatterplots illustrating the relationship between AOD and CO column in Indonesian wildfire smoke are shown in Figure 4.15 for the observations (grey), UFS-RAQMS control (red), and UFS-RAQMS TROPOMI CO DA (blue). The linear regressions are summarized in Table 4.3. VIIRS AOD and TROPOMI CO column exhibit a compact linear

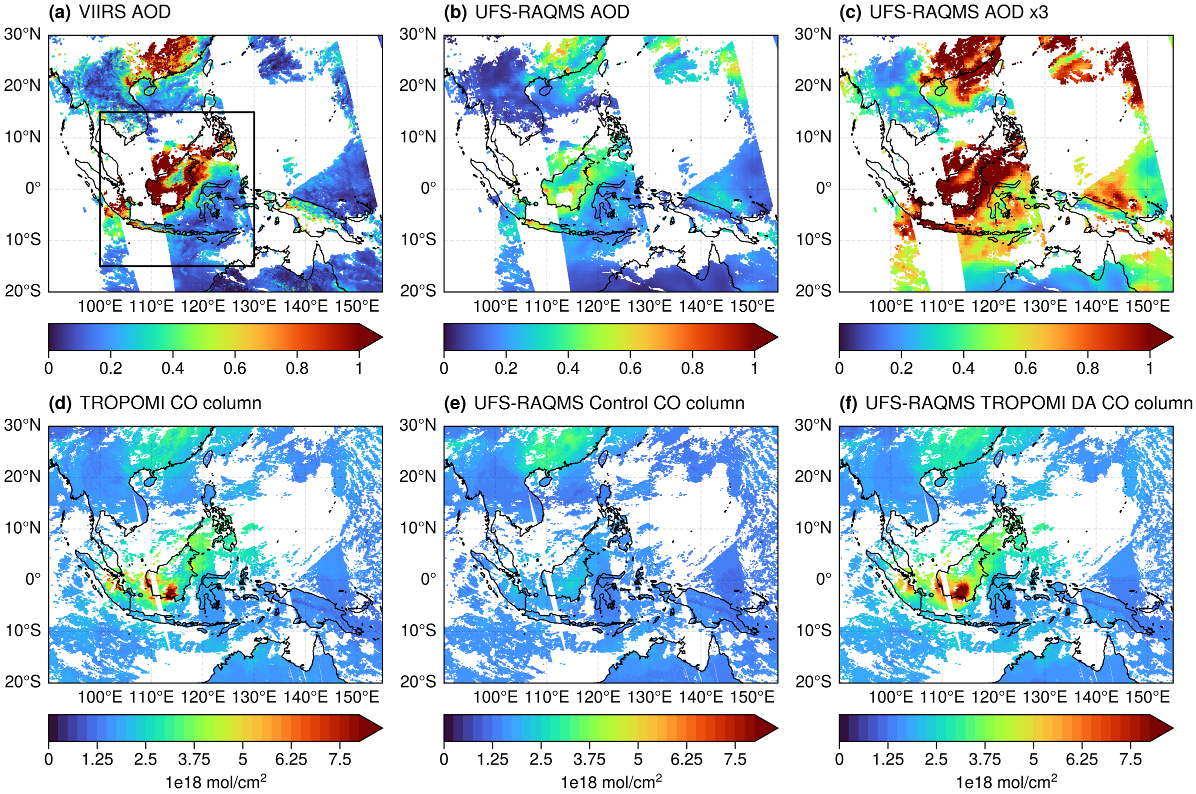

Figure 4.14: 16 September 2019 AOD and CO columns over SE Asia. VIIRS AOD (a), UFS-RAQMS AOD (b), UFS-RAQMS AOD scaled by 3 (c), TROPOMI CO column (d), and UFS-RAQMS control (e) and TROPOMI CO DA (f) CO column. Black box in panel a defines region (100°E -130°E, 15°S - 15°N) for AOD/CO column relationship analysis.

relationship with a slope near 1 and correlation of 0.782. UFS-RAQMS control CO column and AOD are moderately correlated (0.4886), and the slope of the linear relationship is 0.7638, however neither the AOD or CO columns capture the observed high values. TROPOMI CO DA improves the correlation between AOD and CO column to 0.7085 but due to the low bias in UFS-RAQMS AOD over the region, the UFS-RAQMS TROPOMI CO DA experiment significantly overestimates the slope of the relationship. To approximate the modeled AOD/CO relationship without the low AOD bias, I apply a scaling factor of 3 to the UFS-RAQMS AOD. Applying this scaling inflates UFS-RAQMS AOD

Table 4.3: Linear relationship between AOD and CO column in Indonesian wildfire smoke (100°E -130°E, 15°S - 15°N) on 16 September 2019.

	slope	intercept	r
VIIRS AOD/TROPOMI CO column	0.962	1.7872	0.782
UFS-RAQMS Control AOD/CO column	0.7638	1.4755	0.4886
UFS-RAQMS TROPOMI CO DA AOD/CO column	3.8251	1.3404	0.7085
UFS-RAQMS Control AODx3/CO column	0.2546	1.4755	0.4886
UFS-RAQMS TROPOMI CO DA AODx3/CO column	1.275	1.3404	0.7085

enhancements over Borneo to be closer to observed values (Figure 4.14c, Figure 4.15c,d). By accounting for the low AOD bias in this way, I obtain a slope for UFS-RAQMS control CO column and scaled AOD of 0.2546 and for UFS-RAQMS TROPOMI CO DA a slope of 1.275. This points to the need to also assimilate AOD data along with CO column data to improve the agreement with observations in this region.

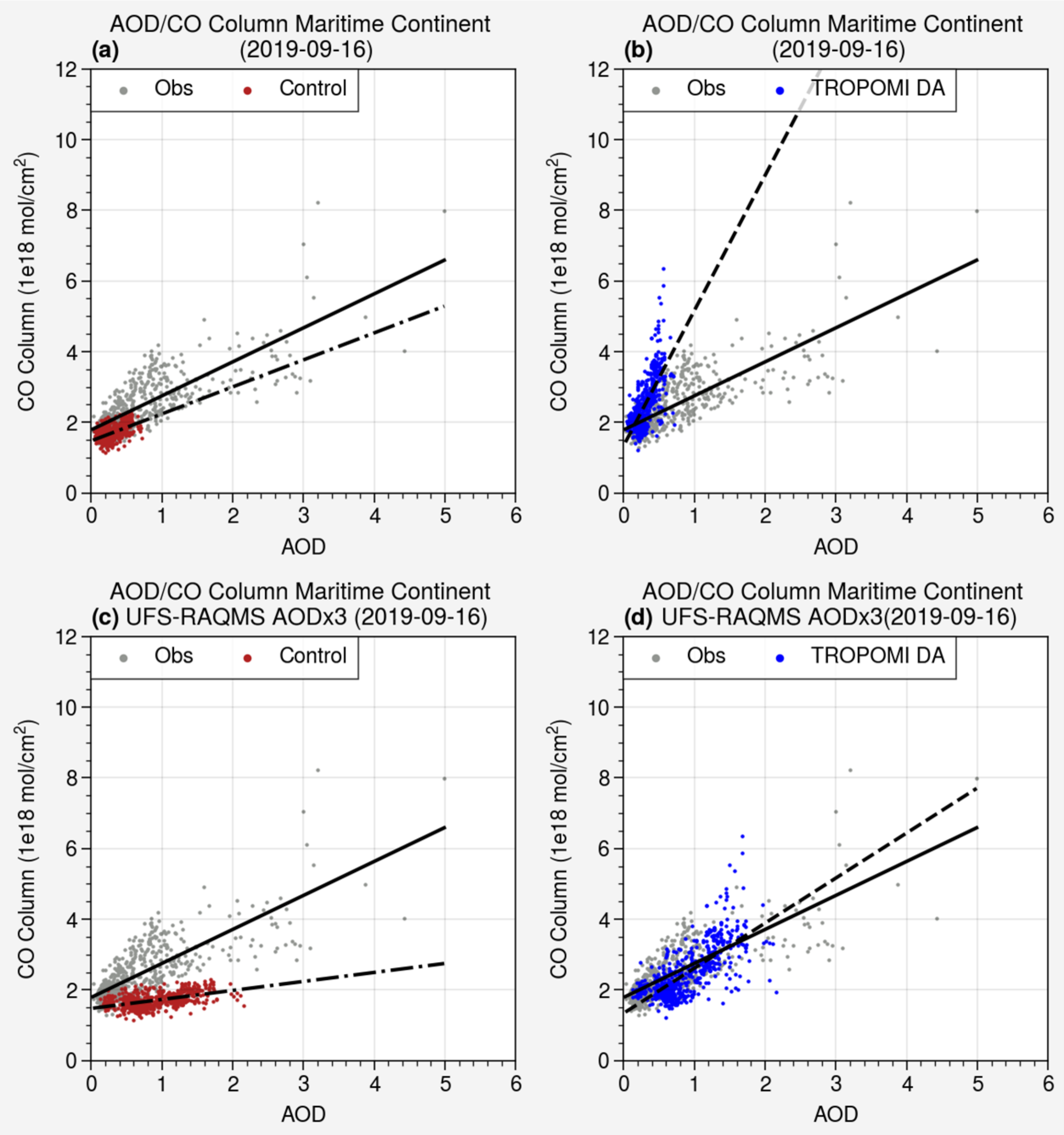

FIGURE 4.15: Linear relationship between AOD and CO column in Indonesian wildfire smoke (100°E -130°E, 15°S - 15°N) on 16 September 2019. UFS-RAQMS control (a, red) and UFS-RAQMS TROPOMI CO DA (b, blue) AOD/CO relationships are compared to observed VIIRS AOD/TROPOMI CO (grey). UFS-RAQMS control (c, red) and UFS-RAQMS TROPOMI CO DA (d, blue) AODx3/CO relationships are compared to observed VIIRS AOD/TROPOMI CO (grey).

4.6 Conclusions

Assimilating TROPOMI CO within UFS-RAQMS using the GSI 3D-var and blended BEC generally resulted in improved UFS-RAQMS CO analyses. Application of the TROPOMI CO DA decreases the average RMSE in CO column relative to MOPITT and improves correlation between UFS-RAQMS and MOPITT within the FIREX-AQ and CAMP^{2}EX domains. TROPOMI CO DA results in an improved agreement of CO profiles relative to NDACC FTIR measurements in the free troposphere at most NDACC sites but does increase surface CO biases at high latitude locations and adds complexity in the vertical structure at many sites. This is a consequence of using a total column measurement to constrain a modeled profile. The DA setup minimizes the difference between the TROPOMI observations and the UFS-RAQMS first guess. While the CO column is well constrained, as indicated by the good agreement between UFS-RAQMS TROPOMI CO DA CO and MOPITT CO, the DA system distributes the analysis increment vertically based on model blended BEC statistics and knowledge of the TROPOMI CO column observation errors and vertical sensitivities. My evaluations with NDACC FTIR CO observations and with field campaign observations show that this can lead to an over-adjustment near the surface and only small adjustments at high altitudes.

TROPOMI CO DA has the largest impacts on CO in the lower troposphere over Siberia and Indonesia. My case studies of the relationship between AOD and CO column over these regions show that in UFS-RAQMS biomass burning signatures in CO column are not consistent with those in AOD near the biomass burning source regions. Assimilating

TROPOMI CO improves the representation of the biomass burning AOD/CO relationship. I believe this is an indication that the GBBEPx biomass burning CO emissions in UFS-RAQMS are too low. GBBEPx adds biomass burning emissions from VIIRS to QFED biomass burning emissions estimates from MODIS, and has not been included in recent biomass burning emissions inventory intercomparisons (Hua et al., 2024, Wiedinmyer et al., 2023). Wiedinmyer et al. (2023) shows that adding VIIRS observations to existing inventories increased biomass burning CO emissions due to improved capture of small fires. Wiedinmyer et al. (2023) shows QFED aerosol and CO emissions do not have the relative consistency present in other inventories like the fire inventory from NCAR (FINN) and the global fire emissions database (GFED) as QFED aerosol emissions are the highest and CO emissions among the lowest. Since the GBBEPx emission inventory is based on QFED, I expect that similar inconsistencies may be present in GBBEPx.

While assimilating CO does compensate for uncertainties in the biomass burning emissions, it does not adjust the biomass burning CO emissions themselves. Since UFS-RAQMS uses emission factors for co-emitted NOx and VOC species that are applied to the GBBEPx biomass burning CO emissions, I anticipate similar uncertainties in these co-emitted species, likely leading to errors in ozone production within the biomass burning plumes. Chapter 5 focuses on developing capabilities to use TROPOMI CO column measurements to adjust the GBBEPx CO biomass burning emissions within UFS-RAQMS. Similar capabilities have been developed using TROPOMI NO2 retrievals to adjust anthropogenic NOx emissions using off-line iterative mass balance approaches (East et al.,

2022) and local ensemble transform Kalman filter (LETKF) techniques (Sekiya et al., 2022).

Chapter 5

Adjustment of GBBEPx CO Emissions

In Chapter 4 I showed that constraining UFS-RAQMS with TROPOMI CO observations with GSI 3Dvar DA improves the agreement between UFS-RAQMS CO analyses and observations. Case studies over significant biomass burning events in Siberia and the maritime continent indicate that the UFS-RAQMS low bias in CO is associated with underestimates of biomass burning CO emissions. The underestimation of biomass burning CO emissions also impacts NOx and VOC emissions since these are included in CTMs by applying species-specific emissions factors (EFs) or emissions ratios (ERs) (e.g. Akagi et al., 2011, Andreae, 2019, Andreae and Merlet, 2001) to biomass burning CO emissions. The TROPOMI CO DA application in Chapter 4 constrains UFS-RAQMS CO fields and not the CO emissions. In this chapter I apply an inverse approach for adjusting GBBEPx CO biomass burning emissions.

Inversion techniques optimize pollutant emissions in order to minimize bias between concentration observations and CTM simulations. Techniques include mass balance (e.g. East et al., 2022, Lamsal et al., 2011, Martin et al., 2003a), ensemble Kalman filters (e.g. Gaubert et al., 2020, Miyazaki et al., 2012), and adjoint models (e.g. Cooper et al., 2017, Parrington et al., 2012). Applications of the ensemble Kalman filter and adjoint techniques have included biomass burning CO emissions as part of the model state vector in the chemical DA cost function, constraining emissions concurrently with the model initial state. Finite-difference mass-balance (FDMB) methods are computationally simpler, using CTMs to derive a linear relationship between a change in emissions and a change in observed concentration. There are significant drawbacks to each approach. Ensemble and adjoint approaches require significant computational resources. The adjoint approach also requires development and maintenance of an adjoint model. FDMB assumes both linearity and that the emissions are the main contributor to the model bias. It is also of some importance to consider that the resulting adjusted emissions are subject to transport and chemistry uncertainties in the specific CTM used. Iterative FDMB approaches address the non-linearity between the emissions and the column by cycling the adjustment until the analysis increments are sufficiently small.

In this chapter, I apply an iterative FDMB approach for optimizing GBBEPx CO emissions using CO column observations from TROPOMI. This approach alters existing

FDMB approaches for updating anthropogenic NOx inventories in order to account for: 1) the high spatiotemporal variability in biomass burning sources and 2) sensitivity of UFS-RAQMS to biomass burning.

5.1 Iterative FDMB for Biomass Burning CO Emissions

The adjustment technique applied here builds on the FDMB approach used for adjusting anthropogenic NOx inventories in East et al. (2022), Lamsal et al. (2011). FDMB relates changes in emissions to changes in column concentrations as expressed in equation 5.1 for each model grid point.

$$\frac{\Delta E}{E} = \beta \frac{\Delta X}{X} \tag{5.1}$$

ΔE is the emissions adjustment, E the prior emissions, and ΔX a change in CO column associated with the change in emissions. Here ΔX is the CO analysis increment from UFS-RAQMS TROPOMI CO DA experiments. This is different than previous FDMB implementations which have defined ΔX as the difference between model and satellite column observations (Lamsal et al., 2011) or the difference between a simulation with data assimilation and one without (East et al., 2022).

β is a scaling parameter describing the sensitivity of UFS-RAQMS CO columns to perturbations in biomass burning CO emissions. Due to the high spatiotemporal variability in biomass burning emissions, I calculate β over 5 day intervals instead of the monthly interval used by Lamsal et al. (2011) and East et al. (2022) and only for grid points emitting CO from biomass burning. β is estimated here using the same 85% GBBEPx CO emissions perturbation experiment used in Chapter 4 to generate the BEC, and calculated as: $\beta = (\frac{\Delta E}{E})/(\frac{\Delta X}{X_{100}})$, where $\frac{\Delta E}{E}$ is the average normalized change in emissions, ΔX is the 5-day average difference in CO column between the control (X_{100}) and perturbation (X_{85}) experiments, and X is the 5-day average CO column of the control experiment. $\frac{\Delta E}{E}$ is fixed at 0.15.

The adjustment process is summarized in Figure 5.1, incorporating iteration of the adjustment as in East et al. (2022) and Cooper et al. (2017). The adjustment is calculated as: $\Delta E = E * \beta * \frac{\Delta X}{X}$, where E is the prior GBBEPx emissions, ΔX is the TROPOMI CO analysis increment, and X is the UFS-RAQMS CO column. An emissions adjustment is only calculated when $\beta \leq 8$ as β is very large where UFS-RAQMS CO sensitivity to biomass burning emissions is weak. To control for cases where the adjustment results in 0 or negative emissions, a cutoff of -90% is applied. This limit primarily affects points where the CO column is more sensitive to transported emissions than local emissions. The CO emissions adjustment is iterated over multiple cycles of UFS-RAQMS TROPOMI CO DA, with the adjusted emissions from the previous DA cycle serving as the prior emissions for the next cycle.

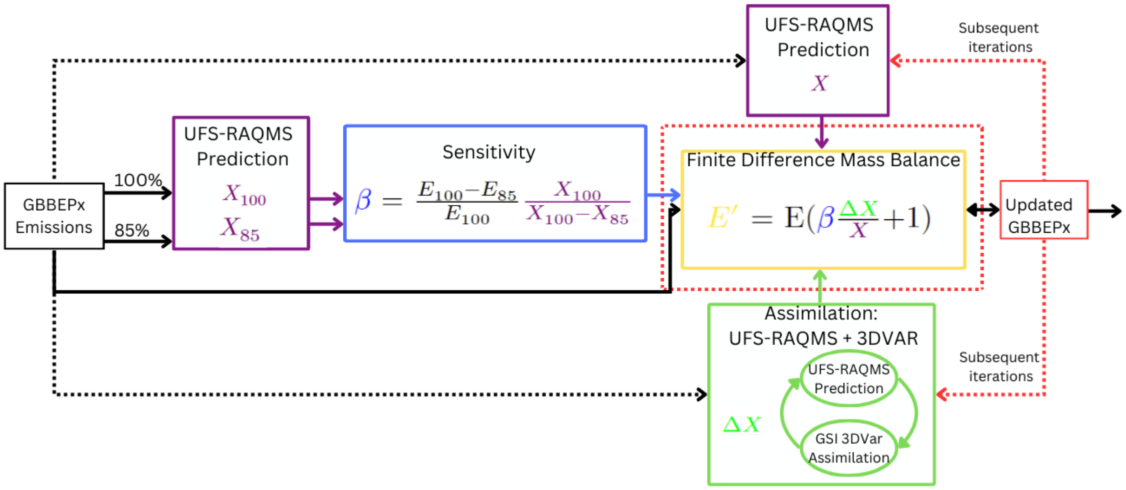

Figure 5.1: Schematic of the iterative FDMB framework.

5.2 Results

5.2.1 Convergence of the emissions updates

Convergence of the GBBEPx emissions update is evaluated for the biomass burning regions defined in Figure 5.2 using the DA analysis increments and the normalized change in emissions. For each iteration of the GBBEPx CO emissions update the change in emissions is calculated relative to the prior iteration. Box plots of the analysis increments and emissions change for each iteration and region are presented in Figure 5.3. Analysis increments are only evaluated for the grid cells where the emissions were updated in order to isolate the immediate impact of the emissions update. Analysis increments farther away from the adjusted biomass burning emissions do not decrease as much as those in the near field as they also account for model deficiencies in transport, chemistry, and other emissions sources. The analysis increments and percent change in emissions

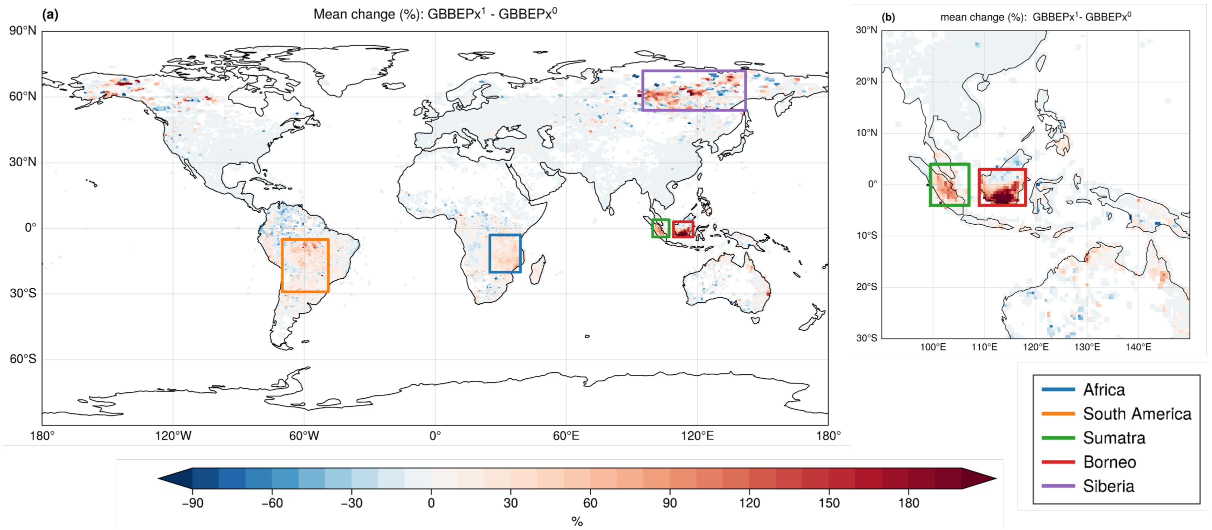

FIGURE 5.2: Percent change in biomass burning CO emissions for the first iteration of FDMB. Panel b zooms in on SE Asia. Convergence of iterated FDMB is evaluated for the boxed regions: Africa (20°S-3°S, 25°E-39°E) (blue), South America (29°S-5°S, 49°W-70°W) (orange), Sumatra (4°S-4°N, 99.5°E-107°E) (green), Borneo (4°S-3°N, 109°E-118°E) (red), and Siberia (54°N-72°N, 95°E-142°E) (purple).

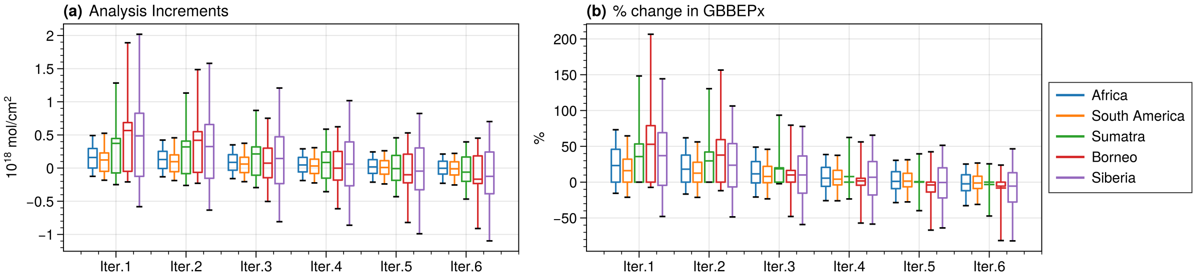

FIGURE 5.3: TROPOMI CO DA analysis increments (a) and percent change in GBBEPx CO emissions (b) for six iterations of FDMB.

is largest for the first iteration of the GBBEPx update. The analysis increments and emissions adjustments are smaller for Africa and South America. For all regions, the analysis increments get smaller with each iteration and the emissions adjustment in each region approaches 0%. After 6 iterations, the mean adjustment in each region is $\sim$ 0% and the 25^{th} to 75^{th} percentiles are within ± 30%.

Time series of the analysis increments and updated GBBEPx emissions are used to evaluate the temporal behavior of the FDMB emissions updates. GBBEPx emissions time series for the globe and the major biomass burning regions are shown in Figure 5.4. The global average unadjusted biomass burning emissions (GBBEPx^0) vary little with time, while the adjusted emissions significantly amplify biomass burning emissions to result in 3 distinct periods of elevated global emissions. Siberian biomass burning emissions peak in July and early August in all iterations of GBBEPx, and the peak is increased from ∼6 $\mu g\ s^{-1} m^{-2}$ in GBBEPx^0 to ∼14 $\mu g s^{-1} m^{-2}$ in GBBEPx^6. Biomass burning emissions in Sumatra and Borneo peak in September and in GBBEPx^0 average $\sim 1\ \mu g\ s^{-1} m^{-2}$ during September. September emissions from Sumatra and Borneo are significantly increased, and GBBEPx^6 emissions peak around 26-30 $\mu g\ s^{-1} m^{-2}$. African biomass burning emissions vary by $< 1\ \mu g\ s^{-1} m^{-2}$ in GBBEPx^0. The iterative FDMB emissions update results in an increasing trend in emissions from Africa between 15 July 2019 and 30 September 2019. South American biomass burning emissions increases are also smaller than in the Siberian and Maritime regions, with a maximum increase of $\sim 3\ \mu g\ s^{-1} m^{-2}$ between GBBEPx^0 and GBBEPx^6.

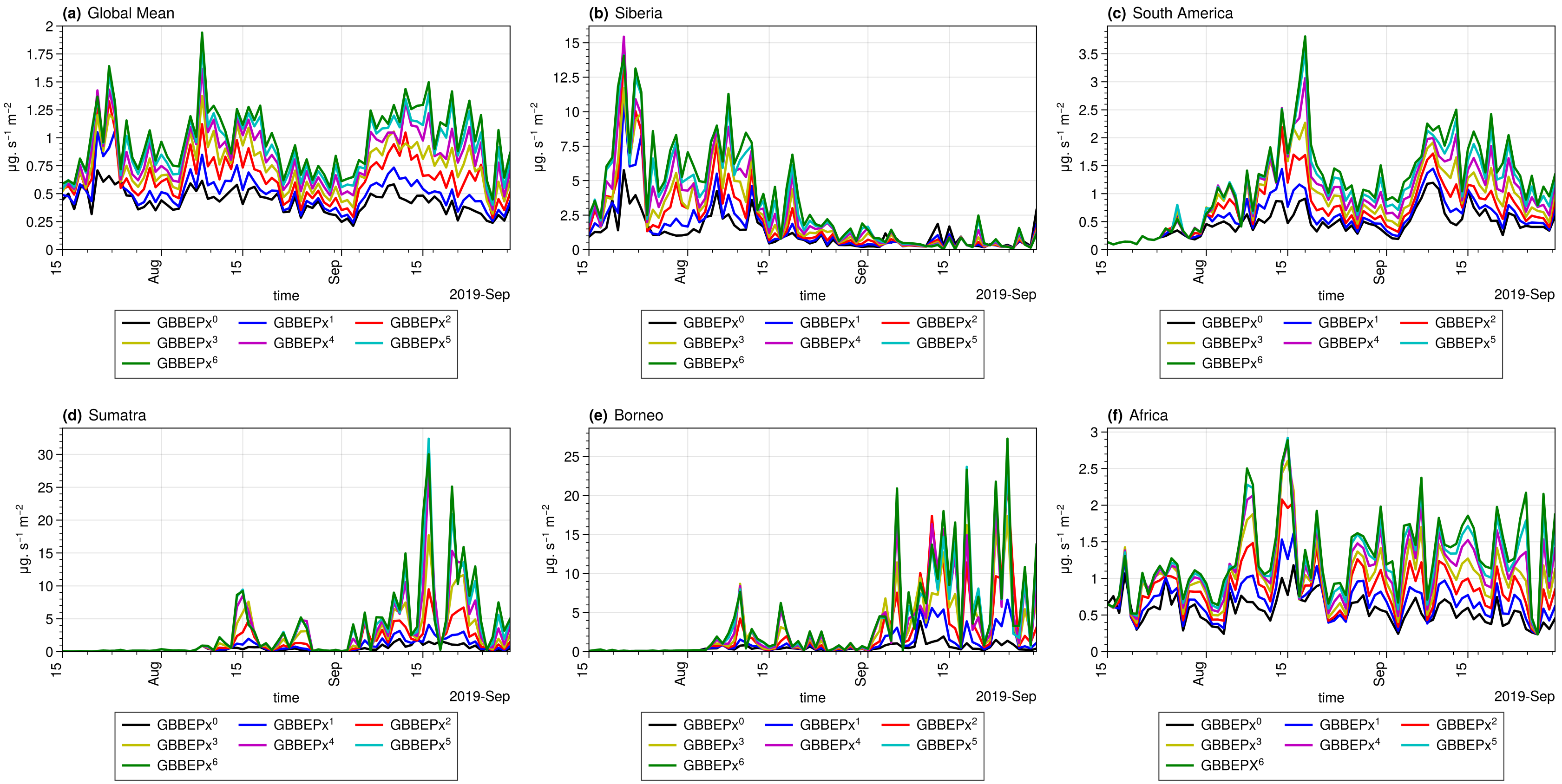

FIGURE 5.4: GBBEPx CO emission timeseries for FDMB iterations 0-6. Global (a), Siberia (54°N-72°N, 95°E-142°E) (b), South America (29°S-5°S, 49°W-70°W) (c), Sumatra (4°S-4°N, 99.5°E-107°E) (d), Borneo (4°S-3°N, 109°E-118°E) (e), and Africa (20°S-3°S, 25°E-39°E) (f).

Analysis increment time series for the major biomass burning emissions regions are shown in Figures 5.5 - 5.9 and are consistent with Figure 5.3. Analysis increments are only included in this analysis where the emissions are adjusted. In each region, the CO analysis increment gradually decreases with each iteration and GBBEPx emissions are incrementally increased. The changes in GBBEPx emissions are small when the analysis increments are small. The mean analysis increment in each region approaches zero with each subsequent iteration. Analysis increments in the Siberia, Sumatra, and Borneo regions decrease over the first 1-3 iterations and then do not vary by much for the last few iterations. Analysis increments in the South America and Africa regions gradually decrease over all iterations. A potential reason for this difference in behavior is the magnitude of the assimilation increment. When the TROPOMI CO DA analysis increment is greater than $\sim$1 x 10^{18} mol/cm^2, the emissions adjustment procedure is most effective. For analysis increments <0.5 x 10^{18} mol/cm^2, such as those for the Africa and South America regions and for the later iterations for Siberia, the emissions adjustment procedure more gradually decreases the difference between the UFS-RAQMS CO analysis and TROPOMI CO.

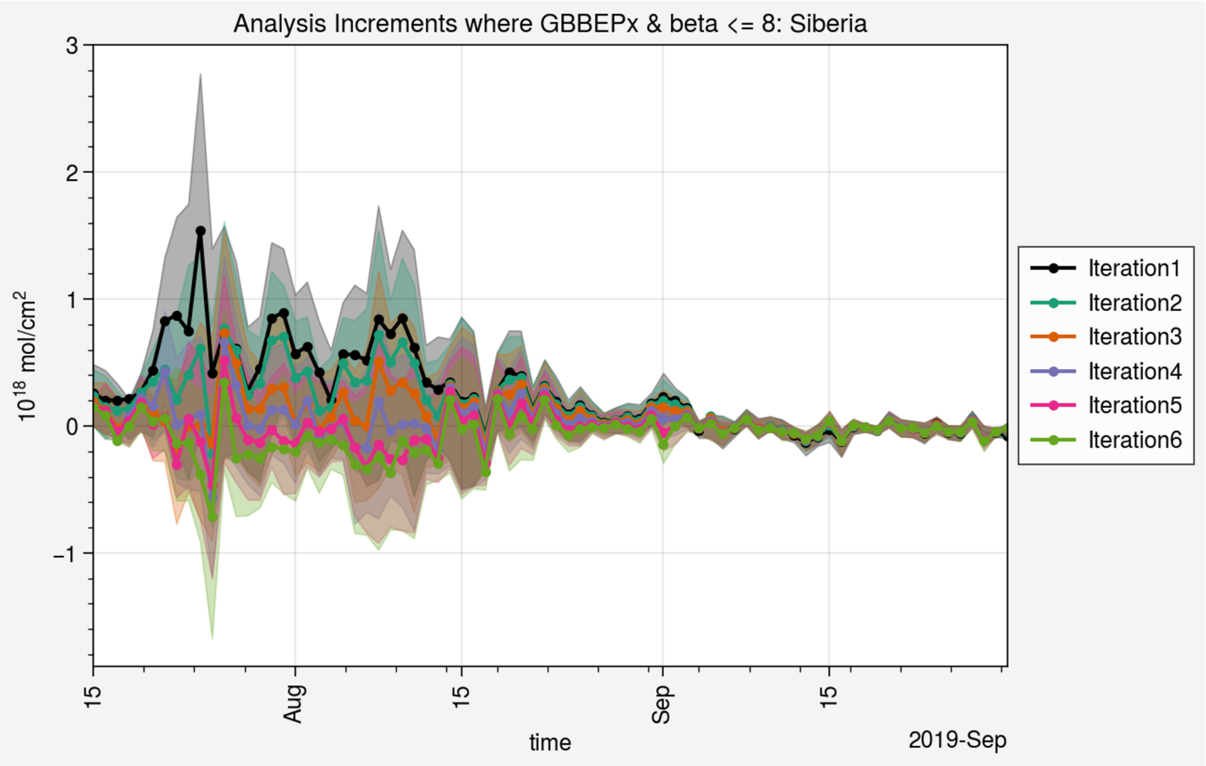

FIGURE 5.5: Time series of the TROPOMI CO DA analysis increments for Siberia for UFS-RAQMS DA cycles 1-6. Only analysis increments for grid points where there are GBBEPx CO emissions and β is ≤ 8 are included in the average.

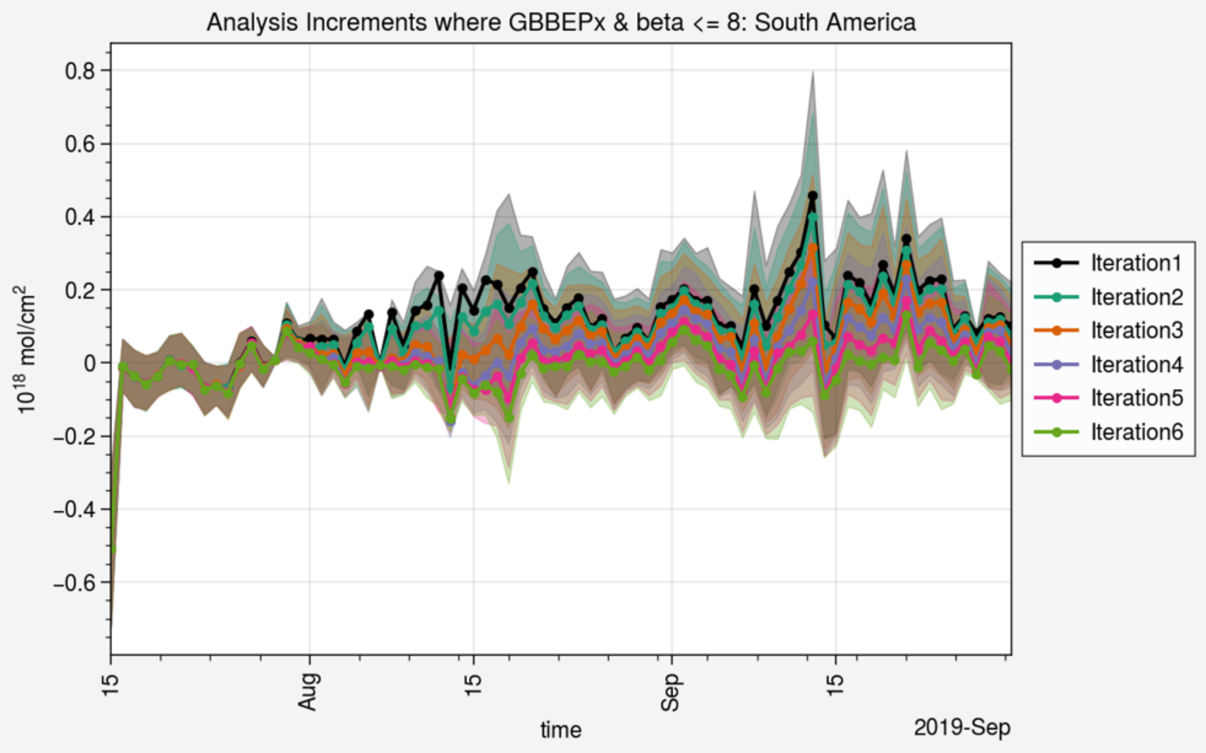

FIGURE 5.6: Time series of the TROPOMI CO DA analysis increments for the South American region for UFS-RAQMS DA cycles 1-6.Only analysis increments for grid points where there are GBBEPx CO emissions and β is ≤ 8 are included in the average.

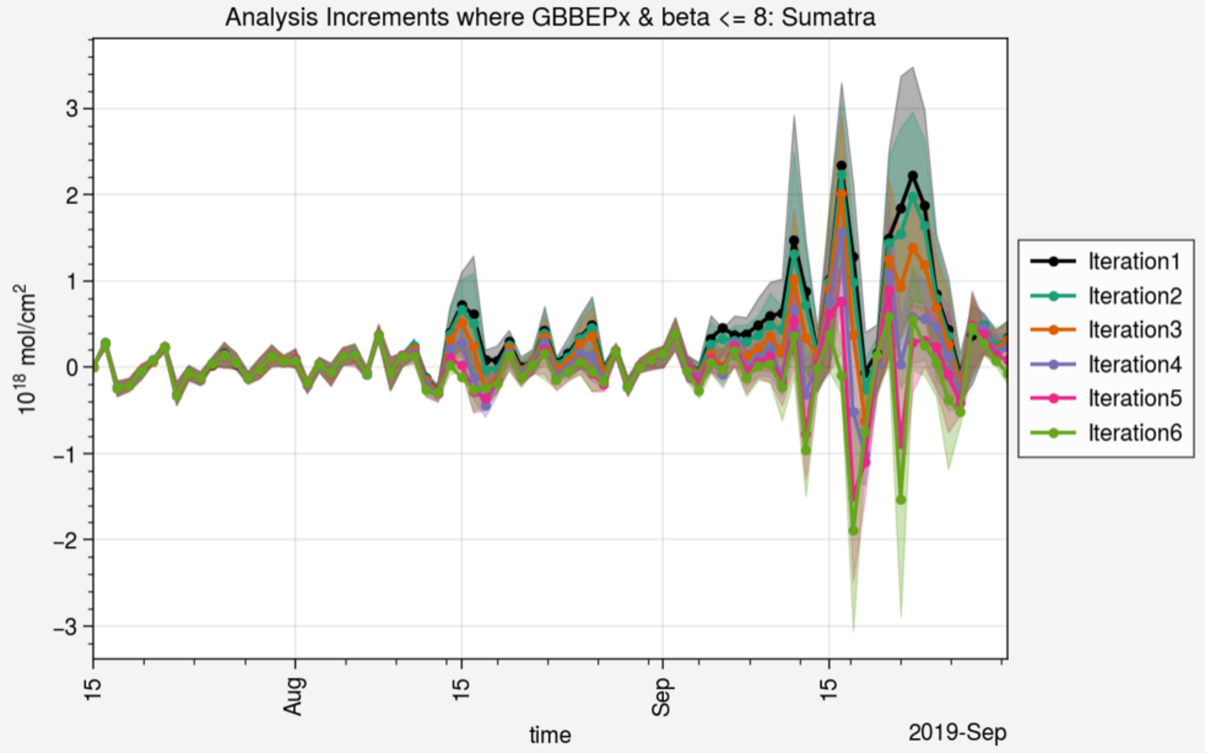

FIGURE 5.7: Time series of the TROPOMI CO DA analysis increments for Sumatra for UFS-RAQMS DA cycles 1-6. Only analysis increments for grid points where there are GBBEPx CO emissions and β is ≤ 8 are included in the average.

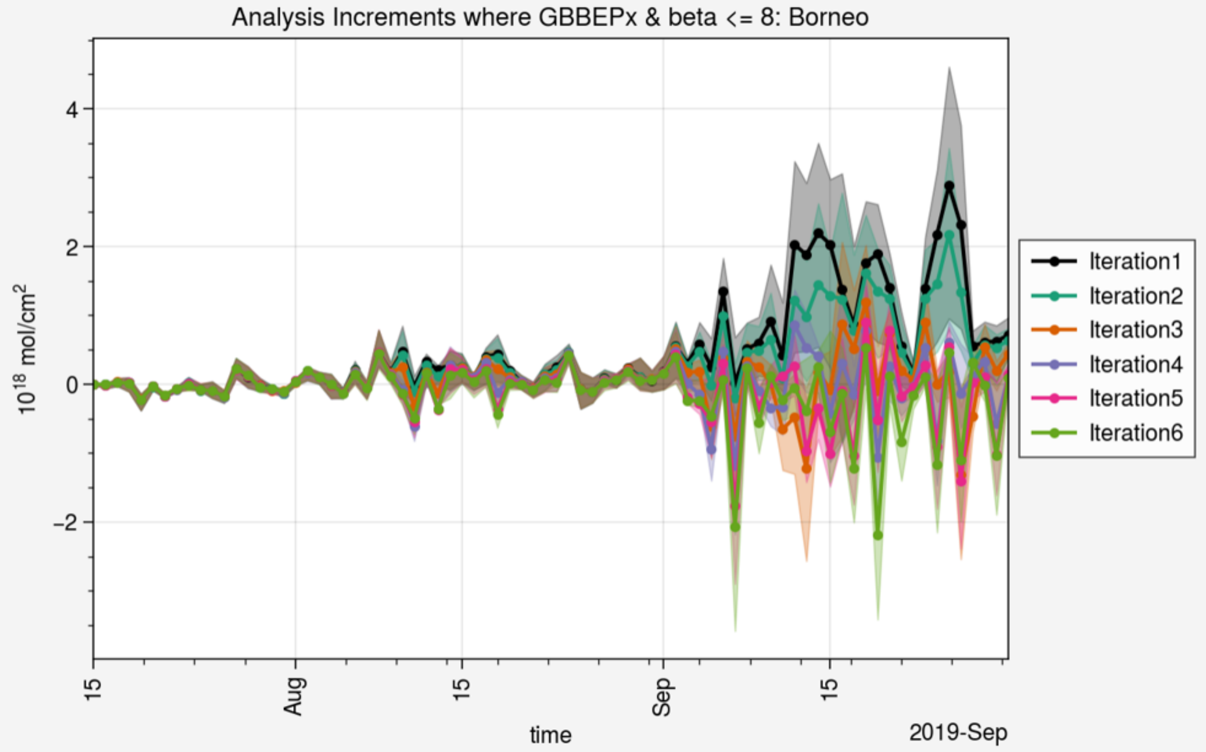

FIGURE 5.8: Time series of the TROPOMI CO DA analysis increments for Borneo for UFS-RAQMS DA cycles 1-6. Only analysis increments for grid points where there are GBBEPx CO emissions and β is ≤ 8 are included in the average.

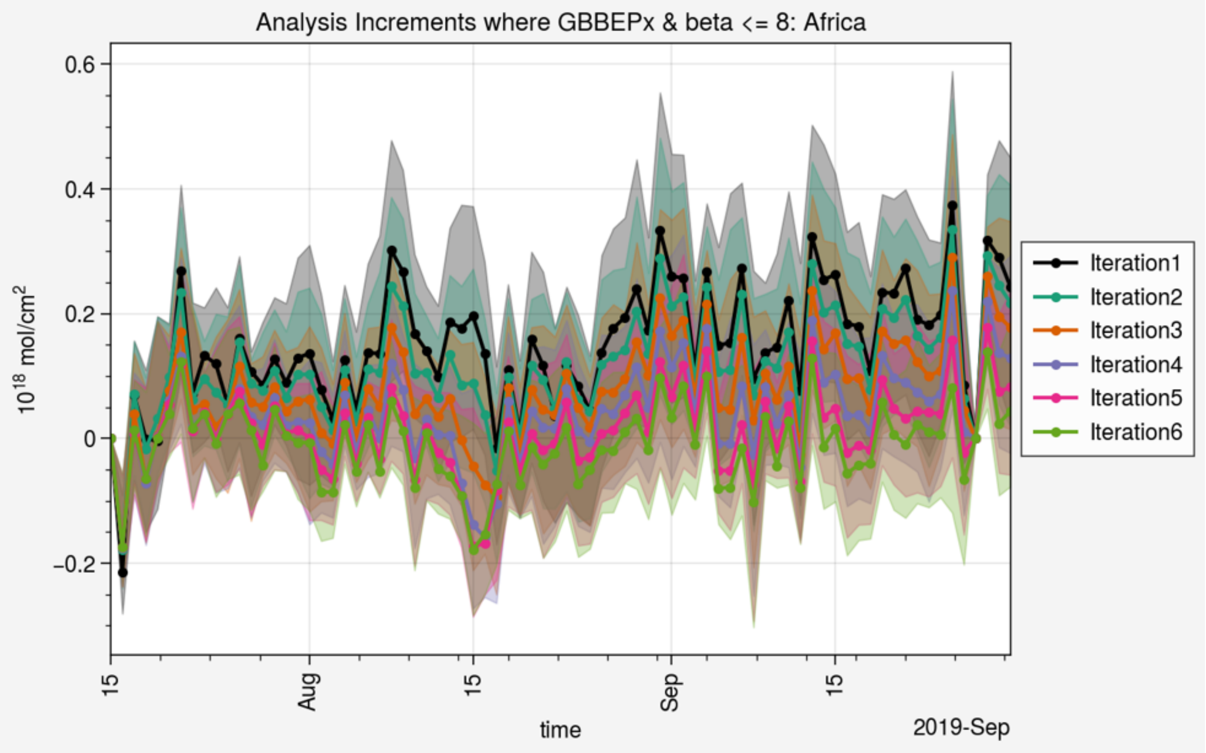

Figure 5.9: Time series of the TROPOMI CO DA analysis increments for the African region for UFS-RAQMS DA cycles 1-6. Only analysis increments for grid points where there are GBBEPx CO emissions and β is ≤ 8 are included in the average.

5.2.2 Adjusted GBBEPx Emissions

The iterated FDMB GBBEPx emissions update substantially increased CO biomass burning emissions from Siberia and the maritime continent, and sufficiently converged within 6 iterations. The 6^{th} iteration of the emissions adjustment, GBBEPx^6, will hereafter be referred to as the adjusted GBBEPx emissions.

Figure 5.10 shows the average percent change in CO biomass burning emissions between GBBEPx^6 and GBBEPx^0. Over the maritime continent JAS GBBEPx emissions are increased by $>$ a factor of 10 (1000%), primarily over peatlands, forests, and agricultural lands (see land cover maps in Chapter B). GBBEPx^6 emissions are generally increased from GBBEPx^0, though there is considerable spatial variability in the magnitude of the change. GBBEPx^0 CO emissions from eastern central Africa are increased by ~200-300%. GBBEPx^0 emissions from western central Africa are decreased by 10-20%. GBBEPx^6 emissions from Alaska, Canada, and the western US are increased relative to GBBEPx^0 for some locations and decreased at others.

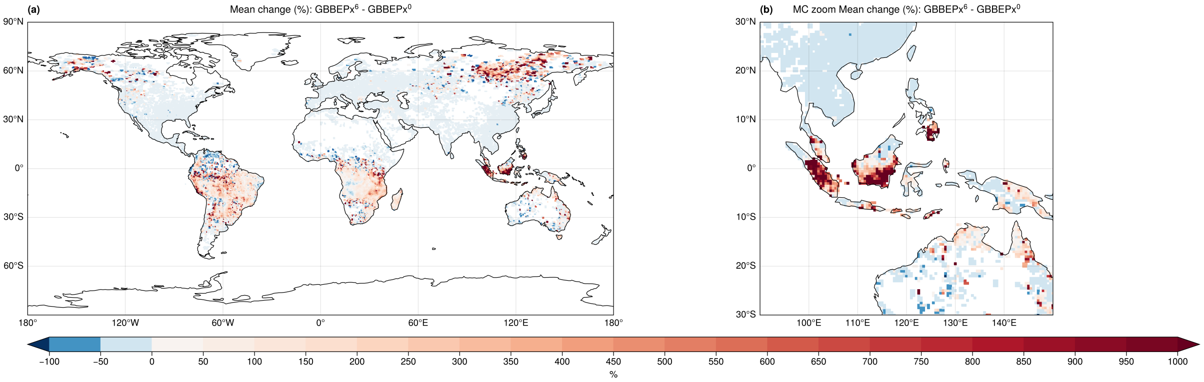

FIGURE 5.10: Percent change in biomass burning CO emissions between GBBEPx^6. Panel b zooms in on SE Asia.

5.2.3 Scale Factors for GBBEPx CO emissions

The iterated FDMB GBBEPx CO emissions update scheme significantly increases CO emissions in the Siberian and Maritime Continent regions during JAS 2019. In QFED, and thereby inherent in the GBBEPx product, biomass burning emissions are calibrated to AOD observations using biome-representative scale factors (Darmenov and da Silva, 2015, Zhang et al., 2019). The QFED AOD scale factors are determined from a regression of the form: $\tau \sim w_{BB}\tau_{BB} + w_{AN}\tau_{AN} + \tau_N$, where the biomass burning AOD (τ_{BB}), anthropogenic AOD (τ_{AN}), and AOD from natural sources (τ_N) were determined from NASA Goddard Earth Observing System Model (GEOS) simulations. QFED scale factors were fit for 46 regions and then reduced to representative scaling factors for tropical forests, extratropical forests, savanna, and grasslands. Readers are referred to tables 5-7 and figure 6 in Darmenov and da Silva (2015) for the QFED scaling factors. Following from the scaling to QFED used in GBBEPx for VIIRS-derived emissions, I define a GBBEPx CO emissions scaling factor using the relationship 5.2, and calculate the average scaling factor for UFS-RAQMS grid points and for the biomass burning regions defined in Figure 5.2. My biomass burning regions are different than those used for the scaling of QFED aerosol emissions in Darmenov and da Silva (2015) and were selected to align with significant biomass burning regions in JAS 2019. The average GBBEPx CO scale factor for each grid point is shown in Figure 5.11 as well as regional average scale factors that have been colored according to the scale factor. The regional average GBBEPx CO scale factors are reported in table 5.1. For each region the standard deviation of the GBBEPx

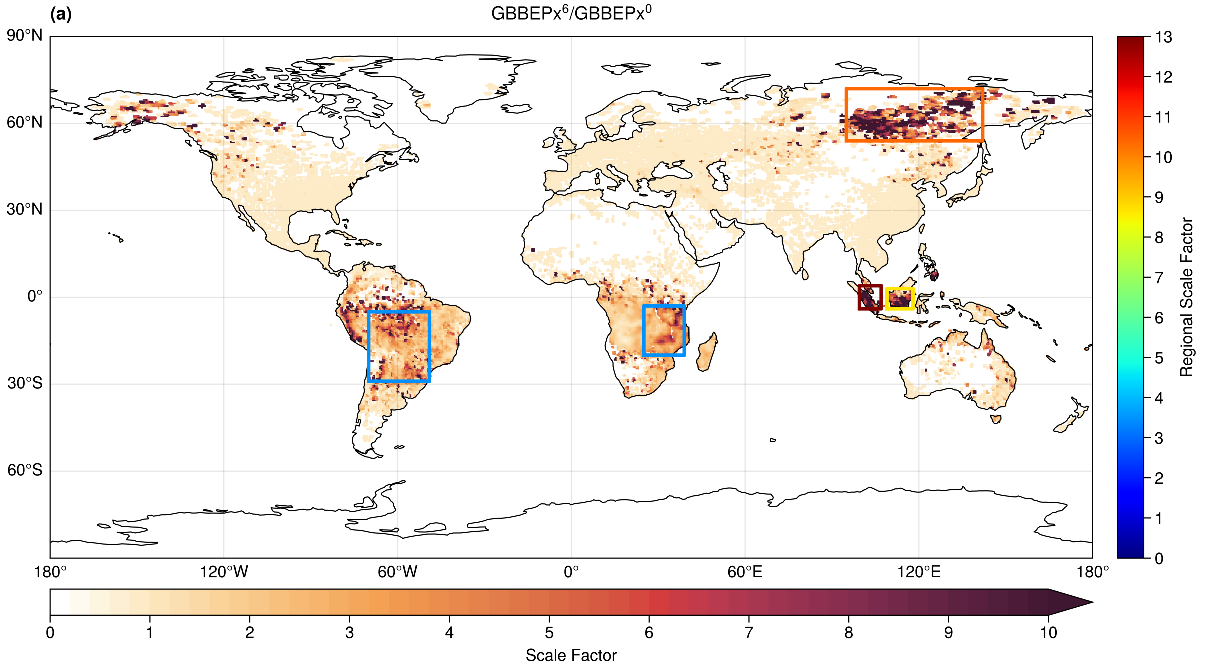

FIGURE 5.11: Average GBBEPx CO biomass burning scale factors for JAS 2019. Boxes are colored according to the regional average scale factor.

TABLE 5.1: Regional scale factors for GBBEPx CO emissions. Standard deviation of FDMB iteration 0 GBBEPx CO emissions (GBBEPx^0) and FDMB iteration 6 GBBEPx CO emissions (GBBEPx^6).

Region	Scale Factor	GBBEPx^0 Standard Deviation	GBBEPx^6 Standard Deviation
Siberia	11.7389	5.9092	18.5136
South America	3.6991	2.211	6.423
Sumatra	14.5011	2.5983	20.2505
Borneo	9.634	3.8585	18.3789
Africa	3.5253	1.0556	2.6684

CO emissions is increased in GBBEPx^6 relative to GBBEPx^0.

$$E_{GBBEPx^6} = wE_{GBBEPx^0} \tag{5.2}$$

The regional average GBBEPx CO emissions scaling factors obtained here are larger than the QFED AOD scaling factors for similar regions. There are several significant potential reasons for this, and further investigation would be necessary before applying the GBBEPx CO scale factors obtained in this study to GBBEPx CO emissions more broadly. First, the GBBEPx CO scale factors are calculated using a 2.5 month simulation while the QFED AOD scale factors are calculated from multi-year simulations. The GBBEPx CO scale factors obtained by this study are sensitive to the biomass burning during JAS 2019 and are not representative of a long-term average. Second, as shown in Figure 5.11 there is considerable spatial variability in the scale factor that is disregarded by aggregating over large geographic regions. Recent intercomparisons of major global fire emissions inventories find that land type classification is a significant driver of the difference in CO emissions between different inventories (Hua et al., 2024, Wiedinmyer et al., 2023). Inventories that account for Indonesian peatlands separately from savannas and grasslands have significantly higher CO and particulate matter emissions for the region due to differences in burning characteristics (Hua et al., 2024, Kiely et al., 2019). Aggregating the biomass burning CO scale factors derived here to the 4 land types considered in GBBEPx and QFED would disregard key biome-driven differences in emissions strength.

5.3 Conclusions

Adjustment of the mean GBBEPx CO biomass burning emissions in Africa, Siberia, South America, Sumatra, and Borneo where there was significant biomass burning in

JAS 2019 with iterative FDMB converged within 6 iterations. GBBEPx CO emissions are significantly increased from the maritime continent and Siberia, and the TROPOMI CO DA increment is smaller at iteration 6 over these regions than in the prior iterations. This indicates that the increase in biomass burning CO emissions are increasing the CO column directly over the source. Chapter 6 will evaluate the impact of the adjusted GBBEPx CO emissions on UFS-RAQMS chemical analyses and compare to the TROPOMI CO DA experiment results from Chapter 4.

Scale factors between GBBEPx^0 and GBBEPx^6 show strong spatial variability, which is consistent with the average percent change between FDMB GBBEPx emissions update cycles. At this stage, application of iterative FDMB for optimizing CO emissions can be said to reduce the bias in UFS-RAQMS CO columns at emission sources. Future work should focus on applying this approach to longer CTM simulations to evaluate the representativeness of the GBBEPx CO scale factors obtained here to a broader time period.

Chapter 6

Impacts of wildfire emissions on global background CO and O_3 during FIREX-AQ and CAMP^{2}Ex

6.1 Introduction

The iterative FDMB biomass burning CO emissions adjustment procedure applied in Chapter 5 increased JAS 2019 GBBEPx CO emissions globally. In this chapter I evaluate the impact these adjusted emissions have on UFS-RAQMS chemical forecasts. First, I validate the UFS-RAQMS adjusted emissions experiment CO forecast through comparisons with independent analyses. Then, I compare the UFS-RAQMS TROPOMI CO DA experiment with the adjusted emissions experiment to determine how changes in the

VOC and NOx emissions that result from the CO emissions adjustment influence ozone production within biomass burning plumes. NO, CH_3CN, ethane (C_2H_6), paraffin carbon (butane, propene, pentane), ethene, and terminal olefin carbons are emitted from biomass burning in UFS-RAQMS by application of emission ratios to GBBEPx CO emissions. From this point, unless explicitly stated, adjusted emissions collectively refers to the adjusted CO biomass burning emissions and the affected NOx and VOC emissions.

6.2 Validation of UFS-RAQMS CO

TROPOMI CO columns, MOPITT CO columns, NDACC FTIR profiles, and field campaign data are used to validate the UFS-RAQMS adjusted emissions experiment. Validation is the practice of comparing CTM output with observations in order to quantify the skill of the CTM in capturing the observed quantity.

6.2.1 TROPOMI and MOPITT Total Column CO

UFS-RAQMS CO columns are evaluated here with TROPOMI CO level 2 observations and MOPITT daily level 3. UFS-RAQMS control and adjusted emissions experiments are sampled following a bilinear interpolation to the higher-resolution TROPOMI. After applying the TROPOMI averaging kernels to UFS-RAQMS CO, the TROPOMI and UFS-RAQMS coincidences are averaged onto a 0.25x0.25 global grid. The UFS-RAQMS CO columns are compared with MOPITT as in Chapter 4.

Statistics comparing the UFS-RAQMS experiments with TROPOMI CO observations

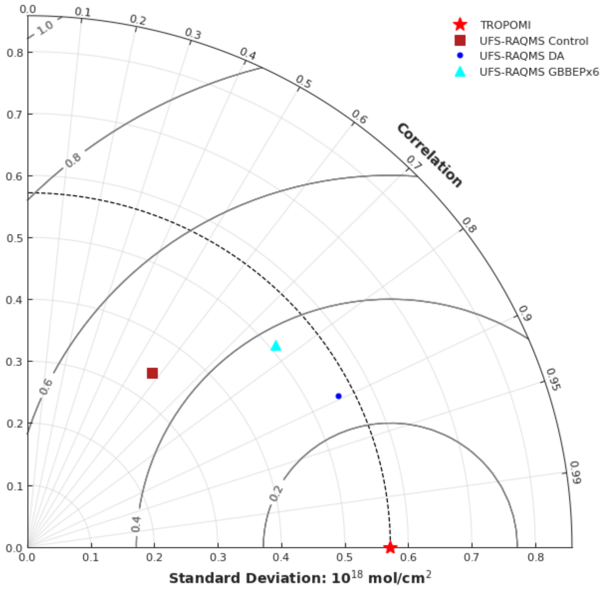

FIGURE 6.1: Global bias and correlation for UFS-RAQMS experiments with TROPOMI CO observations between 16 July-28 September 2019.

globally are summarized in Figure 6.1 with a Taylor diagram. The standard deviation of CO column is higher the UFS-RAQMS adjusted emissions experiment than in the UFS-RAQMS control and is closer to the standard deviation of the TROPOMI CO column observations. UFS-RAQMS adjusted emissions CO columns are strongly correlated (>0.7) with TROPOMI CO and is improved relative to the UFS-RAQMS control experiment, where the UFS-RAQMS CO columns are moderately correlated with TROPOMI CO column observations.

Figure 6.2 shows the average bias in the CO column relative to MOPITT for the UFS-RAQMS control, TROPOMI CO DA, and adjusted emissions experiments. The adjusted emissions decrease the low bias in the NH but increase the bias in the SH over the oceans, central Africa, and western South America. Directly over biomass burning in Siberia and Indonesia the UFS-RAQMS adjusted emissions experiment CO columns are bias

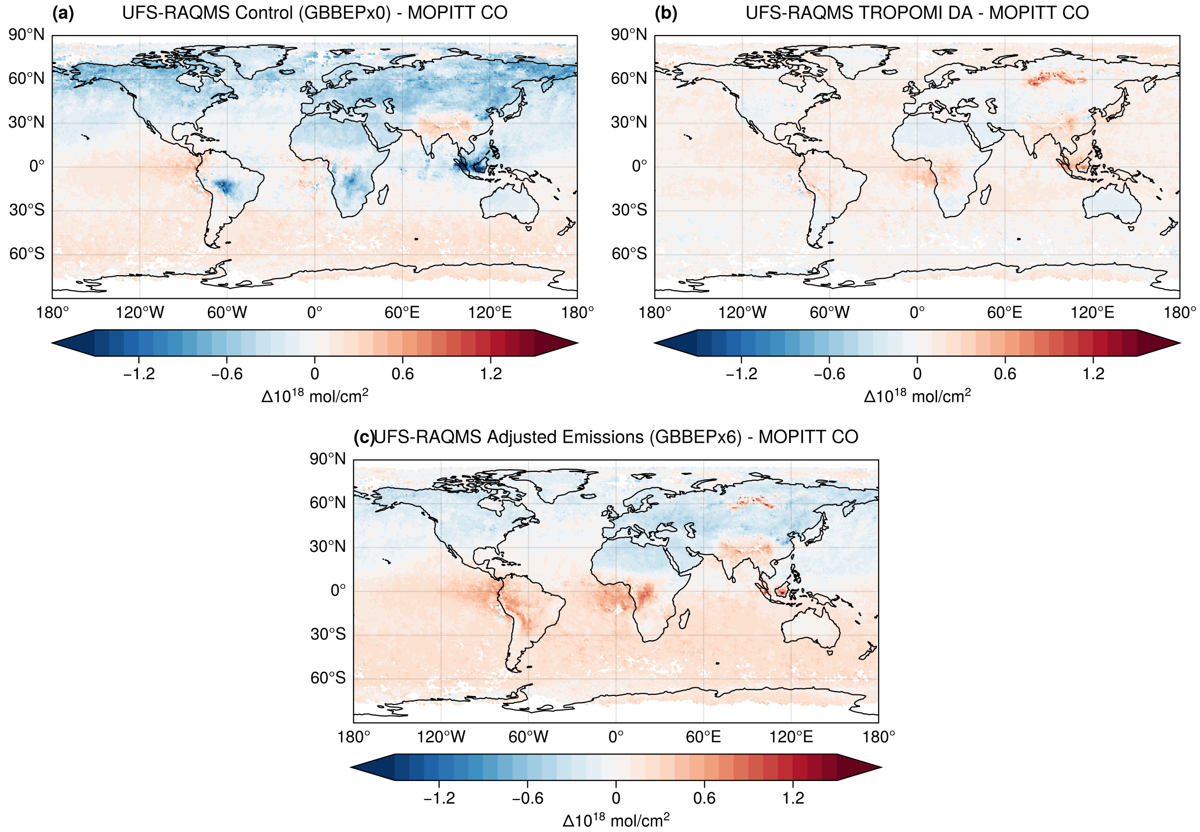

FIGURE 6.2: Mean bias (10^{18} mol/cm^2) in UFS-RAQMS control, TROPOMI CO DA, and adjusted emissions experiments relative to MOPITT CO Columns.

high relative to MOPITT, indicating that the adjustment was too large. Contrasting the evaluation statistics from the UFS-RAQMS TROPOMI CO DA experiment from Chapter 5 with those for the UFS-RAQMS adjusted emissions experiment, MOPITT comparisons support a conclusion that underestimates of biomass burning CO emissions are responsible for a large portion of the bias in UFS-RAQMS NH CO concentration.

6.2.2 FIREX-AQ and CAMP^{2}Ex In-situ CO Observations

Figure 6.3 shows a comparison of the vertical profiles for the field campaign CO observations and coincident UFS-RAQMS analyses. Following the interpolation of the UFS-RAQMS analyses along the flight tracks, the modeled and measured values were binned into 200 m altitude bins. The median (vertical profile), 25th and 75th (shaded) percentiles of the modeled and observed distributions within each 200m altitude bin are shown. Between 1km and 5km, the UFS-RAQMS adjusted emissions mean CO profile agrees closely with the observed FIREX-AQ background profile. Above 5km the UFS-RAQMS adjusted emissions CO profiles do not diverge much from the control experiment. UFS-RAQMS adjusted emissions CO profiles agree better with CAMP^{2}Ex profiles at all altitudes than UFS-RAQMS control but still underestimate CO below 2km by >25 ppbv.

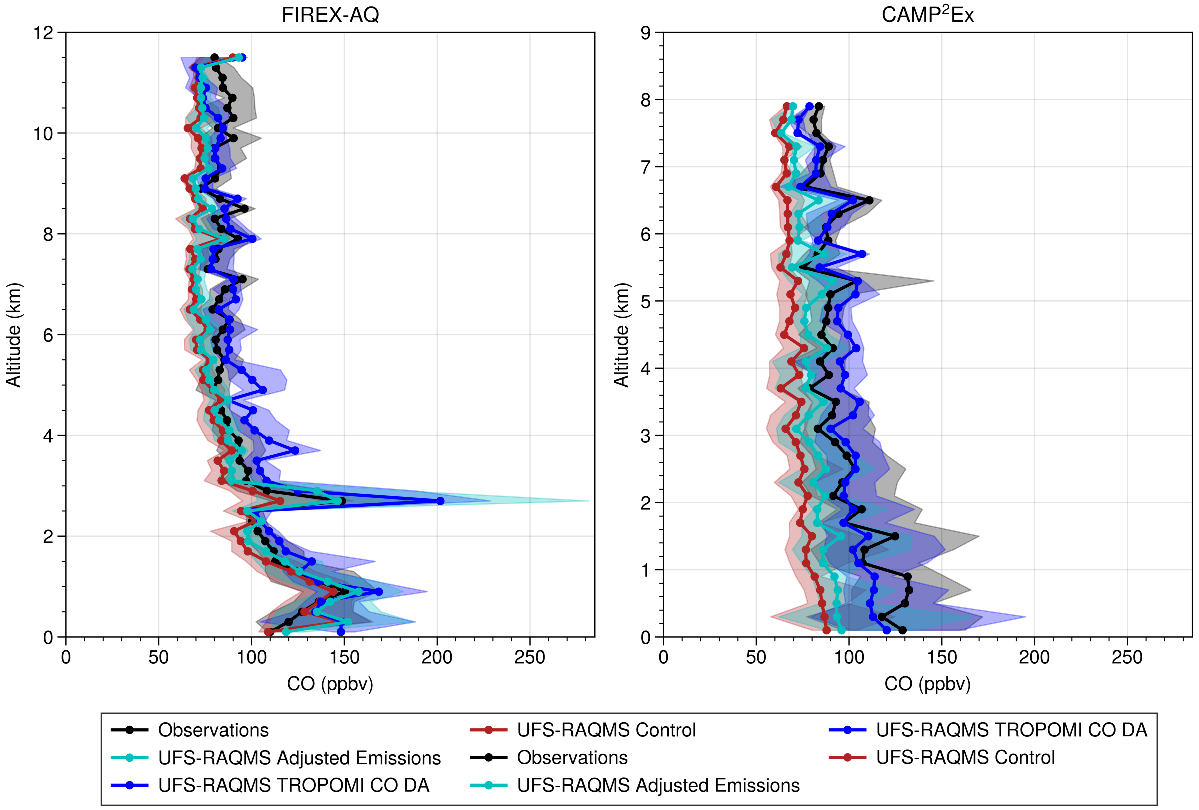

FIGURE 6.3: Vertical profiles of CO for field campaign observations (black), UFS-RAQMS Control experiment (red), UFS-RAQMS TROPOMI CO DA experiment (dark blue), and UFS-RAQMS adjusted emissions experiment (cyan).

6.2.3 NDACC FTIR CO

UFS-RAQMS adjusted emissions CO profiles are evaluated with the same NDACC FTIR sites used in Chapter 4 to evaluate UFS-RAQMS DA. The adjusted biomass burning emissions increase the bias in UFS-RAQMS CO profile at SH sites and reduce the bias at the NH sites, which is consistent with the CO column analyses. At Boulder and Mauna Loa, tropospheric CO mixing ratios are increased by <10 ppbv. The largest changes in UFS-RAQMS CO profile occur at the high latitude Thule site, where below 10km the profile is increased by 15-20 ppbv in the UFS-RAQMS adjusted emissions experiment

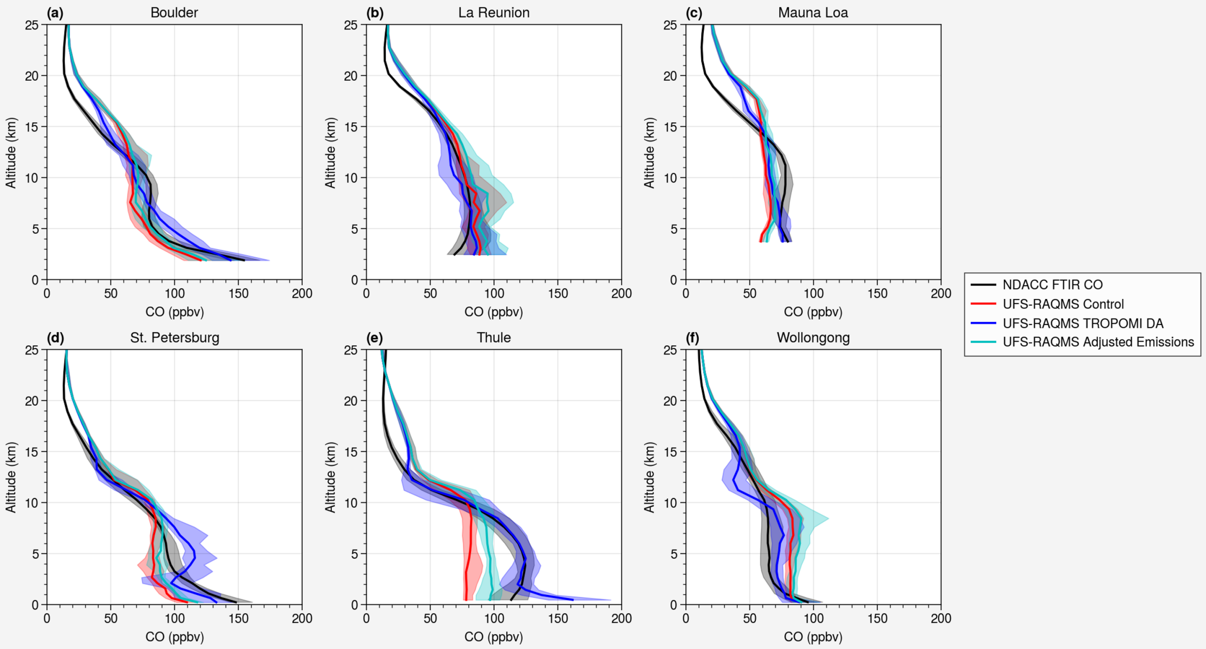

FIGURE 6.4: Comparison of CO profiles from NDACC FTIR sites (black), UFS-RAQMS Control experiment (red), UFS-RAQMS TROPOMI CO DA experiment (dark blue), and UFS-RAQMS adjusted emissions experiment (cyan).

relative to the control.

6.3 Impact of adjusting GBBEPx biomass burning CO emissions on atmospheric composition in UFS-RAQMS

Validation with satellite, ground based, and airborne observations show the adjusted GBBEPx CO emissions improve UFS-RAQMS CO forecasts in the NH. Both TROPOMI CO DA and the adjusted GBBEPx CO emissions result in an increase in CO over central Africa and enhance an overestimate in CO column over the Atlantic. Contrasting the validations of the UFS-RAQMS adjusted emissions and TROPOMI CO DA experiments, I showed underestimation of biomass burning CO emissions in GBBEPx contributes significantly to the low bias in UFS-RAQMS CO that TROPOMI CO DA corrects for but does not fully explain the bias, which points to underestimates in anthropogenic CO emissions. I now look at the impact of increased GBBEPx CO emissions on ozone production in UFS-RAQMS by comparing CO, NO_2, ethane (C_2H_6), and O_3 from the UFS-RAQMS control and adjusted emissions experiments.

6.3.1 CO

Figure 6.5 shows the average percent change in zonal mean CO and CO total column between the UFS-RAQMS control and adjusted emissions experiments. Consistent with the validation of the UFS-RAQMS adjusted emissions experiment in Section 6.2, the CO column and zonal mean CO profile are increased globally due to the adjusted GBBEPx CO emissions. Over the Siberian and Indonesian regions where the adjusted emissions were $\geq$10x greater than the control emissions, the CO column is $\sim$70-100% higher in the UFS-RAQMS adjusted emissions experiment than in the control. The change in the zonal mean CO is largest in the lowest 5km and in the northern high latitudes, where the UFS-RAQMS CO is increased by >28%. The zonal mean CO in the SH tropics is increased by 20-30%.

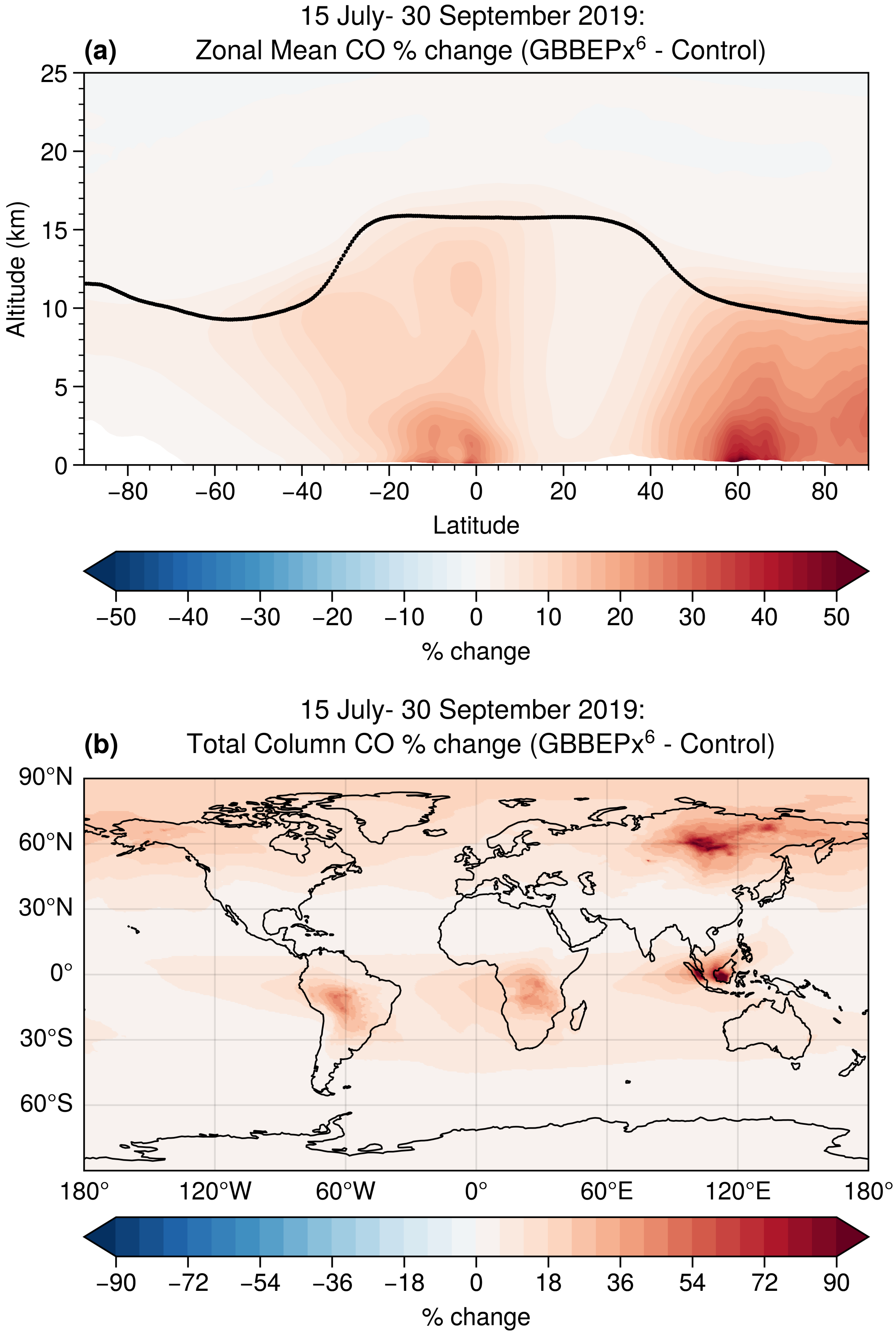

FIGURE 6.5: Percent difference in zonal mean CO profile (a) and total column CO (b) between UFS-RAQMS adjusted emissions and control experiments.

6.3.2 NO_2

UFS-RAQMS emits NOx from biomass burning as NO, which then reacts with oxidized VOCs or HO_2 to form NO_2 and O_3. Figure 6.6 shows the average percent change in zonal mean NO_2 and tropospheric column NO_2 between the UFS-RAQMS control and adjusted emissions experiments. Unlike the CO column enhancements, the NO_2 tropospheric column enhancement due to the adjusted GBBEPx CO emissions remains near-source and the change in tropospheric NO_2 outside of the biomass burning-affected regions is <20%. The change in the zonal mean NO_2 between the UFS-RAQMS control and adjusted emissions experiment is <10% outside of the lowest 3-4km at the tropical and high latitudes where biomass burning occurred during JAS 2019.

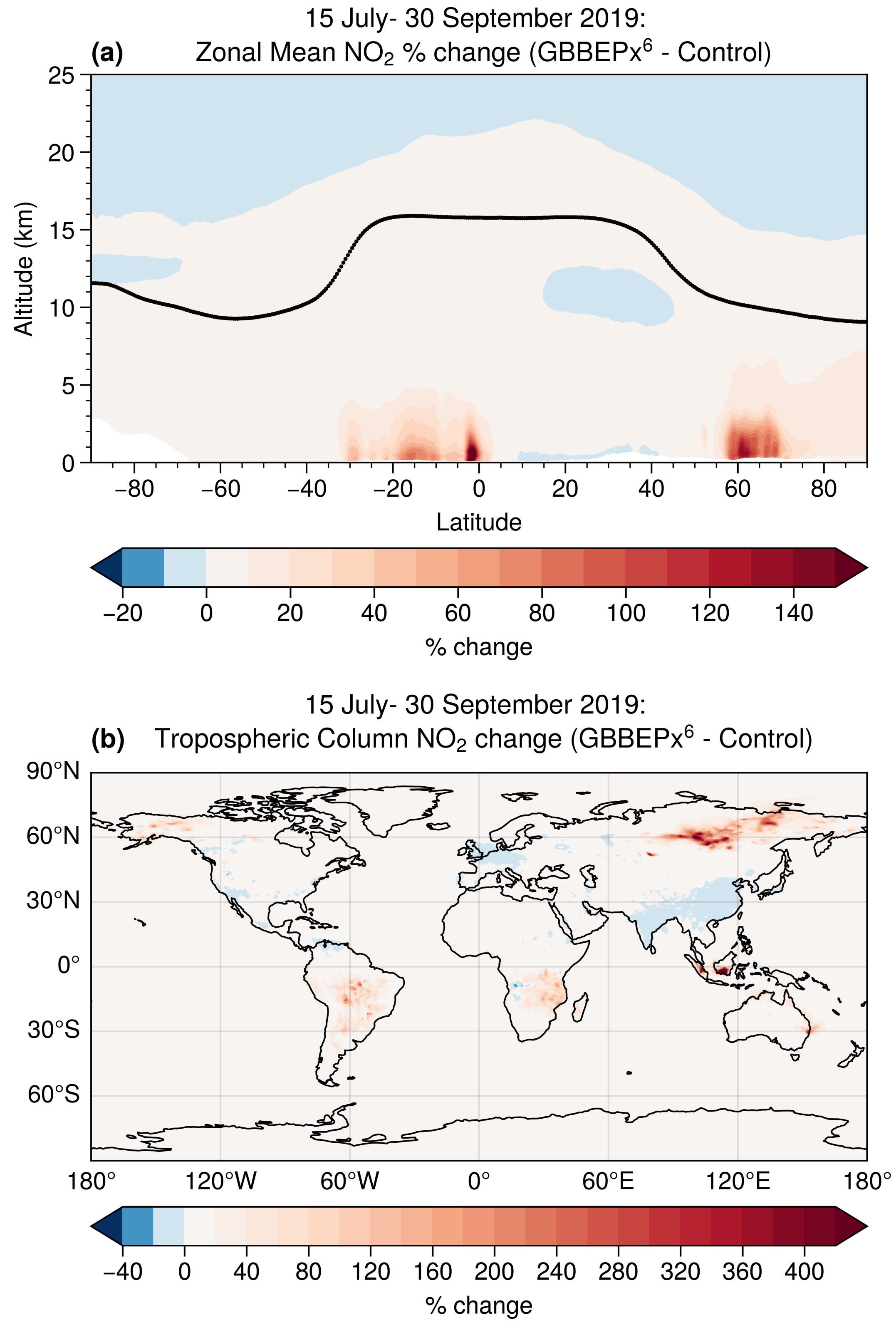

FIGURE 6.6: Percent difference in zonal mean NO_2 profile (a) and tropospheric column NO_2 (b) between UFS-RAQMS adjusted emissions and control experiments.

6.3.3 Ethane

Figure 6.7 shows the average percent change in zonal mean ethane and total column ethane between the UFS-RAQMS control and adjusted emissions experiments. Ethane is among the highest emitted compounds from biomass burning (e.g. Andreae, 2019, Gkatzelis et al., 2024), and as already noted is one of the VOCs emitted from biomass burning in UFS-RAQMS. The zonal mean and total column percent changes in UFS-RAQMS ethane forecasts due to the adjusted GBBEPx CO emissions are very similar to the change in CO and are about 60% as large.

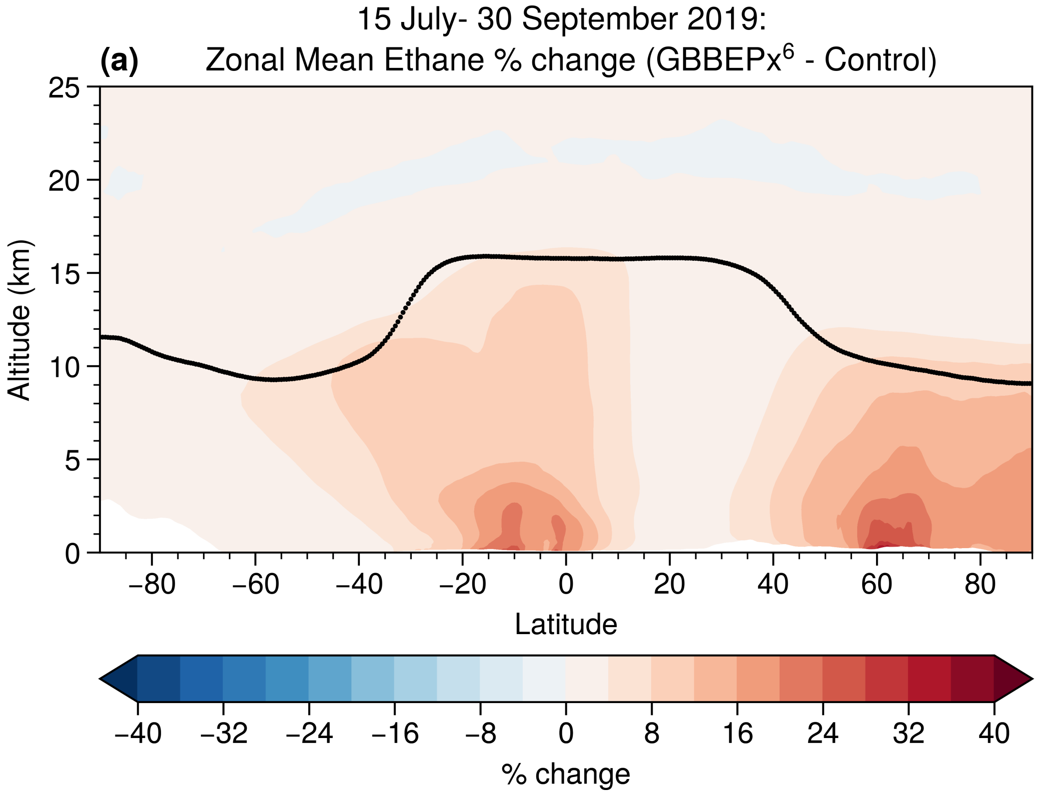

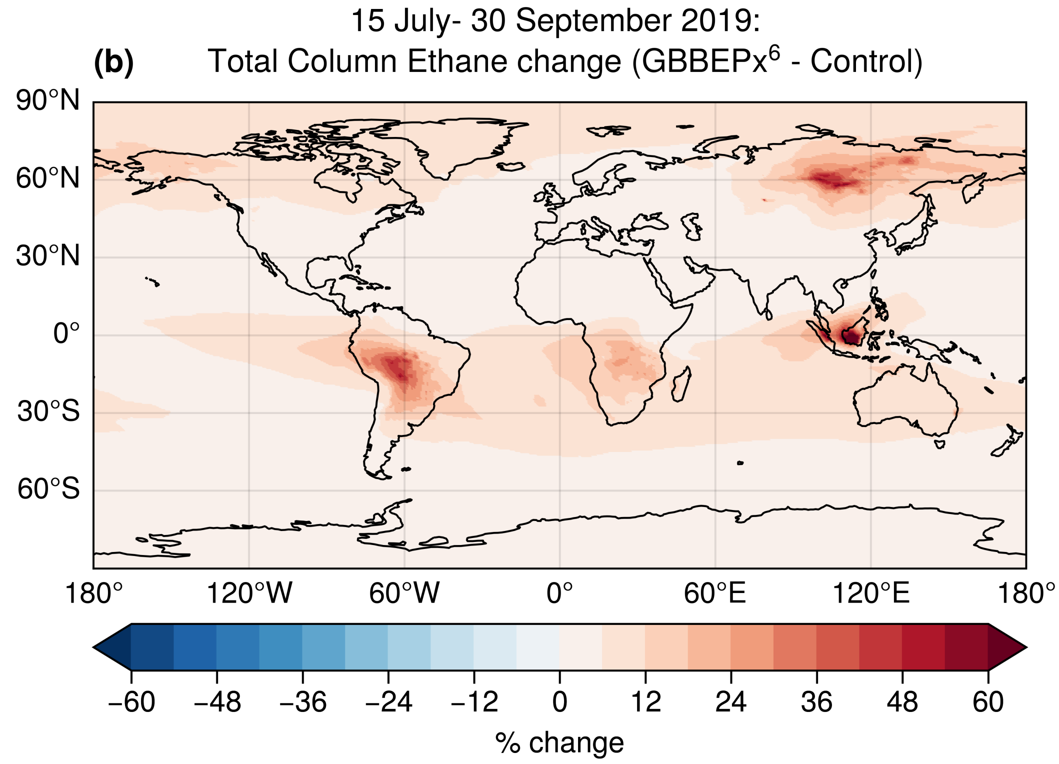

FIGURE 6.7: Percent difference in zonal mean ethane profile (a) and total column ethane (b) between UFS-RAQMS adjusted emissions and control experiments.

6.3.4 Tropospheric Ozone

The adjusted biomass burning emissions result in tropospheric ozone enhancements >4% (Figure 6.8). The strongest tropospheric O_3 enhancements due to increased biomass burning emissions occur in the tropics over the maritime continent. Boreal biomass burning O_3 production is much lower. This contrasts tropospheric CO enhancements due to biomass burning, where boreal biomass burning induces a stronger response than tropical burning. The differences in O_3 production from boreal and tropical biomass buring emissions is due to the higher photolysis rates in the tropics (Natarajan et al., 2012).

Figure 6.9 shows the change in surface O_3 between the UFS-RAQMS control and adjusted emissions experiment. In central Africa and Brazil, the adjusted emissions increased the surface O_3 concentration by 7-10 ppbv. In Borneo and Sumatra, the adjusted emissions increased surface O_3 by 10-15 ppbv. Surface O_3 concentrations in Siberia are increased by 2-6ppbv. These increases are not inconsequential and can result in exceeding air quality standards for regions that are near the standard (70 ppbv in the US).

The changes in modeled tropospheric ozone presented in Figures 6.8 and 6.9 are linked to the uncertainty in biomass burning CO emissions. A complete assessment of the impact of biomass burning emissions on tropospheric ozone concentrations would compare a simulation with all emissions sources to a simulation without biomass burning emissions (e.g. Galanter et al., 2000, Natarajan et al., 2012, Ziemke et al., 2009). Ziemke et al.

(2009) evaluates the ozone response to biomass burning only in the tropics; Natarajan et al. (2012) evaluates the ozone response to biomass burning in Asia; and Galanter et al. (2000) evaluates the global ozone response to biomass burning. The larger response of tropospheric ozone to biomass burning in the tropics than in boreal regions found here is consistent with Galanter et al. (2000) and Natarajan et al. (2012). The magnitude of the tropical response over the maritime continent found in this study is highly similar to the September 2006 analysis in Ziemke et al. (2009). Extreme biomass burning events occured in the region during 2006 and 2019 during moderate El Niño conditions (Field et al., 2016, Reid et al., 2023).

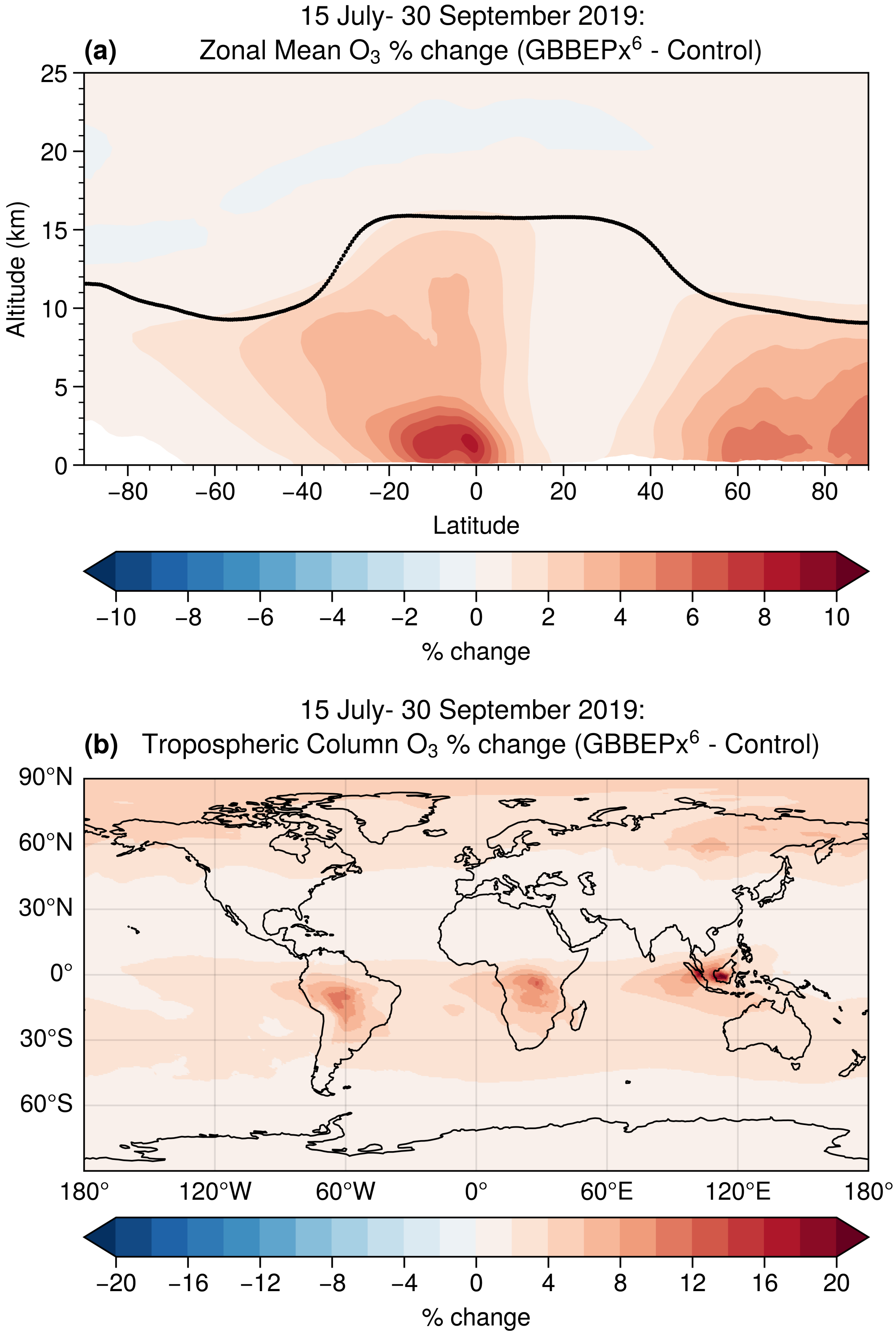

FIGURE 6.8: Percent difference in zonal mean O_3 profile (a) and tropospheric column O_3 (b) between UFS-RAQMS adjusted GBBEP^6 and control experiments.

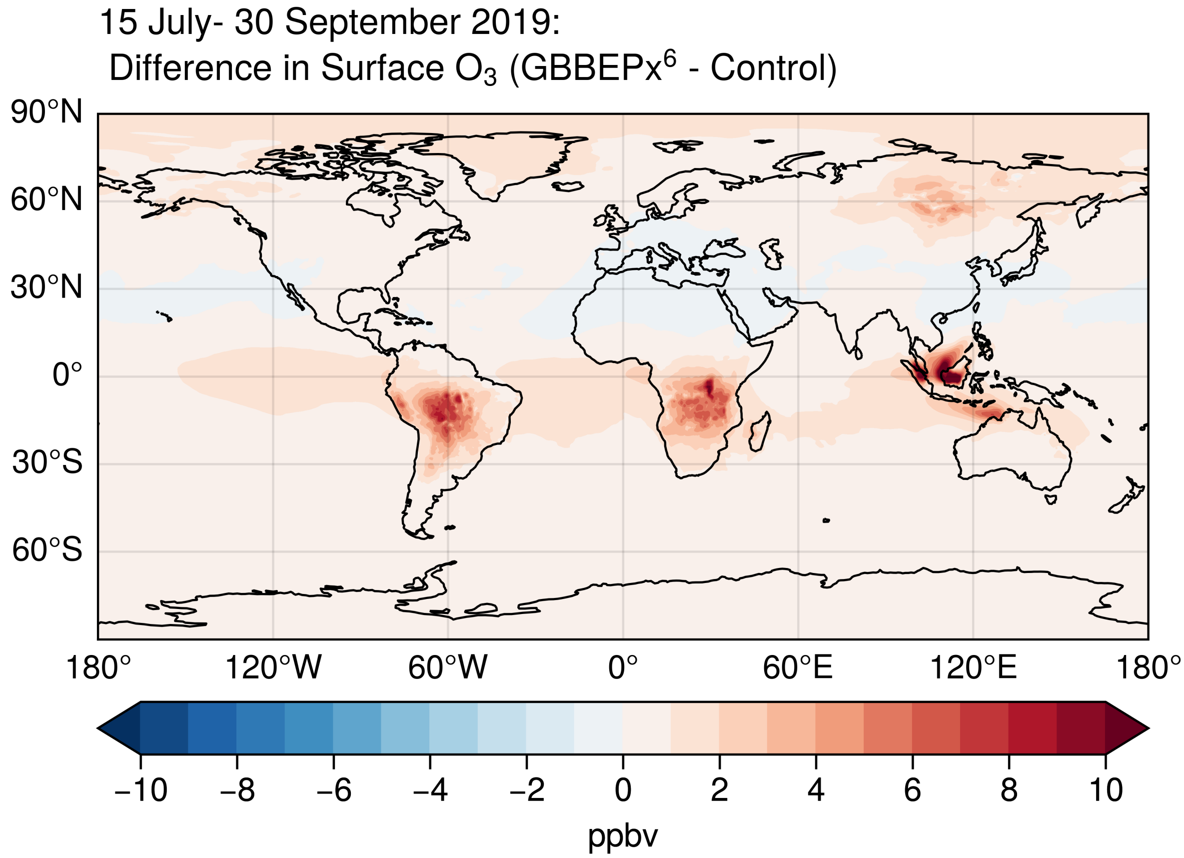

FIGURE 6.9: Difference (ppbv) in surface O_3 between UFS-RAQMS adjusted emissions and control experiments.

6.4 Conclusions

UFS-RAQMS chemical forecasts using the adjusted GBBEPx CO emissions calculated in Chapter 5 differ from those using the unadjusted GBBEPx CO emissions. The global bias in CO column relative to TROPOMI CO is reduced in the UFS-RAQMS adjusted emissions experiment and the correlation with TROPOMI CO is improved. Comparison with MOPITT observations shows that CO columns in the NH are improved in the adjusted emissions experiment relative to the control while the CO column bias in the SH increases. The increased SH CO bias in the UFS-RAQMS adjusted emissions experiment in the SH is likely related to the small adjustments in biomass burning emissions from east central Africa, though further analysis is necessary to examine why this occurred. Evaluation of UFS-RAQMS adjusted emissions CO profiles with NDACC, FIREX-AQ, and CAMP^{2}Ex observations are consistent with the column validation results and show that the reduction in the CO bias in the NH is due to increased CO in the troposphere.

CO, ethane, NO_2, tropospheric O_3, and surface O_3 forecasts from the UFS-RAQMS adjusted emissions and control experiment were compared. Changes in ethane and NO_2 at the emission source are proportional to the change in CO. This is due to biomass burning emissions for NO, CH_3CN, ethane (C_2H_6), paraffin carbon (butane, propene, pentane), ethene, and terminal olefin carbons in UFS-RAQMS being obtained by applying species-specific emissions factors to the GBBEPx emissions. The adjusted emissions increase tropospheric ozone concentrations more in the tropics than in the boreal region. While the change in biomass burning CO emissions from the South America and Africa regions was small relative to that from the Siberian region, the change in O_3 is approximately twice as large due to the stronger photolysis rates in the tropics.

Chapter 7

Conclusions and Future Work

Global biomass burning activity and emissions are projected to change significantly due to climate change (e.g. Chen et al., 2023, Senande-Rivera et al., 2022, Zheng et al., 2021). Global burned area has declined since 2000 due to decreases in tropical biomass burning regions while burned area in temperate and boreal biomass burning regions has increased (Chen et al., 2023, Jones et al., 2022). Regional trend analyses of biomass burning emissions show that increased emissions from biomass burning in forests and boreal areas compensate for decreased emissions from tropical regions (Liu and Ding, 2024, Zheng et al., 2021). The biomass burning emissions inventories used in CTMs have high uncertainties and present a significant challenge to modeling tropospheric air quality (Archibald et al., 2020, and references therein). Due to projected increases in biomass burning in a changing climate, improved predictions of biomass burning emissions are necessary for providing accurate air quality forecasts. This dissertation sought to improve our ability to model the impacts of biomass burning on atmospheric composition by evaluating how tropical biomass burning emissions impact variability in tropical tropospheric ozone concentrations and how well tropical and boreal biomass burning emissions are represented in global CTMs. In this chapter I summarize my results and discuss future directions for study.

7.1 Summary of Results

1) How is variability in tropical tropospheric ozone related to biomass burning emissions? ENSO has previously been found to be a dominant influence on tropical tropospheric ozone interannual variability (e.g. Doherty et al., 2006, Oman et al., 2013, 2011, Ziemke et al., 2010). ENSO signatures in tropical tropspheric ozone columns are predominantly due to the shifts in the location of the ascending and descending branches of the Walker circulation, though it has been indicated that biomass burning emissions contribute to the response (Doherty et al., 2006, Inness et al., 2015a, Peters et al., 2001, Sekiya and Sudo, 2012, e.g.). Chemical transport models that include the tropical tropospheric ozone column response to ENSO can be used to investigate the vertical sturcture of the response and the drivers of the response (e.g. Doherty et al., 2006, Hou et al., 2016, Inness et al., 2015a, Rowlinson et al., 2019) In Chapter 3 the RAQMS-Aura chemical reanalysis is used to investigate the influence of biomass burning and convective precipitation on ENSO variability in tropical tropospheric ozone. Validation of RAQMS-Aura with TRMM precipitation estimates, SHADOZ ozonesondes, MOPITT CO columns, and

OMI-MLS TOR showed that the RAQMS-Aura reasonably captures the observed variability in CO, tropospheric O_3, and convective precipitation during 2006-2016. Over the maritime continent ozone production in the lower troposphere is increased during El Niño and decreased during La Niña. Consistent with previous studies, in the RAQMS-Aura reanalysis a portion of the ENSO variability in TTOC is due to biomass burning though most of the ENSO variability in TTOC is driven by shifts in the location of the ascending and descending branches of the Walker circulation.

2) How well do global models capture emissions from biomass burning?

Biomass burning emissions inventories vary significantly due to uncertainty in burned area, consideration of vegetation type, inclusion of small fires, and other factors (e.g. Hyer and Reid, 2009, Pan et al., 2020, Stockwell et al., 2022, Wiedinmyer et al., 2023). CTM forecasts vary significantly depending on which inventory is used (e.g. Bian et al., 2007, Hua et al., 2024, Pan et al., 2020). CO observations have been used extensively to evaluate CTMs using biomass burning emissions. GBBEPx CO emissions are used in NOAA's operational global atmospheric composition models (Bhattacharjee et al., 2023, Tang et al., 2022, Zhang et al., 2022). In Chapter 4 I showed that the GBBEPx emissions inventory used in UFS-RAQMS underestimates biomass burning CO emissions. UFS-RAQMS control and TROPOMI CO DA experiments were validated with satellite, ground-based, and airborne observations of CO in JAS 2019. The UFS-RAQMS control run using standard GBBEPx CO emissions underestimates the CO column in biomass burning regions and in the NH. UFS-RAQMS control tropospheric CO profiles are also biased low, especially at northern high latitudes and in the maritime continent which were impacted by biomass burning plumes during JAS 2019. TROPOMI CO DA improved UFS-RAQMS CO column analyses but improvement in the UFS-RAQMS CO vertical structure was mixed. Consistency between biomass burning aersol and CO emissions in UFS-RAQMS was evaluated for two case studies using the relationship between AOD and CO columns. In the 22 July 2019 Siberia case study, the AOD/CO relationship in the biomass burning smoke plume was underestimated in UFS-RAQMS control due to a low bias in CO column. In the 16 September 2019 Indonesia case study, the AOD/CO relationship in the biomass burning in the UFS-RAQMS control appears realistic due low biases in both AOD and CO columns in the biomass burning smoke plume. Assimilating TROPOMI CO improves the representation of the biomass burning AOD/CO relationship but does not address the underlying cause of the inconsistency between AOD and CO in biomass burning plumes.

Inversion techniques including mass balance (e.g. East et al., 2022, Lamsal et al., 2011, Martin et al., 2003a), ensemble Kalman filters (e.g. Gaubert et al., 2020, Miyazaki et al., 2012), and adjoint models (e.g. Cooper et al., 2017, Parrington et al., 2012) optimize pollutant emissions in order to minimize bias between concentration observations and CTM simulations. Cooper et al. (2017) showed that the iterative FDMB approach and the adjoint approach result in similar posterior emissions inventories. Iterative FDMB does not require development of an adjoint and is less computationally expensive to run than other approaches. In Chapter 5 application of an iterative FDMB approach for adjusting the GBBEPx CO emissions using the analysis increments from TROPOMI CO DA significantly increases biomass burning CO emissions from Siberia and the maritime continent in JAS 2019. Convergence of the emissions update method was determined based on mean analysis increments and change in emissions for regions of Siberia, Borneo, Sumatra, South America, and Africa approaching zero. The mean adjustment in biomass burning CO emissions for these regions converged within 6 iterations of FDMB. Biomass burning CO emissions from Siberia and the maritime continent regions were increased by a factor of 10 or more. Biomass burning emissions from the South America and African regions were increased by a factor of ∼3.

3) What is the contribution of biomass burning emissions to global background air quality?

The analysis of the ENSO signature in tropical tropospheric O_3 in Chapter 3 showed that ENSO variability in tropical tropospheric ozone is primarily driven by variability in convective mass flux but that some of the response is due to variability in ozone production from biomass burning emissions. In Chapter 6 it was shown that the adjusted GBBEPx CO emissions from Chapter 5 impacted UFS-RAQMS CO, NO_2, ethane, and tropospheric O_3 forecasts. The influence of biomass burning emissions was the strongest below 5km and close to the source. For JAS 2019 the majority of the UFS-RAQMS NH low bias in CO column was due to an underestimate of biomass burning CO emissions. The impact of emissions increases from biomass burning on CO, NO_2, and ethane is proportional to the magnitude of the change in emissions, as UFS-RAQMS forecasts of these constituents increased by a larger percent in the Siberia and maritime continent regions than the other regions. Increased biomass burning emissions increased tropospheric ozone columns by >4% in the smoke plume. Boreal biomass burning produced less O_3 enhancement than tropical biomass burning, likely due to the decreased photolysis in the high latitudes relative to the tropics and faster photochemistry in the tropics (e.g. Natarajan et al., 2012). Surface O_3 enhancements due to the adjusted biomass burning emissions in the tropics were >5 ppbv and ∼4 ppbv in Siberia. The results of the UFS-RAQMS adjusted emissions experiment contribute to the consensus that uncertainties in biomass burning emissions has a significant impact on CTM forecasts.

7.2 Future Work

In this dissertation the RAQMS-Aura chemical reanalysis and UFS-RAQMS model were used to show that biomass burning emissions have significant impacts on global atmospheric composition. Composite analysis, EOF analysis, and linear regression were applied to the RAQMS-Aura chemical reanalysis to show that variability in tropical convection and Indonesian biomass burning emissions contribute to observed El Niño Southern Oscillation (ENSO) variability in tropical tropospheric ozone. Experiments using the UFS-RAQMS model and GBBEPx CO emissions showed that high uncertainty in both tropical and boreal biomass burning emissions can result in a ∼5-10% uncertainty in tropospheric ozone forecasts. The UFS-RAQMS experiments also showed that the low bias in CO in global models is predominantly due to underestimation of biomass burning emissions. In a changing climate where boreal biomass burning becomes more frequent, improved predictions of biomass burning emissions are necessary for providing accurate air quality forecasts.

Additional analysis of the UFS-RAQMS adjusted emissions experiment will be done, investigating the impact of the adjusted emissions on the smoke plumes in greater detail than done in this work. This work analyzed the GBBEPx emissions during a year where there was not significant biomass burning in North America. Future studies should evaluate the performance of global models using GBBEPx CO emissions during years with high fire activity in North America such as 2020 or 2023 in order to obtain a better sense of the uncertainty in GBBEPx CO emissions from North American biomass burning, as well as estimates of the impact on tropospheric ozone concentrations in North America.

Appendix A

Supplemental Material for Chapter 3

A.1 Influence of the QBO on RAQMS-Aura upper tropospheric ozone

It has been suggested by prior studies (Chandra et al., 2002, Lee et al., 2010, Oman et al., 2013, Ziemke and Chandra, 2012, eg) that tropical upper troposphere ozone is impacted by the QBO. Here I 1) confirm the presence of a QBO in RAQMS-Aura, 2) evaluate the response of the tropical ozone profile to the QBO, and 3) compare the magnitude of the tropospheric ozone QBO response to the tropospheric ozone ENSO response.

Due to the re-initialization of RAQMS-Aura meteorology with archived NCEP GDAS analyses at 6-hour intervals, a QBO signature is present in the analysis (Figure A.1) in spite of the relatively coarse vertical resolution in the stratosphere. A similar ozone QBO

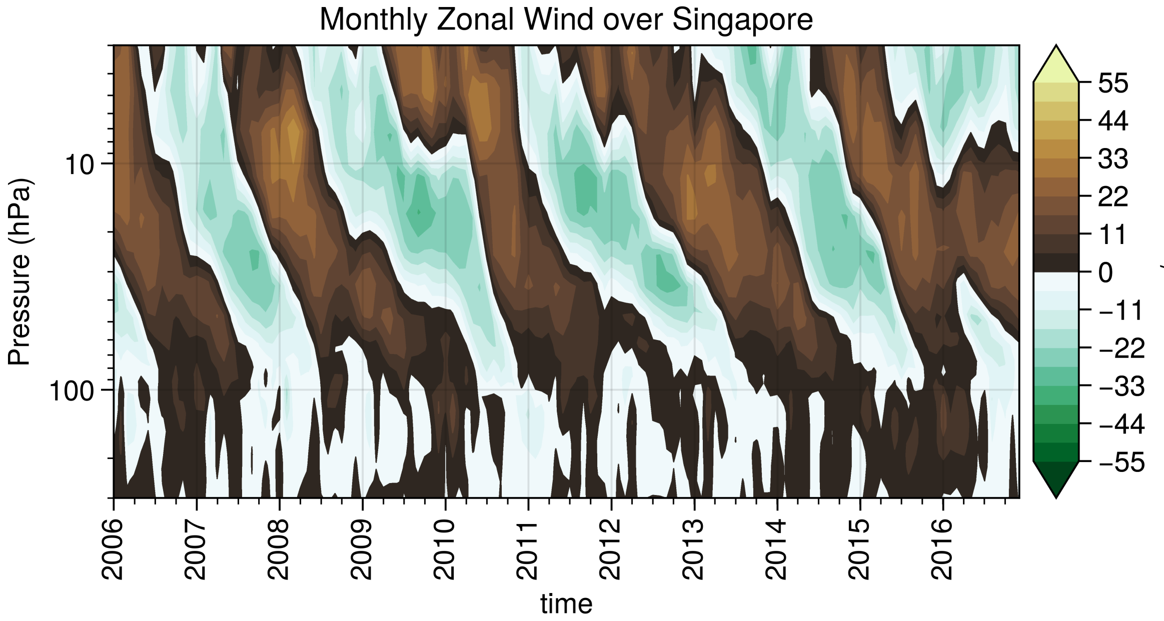

FIGURE A.1: Deseasonalized RAQMS-Aura monthly zonal wind over Singapore.

feature is present in RAQMS-Aura due to the assimilation of Microwave Limb Sounder (MLS) stratospheric ozone profiles. I calculate QBO EOFs from the monthly mean zonal winds over Singapore (1°N, 104°E) from 70 to 10hPa (Wallace et al., 1993). The RAQMS-Aura QBO PCs are compared to QBO coefficients available from the NASA Atmospheric Chemistry and Dynamics Laboratory QBO website (`https://acd-ext.gsfc.nasa.gov/Data_services/met/qbo/qbo.html`) (Figure A.2). The RAQMS-Aura QBO PCs and NASA QBO coefficients agree well, signifying that RAQMS-Aura has a realistic QBO zonal mean zonal wind signature.

Following Oman et al. (2013) I fit the multiple linear regression $\Delta O_3(t) = \sum w_{x_j} \Delta X_j(t) + \varepsilon(t)$ for the 2006-2016 period. X_j are the Nino 3.4 index, QBO PC_1, and QBO PC_2; ΔO_3 is the deseasonalized RAQMS-Aura ozone mixing ratio at 100 hPa over the equator averaged over 180°W - 110°W; w_{x_j} and ε are the regression coefficients. The regression

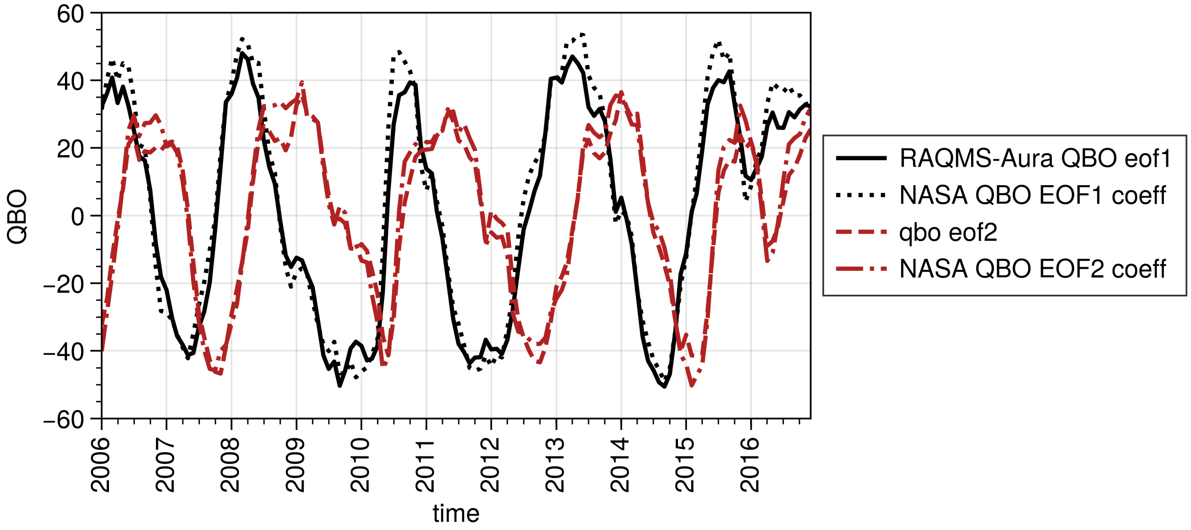

Figure A.2: Time series of the first (black) and second (red) QBO EOFs from 2006-2016 from RAQMS-Aura (solid) and NASA Atmospheric Chemistry and Dynamics Laboratory QBO website (`https://acd-ext.gsfc.nasa.gov/Data_services/met/qbo/qbo.html`) (dashed).

fit is shown in Figure A.3a and should be compared to Figure 2 in Oman et al. (2013). The individual contributions to the regression are shown in Figure A.3b. The obtained fit is not directly comparable to that obtained from MLS data by Oman et al. (2013) as my regression is fit over a different time period. Despite these differences, I find the magnitude of the QBO contributions to the regression fit to be relatively small compared to the ENSO contribution, which is consistent with Oman et al. (2013). From this, I conclude that the QBO has a slight impact on interannual variability in the tropical upper troposphere but this impact is generally small relative to the ENSO impact on the region.

(a) Deaseaonalized RAQMS-Aura, 100 hPa 0°N, 180°W - 110°W

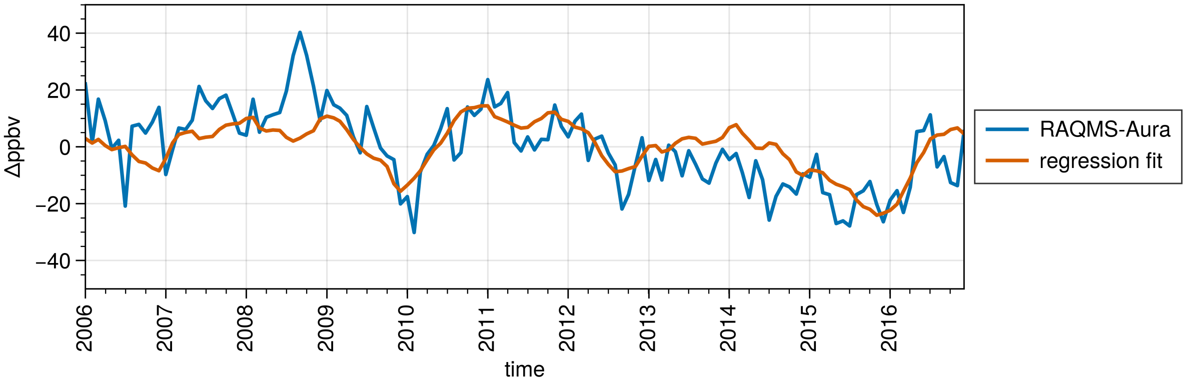

(b) Contribution to regression fit

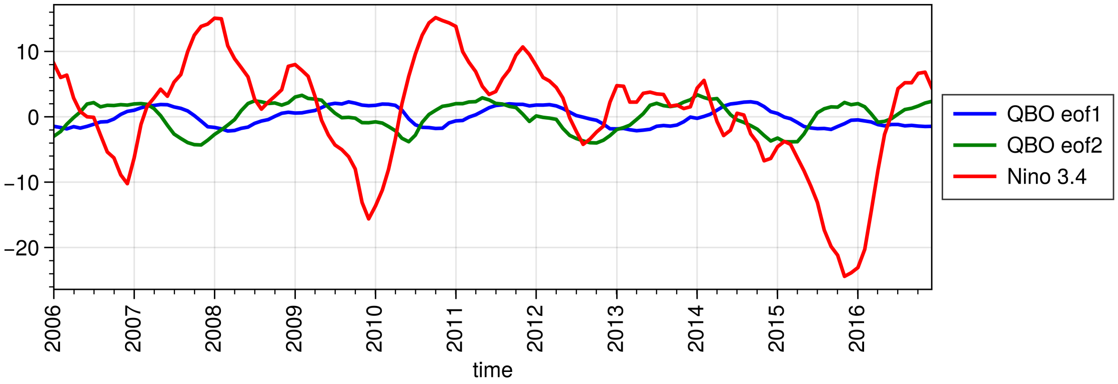

FIGURE A.3: a) Deseasonalized RAQMS-Aura ozone anomaly at 100 hPa over the equator averaged over 180°W - 110°W and reconstructed from multiple linear regression. b) Contribution to the regression of the Nino 3.4 index, RAQMS-Aura QBO PC_1, and RAQMS-Aura QBO PC_2.

A.2 October ENSO Anomaly composites

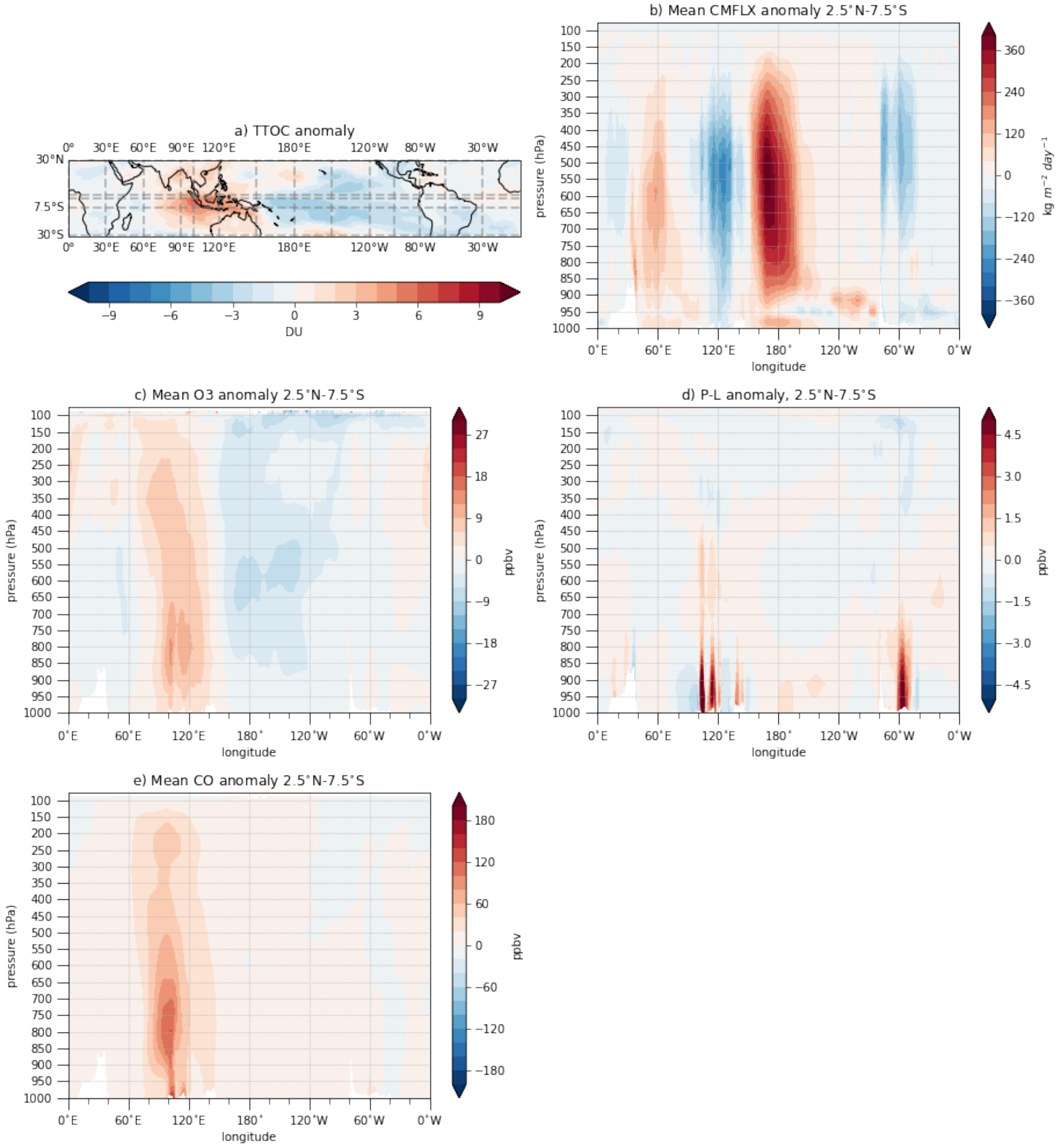

Figure A.4: RAQMS-Aura October ENSO a) TTOC anomaly, b) convective mass flux anomaly, and c) tropospheric ozone profile anomaly, d) P-L, e) CO.

Appendix B

Supplementary figure for Chaper 5

Reproduced here is a land cover map for Indonesia from Xin et al. (2021).

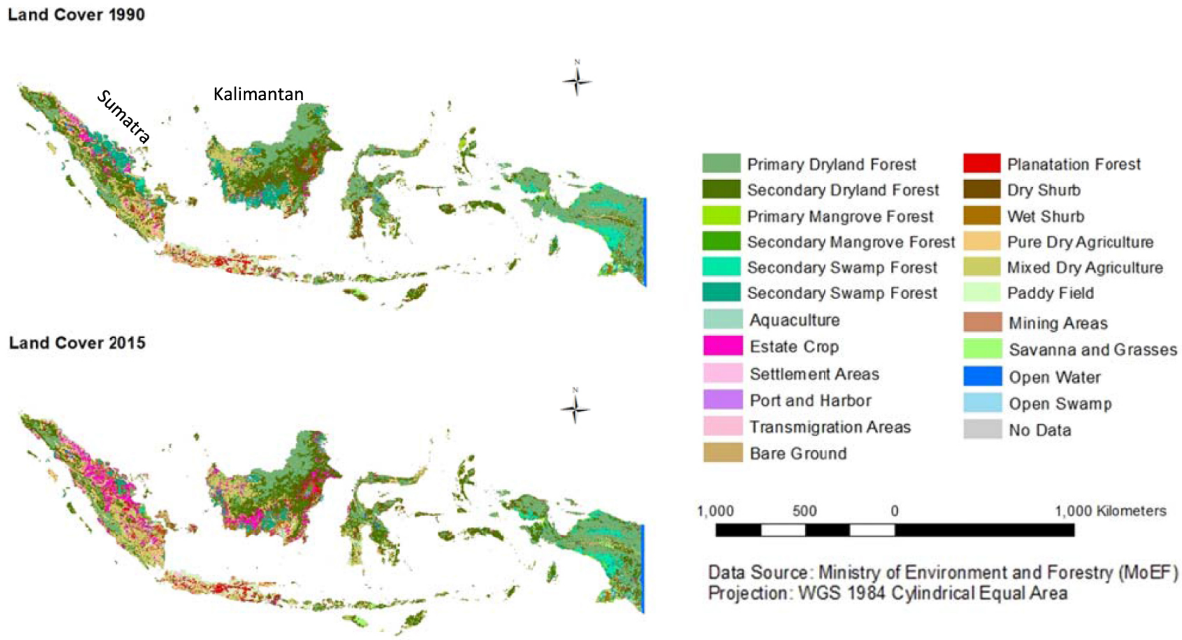

Data Source: Ministry of Environment and Forestry (MoEF)
Projection: WGS 1984 Cylindrical Equal Area

Figure B.1: Land cover maps of Indonesia from Xin et al. (2021).

Bibliography

Abatzoglou, J. T. and A. P. Williams, 2016: Impact of anthropogenic climate change on wildfire across western US forests. *Proceedings of the National Academy of Sciences*, **113**, 11770–11775, doi:10.1073/pnas.1607171113.

Akagi, S. K., R. J. Yokelson, C. Wiedinmyer, M. J. Alvarado, J. S. Reid, T. Karl, J. D. Crounse, and P. O. Wennberg, 2011: Emission factors for open and domestic biomass burning for use in atmospheric models. *Atmospheric Chemistry and Physics*, **11**, 4039–4072, doi:10.5194/ACP-11-4039-2011.

Al-Saadi, J., A. Soja, R. B. Pierce, J. Szykman, C. Wiedinmyer, L. Emmons, S. Kondragunta, X. Zhang, C. Kittaka, T. Schaack, and K. Bowman, 2008: Intercomparison of near-real-time biomass burning emissions estimates constrained by satellite fire data. doi:10.1117/1.2948785.

Andela, N., D. C. Morton, L. Giglio, Y. Chen, G. R. van der Werf, P. S. Kasibhatla, R. S. DeFries, G. J. Collatz, S. Hantson, S. Kloster, D. Bachelet, M. Forrest, G. Lasslop, F. Li, S. Mangeon, J. R. Melton, C. Yue, and J. T. Randerson, 2017: A human-driven decline in global burned area. *Science*, **356**, 1356–1362, doi:10.1126/science.aal4108.

Andreae, M. O., 2019: Emission of trace gases and aerosols from biomass burning-an updated assessment. *Atmos. Chem. Phys*, **19**, 8523–8546, doi:10.5194/acp-19-8523-2019.

Andreae, M. O. and P. Merlet, 2001: Emission of trace gases and aerosols from biomass burning. *Global Biogeochemical Cycles*, **15**, 955–966, doi:10.1029/2000GB001382.

Archibald, A. T., J. L. Neu, Y. F. Elshorbany, O. R. Cooper, P. J. Young, H. Akiyoshi, R. A. Cox, M. Coyle, R. G. Derwent, M. Deushi, A. Finco, G. J. Frost, I. E. Galbally, G. Gerosa, C. Granier, P. T. Griffiths, R. Hossaini, L. Hu, P. Jöckel, B. Josse, M. Y. Lin, M. Mertens, O. Morgenstern, M. Naja, V. Naik, S. Oltmans, D. A. Plummer, L. E. Revell, A. Saiz-Lopez, P. Saxena, Y. M. Shin, I. Shahid, D. Shallcross, S. Tilmes, T. Trickl, T. J. Wallington, T. Wang, H. M. Worden, and G. Zeng, 2020: Tropospheric Ozone Assessment Report: A critical review of changes in the tropospheric ozone burden and budget from 1850 to 2100. *Elementa: Science of the Anthropocene*, **8**, 034, doi:10.1525/elementa.2020.034.

Archibald, S., C. E. R. Lehmann, J. L. Gómez-Dans, and R. A. Bradstock, 2013: Defining pyromes and global syndromes of fire regimes. *Proceedings of the National Academy of Sciences*, **110**, 6442–6447, doi:10.1073/pnas.1211466110.

Arellano Jr., A. F., P. G. Hess, D. P. Edwards, and D. Baumgardner, 2010: Constraints on black carbon aerosol distribution from Measurement of Pollution in the Troposphere (MOPITT) CO. *Geophysical Research Letters*, **37**, doi:10.1029/2010GL044416.

Ashok, K., S. K. Behera, S. A. Rao, H. Weng, and T. Yamagata, 2007: El Niño Modoki and its possible teleconnection. *Journal of Geophysical Research: Oceans*, **112**, doi:10.1029/2006JC003798.

Bamston, A. G., M. Chelliah, and S. B. Goldenberg, 1997: Documentation of a highly ENSO-related sst region in the equatorial pacific: Research note. *Atmosphere-Ocean*, **35**, 367–383, doi:10.1080/07055900.1997.9649597.

Barré, J., B. Gaubert, A. F. J. Arellano, H. M. Worden, D. P. Edwards, M. N. Deeter, J. L. Anderson, K. Raeder, N. Collins, S. Tilmes, G. Francis, C. Clerbaux, L. K. Emmons, G. G. Pfister, P.-F. Coheur, and D. Hurtmans, 2015: Assessing the impacts of assimilating IASI and MOPITT CO retrievals using CESM-CAM-chem and DART. *Journal of Geophysical Research: Atmospheres*, **120**, 10,501–10,529, doi:10.1002/2015JD023467.

Bhattacharjee, P. S., L. Zhang, B. Baker, L. Pan, R. Montuoro, G. A. Grell, and J. T. McQueen, 2023: Evaluation of Aerosol Optical Depth Forecasts from NOAA's Global Aerosol Forecast Model (GEFS-Aerosols). *Weather and Forecasting*, **38**, 225–249, doi:10.1175/WAF-D-22-0083.1.

Bian, H., M. Chin, S. R. Kawa, B. Duncan, A. Arellano, and P. Kasibhatla, 2007: Sensitivity of global CO simulations to uncertainties in biomass burning sources. *Journal of Geophysical Research: Atmospheres*, **112**, doi:10.1029/2006JD008376.

Bian, H., M. Chin, S. R. Kawa, H. Yu, T. Diehl, and T. Kucsera, 2010: Multiscale carbon monoxide and aerosol correlations from satellite measurements and the GOCART model: Implication for emissions and atmospheric evolution. *Journal of Geophysical Research: Atmospheres*, **115**, doi:10.1029/2009JD012781.

Bian, H. and M. J. Prather, 2002: Fast-J2: Accurate Simulation of Stratospheric Photolysis in Global Chemical Models. *Journal of Atmospheric Chemistry*, **41**, 281–296, doi:10.1023/A:1014980619462.

Boersma, K. F., H. J. Eskes, J. P. Veefkind, E. J. Brinksma, R. J. van der A, M. Sneep, G. H. J. van den Oord, P. F. Levelt, P. Stammes, J. F. Gleason, and E. J. Bucsela, 2007: Near-real time retrieval of tropospheric NO_2 from OMI. *Atmospheric Chemistry and Physics*, **7**, 2103–2118, doi:10.5194/acp-7-2103-2007.

Borsdorff, T., J. aan de Brugh, A. Schneider, A. Lorente, M. Birk, G. Wagner, R. Kivi, F. Hase, D. G. Feist, R. Sussmann, M. Rettinger, D. Wunch, T. Warneke, and J. Landgraf, 2019: Improving the TROPOMI CO data product: Update of the spectroscopic database and destriping of single orbits. *Atmospheric Measurement Techniques*, **12**, 5443–5455, doi:10.5194/amt-12-5443-2019.

Bourgeois, I., J. Peischl, J. A. Neuman, S. S. Brown, C. R. Thompson, K. C. Aikin, H. M. Allen, H. Angot, E. C. Apel, C. B. Baublitz, J. F. Brewer, P. Campuzano-Jost, R. Commane, J. D. Crounse, B. C. Daube, J. P. DiGangi, G. S. Diskin, L. K. Emmons, A. M. Fiore, G. I. Gkatzelis, A. Hills, R. S. Hornbrook, L. G. Huey, J. L. Jimenez, M. Kim, F. Lacey, K. McKain, L. T. Murray, B. A. Nault, D. D. Parrish, E. Ray, C. Sweeney,

D. Tanner, S. C. Wofsy, and T. B. Ryerson, 2021: Large contribution of biomass burning emissions to ozone throughout the global remote troposphere. *Proceedings of the National Academy of Sciences*, **118**, e2109628118, doi:10.1073/pnas.2109628118.

Bruckner, M., R. B. Pierce, and A. Lenzen, 2024: Examining ENSO related variability in tropical tropospheric ozone in the RAQMS-Aura chemical reanalysis. *EGUsphere*, 1–33, doi:10.5194/egusphere-2024-1178.

Buchholz, R. R., H. M. Worden, M. Park, G. Francis, M. N. Deeter, D. P. Edwards, L. K. Emmons, B. Gaubert, J. Gille, S. Martínez-Alonso, W. Tang, R. Kumar, J. R. Drummond, C. Clerbaux, M. George, P.-F. Coheur, D. Hurtmans, K. W. Bowman, M. Luo, V. H. Payne, J. R. Worden, M. Chin, R. C. Levy, J. Warner, Z. Wei, and S. S. Kulawik, 2021: Air pollution trends measured from Terra: CO and AOD over industrial, fire-prone, and background regions. *Remote Sensing of Environment*, **256**, 112275, doi:10.1016/j.rse.2020.112275.

Bucsela, E. J., N. A. Krotkov, E. A. Celarier, L. N. Lamsal, W. H. Swartz, P. K. Bhartia, K. F. Boersma, J. P. Veefkind, J. F. Gleason, and K. E. Pickering, 2013: A new stratospheric and tropospheric NO2 retrieval algorithm for nadir-viewing satellite instruments: Applications to OMI. *Atmospheric Measurement Techniques*, **6**, 2607–2626, doi:10.5194/AMT-6-2607-2013.

Chandra, S., J. R. Ziemke, P. K. Bhartia, and R. V. Martin, 2002: Tropical tropospheric ozone: Implications for dynamics and biomass burning. *Journal of Geophysical Research: Atmospheres*, **107**, ACH 3–1–ACH 3–17, doi:10.1029/2001JD000447.

Chandra, S., J. R. Ziemke, B. N. Duncan, T. L. Diehl, N. J. Livesey, and L. Froidevaux, 2009: Effects of the 2006 El Niño on tropospheric ozone and carbon monoxide: Implications for dynamics and biomass burning. *Atmospheric Chemistry and Physics*, **9**, 4239–4249, doi:10.5194/acp-9-4239-2009.

Chandra, S., J. R. Ziemke, W. Min, and W. G. Read, 1998: Effects of 1997–1998 El Niño on tropospheric ozone and water vapor. *Geophysical Research Letters*, **25**, 3867–3870, doi:10.1029/98GL02695.

Chen, D. and A. Dai, 2019: Precipitation Characteristics in the Community Atmosphere Model and Their Dependence on Model Physics and Resolution. *Journal of Advances in Modeling Earth Systems*, **11**, 2352–2374, doi:10.1029/2018MS001536.

Chen, D., A. Dai, and A. Hall, 2021: The Convective-To-Total Precipitation Ratio and the "Drizzling" Bias in Climate Models. *Journal of Geophysical Research: Atmospheres*, **126**, e2020JD034198, doi:10.1029/2020JD034198.

Chen, Y., J. Hall, D. van Wees, N. Andela, S. Hantson, L. Giglio, G. R. van der Werf, D. C. Morton, and J. T. Randerson, 2023: Multi-decadal trends and variability in burned area from the fifth version of the Global Fire Emissions Database (GFED5). *Earth System Science Data*, **15**, 5227–5259, doi:10.5194/essd-15-5227-2023.

Chin, M., P. Ginoux, S. Kinne, O. Torres, B. N. Holben, B. N. Duncan, R. V. Martin, J. A. Logan, A. Higurashi, and T. Nakajima, 2002: Tropospheric Aerosol Optical Thickness from the GOCART Model and Comparisons with Satellite and Sun Photometer Measurements.

Chuvieco, E., F. Mouillot, G. R. van der Werf, J. San Miguel, M. Tanase, N. Koutsias, M. García, M. Yebra, M. Padilla, I. Gitas, A. Heil, T. J. Hawbaker, and L. Giglio, 2019: Historical background and current developments for mapping burned area from satellite Earth observation. *Remote Sensing of Environment*, **225**, 45–64, doi:10.1016/j.rse.2019.02.013.

Clerbaux, C., J. Hadji-Lazaro, D. Hauglustaine, G. Mégie, B. Khattatov, and J.-F. Lamarque, 2001: Assimilation of carbon monoxide measured from satellite in a three-dimensional chemistry-transport model. *Journal of Geophysical Research: Atmospheres*, **106**, 15385–15394, doi:10.1029/2000JD900682.

Cooper, M., R. V. Martin, A. Padmanabhan, and D. K. Henze, 2017: Comparing mass balance and adjoint methods for inverse modeling of nitrogen dioxide columns for global nitrogen oxide emissions. *Journal of Geophysical Research: Atmospheres*, **122**, 4718–4734, doi:10.1002/2016JD025985.

Cottle, P., K. Strawbridge, and I. McKendry, 2014: Long-range transport of Siberian wildfire smoke to British Columbia: Lidar observations and air quality impacts. *Atmospheric Environment*, **90**, 71–77, doi:10.1016/j.atmosenv.2014.03.005.

Crutzen, P. J., L. E. Heidt, J. P. Krasnec, W. H. Pollock, and W. Seiler, 1979: Biomass burning as a source of atmospheric gases CO, H2, N2O, NO, CH3Cl and COS. *Nature*, **282**, 253–256, doi:10.1038/282253a0.

Darmenov, A. and A. da Silva, 2015: The quick fire emissions dataset (QFED): Documentation of versions 2.1, 2.2 and 2.4. *NASA Technical Report Series on Global Modeling and Data Assimilation, NASA TM-2013-104606*, **32**, 183.

De Mazière, M., A. M. Thompson, M. J. Kurylo, J. D. Wild, G. Bernhard, T. Blumenstock, G. O. Braathen, J. W. Hannigan, J.-C. Lambert, T. Leblanc, T. J. McGee, G. Nedoluha, I. Petropavlovskikh, G. Seckmeyer, P. C. Simon, W. Steinbrecht, and S. E. Strahan, 2018: The Network for the Detection of Atmospheric Composition Change (NDACC): History, status and perspectives. *Atmospheric Chemistry and Physics*, **18**, 4935–4964, doi:10.5194/acp-18-4935-2018.

Deeter, M., G. Francis, J. Gille, D. Mao, S. Martínez-Alonso, H. Worden, D. Ziskin, J. Drummond, R. Commane, G. Diskin, and K. McKain, 2022: The MOPITT Version 9 CO product: Sampling enhancements and validation. *Atmospheric Measurement Techniques*, **15**, 2325–2344, doi:10.5194/amt-15-2325-2022.

Deeter, M. N., S. Martínez-Alonso, M. O. Andreae, and H. Schlager, 2018: Satellite-Based Analysis of CO Seasonal and Interannual Variability Over the Amazon Basin. *Journal of Geophysical Research: Atmospheres*, **123**, 5641–5656, doi:10.1029/2018JD028425.

Descombes, G., T. Auligné, F. Vandenberghe, D. M. Barker, and J. Barré, 2015: Generalized background error covariance matrix model (GEN_BE v2.0). *Geoscientific Model Development*, **8**, 669–696, doi:10.5194/gmd-8-669-2015.

DiGangi, J. P., Y. Choi, J. B. Nowak, H. S. Halliday, G. S. Diskin, S. Feng, Z. R. Barkley, T. Lauvaux, S. Pal, K. J. Davis, B. C. Baier, and C. Sweeney, 2021: Seasonal Variability in Local Carbon Dioxide Biomass Burning Sources Over Central and Eastern US Using Airborne In Situ Enhancement Ratios. *Journal of Geophysical Research: Atmospheres*, **126**, e2020JD034525, doi:10.1029/2020JD034525.

Doherty, R. M., D. S. Stevenson, C. E. Johnson, W. J. Collins, and M. G. Sanderson, 2006: Tropospheric ozone and El Niño–Southern Oscillation: Influence of atmospheric dynamics, biomass burning emissions, and future climate change. *Journal of Geophysical Research: Atmospheres*, **111**, doi:10.1029/2005JD006849.

Duncan, B. N., R. V. Martin, A. C. Staudt, R. Yevich, and J. A. Logan, 2003: Interannual and seasonal variability of biomass burning emissions constrained by satellite observations. *Journal of Geophysical Research: Atmospheres*, **108**, ACH 1–1–ACH 1–22, doi:10.1029/2002JD002378.

East, J. D., B. H. Henderson, S. L. Napelenok, S. N. Koplitz, G. Sarwar, R. Gilliam, A. Lenzen, D. Q. Tong, R. B. Pierce, and F. Garcia-Menendez, 2022: Inferring and evaluating satellite-based constraints on NO $_x$ emissions estimates in air quality simulations. *Atmospheric Chemistry and Physics*, **22**, 15981–16001, doi:10.5194/acp-22-15981-2022.

Eck, T. F., B. N. Holben, J. S. Reid, A. Sinyuk, D. M. Giles, A. Arola, I. Slutsker, J. S. Schafer, M. G. Sorokin, A. Smirnov, A. D. LaRosa, J. Kraft, E. A. Reid, N. T. O'Neill, E. J. Welton, and A. R. Menendez, 2023: The extreme forest fires in California/Oregon in 2020: Aerosol optical and physical properties and comparisons of aged versus fresh smoke. *Atmospheric Environment*, **305**, 119798, doi:10.1016/j.atmosenv.2023.119798.

Eckman, R. S., W. L. Grose, R. E. Turner, W. T. Blackshear, J. M. Russell III, L. Froidevaux, J. W. Waters, J. B. Kumer, and A. E. Roche, 1995: Stratospheric trace constituents simulated by a three-dimensional general circulation model: Comparison with UARS data. *Journal of Geophysical Research: Atmospheres*, **100**, 13951–13966, doi:10.1029/95JD01278.

Edwards, D. P., L. K. Emmons, J. C. Gille, A. Chu, J.-L. Attié, L. Giglio, S. W. Wood, J. Haywood, M. N. Deeter, S. T. Massie, D. C. Ziskin, and J. R. Drummond, 2006: Satellite-observed pollution from Southern Hemisphere biomass burning. *Journal of Geophysical Research: Atmospheres*, **111**, doi:10.1029/2005JD006655.

Edwards, D. P., L. K. Emmons, D. A. Hauglustaine, D. A. Chu, J. C. Gille, Y. J. Kaufman, G. Pétron, L. N. Yurganov, L. Giglio, M. N. Deeter, V. Yudin, D. C. Ziskin, J. Warner, J.-F. Lamarque, G. L. Francis, S. P. Ho, D. Mao, J. Chen, E. I. Grechko, and J. R. Drummond, 2004: Observations of carbon monoxide and aerosols from the Terra satellite: Northern Hemisphere variability. *Journal of Geophysical Research: Atmospheres*, **109**, doi:10.1029/2004JD004727.

Emmons, L. K., M. N. Deeter, J. C. Gille, D. P. Edwards, J.-L. Attié, J. Warner, D. Ziskin, G. Francis, B. Khattatov, V. Yudin, J.-F. Lamarque, S.-P. Ho, D. Mao, J. S. Chen, J. Drummond, P. Novelli, G. Sachse, M. T. Coffey, J. W. Hannigan, C. Gerbig, S. Kawakami, Y. Kondo, N. Takegawa, H. Schlager, J. Baehr, and H. Ziereis, 2004: Validation of Measurements of Pollution in the Troposphere (MOPITT) CO retrievals with aircraft in situ profiles. *Journal of Geophysical Research: Atmospheres*,

109, doi:10.1029/2003JD004101.

Field, R. D., G. R. van der Werf, T. Fanin, E. J. Fetzer, R. Fuller, H. Jethva, R. Levy, N. J. Livesey, M. Luo, O. Torres, and H. M. Worden, 2016: Indonesian fire activity and smoke pollution in 2015 show persistent nonlinear sensitivity to El Niño-induced drought. *Proceedings of the National Academy of Sciences*, **113**, 9204–9209, doi:10.1073/pnas.1524888113.

Fishman, J. and A. E. Balok, 1999: Calculation of daily tropospheric ozone residuals using TOMS and empirically improved SBUV measurements: Application to an ozone pollution episode over the eastern United States. *Journal of Geophysical Research: Atmospheres*, **104**, 30319–30340, doi:10.1029/1999JD900875.

Fishman, J., J. K. Creilson, A. E. Wozniak, and P. J. Crutzen, 2005: Interannual variability of stratospheric and tropospheric ozone determined from satellite measurements. *Journal of Geophysical Research: Atmospheres*, **110**, doi:10.1029/2005JD005868.

Fishman, J., K. Fakhruzzaman, B. Cros, and D. Nganga, 1991: Identification of widespread pollution in the southern hemisphere deduced from satellite analyses. *Science (New York, N.Y.)*, **252**, 1693–6, doi:10.1126/science.252.5013.1693.

Fishman, J., J. M. Hoell Jr., R. D. Bendura, R. J. McNeal, and V. W. J. H. Kirchhoff, 1996: NASA GTE TRACE A experiment (September–October 1992): Overview. *Journal of Geophysical Research: Atmospheres*, **101**, 23865–23879, doi:10.1029/96JD00123.

Fishman, J. and J. C. Larsen, 1987: Distribution of total ozone and stratospheric ozone in the tropics: Implications for the distribution of tropospheric ozone. *Journal of Geophysical Research: Atmospheres*, **92**, 6627–6634, doi:10.1029/JD092iD06p06627.

Fishman, J., C. E. Watson, J. C. Larsen, and J. A. Logan, 1990: Distribution of tropospheric ozone determined from satellite data. *Journal of Geophysical Research: Atmospheres*, **95**, 3599–3617, doi:10.1029/JD095iD04p03599.

Fishman, J., A. E. Wozniak, and J. K. Creilson, 2003: Global distribution of tropospheric ozone from satellite measurements using the empirically corrected tropospheric ozone residual technique: Identification of the regional aspects of air pollution. *Atmospheric Chemistry and Physics*, **3**, 893–907, doi:10.5194/acp-3-893-2003.

Froidevaux, L., Y. B. Jiang, A. Lambert, N. J. Livesey, W. G. Read, J. W. Waters, E. V. Browell, J. W. Hair, M. A. Avery, T. J. McGee, L. W. Twigg, G. K. Sumnicht, K. W. Jucks, J. J. Margitan, B. Sen, R. A. Stachnik, G. C. Toon, P. F. Bernath, C. D. Boone, K. A. Walker, M. J. Filipiak, R. S. Harwood, R. A. Fuller, G. L. Manney, M. J. Schwartz, W. H. Daffer, B. J. Drouin, R. E. Cofield, D. T. Cuddy, R. F. Jarnot, B. W. Knosp, V. S. Perun, W. V. Snyder, P. C. Stek, R. P. Thurstans, and P. A. Wagner, 2008: Validation of Aura Microwave Limb Sounder stratospheric ozone measurements. *Journal of Geophysical Research: Atmospheres*, **113**, doi:10.1029/2007JD008771@10.1002/(ISSN)2169-8996.AURA1.

Galanter, M., H. Levy II, and G. R. Carmichael, 2000: Impacts of biomass burning on tropospheric CO, NO , and O3. *Journal of Geophysical Research: Atmospheres*, **105**, 6633–6653, doi:10.1029/1999JD901113.

Gaubert, B., D. P. Edwards, J. L. Anderson, A. F. Arellano, J. Barré, R. R. Buchholz, S. Darras, L. K. Emmons, D. Fillmore, C. Granier, J. W. Hannigan, I. Ortega, K. Raeder, A. Soulié, W. Tang, H. M. Worden, and D. Ziskin, 2023: Global Scale Inversions from MOPITT CO and MODIS AOD. *Remote Sensing*, **15**, 4813, doi:10.3390/rs15194813.

Gaubert, B., L. K. Emmons, K. Raeder, S. Tilmes, K. Miyazaki, A. F. Arellano Jr., N. Elguindi, C. Granier, W. Tang, J. Barré, H. M. Worden, R. R. Buchholz, D. P. Edwards, P. Franke, J. L. Anderson, M. Saunois, J. Schroeder, J.-H. Woo, I. J. Simpson, D. R. Blake, S. Meinardi, P. O. Wennberg, J. Crounse, A. Teng, M. Kim, R. R. Dickerson, H. He, X. Ren, S. E. Pusede, and G. S. Diskin, 2020: Correcting model biases of CO in East Asia: Impact on oxidant distributions during KORUS-AQ. *Atmospheric Chemistry and Physics*, **20**, 14617–14647, doi:10.5194/acp-20-14617-2020.

Gkatzelis, G. I., M. M. Coggon, C. E. Stockwell, R. S. Hornbrook, H. Allen, E. C. Apel, M. M. Bela, D. R. Blake, I. Bourgeois, S. S. Brown, P. Campuzano-Jost, J. M. St. Clair, J. H. Crawford, J. D. Crounse, D. A. Day, J. P. DiGangi, G. S. Diskin, A. Fried, J. B. Gilman, H. Guo, J. W. Hair, H. S. Halliday, T. F. Hanisco, R. Hannun, A. Hills, L. G. Huey, J. L. Jimenez, J. M. Katich, A. Lamplugh, Y. R. Lee, J. Liao, J. Lindaas, S. A. McKeen, T. Mikoviny, B. A. Nault, J. A. Neuman, J. B. Nowak, D. Pagonis, J. Peischl, A. E. Perring, F. Piel, P. S. Rickly, M. A. Robinson, A. W. Rollins, T. B. Ryerson, M. K. Schueneman, R. H. Schwantes, J. P. Schwarz, K. Sekimoto, V. Selimovic, T. Shingler,

D. J. Tanner, L. Tomsche, K. T. Vasquez, P. R. Veres, R. Washenfelder, P. Weibring, P. O. Wennberg, A. Wisthaler, G. M. Wolfe, C. C. Womack, L. Xu, K. Ball, R. J. Yokelson, and C. Warneke, 2024: Parameterizations of US wildfire and prescribed fire emission ratios and emission factors based on FIREX-AQ aircraft measurements. *Atmospheric Chemistry and Physics*, **24**, 929–956, doi:10.5194/acp-24-929-2024.

Hack, J. J., 1994: Parameterization of moist convection in the National Center for Atmospheric Research community climate model (CCM2). *Journal of Geophysical Research: Atmospheres*, **99**, 5551–5568, doi:10.1029/93JD03478.

Haines, D. A., 1989: A lower atmosphere severity index for wildlife fires. *National Weather Digest*, **13**, 23–27.

Harris, L. M. and S. J. Lin, 2013: A two-way nested global-regional dynamical core on the cubed-sphere grid. *Monthly Weather Review*, **141**, 283–306, doi:10.1175/MWR-D-11-00201.1.

Holloway, T., H. Levy II, and P. Kasibhatla, 2000: Global distribution of carbon monoxide. *Journal of Geophysical Research: Atmospheres*, **105**, 12123–12147, doi:10.1029/1999JD901173.

Hou, X., B. Zhu, D. Fei, X. Zhu, H. Kang, and D. Wang, 2016: Simulation of tropical tropospheric ozone variation from 1982 to 2010: The meteorological impact of two types of ENSO event. *Journal of Geophysical Research: Atmospheres*, **121**, 9220–9236, doi:10.1002/2016JD024945.

Hua, W., S. Lou, X. Huang, L. Xue, K. Ding, Z. Wang, and A. Ding, 2024: Diagnosing uncertainties in global biomass burning emission inventories and their impact on modeled air pollutants. *Atmospheric Chemistry and Physics*, **24**, 6787–6807, doi:10.5194/acp-24-6787-2024.

Huffman, G. J., D. T. Bolvin, E. J. Nelkin, D. B. Wolff, R. F. Adler, G. Gu, Y. Hong, K. P. Bowman, and E. F. Stocker, 2007: The TRMM Multisatellite Precipitation Analysis (TMPA): Quasi-Global, Multiyear, Combined-Sensor Precipitation Estimates at Fine Scales. *Journal of Hydrometeorology*, **8**, 38–55, doi:10.1175/JHM560.1.

Huijnen, V., K. Miyazaki, J. Flemming, A. Inness, T. Sekiya, and M. G. Schultz, 2020: An intercomparison of tropospheric ozone reanalysis products from CAMS, CAMS interim, TCR-1, and TCR-2. *Geoscientific Model Development*, **13**, 1513–1544, doi:10.5194/gmd-13-1513-2020.

Hyer, E. J. and J. S. Reid, 2009: Baseline uncertainties in biomass burning emission models resulting from spatial error in satellite active fire location data. *Geophysical Research Letters*, **36**, doi:10.1029/2008GL036767.

Inness, A., I. Aben, M. Ades, T. Borsdorff, J. Flemming, L. Jones, J. Landgraf, B. Langerock, P. Nedelec, M. Parrington, and R. Ribas, 2022a: Assimilation of S5P/TROPOMI carbon monoxide data with the global CAMS near-real-time system. *Atmospheric Chemistry and Physics*, **22**, 14355–14376, doi:10.5194/acp-22-14355-2022.

Inness, A., M. Ades, A. Agustí-Panareda, J. Barré, A. Benedictow, A.-M. Blechschmidt, J. J. Dominguez, R. Engelen, H. Eskes, J. Flemming, V. Huijnen, L. Jones, Z. Kipling,

S. Massart, M. Parrington, V.-H. Peuch, M. Razinger, S. Remy, M. Schulz, and M. Suttie, 2019: The CAMS reanalysis of atmospheric composition. *Atmospheric Chemistry and Physics*, **19**, 3515–3556, doi:10.5194/acp-19-3515-2019.

Inness, A., M. Ades, D. Balis, D. Efremenko, J. Flemming, P. Hedelt, M. E. Koukouli, D. Loyola, and R. Ribas, 2022b: Evaluating the assimilation of S5P/TROPOMI near real-time SO2columns and layer height data into the CAMS integrated forecasting system (CY47R1), based on a case study of the 2019 Raikoke eruption. *Geoscientific Model Development*, **15**, 971–994, doi:10.5194/GMD-15-971-2022.

Inness, A., A. Benedetti, J. Flemming, V. Huijnen, J. W. Kaiser, M. Parrington, and S. Remy, 2015a: The ENSO signal in atmospheric composition fields: Emission-driven versus dynamically induced changes. *Atmospheric Chemistry and Physics*, **15**, 9083–9097, doi:10.5194/acp-15-9083-2015.

Inness, A., A.-M. Blechschmidt, I. Bouarar, S. Chabrillat, M. Crepulja, R. J. Engelen, H. Eskes, J. Flemming, A. Gaudel, F. Hendrick, V. Huijnen, L. Jones, J. Kapsomenakis, E. Katragkou, A. Keppens, B. Langerock, M. de Mazière, D. Melas, M. Parrington, V. H. Peuch, M. Razinger, A. Richter, M. G. Schultz, M. Suttie, V. Thouret, M. Vrekoussis, A. Wagner, and C. Zerefos, 2015b: Data assimilation of satellite-retrieved ozone, carbon monoxide and nitrogen dioxide with ECMWF's Composition-IFS. *Atmospheric Chemistry and Physics*, **15**, 5275–5303, doi:10.5194/acp-15-5275-2015.

Jaffe, D., I. Bertschi, L. Jaeglé, P. Novelli, J. S. Reid, H. Tanimoto, R. Vingarzan, and D. L. Westphal, 2004: Long-range transport of Siberian biomass burning emissions and impact on surface ozone in western North America. *Geophysical Research Letters*, **31**, doi:10.1029/2004GL020093.

Jaffe, D. A. and N. L. Wigder, 2012: Ozone production from wildfires: A critical review. *Atmospheric Environment*, **51**, 1–10, doi:10.1016/j.atmosenv.2011.11.063.

Jiang, Z., J. R. Worden, H. Worden, M. Deeter, D. B. A. Jones, A. F. Arellano, and D. K. Henze, 2017: A 15-year record of CO emissions constrained by MOPITT CO observations. *Atmospheric Chemistry and Physics*, **17**, 4565–4583, doi:10.5194/acp-17-4565-2017.

Johnson, M. S., K. Strawbridge, K. E. Knowland, C. Keller, and M. Travis, 2021: Long-range transport of Siberian biomass burning emissions to North America during FIREX-AQ. *Atmospheric Environment*, **252**, 118241, doi:10.1016/J.ATMOSENV.2021.118241.

Jolly, W. M., M. A. Cochrane, P. H. Freeborn, Z. A. Holden, T. J. Brown, G. J. Williamson, and D. M. J. S. Bowman, 2015: Climate-induced variations in global wildfire danger from 1979 to 2013. *Nature Communications*, **6**, 7537, doi:10.1038/ncomms8537.

Jones, M. W., J. T. Abatzoglou, S. Veraverbeke, N. Andela, G. Lasslop, M. Forkel, A. J. Smith, C. Burton, R. A. Betts, G. R. van der Werf, S. Sitch, J. G. Canadell, C. Santín, C. Kolden, S. H. Doerr, and C. Le Quéré, 2022: Global and Regional Trends and Drivers of Fire Under Climate Change. *Reviews of Geophysics*, **60**, e2020RG000726, doi:10.1029/2020RG000726.

Kaiser, J. W., A. Heil, M. O. Andreae, A. Benedetti, N. Chubarova, L. Jones, J. J. Morcrette, M. Razinger, M. G. Schultz, M. Suttie, and G. R. Van Der Werf, 2012: Biomass burning emissions estimated with a global fire assimilation system based on observed fire radiative power. *Biogeosciences*, **9**, 527–554, doi:10.5194/BG-9-527-2012.

Kiehl, J. T., J. J. Hack, G. B. Bonan, B. A. Boville, D. L. Williamson, and P. J. Rasch, 1998: The National Center for Atmospheric Research Community Climate Model: CCM3. *Journal of Climate*, **11**, 1131–1149, doi:10.1175/1520-0442(1998)011¡1131:TNCFAR¿2.0.CO;2.

Kiely, L., D. V. Spracklen, C. Wiedinmyer, L. Conibear, C. L. Reddington, S. Archer-Nicholls, D. Lowe, S. R. Arnold, C. Knote, M. F. Khan, M. T. Latif, M. Kuwata, S. H. Budisulistiorini, and L. Syaufina, 2019: New estimate of particulate emissions from Indonesian peat fires in 2015. *Atmospheric Chemistry and Physics*, **19**, 11105–11121, doi:10.5194/acp-19-11105-2019.

Kim, S. T. and J.-Y. Yu, 2012: The two types of ENSO in CMIP5 models. *Geophysical Research Letters*, **39**, doi:10.1029/2012GL052006.

Kleist, D. T., D. F. Parrish, J. C. Derber, R. Treadon, W.-S. Wu, and S. Lord, 2009: Introduction of the GSI into the NCEP Global Data Assimilation System. *Weather and Forecasting*, **24**, 1691–1705, doi:10.1175/2009WAF2222201.1.

Lamarque, J.-F. and J. C. Gille, 2003: Improving the modeling of error variance evolution in the assimilation of chemical species: Application to MOPITT data. *Geophysical Research Letters*, **30**, doi:10.1029/2003GL016994.

Lamarque, J.-F., B. V. Khattatov, J. C. Gille, and G. P. Brasseur, 1999: Assimilation of Measurement of Air Pollution from Space (MAPS) CO in a global three-dimensional model. *Journal of Geophysical Research: Atmospheres*, **104**, 26209–26218, doi:10.1029/1999JD900807.

Lamsal, L. N., R. V. Martin, A. Padmanabhan, A. Van Donkelaar, Q. Zhang, C. E. Sioris, K. Chance, T. P. Kurosu, and M. J. Newchurch, 2011: Application of satellite observations for timely updates to global anthropogenic NOx emission inventories. *Geophysical Research Letters*, **38**, doi:10.1029/2010GL046476.

Larkin, N. K. and D. E. Harrison, 2005: On the definition of El Niño and associated seasonal average U.S. weather anomalies. *Geophysical Research Letters*, **32**, doi:10.1029/2005GL022738.

Lee, S., D. M. Shelow, A. M. Thompson, and S. K. Miller, 2010: QBO and ENSO variability in temperature and ozone from SHADOZ, 1998–2005. *Journal of Geophysical Research: Atmospheres*, **115**, doi:10.1029/2009JD013320.

Lee, T. and M. J. McPhaden, 2010: Increasing intensity of El Niño in the central-equatorial Pacific. *Geophysical Research Letters*, **37**, doi:10.1029/2010GL044007.

Lewis, A. C., M. J. Evans, J. R. Hopkins, S. Punjabi, K. A. Read, R. M. Purvis, S. J. Andrews, S. J. Moller, L. J. Carpenter, J. D. Lee, A. R. Rickard, P. I. Palmer, and M. Parrington, 2013: The influence of biomass burning on the global distribution of selected non-methane organic compounds. *Atmospheric Chemistry and Physics*, **13**, 851–867, doi:10.5194/ACP-13-851-2013.

Li, Y., D. Tong, S. Ma, X. Zhang, S. Kondragunta, F. Li, and R. Saylor, 2021: Dominance of Wildfires Impact on Air Quality Exceedances During the 2020 Record-Breaking Wildfire Season in the United States. *Geophysical Research Letters*, **48**, doi:10.1029/2021GL094908.

Lindaas, J., I. B. Pollack, L. A. Garofalo, M. A. Pothier, D. K. Farmer, S. M. Kreidenweis, T. L. Campos, F. Flocke, A. J. Weinheimer, D. D. Montzka, G. S. Tyndall, B. B. Palm, Q. Peng, J. A. Thornton, W. Permar, C. Wielgasz, L. Hu, R. D. Ottmar, J. C. Restaino, A. T. Hudak, I.-T. Ku, Y. Zhou, B. C. Sive, A. Sullivan, J. L. Collett Jr, and E. V. Fischer, 2021: Emissions of Reactive Nitrogen From Western U.S. Wildfires During Summer 2018. *Journal of Geophysical Research: Atmospheres*, **126**, e2020JD032657, doi:10.1029/2020JD032657.

Liu, Y. and A. Ding, 2024: Contrasting trends of carbon emission from savanna and boreal forest fires during 1999–2022. *Meteorological Applications*, **31**, e2177, doi:10.1002/met.2177.

Liu, Y., Y. Liu, J. Fu, C.-E. Yang, X. Dong, H. Tian, B. Tao, J. Yang, Y. Wang, Y. Zou, and Z. Ke, 2021: Projection of future wildfire emissions in western USA under climate change: Contributions from changes in wildfire, fuel loading and fuel moisture. *International Journal of Wildland Fire*, **31**, 1–13, doi:10.1071/WF20190.

Lobert, J. M., W. C. Keene, J. A. Logan, and R. Yevich, 1999: Global chlorine emissions from biomass burning: Reactive Chlorine Emissions Inventory. *Journal of Geophysical Research: Atmospheres*, **104**, 8373–8389, doi:10.1029/1998JD100077.

Logan, J. A., M. J. Prather, S. C. Wofsy, and M. B. McElroy, 1981: Tropospheric chemistry: A global perspective. *Journal of Geophysical Research*, **86**, 7210–7254, doi:10.1029/JC086iC08p07210.

Lutsch, E., K. Strong, D. B. A. Jones, T. Blumenstock, S. Conway, J. A. Fisher, J. W. Hannigan, F. Hase, Y. Kasai, E. Mahieu, M. Makarova, I. Morino, T. Nagahama, J. Notholt, I. Ortega, M. Palm, A. V. Poberovskii, R. Sussmann, and T. Warneke, 2020: Detection and attribution of wildfire pollution in the Arctic and northern mid-latitudes using a network of Fourier-transform infrared spectrometers and GEOS-Chem. *Atmospheric Chemistry and Physics*, **20**, 12813–12851, doi:10.5194/acp-20-12813-2020.

Maddy, E. S. and C. D. Barnet, 2008: Vertical Resolution Estimates in Version 5 of AIRS Operational Retrievals. *IEEE Transactions on Geoscience and Remote Sensing*, **46**, 2375–2384, doi:10.1109/TGRS.2008.917498.

Makkaroon, P., D. Q. Tong, Y. Li, E. J. Hyer, P. Xian, S. Kondragunta, P. C. Campbell, Y. Tang, B. D. Baker, M. D. Cohen, A. Darmenov, A. Lyapustin, R. D. Saylor, Y. Wang, and I. Stajner, 2023: Development and Evaluation of a North America Ensemble Wildfire Air Quality Forecast: Initial Application to the 2020 Western United States "Gigafire". *Journal of Geophysical Research: Atmospheres*, **128**, e2022JD037298, doi:10.1029/2022JD037298.

Martin, R. V., D. J. Jacob, K. Chance, T. P. Kurosu, P. I. Palmer, and M. J. Evans, 2003a: Global inventory of nitrogen oxide emissions constrained by space-based observations of NO2 columns. *Journal of Geophysical Research: Atmospheres*, **108**, doi:10.1029/2003JD003453.

Martin, R. V., D. J. Jacob, R. M. Yantosca, M. Chin, and P. Ginoux, 2003b: Global and regional decreases in tropospheric oxidants from photochemical effects of aerosols. *Journal of Geophysical Research: Atmospheres*, **108**, doi:10.1029/2002JD002622.

McDuffie, E. E., S. J. Smith, P. O'Rourke, K. Tibrewal, C. Venkataraman, E. A. Marais, B. Zheng, M. Crippa, M. Brauer, and R. V. Martin, 2020: A global anthropogenic emission inventory of atmospheric pollutants from sector- and fuel-specific sources (1970–2017): An application of the Community Emissions Data System (CEDS). *Earth System Science Data*, **12**, 3413–3442, doi:10.5194/essd-12-3413-2020.

McMillan, W. W., C. Barnet, L. Strow, M. T. Chahine, M. L. McCourt, J. X. Warner, P. C. Novelli, S. Korontzi, E. S. Maddy, and S. Datta, 2005: Daily global maps of carbon monoxide from NASA's Atmospheric Infrared Sounder. *Geophysical Research Letters*, **32**, doi:10.1029/2004GL021821.

McPeters, R., M. Kroon, G. Labow, E. Brinksma, D. Balis, I. Petropavlovskikh, J. P. Veefkind, P. K. Bhartia, and P. F. Levelt, 2008: Validation of the Aura Ozone Monitoring Instrument total column ozone product. *Journal of Geophysical Research: Atmospheres*, **113**, doi:10.1029/2007JD008802.

McPhaden, M. J., S. E. Zebiak, and M. H. Glantz, 2006: ENSO as an Integrating Concept in Earth Science. *Science*, **314**, 1740–1745, doi:10.1126/science.1132588.

Miettinen, J., C. Shi, and S. C. Liew, 2017: Fire Distribution in Peninsular Malaysia, Sumatra and Borneo in 2015 with Special Emphasis on Peatland Fires. *Environmental Management*, **60**, 747–757, doi:10.1007/s00267-017-0911-7.

Miyazaki, K., K. Bowman, T. Sekiya, H. Eskes, F. Boersma, H. Worden, N. Livesey, V. H. Payne, K. Sudo, Y. Kanaya, M. Takigawa, and K. Ogochi, 2020: Updated tropospheric chemistry reanalysis and emission estimates, TCR-2, for 2005–2018. *Earth System Science Data*, **12**, 2223–2259, doi:10.5194/essd-12-2223-2020.

Miyazaki, K., H. J. Eskes, K. Sudo, M. Takigawa, M. van Weele, and K. F. Boersma, 2012: Simultaneous assimilation of satellite NO_2, O_3, CO, and HNO_3 data for the analysis of tropospheric chemical composition and emissions. *Atmospheric Chemistry and Physics*, **12**, 9545–9579, doi:10.5194/acp-12-9545-2012.

Naik, V., A. Voulgarakis, A. M. Fiore, L. W. Horowitz, J.-F. Lamarque, M. Lin, M. J. Prather, P. J. Young, D. Bergmann, P. J. Cameron-Smith, I. Cionni, W. J. Collins, S. B. Dalsøren, R. Doherty, V. Eyring, G. Faluvegi, G. A. Folberth, B. Josse, Y. H. Lee, I. A. MacKenzie, T. Nagashima, T. P. C. van Noije, D. A. Plummer, M. Righi, S. T. Rumbold, R. Skeie, D. T. Shindell, D. S. Stevenson, S. Strode, K. Sudo, S. Szopa, and G. Zeng, 2013: Preindustrial to present-day changes in tropospheric hydroxyl radical and methane lifetime from the Atmospheric Chemistry and Climate Model Intercomparison Project (ACCMIP). *Atmospheric Chemistry and Physics*, **13**, 5277–5298, doi:10.5194/acp-13-5277-2013.

Natarajan, M., R. B. Pierce, T. K. Schaack, A. J. Lenzen, J. A. Al-Saadi, A. J. Soja, T. P. Charlock, F. G. Rose, D. M. Winker, and J. R. Worden, 2012: Radiative forcing due to enhancements in tropospheric ozone and carbonaceous aerosols caused by Asian fires during spring 2008. *Journal of Geophysical Research: Atmospheres*, **117**, doi:10.1029/2011JD016584.

Olsen, M. A., K. Wargan, and S. Pawson, 2016: Tropospheric column ozone response to ENSO in GEOS-5 assimilation of OMI and MLS ozone data. *Atmospheric Chemistry and Physics*, **16**, 7091–7103, doi:10.5194/acp-16-7091-2016.

Oman, L. D., A. R. Douglass, J. R. Ziemke, J. M. Rodriguez, D. W. Waugh, and J. E. Nielsen, 2013: The ozone response to ENSO in Aura satellite measurements and a chemistry-climate simulation. *Journal of Geophysical Research: Atmospheres*, **118**, 965–976, doi:10.1029/2012JD018546.

Oman, L. D., J. R. Ziemke, A. R. Douglass, D. W. Waugh, C. Lang, J. M. Rodriguez, and J. E. Nielsen, 2011: The response of tropical tropospheric ozone to ENSO. *Geophysical Research Letters*, **38**, doi:10.1029/2011GL047865.

Pagowski, M., G. A. Grell, S. A. McKeen, S. E. Peckham, and D. Devenyi, 2010: Three-dimensional variational data assimilation of ozone and fine particulate matter observations: Some results using the Weather Research and Forecasting-Chemistry model and Grid-point Statistical Interpolation. *Quarterly Journal of the Royal Meteorological Society*, **136**, 2013–2024, doi:10.1002/QJ.700.

Pan, X., C. Ichoku, M. Chin, H. Bian, A. Darmenov, P. Colarco, L. Ellison, T. Kucsera, A. Da Silva, J. Wang, T. Oda, and G. Cui, 2020: Six global biomass burning emission datasets: Intercomparison and application in one global aerosol model. *Atmospheric Chemistry and Physics*, **20**, 969–994, doi:10.5194/ACP-20-969-2020.

Park, M., H. M. Worden, D. E. Kinnison, B. Gaubert, S. Tilmes, L. K. Emmons, M. L. Santee, L. Froidevaux, and C. D. Boone, 2021: Fate of Pollution Emitted During the 2015 Indonesian Fire Season. *Journal of Geophysical Research: Atmospheres*, **126**, e2020JD033474, doi:10.1029/2020JD033474.

Parrington, M., P. I. Palmer, D. K. Henze, D. W. Tarasick, E. J. Hyer, R. C. Owen, D. Helmig, C. Clerbaux, K. W. Bowman, M. N. Deeter, E. M. Barratt, P.-F. Coheur, D. Hurtmans, Z. Jiang, M. George, and J. R. Worden, 2012: The influence of boreal biomass burning emissions on the distribution of tropospheric ozone over North America and the North Atlantic during 2010. *Atmos. Chem. Phys*, **12**, doi:10.5194/acp-12-2077-2012.

Parrington, M., P. I. Palmer, A. C. Lewis, J. D. Lee, A. R. Rickard, P. Di Carlo, J. W. Taylor, J. R. Hopkins, S. Punjabi, D. E. Oram, G. Forster, E. Aruffo, S. J. Moller, S. J.-B. Bauguitte, J. D. Allan, H. Coe, and R. J. Leigh, 2013: Ozone photochemistry in boreal biomass burning plumes. *Atmos. Chem. Phys*, **13**, 7321–7341, doi:10.5194/acp-13-7321-2013.

Parrish, D. F. and J. C. Derber, 1992: The National Meteorological Center's Spectral Statistical-Interpolation Analysis System. *Monthly Weather Review*, **120**, 1747–1763, doi:10.1175/1520-0493(1992)120¡1747:TNMCSS¿2.0.CO;2.

Permar, W., Q. Wang, V. Selimovic, C. Wielgasz, R. J. Yokelson, R. S. Hornbrook, A. J. Hills, E. C. Apel, I.-T. Ku, Y. Zhou, B. C. Sive, A. P. Sullivan, J. L. Collett Jr, T. L. Campos, B. B. Palm, Q. Peng, J. A. Thornton, L. A. Garofalo, D. K. Farmer, S. M. Kreidenweis, E. J. T. Levin, P. J. DeMott, F. Flocke, E. V. Fischer, and L. Hu, 2021: Emissions of Trace Organic Gases From Western U.S. Wildfires Based on WE-CAN Aircraft Measurements. *Journal of Geophysical Research: Atmospheres*, **126**, e2020JD033838, doi:10.1029/2020JD033838.

Peters, W., M. Krol, F. Dentener, and J. Lelieveld, 2001: Identification of an El Niño-Southern Oscillation signal in a multiyear global simulation of tropospheric ozone. Technical report.

Peterson, D. A., E. J. Hyer, J. R. Campbell, M. D. Fromm, J. W. Hair, C. F. Butler, and M. A. Fenn, 2015: The 2013 Rim Fire: Implications for Predicting Extreme Fire Spread, Pyroconvection, and Smoke Emissions. doi:10.1175/BAMS-D-14-00060.1.

Pierce, R. B., J. Al-Saadi, C. Kittaka, T. Schaack, A. Lenzen, K. Bowman, J. Szykman, A. Soja, T. Ryerson, A. M. Thompson, P. Bhartia, and G. A. Morris, 2009: Impacts of background ozone production on Houston and Dallas, Texas, air quality during the Second Texas Air Quality Study field mission. *Journal of Geophysical Research: Atmospheres*, **114**, doi:10.1029/2008JD011337.

Pierce, R. B., J. A. Al-Saadi, R. S. Eckman, T. D. Fairlie, W. L. Grose, M. M. Kleb, M. Natarajan, and J. R. Olson, 2000: Dynamical climatology of the NASA Langley Research Center Interactive Modeling Project for Atmospheric Chemistry and Transport (IMPACT) model. *Journal of Geophysical Research: Atmospheres*, **105**, 29109–29134, doi:10.1029/2000JD900248.

Pierce, R. B., J. A. Al-Saadi, T. Schaack, A. Lenzen, T. Zapotocny, D. Johnson, C. Kittaka, M. Buker, M. H. Hitchman, G. Tripoli, T. D. Fairlie, J. R. Olson, M. Natarajan, J. Crawford, J. Fishman, M. Avery, E. V. Browell, J. Creilson, Y. Kondo, and S. T. Sandholm, 2003: Regional Air Quality Modeling System (RAQMS) predictions of the tropospheric ozone budget over east Asia. *Journal of Geophysical Research: Atmospheres*, **108**, doi:10.1029/2002JD003176.

Pierce, R. B., T. Schaack, J. A. Al-Saadi, T. D. Fairlie, C. Kittaka, G. S. Lingenfelser, M. Natarajan, J. R. Olson, A. J. Soja, T. Zapotocny, A. Lenzen, J. Stobie, D. Johnson, M. A. Avery, G. W. Sachse, A. Thompson, R. Cohen, J. E. Dibb, J. H. Crawford, D. F. Rault, R. Martin, J. Szykman, and J. Fishman, 2007: Chemical data assimilation estimates of continental U.S. ozone and nitrogen budgets during the Intercontinental Chemical Transport Experiment-North America. *Journal of Geophysical Research Atmospheres*, **112**, doi:10.1029/2006JD007722.

Putman, W. M. and S. J. Lin, 2007: Finite-volume transport on various cubed-sphere grids. *Journal of Computational Physics*, **227**, 55–78, doi:10.1016/j.jcp.2007.07.022.

Reid, J. S., E. J. Hyer, R. S. Johnson, B. N. Holben, R. J. Yokelson, J. Zhang, J. R. Campbell, S. A. Christopher, L. Di Girolamo, L. Giglio, R. E. Holz, C. Kearney, J. Miettinen, E. A. Reid, F. J. Turk, J. Wang, P. Xian, G. Zhao, R. Balasubramanian, B. N. Chew, S. Janjai, N. Lagrosas, P. Lestari, N.-H. Lin, M. Mahmud, A. X. Nguyen, B. Norris, N. T. K. Oanh, M. Oo, S. V. Salinas, E. J. Welton, and S. C. Liew, 2013: Observing and understanding the Southeast Asian aerosol system by remote sensing: An initial review and analysis for the Seven Southeast Asian Studies (7SEAS) program. *Atmospheric Research*, **122**, 403–468, doi:10.1016/j.atmosres.2012.06.005.

Reid, J. S., H. B. Maring, G. T. Narisma, S. van den Heever, L. D. Girolamo, R. Ferrare, P. Lawson, G. G. Mace, J. B. Simpas, S. Tanelli, L. Ziemba, B. van Diedenhoven, R. Bruintjes, A. Bucholtz, B. Cairns, M. O. Cambaliza, G. Chen, G. S. Diskin, J. H. Flynn, C. A. Hostetler, R. E. Holz, T. J. Lang, K. S. Schmidt, G. Smith, A. Sorooshian, E. J. Thompson, K. L. Thornhill, C. Trepte, J. Wang, S. Woods, S. Yoon, M. Alexandrov, S. Alvarez, C. G. Amiot, J. R. Bennett, M. Brooks, S. P. Burton, E. Cayanan, H. Chen, A. Collow, E. Crosbie, A. DaSilva, J. P. DiGangi, D. D. Flagg, S. W. Freeman, D. Fu, E. Fukada, M. R. A. Hilario, Y. Hong, S. M. Hristova-Veleva, R. Kuehn, R. S. Kowch, G. R. Leung, J. Loveridge, K. Meyer, R. M. Miller, M. J. Montes, J. N. Moum, A. Nenes, S. W. Nesbitt, M. Norgren, E. P. Nowottnick, R. M. Rauber, E. A. Reid, S. Rutledge, J. S. Schlosser, T. T. Sekiyama, M. A. Shook, G. A. Sokolowsky, S. A. Stamnes, T. Y. Tanaka, A. Wasilewski, P. Xian, Q. Xiao, Z. Xu, and J. Zavaleta, 2023: The Coupling Between Tropical Meteorology, Aerosol Lifecycle, Convection, and Radiation during the Cloud, Aerosol and Monsoon Processes Philippines Experiment

(CAMP2Ex). *Bulletin of the American Meteorological Society*, **104**, E1179–E1205, doi:10.1175/BAMS-D-21-0285.1.

Remer, L. A., Y. J. Kaufman, D. Tanré, S. Mattoo, D. A. Chu, J. V. Martins, R. R. Li, C. Ichoku, R. C. Levy, R. G. Kleidman, T. F. Eck, E. Vermote, and B. N. Holben, 2005: The MODIS Aerosol Algorithm, Products, and Validation. *Journal of the Atmospheric Sciences*, **62**, 947–973, doi:10.1175/JAS3385.1.

Rowlinson, M. J., A. Rap, S. R. Arnold, R. J. Pope, M. P. Chipperfield, J. McNorton, P. Forster, H. Gordon, K. J. Pringle, W. Feng, B. J. Kerridge, B. L. Latter, and R. Siddans, 2019: Impact of El Niño–Southern Oscillation on the interannual variability of methane and tropospheric ozone. *Atmospheric Chemistry and Physics*, **19**, 8669–8686, doi:10.5194/acp-19-8669-2019.

Sachse, G. W., J. E. C. Jr, G. F. Hill, L. O. Wade, L. G. Burney, and J. A. Ritter, 1991: Airborne tunable diode laser sensor for high-precision concentration and flux measurements of carbon monoxide and methane. *Measurement of Atmospheric Gases*, SPIE, volume 1433, 157–166.

Santoso, A., M. J. Mcphaden, and W. Cai, 2017: The Defining Characteristics of ENSO Extremes and the Strong 2015/2016 El Niño. *Reviews of Geophysics*, **55**, 1079–1129, doi:10.1002/2017RG000560.

Schaack, T. K., T. H. Zapotocny, A. J. Lenzen, and D. R. Johnson, 2004: Global Climate Simulation with the University of Wisconsin Global Hybrid Isentropic Coordinate Model. *Journal of Climate*, **17**, 2998–3016, doi:10.1175/1520-0442(2004)017¡2998:GCSWTU¿2.0.CO;2.

Seiler, W. and P. J. Crutzen, 1980: Estimates of gross and net fluxes of carbon between the biosphere and the atmosphere from biomass burning. *Climatic Change 1980 2:3*, **2**, 207–247, doi:10.1007/BF00137988.

Sekiya, T., K. Miyazaki, H. Eskes, K. Sudo, M. Takigawa, and Y. Kanaya, 2022: A comparison of the impact of TROPOMI and OMI tropospheric NO_2 on global chemical data assimilation. *Atmospheric Measurement Techniques*, **15**, 1703–1728, doi:10.5194/amt-15-1703-2022.

Sekiya, T., K. Miyazaki, K. Ogochi, K. Sudo, M. Takigawa, H. Eskes, and K. F. Boersma, 2021: Impacts of Horizontal Resolution on Global Data Assimilation of Satellite Measurements for Tropospheric Chemistry Analysis. *Journal of Advances in Modeling Earth Systems*, **13**, e2020MS002180, doi:10.1029/2020MS002180.

Sekiya, T. and K. Sudo, 2012: Role of meteorological variability in global tropospheric ozone during 1970–2008. *Journal of Geophysical Research: Atmospheres*, **117**, doi:10.1029/2012JD018054.

— 2014: Roles of transport and chemistry processes in global ozone change on interannual and multidecadal time scales. *Journal of Geophysical Research: Atmospheres*, **119**, 4903–4921, doi:10.1002/2013JD020838.

Senande-Rivera, M., D. Insua-Costa, and G. Miguez-Macho, 2022: Spatial and temporal expansion of global wildland fire activity in response to climate change. *Nature Communications*, **13**, 1208, doi:10.1038/s41467-022-28835-2.

Shindell, D. T., G. Faluvegi, D. S. Stevenson, M. C. Krol, L. K. Emmons, J.-F. Lamarque, G. Pétron, F. J. Dentener, K. Ellingsen, M. G. Schultz, O. Wild, M. Amann, C. S. Atherton, D. J. Bergmann, I. Bey, T. Butler, J. Cofala, W. J. Collins, R. G. Derwent, R. M. Doherty, J. Drevet, H. J. Eskes, A. M. Fiore, M. Gauss, D. A. Hauglustaine, L. W. Horowitz, I. S. A. Isaksen, M. G. Lawrence, V. Montanaro, J.-F. Müller, G. Pitari, M. J. Prather, J. A. Pyle, S. Rast, J. M. Rodriguez, M. G. Sanderson, N. H. Savage, S. E. Strahan, K. Sudo, S. Szopa, N. Unger, T. P. C. van Noije, and G. Zeng, 2006: Multimodel simulations of carbon monoxide: Comparison with observations and projected near-future changes. *Journal of Geophysical Research: Atmospheres*, **111**, doi:10.1029/2006JD007100.

Singh, H. B., W. Viezee, Y. Chen, J. Bradshaw, S. Sandholm, D. Blake, N. Blake, B. Heikes, J. Snow, R. Talbot, E. Browell, G. Gregory, G. Sachse, and S. Vay, 2000: Biomass burning influences on the composition of the remote South Pacific troposphere: Analysis based on observations from PEM-Tropics-A. *Atmospheric Environment*, **34**, 635–644, doi:10.1016/S1352-2310(99)00380-5.

Soja, A. J., W. R. Cofer, H. H. Shugart, A. I. Sukhinin, P. W. Stackhouse Jr., D. J. McRae, and S. G. Conard, 2004: Estimating fire emissions and disparities in boreal Siberia (1998–2002). *Journal of Geophysical Research: Atmospheres*, **109**, doi:10.1029/2004JD004570.

Spackman, J. R., J. P. Schwarz, R. S. Gao, L. A. Watts, D. S. Thomson, D. W. Fahey, J. S. Holloway, J. A. de Gouw, M. Trainer, and T. B. Ryerson, 2008: Empirical correlations between black carbon aerosol and carbon monoxide in the lower and middle troposphere. *Geophysical Research Letters*, **35**, doi:10.1029/2008GL035237.

Sterling, C. W., B. J. Johnson, S. J. Oltmans, H. G. J. Smit, A. F. Jordan, P. D. Cullis, E. G. Hall, A. M. Thompson, and J. C. Witte, 2018: Homogenizing and estimating the uncertainty in NOAA's long-term vertical ozone profile records measured with the electrochemical concentration cell ozonesonde. *Atmospheric Measurement Techniques*, **11**, 3661–3687, doi:10.5194/amt-11-3661-2018.

Stobie, JM., 2000: Algorithm theoretical basis document for statistical digital filter (SDF) analysis system (stretch-grid version). *Data Assimilation Office, NASA Goddard Space Flight Center, Greenbelt, MD*, **20771**.

Stockwell, C. E., M. M. Bela, M. M. Coggon, G. I. Gkatzelis, E. Wiggins, E. M. Gargulinski, T. Shingler, M. Fenn, D. Griffin, C. D. Holmes, X. Ye, P. E. Saide, I. Bourgeois, J. Peischl, C. C. Womack, R. A. Washenfelder, P. R. Veres, J. A. Neuman, J. B. Gilman, A. Lamplugh, R. H. Schwantes, S. A. McKeen, A. Wisthaler, F. Piel, H. Guo, P. Campuzano-Jost, J. L. Jimenez, A. Fried, T. F. Hanisco, L. G. Huey, A. Perring, J. M. Katich, G. S. Diskin, J. B. Nowak, T. P. Bui, H. S. Halliday, J. P. DiGangi, G. Pereira, E. P. James, R. Ahmadov, C. A. McLinden, A. J. Soja, R. H. Moore, J. W.

Hair, and C. Warneke, 2022: Airborne Emission Rate Measurements Validate Remote Sensing Observations and Emission Inventories of Western U.S. Wildfires. *Environmental Science & Technology*, **56**, 7564–7577, doi:10.1021/acs.est.1c07121.

Strode, S. A., B. N. Duncan, E. A. Yegorova, J. Kouatchou, J. R. Ziemke, and A. R. Douglass, 2015: Implications of carbon monoxide bias for methane lifetime and atmospheric composition in chemistry climate models. *Atmospheric Chemistry and Physics*, **15**, 11789–11805, doi:10.5194/acp-15-11789-2015.

Sudo, K. and M. Takahashi, 2001: Simulation of tropospheric ozone changes during 1997–1998 El Niño: Meteorological impact on tropospheric photochemistry. *Geophysical Research Letters*, **28**, 4091–4094, doi:10.1029/2001GL013335.

Tang, Y., P. C. Campbell, P. Lee, R. Saylor, F. Yang, B. Baker, D. Tong, A. Stein, J. Huang, H.-C. Huang, L. Pan, J. McQueen, I. Stajner, J. Tirado-Delgado, Y. Jung, M. Yang, I. Bourgeois, J. Peischl, T. Ryerson, D. Blake, J. Schwarz, J.-L. Jimenez, J. Crawford, G. Diskin, R. Moore, J. Hair, G. Huey, A. Rollins, J. Dibb, and X. Zhang, 2022: Evaluation of the NAQFC driven by the NOAA Global Forecast System (version 16): Comparison with the WRF-CMAQ during the summer 2019 FIREX-AQ campaign. *Geoscientific Model Development*, **15**, 7977–7999, doi:10.5194/gmd-15-7977-2022.

Thompson, A. M., R. M. Stauffer, K. Wargan, J. C. Witte, D. E. Kollonige, and J. R. Ziemke, 2021: Regional and Seasonal Trends in Tropical Ozone From SHADOZ Profiles: Reference for Models and Satellite Products. *Journal of Geophysical Research:*

Atmospheres, **126**, e2021JD034691, doi:10.1029/2021JD034691.

Thompson, A. M., J. C. Witte, C. Sterling, A. Jordan, B. J. Johnson, S. J. Oltmans, M. Fujiwara, H. Vömel, M. Allaart, A. Piters, G. J. R. Coetzee, F. Posny, E. Corrales, J. A. Diaz, C. Félix, N. Komala, N. Lai, H. T. Ahn Nguyen, M. Maata, F. Mani, Z. Zainal, S.-y. Ogino, F. Paredes, T. L. B. Penha, F. R. da Silva, S. Sallons-Mitro, H. B. Selkirk, F. J. Schmidlin, R. Stübi, and K. Thiongo, 2017: First Reprocessing of Southern Hemisphere Additional Ozonesondes (SHADOZ) Ozone Profiles (1998–2016): 2. Comparisons With Satellites and Ground-Based Instruments. *Journal of Geophysical Research: Atmospheres*, **122**, 13,000–13,025, doi:10.1002/2017JD027406.

Tian, C., X. Yue, J. Zhu, H. Liao, Y. Yang, L. Chen, X. Zhou, Y. Lei, H. Zhou, and Y. Cao, 2023: Projections of fire emissions and the consequent impacts on air quality under 1.5 °C and 2 °C global warming. *Environmental Pollution*, **323**, 121311, doi:10.1016/j.envpol.2023.121311.

Trenberth, K. E., 1997: The Definition of El Niño. *Bulletin of the American Meteorological Society*, **78**, 2771–2778, doi:10.1175/1520-0477(1997)078¡2771:TDOENO¿2.0.CO;2.

van der Werf, G. R., J. Dempewolf, S. N. Trigg, J. T. Randerson, P. S. Kasibhatla, L. Giglio, D. Murdiyarso, W. Peters, D. C. Morton, G. J. Collatz, A. J. Dolman, and R. S. DeFries, 2008: Climate regulation of fire emissions and deforestation in equatorial Asia. *Proceedings of the National Academy of Sciences*, **105**, 20350–20355, doi:10.1073/pnas.0803375105.

van der Werf, G. R., J. T. Randerson, L. Giglio, T. T. van Leeuwen, Y. Chen, B. M. Rogers, M. Mu, M. J. E. van Marle, D. C. Morton, G. J. Collatz, R. J. Yokelson, and P. S. Kasibhatla, 2017: Global fire emissions estimates during 1997–2016. *Earth System Science Data*, **9**, 697–720, doi:10.5194/essd-9-697-2017.

Veefkind, J. P., I. Aben, K. McMullan, H. Förster, J. de Vries, G. Otter, J. Claas, H. J. Eskes, J. F. de Haan, Q. Kleipool, M. van Weele, O. Hasekamp, R. Hoogeveen, J. Landgraf, R. Snel, P. Tol, P. Ingmann, R. Voors, B. Kruizinga, R. Vink, H. Visser, and P. F. Levelt, 2012: TROPOMI on the ESA Sentinel-5 Precursor: A GMES mission for global observations of the atmospheric composition for climate, air quality and ozone layer applications. *Remote Sensing of Environment*, **120**, 70–83, doi:10.1016/j.rse.2011.09.027.

Wallace, J. M., R. L. Panetta, and J. Estberg, 1993: Representation of the Equatorial Stratospheric Quasi-Biennial Oscillation in EOF Phase Space.

Wang, X., D. Parrish, D. Kleist, and J. Whitaker, 2013: GSI 3DVar-Based Ensemble–Variational Hybrid Data Assimilation for NCEP Global Forecast System: Single-Resolution Experiments. *Monthly Weather Review*, **141**, 4098–4117, doi:10.1175/MWR-D-12-00141.1.

Warneke, C., J. P. Schwarz, J. Dibb, O. Kalashnikova, G. Frost, J. Al-Saad, S. S. Brown, W. A. Brewer, A. Soja, F. C. Seidel, R. A. Washenfelder, E. B. Wiggins, R. H. Moore, B. E. Anderson, C. Jordan, T. I. Yacovitch, S. C. Herndon, S. Liu, T. Kuwayama, D. Jaffe, N. Johnston, V. Selimovic, R. Yokelson, D. M. Giles, B. N. Holben, P. Goloub,

I. Popovici, M. Trainer, A. Kumar, R. B. Pierce, D. Fahey, J. Roberts, E. M. Gargulinski, D. A. Peterson, X. Ye, L. H. Thapa, P. E. Saide, C. H. Fite, C. D. Holmes, S. Wang, M. M. Coggon, Z. C. J. Decker, C. E. Stockwell, L. Xu, G. Gkatzelis, K. Aikin, B. Lefer, J. Kaspari, D. Griffin, L. Zeng, R. Weber, M. Hastings, J. Chai, G. M. Wolfe, T. F. Hanisco, J. Liao, P. Campuzano Jost, H. Guo, J. L. Jimenez, J. Crawford, and T. F.-A. S. Team, 2023: Fire Influence on Regional to Global Environments and Air Quality (FIREX-AQ). *Journal of Geophysical Research: Atmospheres*, **128**, e2022JD037758, doi:10.1029/2022JD037758.

Watson, C. E., J. Fishman, and H. G. Reichle, 1990: The significance of biomass burning as a source of carbon monoxide and ozone in the southern hemisphere tropics: A satellite analysis. *Journal of Geophysical Research: Atmospheres*, **95**, 16443–16450, doi:10.1029/JD095ID10P16443.

Wiedinmyer, C., S. K. Akagi, R. J. Yokelson, L. K. Emmons, J. A. Al-Saadi, J. J. Orlando, and A. J. Soja, 2011: The Fire INventory from NCAR (FINN): A high resolution global model to estimate the emissions from open burning. *Geoscientific Model Development*, **4**, 625–641, doi:10.5194/gmd-4-625-2011.

Wiedinmyer, C., Y. Kimura, E. C. McDonald-Buller, L. K. Emmons, R. R. Buchholz, W. Tang, K. Seto, M. B. Joseph, K. C. Barsanti, A. G. Carlton, and R. Yokelson, 2023: The Fire Inventory from NCAR version 2.5: An updated global fire emissions model for climate and chemistry applications. *Geoscientific Model Development*, **16**, 3873–3891, doi:10.5194/gmd-16-3873-2023.

Wiedinmyer, C., B. Quayle, C. Geron, A. Belote, D. McKenzie, X. Zhang, S. O'Neill, and K. K. Wynne, 2006: Estimating emissions from fires in North America for air quality modeling. *Atmospheric Environment*, **40**, 3419–3432, doi:10.1016/j.atmosenv.2006.02.010.

Wiggins, E. B., A. J. Soja, E. Gargulinski, H. S. Halliday, R. B. Pierce, C. C. Schmidt, J. B. Nowak, J. P. DiGangi, G. S. Diskin, J. M. Katich, A. E. Perring, J. P. Schwarz, B. E. Anderson, G. Chen, E. C. Crosbie, C. Jordan, C. E. Robinson, K. J. Sanchez, T. J. Shingler, M. Shook, K. L. Thornhill, E. L. Winstead, L. D. Ziemba, and R. H. Moore, 2020: High Temporal Resolution Satellite Observations of Fire Radiative Power Reveal Link Between Fire Behavior and Aerosol and Gas Emissions. *Geophysical Research Letters*, **47**, e2020GL090707, doi:10.1029/2020GL090707.

Witte, J. C., A. M. Thompson, H. G. J. Smit, M. Fujiwara, F. Posny, G. J. R. Coetzee, E. T. Northam, B. J. Johnson, C. W. Sterling, M. Mohamad, S.-Y. Ogino, A. Jordan, and F. R. da Silva, 2017: First reprocessing of Southern Hemisphere ADditional OZonesondes (SHADOZ) profile records (1998–2015): 1. Methodology and evaluation. *Journal of Geophysical Research: Atmospheres*, **122**, 6611–6636, doi:10.1002/2016JD026403.

Witte, J. C., A. M. Thompson, H. G. J. Smit, H. Vömel, F. Posny, and R. Stübi, 2018: First Reprocessing of Southern Hemisphere ADditional OZonesondes Profile Records: 3. Uncertainty in Ozone Profile and Total Column. *Journal of Geophysical Research: Atmospheres*, **123**, 3243–3268, doi:10.1002/2017JD027791.

Wooster, M. J., G. J. Roberts, L. Giglio, D. P. Roy, P. H. Freeborn, L. Boschetti, C. Justice, C. Ichoku, W. Schroeder, D. Davies, A. M. S. Smith, A. Setzer, I. Csiszar, T. Strydom, P. Frost, T. Zhang, W. Xu, M. C. de Jong, J. M. Johnston, L. Ellison, K. Vadrevu, A. M. Sparks, H. Nguyen, J. McCarty, V. Tanpipat, C. Schmidt, and J. San-Miguel-Ayanz, 2021: Satellite remote sensing of active fires: History and current status, applications and future requirements. *Remote Sensing of Environment*, **267**, 112694, doi:10.1016/j.rse.2021.112694.

Wooster, M. J., B. Zhukov, and D. Oertel, 2003: Fire radiative energy for quantitative study of biomass burning: Derivation from the BIRD experimental satellite and comparison to MODIS fire products. *Remote Sensing of Environment*, **86**, 83–107, doi:10.1016/S0034-4257(03)00070-1.

Wu, W.-S., R. Purser, and D. Parrish, 2002: Three-Dimensional Variational Analysis with Spatially Inhomogeneous Covariances. *Monthly Weather Review - MON WEATHER REV*, **130**, doi:10.1175/1520-0493(2002)130¡2905:TDVAWS¿2.0.CO;2.

Xie, Y., M. Lin, B. Decharme, C. Delire, L. W. Horowitz, D. M. Lawrence, F. Li, and R. Séférian, 2022: Tripling of western US particulate pollution from wildfires in a warming climate. *Proceedings of the National Academy of Sciences*, **119**, e2111372119, doi:10.1073/pnas.2111372119.

Xin, Y., L. Sun, and M. C. Hansen, 2021: Biophysical and socioeconomic drivers of oil palm expansion in Indonesia. *Environmental Research Letters*, **16**, 034048, doi:10.1088/1748-9326/abce83.

Yin, Y., P. Ciais, F. Chevallier, G. R. van der Werf, T. Fanin, G. Broquet, H. Boesch, A. Cozic, D. Hauglustaine, S. Szopa, and Y. Wang, 2016: Variability of fire carbon emissions in equatorial Asia and its nonlinear sensitivity to El Niño. *Geophysical Research Letters*, **43**, 10,472–10,479, doi:10.1002/2016GL070971.

Young, P. J., V. Naik, A. M. Fiore, A. Gaudel, J. Guo, M. Y. Lin, J. L. Neu, D. D. Parrish, H. E. Rieder, J. L. Schnell, S. Tilmes, O. Wild, L. Zhang, J. Ziemke, J. Brandt, A. Delcloo, R. M. Doherty, C. Geels, M. I. Hegglin, L. Hu, U. Im, R. Kumar, A. Luhar, L. Murray, D. Plummer, J. Rodriguez, A. Saiz-Lopez, M. G. Schultz, M. T. Woodhouse, and G. Zeng, 2018: Tropospheric Ozone Assessment Report: Assessment of global-scale model performance for global and regional ozone distributions, variability, and trends. *Elementa: Science of the Anthropocene*, **6**, 10, doi:10.1525/elementa.265.

Yu, P., O. B. Toon, C. G. Bardeen, Y. Zhu, K. H. Rosenlof, R. W. Portmann, T. D. Thornberry, R.-S. Gao, S. M. Davis, E. T. Wolf, J. de Gouw, D. A. Peterson, M. D. Fromm, and A. Robock, 2019: Black carbon lofts wildfire smoke high into the stratosphere to form a persistent plume. *Science*, **365**, 587–590, doi:10.1126/science.aax1748.

Yue, X., L. J. Mickley, J. A. Logan, R. C. Hudman, M. V. Martin, and R. M. Yantosca, 2015: Impact of 2050 climate change on North American wildfire: Consequences for ozone air quality. *Atmospheric Chemistry and Physics*, **15**, 10033–10055, doi:10.5194/acp-15-10033-2015.

Yumimoto, K., T. Y. Tanaka, N. Oshima, and T. Maki, 2017: JRAero: The Japanese Reanalysis for Aerosol v1.0. *Geoscientific Model Development*, **10**, 3225–3253, doi:10.5194/gmd-10-3225-2017.

Yurganov, L. N., W. W. McMillan, A. V. Dzhola, E. I. Grechko, N. B. Jones, and G. R. van der Werf, 2008: Global AIRS and MOPITT CO measurements: Validation, comparison, and links to biomass burning variations and carbon cycle. *Journal of Geophysical Research: Atmospheres*, **113**, doi:10.1029/2007JD009229.

Zaveri, R. A. and L. K. Peters, 1999: A new lumped structure photochemical mechanism for large-scale applications. *Journal of Geophysical Research: Atmospheres*, **104**, 30387–30415, doi:10.1029/1999JD900876.

Zhang, G. and N. A. McFarlane, 1995: Sensitivity of climate simulations to the parameterization of cumulus convection in the Canadian climate centre general circulation model. *Atmosphere-Ocean*, **33**, 407–446, doi:10.1080/07055900.1995.9649539.

Zhang, G. J., J. T. Kiehl, and P. J. Rasch, 1998: Response of Climate Simulation to a New Convective Parameterization in the National Center for Atmospheric Research Community Climate Model (CCM3). *Journal of Climate*, **11**, 2097–2115, doi:10.1175/1520-0442(1998)011¡2097:ROCSTA¿2.0.CO;2.

Zhang, L., R. Montuoro, S. A. McKeen, B. Baker, P. S. Bhattacharjee, G. A. Grell, J. Henderson, L. Pan, G. J. Frost, J. McQueen, R. Saylor, H. Li, R. Ahmadov, J. Wang, I. Stajner, S. Kondragunta, X. Zhang, and F. Li, 2022: Development and evaluation of the Aerosol Forecast Member in the National Center for Environment Prediction (NCEP)'s Global Ensemble Forecast System (GEFS-Aerosols v1). *Geoscientific Model Development*, **15**, 5337–5369, doi:10.5194/gmd-15-5337-2022.

Zhang, X., S. Kondragunta, A. Da Silva, S. Lu, H. Ding, F. Li, and Y. Zhu, 2019: The Blended Global Biomass Burning Emissions Product from MODIS, VIIRS, and Geostaionary Satellites (GBBEPx) Version 3.1.

Zheng, B., F. Chevallier, Y. Yin, P. Ciais, A. Fortems-Cheiney, M. N. Deeter, R. J. Parker, Y. Wang, H. M. Worden, and Y. Zhao, 2019: Global atmospheric carbon monoxide budget 2000–2017 inferred from multi-species atmospheric inversions. *Earth System Science Data*, **11**, 1411–1436, doi:10.5194/essd-11-1411-2019.

Zheng, B., P. Ciais, F. Chevallier, E. Chuvieco, Y. Chen, and H. Yang, 2021: Increasing forest fire emissions despite the decline in global burned area. *Science Advances*, **7**, eabh2646, doi:10.1126/sciadv.abh2646.

Ziemke, J. R. and S. Chandra, 2003: La Nina and El Nino—induced variabilities of ozone in the tropical lower atmosphere during 1970–2001. *Geophysical Research Letters*, **30**, doi:10.1029/2002GL016387.

— 2012: Development of a climate record of tropospheric and stratospheric column ozone from satellite remote sensing: Evidence of an early recovery of global stratospheric ozone. *Atmos. Chem. Phys. Atmospheric Chemistry and Physics*, **12**, 5737–5753, doi:10.5194/acp-12-5737-2012.

Ziemke, J. R., S. Chandra, B. N. Duncan, L. Froidevaux, P. K. Bhartia, P. F. Levelt, and J. W. Waters, 2006: Tropospheric ozone determined from Aura OMI and

MLS: Evaluation of measurements and comparison with the Global Modeling Initiative's Chemical Transport Model. *Journal of Geophysical Research: Atmospheres*, **111**, doi:10.1029/2006JD007089.

Ziemke, J. R., S. Chandra, B. N. Duncan, M. R. Schoeberl, O. Torres, M. R. Damon, and P. K. Bhartia, 2009: Recent biomass burning in the tropics and related changes in tropospheric ozone. *Geophysical Research Letters*, **36**, doi:10.1029/2009GL039303.

Ziemke, J. R., S. Chandra, L. D. Oman, and P. K. Bhartia, 2010: A new ENSO index derived from satellite measurements of column ozone. *Atmospheric Chemistry and Physics*, **10**, 3711–3721, doi:10.5194/acp-10-3711-2010.

Ziemke, J. R., A. R. Douglass, L. D. Oman, S. E. Strahan, and B. N. Duncan, 2015: Tropospheric ozone variability in the tropics from ENSO to MJO and shorter timescales. *Atmospheric Chemistry and Physics*, **15**, 8037–8049, doi:10.5194/acp-15-8037-2015.